UNIVERSITY OF CAMBRIDGE

Alteration mechanisms of spent nuclear fuel and characterization of potential uranium secondary phases.

Beng Thye Tan

Wolfson College

April 2019

This dissertation is submitted for the degree of Doctor of Philosophy in Earth Sciences.

Preface

• This dissertation is the result of my own work and includes nothing which is the outcome of work done in collaboration except as declared in the Preface and specified in the text.

• It is not substantially the same as any that I have submitted, or, is being concurrently submitted for a degree or diploma or other qualification at the University of Cambridge or any other University or similar institution except as declared in the Preface and specified in the text. I further state that no substantial part of my dissertation has already been submitted, or, is being concurrently submitted for any such degree, diploma or other qualification at the University of Cambridge or any other University of similar institution except as declared in the Preface and specified in the text

• It does not exceed the prescribed word limit for the relevant Degree Committee, that is, it does not exceed 275 numbered pages of which not more than 225 pages are text, appendices, illustrations and bibliography.

Acknowledgements

I acknowledge funding from Singapore Nuclear Research and Safety Initiative, Cambridge Philosophical Society and the Earth Sciences Department of University of Cambridge. I am grateful for the kind advice and thorough guidance from many people who have made this dissertation possible.

I will like to express my heartfelt gratitude to my supervisor Dr Ian Farnan for his kind patience and guidance. Dr Gulio Lampronti's positive attitude towards radiation safety and enabling research is greatly appreciated. Lastly, I will like to thank my fellow PhD compatriots, who encouraged me to produce this work, such as Rui Guo, Tom Gout and most importantly, Aleksej Popel. The PhD process will be a lonely one without friends.

Isotopic enrichment of uranium secondary phases and the corresponding analysis was completed in Trinity College, Dublin. I will like to thank Prof Robert Baker and his staff for making this possible, particularly in the isotopic enrichment of studtite, which has been the centre piece of a paper on variable temperature NMR studies done to elucidate the differences between studtite and metastudtite.

Electrochemistry work was done at the University of Lancaster under close collaboration with Dr Richard Wilbraham where we worked closely on elucidating the electrochemical evolution of uranium electrodes under dissolution in anoxic conditions with various dopants.

ICPMS data was obtained with the help of Dr Jason Day and SEM/ EDX/ XRD/ EBSD techniques was taught by Dr Gulio Lampronti from the Earth Sciences Department. NMR techniques, data analysis and critical thinking skills were improved under the tutelage of Dr Ian Farnan.

Table of Contents

Table of Figures

Chapter 1 Context of Research

In recent times, a renaissance of nuclear power is occurring with 50 new reactors under construction in 15 countries adding to the current 450 operating power reactors (World Nuclear Association, 2018) worldwide due to three main reasons; international efforts to decarbonise the global energy system because of climate change; concerns of some nations about energy security; China's change of energy policy driven by the need for cleaner air in cities, which brings with it a decarbonisation of its energy system.

1.1 Decarbonisation

At the Paris climate conference (COP21) (European Commision, 2015) in December 2015, 195 countries adopted the first-ever universal, legally binding global climate deal. This agreement aims to avoid climate change by limiting global warming to well below 2°C above pre-industrial levels by 2020. Concurring on the need for global emissions to peak as soon as possible and subsequently reduce rapidly, signatories undertook to ensure low greenhouse gas emissions development with successive nationally determined contributions to be prepared, communicated and achieved by domestic mitigation measures. Additionally, finance flows will be channelled towards development of low greenhouse gas emissions and climate-resilient developments. With this perspective, the International Atomic Energy Agency (IAEA) encouraged countries to consider nuclear energy on **equal footing** with other low-carbon energy sources because of its low life-cycle greenhouse gas emissions and high potential to bolster development effectively and sustainably.

Calculations from International Energy Agency (IEA) projects that, in order to achieve a reduced carbon emissions goal, the share of nuclear energy in global electricity generating capacity needs to rise from about 400 GW now to 1,000 GW by 2050, producing about 9 trillion kWh/ year. The case for rapid construction of nuclear reactors was made prominently by prominent scientists to building a new nuclear power station weekly (Caldeira *et al.*, 2013) to meet future energy demands without burning more fossil fuel by 2025, as baseload electricity cannot be fulfilled by renewables, especially in regions of high population density, such as Singapore.

1.2 Energy security and scarcity of fossil fuels

Energy security is defined by the IEA (International Energy Agency, 2016) to be the uninterruptible availability of energy sources at an affordable price. Energy security and scarcity of fossil fuels are reasons that propel even oil-rich countries such as Saudi Arabia to construct nuclear power plants for power and desalination purposes (Ahmad and Ramana, 2014; World Nuclear Association, 2018b) . 2014 and 2015 saw the prices of oil fluctuating between US$27 and US$145 per barrel. States grappled with volatile oil and gas markets with volatile fuel costs and hedging costs resulting in fiscal and monetary difficulties in both oil-importing and exporting nations. The use of nuclear power for base load electricity helps to reduce such uncertainties.

1.3 China's policy

1.3.1 Change in energy mix to address air pollution

Heavy air pollution in China has led to strong political will on the reduction of fossil- fuel energy production. It was announced in China's 2016 5- Year Plan, which mapped out its developmental focus, that 20% of its projected primary energy consumption by 2030 will be non-fossil-fuel dependent along with reducing CO_2 emissions by 60 to 65% from 2005 levels by 2030. To achieve that, planned nuclear energy will provide an electric output of 120 to 150 GW, a significant 8% to 10% of the total energy production. This marks a threefold increase from the 40.6 GW output from nuclear energy currently (World Nuclear Association, 2018a). In fact, even in recent years, nuclear energy production has gone up by 24% from 2015 to 2016 and 16% from 2016 to 2017, culminating to 4% of the total electricity supply. 11 out of 24 of the new build reactors in 2019 to 2020 will be built in China, accounting for 44% of the new nuclear power (11.8 GW electric output) [See Appendix 1]

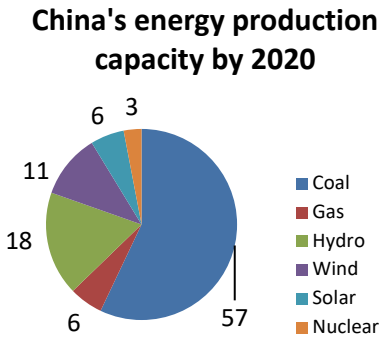

Figure 1-1 Planned energy generation capacity in China in 2020: Note that the increase in production capacity does not correspond directly with energy output due to curtailment by inadequate grid connections (for wind energy) and variable weather.

1.3.2 Nuclear energy export

China's recent efforts in exporting nuclear technology have met with a large degree of success. In January 2015, China announced new incentives and financing for industry exports, particularly nuclear power and railways, on the back of $103 billion outbound trade and investment in 2014. These incentives are backed with strong political will of the Chinese Communist Party. Notably, President Xi Jinping visited Argentina, Pakistan, United Kingdom, Romania and Turkey in 2014 and 2015. These visits have been constructive diplomatic trips that have seen the conclusion of nuclear power deals with the upfront financial requirements often borne by China. [See Appendix 2]

The Belt & Road Initiative (BRI) was formally launched in May 2017 to boost global connectivity and trade. Projects in Pakistan, Indonesia, eastern Europe and northern Africa were supported as part of this initiatives with Chinese funding of $75 billion from banks, $20 billion through a new Silk Road Fund, and $12 billion as foreign aid. From China's enthusiasm in sealing nuclear deals on its trade diplomacy strategy and its ability to finance the large capital investment in nuclear power plants for its clientele, it is foreseeable that more nuclear power plants being built and accepted in many countries.

1.3.3 Deep sea exploration and militarization of the South China Sea

Russian nuclear corporation launched its first floating nuclear power plant on April 28, 2018 to meet its growing electricity needs to develop oil resources in remote Arctic region. China National Nuclear Corporation (CNNC) and China General Nuclear Power Group (CGN) has planned to jointly deploy a Chinese nuclear power barge for deployment in the South China Sea to provide much- needed electricity and desalinated water to support its disputed island claims and offshore oil and gas exploration. The high energy density of uranium dioxide in nuclear fuel made such power barges feasible as this reduces the need to refuel for years. The amount of energy produced by 10 g of uranium dioxide is equivalent to the energy obtained from about 1100 m^3 gas, 900 dm^3 oil, or 5 tons of coal (Kónya and Nagy, 2012).

1.4 Spent Nuclear Fuel (SNF)

Additional nuclear reactors being planned and built will increase the generation of spent nuclear fuel, a problem that is slightly alleviated by the high energy density of uranium dioxide (Kónya and Nagy, 2012). However, given the long half-lives of uranium isotopes of about 700 million years for U-235 and 4.47 billion years for U-238, this is a long-term problem and needs to be assessed rigorously. There is some resistance to the expansion of nuclear power in western countries unless this problem is tackled. This thesis touches on some facets of this problem that are faced with the handling of spent nuclear fuel.

There are four major types of nuclear power plants which uses different media to slow down (moderate) fast- moving neutrons from fission reactions which means that they are more likely to result in other fission reactions due to the higher nuclear cross-sections of fissile elements for thermalized neutrons. Light Water Reactors (LWRs), uses water as a moderator and a coolant to carry away the produced heat and come in two forms, the most popular Pressurized Water Reactors (PWR) and Boiling Water Reactors (BWR). Apart from LWR, there is the Pressurized Heavy Water Reactor, which uses heavy water instead of normal water for moderation. The higher effective moderation by heavy water (D_2O) implies that the fuel need not be enriched, but its low power density and high cost of maintenance make it a less popular reactor. A third reactor type, Reaktor Bolshoy Moshchnosty Kanalny (RBMK) uses graphite as a moderator and light water as a coolant (Feiveson *et al.*, 2011). The last type of reactor that is particular significant in the UK is the Advanced Gas-cooled Reactor (AGR) as it accounts for 14 out of the 15 reactors operating here with the last being a PWR at Sizewell B. The AGR uses graphite as a moderator and carbon dioxide as a coolant(Nonbol, 1996). Nonetheless, most of these reactor fuels are composed primarily of uranium dioxide with varying degrees of U-235 enrichment. Table 1-1 was compiled for a reactor of 1GWe operating at 90% capacity and averaged over a reload cycle of 500 days for PWR at which point only 1/3 of fuel is removed and loaded with fresh fuel. Under most cases, the fuel will remain in the reactor for ~ 5 years.

Table 1-1 Annual discharge of spent fuel for three common reactor types. GWd/t_{HM} is the amount of thermal energy (heat in gigawatt-days released per ton of heavy metal (HM) in the fuel (Feiveson, Mian, et al., 2011).

Reactor type	Typical burnt-up (GWd/ t_{HM})	Annual Discharge of spent fuel (tons)
LWR	50	20
PHWR	7	140
RBMK	15	65
AGR	25	40

Hence by considering an efficiency of 30 % and an electrical output of 150 GW in one year, there will be an accrual of more than 200 tonnes of spent nuclear fuel per annum from China by 2030.

1.5 Chemical composition of SNF

Spent nuclear fuel is predominantly made up of uranium dioxide (Bruno and Ewing, 2006). Depending on burn-up and local position in the rod (the linear power rating), spent fuel is comprised of ~96 at% uranium dioxide (UO_2) matrix with ~3 at% of fission products and ~1 at% of transuranium elements. As such, previous studies have shown that the release of radionuclides (apart from instant release fractions (Serrano-Purroy *et al.*, 2012; Lemmens *et al.*, 2017) of several percent of total inventory for some radionuclides), is mainly dependent on dissolution of the UO_2 matrix under the oxygen-free environment of deep geological facilities (Shoesmith and Sunder, 1992; Shoesmith, 2000).

1.6 Open Disposal Cycle

With the large increase in nuclear power stations, nuclear waste management research is imperative. In “The Future of the Nuclear Fuel Cycle” (Massachusetts Institute of Technology, 2011), it was noted that the “once through” or open fuel cycle is likely to be the dominant feature of nuclear energy systems globally. It is the economically preferred option as there is no shortage of uranium resources that might constrain future commitments to build new nuclear plants for this century. The open fuel cycle reduces the need for processing of spent nuclear fuel, hence reducing the likelihood of nuclear proliferation of plutonium which may be obtained from processing. For a successful open fuel cycle, further research in long-term storage of spent nuclear fuel is vital. Such research can help to incorporate options for possible future utilization of the spent nuclear fuel to ensure that the future generation will be able to enjoy a world with a conducive climate for living and yet a safe environment from nuclear waste.

1.7 Spent Fuel Pool

After a few years of being in the reactor, spent nuclear fuel rods are replaced with fresh fuel rods from the reactor. At that present moment, these spent fuel rods generate intense heat and produce dangerous radiation. These fuel rods are placed into a 12- m deep spent nuclear fuel pool. The fuel bundles are cooled by water circulating through the pool for cooling before

being sorted into other parts of the pool to wait for final disposal. Water quality is tightly controlled to prevent the fuel or its cladding from degrading.

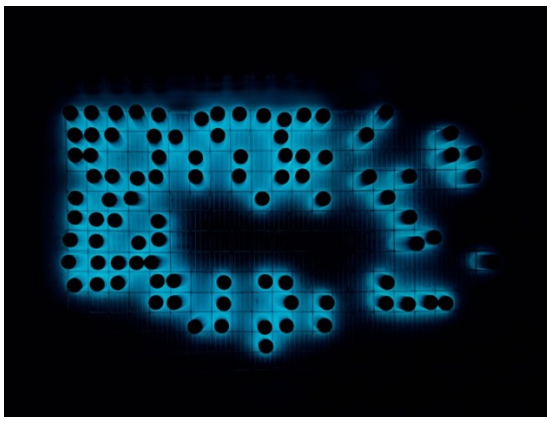

Figure 1-2 Nuclear Waste Encapsulation and Storage Facility, Hanford Site, Washington ©Taryn Simon

The Cherenkov radiation is the electromagnetic radiation that is produced when a charged particle, such as an electron passes through a medium with a velocity greater than the phase velocity of light.

Scientifically, this is a visual guide to show how the radiation emanates and decreases with increasing distance from the spent nuclear fuel. So, at the boundary of the spent nuclear fuel, there is possible interaction of spent nuclear fuel, radiation and water with its constituents.

1.8 Deep underground repository's conditions

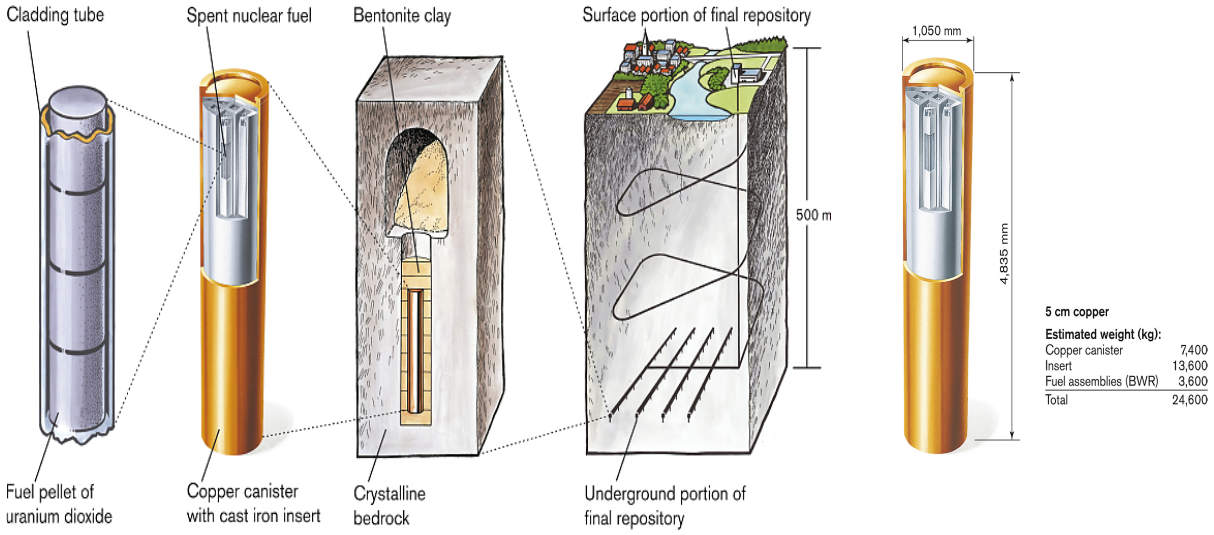

Figure 1-2 Loading of spent nuclear fuel into copper canister before disposal into a repository.

In the case of the KBS-3 disposal technology designed by the Swedish Nuclear and Waste Company (SKB), the depth of the planned nuclear waste repositories is 500 m below the surface of the ground (SKB, 2014). This technology will also be used in Finland's Onkalo spent nuclear fuel repository.

For planned nuclear fuel repositories, the depth of 500-1000 meters below the ground surface and the geological environment (granite or clay host rock) imposes chemical conditions on the dissolution mechanisms and hence experiments should be conducted in an attempt to simulate the possible real-life scenarios. The development of model systems related to the SimFuel experiments of the 1990s (Lucuta, Verrall, & Matzke, 1991) will allow a greater mechanistic understanding of dissolution mechanisms where simulated high-burnup nuclear fuel (SIMFUEL) replicates the chemical state and microstructure of irradiated fuel so that detailed experiments on fission-gas release, thermal conductivity and leaching can be undertaken in the laboratory.

The most probable mechanism by which radioactive actinides may escape into the environment from a deep geological repository is the intrusion of groundwater into the underground repository and the subsequent dissolution and transport of actinides out of the underground repository (Brotzen, 1983). Considering the timescale of the nuclear waste storage of $10^4 – 10^6$ years and hence high probability of water coming into contact with the waste during this period, a thorough understanding of the chemical reactions involved in this mechanism is needed in addition to the dissolution testing of spent nuclear fuel.

Chapter 2 Project Outline

This research thesis progresses along two pathways, alteration of spent nuclear fuel and identification of said alteration. The relative abundance of uranium as an energy resource, coupled with the high costs of spent nuclear fuel (SNF) reprocessing and the associated risks of nuclear proliferation make a strong case for direct disposal of SNF in deep underground geological disposal facilities (MIT, 2011; Tan *et al.*, 2019). The escape of radionuclides from underground spent nuclear fuel disposal facilities will likely result from anoxic dissolution of spent nuclear fuel by intruding groundwater with potential high alpha radioactivity from the spent fuel even after hundreds of years. Considering the lack of oxygen at repository depths of 500 m to few km below the Earth, anoxic dissolution experiments with uranium dioxide in various solid forms were conducted to investigate secondary phase formation, the escape of radioactivity in the form of dissolved uranium and electrochemical evolution to understand the redox changes happening in the surface and in the solution due to the interaction of water and spent nuclear fuel.

The other research thrust in this thesis is the analysis of potential secondary phases via non-destructive scientific techniques such as scanning electron microscopy (SEM), energy dispersive x-ray analysis (EDX), electron- backscattered diffraction (EBSD), X Ray Diffraction (XRD), Raman spectroscopy with a chapter dedicated to ^{17}O NMR. For the latter, given the long alteration timeline for uranium dioxide (as the solubility of uranium dioxide is in the order of 10^{-9} mol L^{-1}), it is challenging to achieve sufficient alteration products for analysis within a short 4-year PhD program. Some known uranium compounds were synthesized and enriched with ^{17}O, an NMR active isotope with spin 5/2 for investigation of their properties. The many advantages of NMR over conventional x- ray, or other diffraction-based techniques render this an important chapter, especially when alteration products may not be single- phase or crystalline.

2.1 Structure of Uranium Dioxide (UO_2)

Crystalline UO_2 exists as a face-centered cubic (fcc) sublattice of U^{4+} ions within a cubic O^{2-} sublattice to form a fluorite structure. In perfect stoichiometry, the uranium atom is coordinated by eight equivalent oxygen atoms at the corners of a cube, each of which is in turn surrounded by a tetrahedron of four equivalent U atoms. This fluorite structure is the most flexible in generating many derivative structures. This can be attributed to the existence of a large number of octahedral holes, which gives UO_2 the ability to accommodate large amounts of interstitial O to form hyper stoichiometric UO_{2+x} (shown in Figure 2-1) which are much more soluble, with the solubility product at the standard state, Ksp^o of U(VI) being significantly higher than that of U(IV), -22.46 vs -52.0 (Fujiwara *et al.*, 2005; Opel *et al.*, 2007).

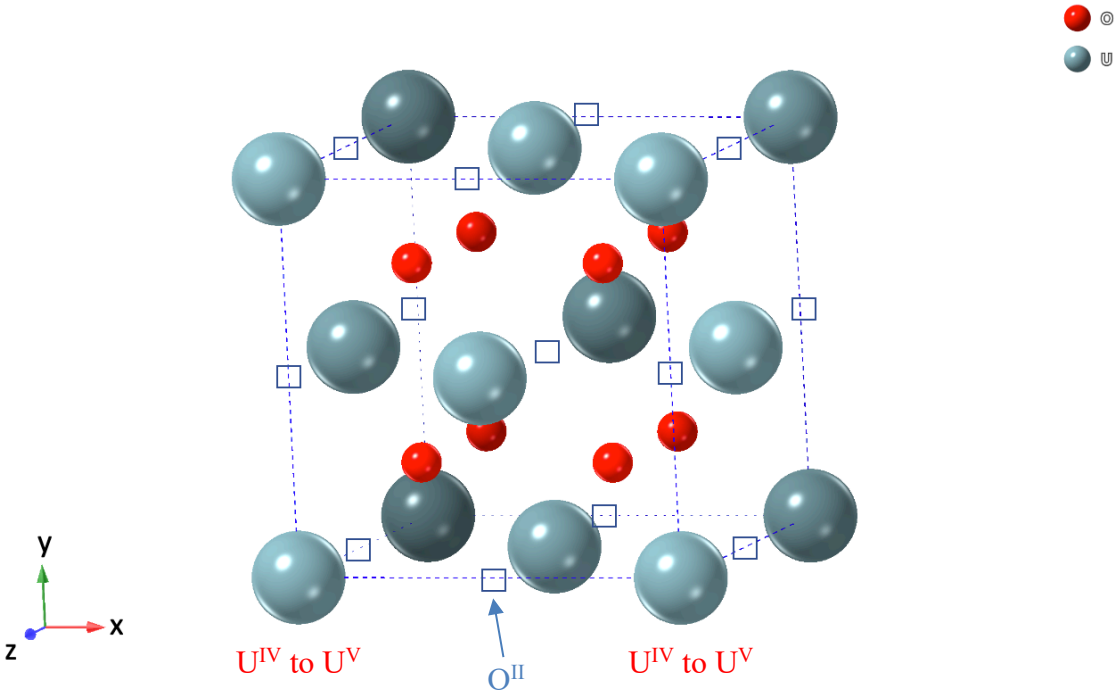

Figure 2-1 Structure of cubic fluorite structure of uranium dioxides and other actinide dioxides with the shaded dots being uranium atoms and the open dots being oxygen atoms. Added squares are cubically coordinated empty lattice sites which allows insertion of oxygen atoms during the onset of non-stoichiometry which will results in the formation of U(V) and U(VI) atoms to maintain charge balance.

Insertion of oxygen into these interstitial spacing occur readily thermodynamically since the energy of formation is negative at -0.37 to -2.5 eV (Nerikar *et al.*, 2009). Coupled with the ability of uranium to form multiple oxidation states from U(IV) to U(VI), this allows the formation of a complex family of binary metal oxides within the range UO_2 to U_3O_7 (Conradson *et al.*, 2004).

2.2 Anoxic dissolution of UO_2 of different forms

Anoxic conditions are likely to prevail in an underground repository. As the solubilities of An(IV) hydroxides or oxides are low, the possibility to investigate the aqueous speciation by spectroscopic methods is rather poor (Neck and Kim, 2001). The reported solubilities may include polynuclear or colloidal species but little information was available to quantify their presence in the past. In order to have a better understanding, a series of anoxic dissolution experiments was planned and executed (Tan *et al.*, 2019).

Anoxic dissolution involves the exclusion of dissolved oxygen in the experiments as far as reasonably possible. All dissolution experiments were conducted in positive pressure gloveboxes with an argon atmosphere with oxygen concentrations controlled to 0.1 ppm O_2 for the thin film and powder experiments and a nitrogen atmosphere of 2.0 ppm O_2 for the solid pellet experiments. In all cases, the dissolution experiments took place in sealed containers containing deoxygenated water. Deionized Milli-Q water (18.2 MΩ/cm), for both dissolution and sample washing, was sparged with 5 vol% H_2 in 95 vol% Ar gas mixture for 6 hours to reduce the amount of dissolved oxygen to a suitable low level. Post-sparging testing with CHEMetrics® Oxygen CHEMets Kit K-7540 revealed dissolved oxygen content below the detection limit of 2.5 ppb. Post-experimental solutions retained similar amount of dissolved oxygen content below the detection limit.

2.2.1 Sample preparation for dissolution experiments

Efforts have been taken to reduce the amount of U(VI) and U(V) from surface oxidation of the nominal UO_2 samples stored in an ambient atmosphere. Powder and thin film samples were reduced in a 5 vol% H_2, 95 vol% Ar atmosphere and heating to 800º C (Pijolat *et al.*, 1997). Sintered UO_2 pellets were polished with silicon carbide (SiC) sandpaper under deionized water to remove any oxidized surface layer of UO_{2+x} that arises from exposure to the atmosphere for extended periods of time (Leinders, 2018). Anderson *et al*. (Anderson, Roberts and Harper, 1949) have previously reported that such surface oxidation occurs slowly as a logarithmic function of time due to the chemisorption of oxygen at room temperatures. Pellet and thin film samples were subsequently pre-washed before undertaking dissolution experiments.

2.2.1.1 Solid Pellet Modification

For this research, sintered UO_2 pellets were used directly and their fabrication and initial characterisation of sintered UO_2 pellets has been previously reported by Hiezl *et al*. (Hiezl *et al.*, 2015) with additional characterisation by Popel *et al*. (Popel *et al.*, 2018). Briefly, the synthesis involved the sintering of depleted uranium (0.3 g ^{235}U/ 100 g UO_2) powder of particle size 3.80 ± 0.25 μm at a heating rate of 5 °C/ min to 300 °C, then 15 °C/ min to 1730 °C. Sintering was done in 300 min under atmosphere of 99.5% vol.% H_2 and 0.5 vol.% CO_2 with a subsequent 15 °C/ min cooling rate to room temperature. In order to make suitable electrodes for use in long-term dissolution experiments, stoichiometric UO_2, disc-shaped slices of sintered pellets (~1 cm diameter and ~1 mm thickness) were mounted onto a threaded brass rod using silver-loaded epoxy. This assembly was then placed in a cylindrically shaped mould and cast in epoxy resin in order to produce a suitable sealed working electrode. Prior to being characterised, the working electrodes were polished using 600 and 1200 grit SiC paper under deionized water (to avoid uranium dust formation). Such a polishing process reduces differences in electrode surface area between samples and enhances the reproducibility of triplicate dissolution experiments (5.2 Solid Pellet- ICP-MS results). Prior to dissolution, the polished surfaces were examined by scanning electron microscopy and Raman spectroscopy (5.3 Solid Pellet- Raman spectra) before placing them in 10 ml of deoxygenated, deionized water in a Nalgene® bottle for 21-hours pre-washing under a N_2 atmosphere with 2.0 ppm O_2. This pre-wash step again aims to remove any higher oxidation state uranium oxide phases which might have been formed, albeit slowly, in the processing atmosphere and relies on the higher solubility of surface UO_{2+x} phases vs. bulk UO_2. Previous literature studies (Rai, Felmy and Ryan, 1990; Neck and Kim, 2001; Fujiwara *et al.*, 2005) have found that the solubility product at the standard state, Ksp^o of U(VI) is -22.46, significantly higher than that of U(IV), -52.0 with slight variation dependent on solid form (Opel *et al.*, 2007).

2.2.1.2 Thin Film Fabrication

The thin film of UO_2 was produced by direct current reactive sputtering onto a single crystal Si substrate with (001) orientation using a Labstation machine at the European Commission Joint Research Centre (EC-JRC), Karlsruhe. The substrate was cleaned before the film deposition with ethanol and heated to ~600 °C under pO_2 of 2×10^{-6} mbar for 40–60 min (Tan *et al.*, 2019). A natural uranium metal target was used as a source of uranium with argon used as the sputtering gas at a pAr set to 5×10^{-3} mbar and O_2 used as the reactive gas at a pO_2 set

to 7 × 10^{-6} mbar. The Si substrate was maintained at a temperature close to 600 °C. The film was deposited for 30 minutes with deposition conditions which should give film thickness in the range from 90 to 270 nm. After fabrication, it was transferred to University of Cambridge for analysis and the sample was found to be stoichiometrically UO_2 from XRD data which remained similar after the leaching experiment . The thin film sample was then annealed in an anoxic glove box-attached furnace at 800 °C with a reducing mixture of 5 vol% H_2 in 95 vol% Ar for two hours, taking one hour to heat up and three hours to cool down. It was subsequently transferred under argon to another glove box, where the dissolution experiment took place under an argon atmosphere at 0.1 ppm O_2. Finally, pre-washing of the thin film in 20 ml of sparged deionized water in a plastic bottle for 12 hours was carried out before transfer to a fresh deionized and deoxygenated water solution for the dissolution experimental run (5.4 Thin film sample- ICP-MS, ICP-OES and DLS results).

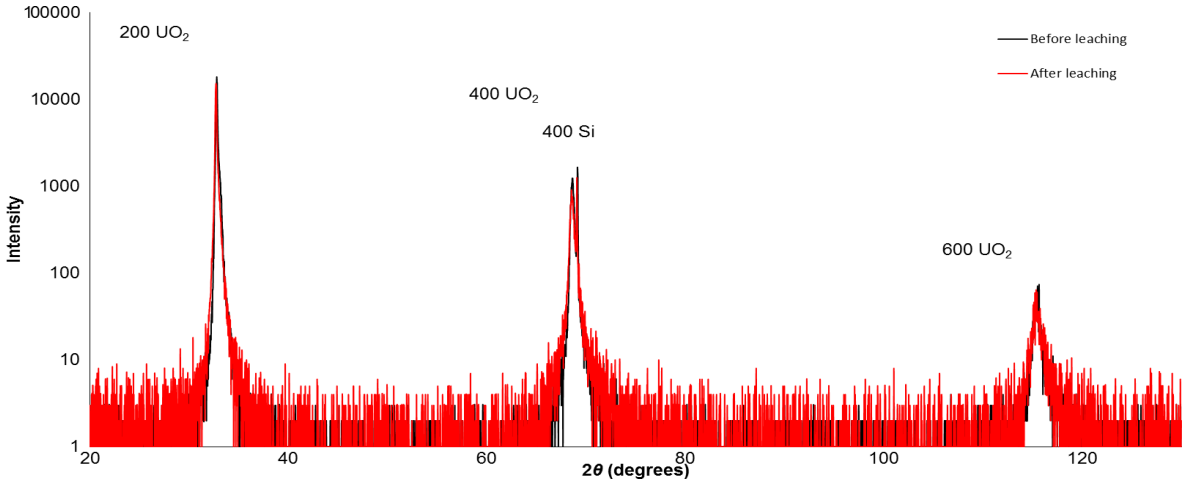

Figure 2-2 An XRD diffractogram for the preleached and postleached UO_2 thin film sample on a silicon substrate. Note, only 200, 400, and 600 UO_2 reflections corresponding to the (001) crystallographic orientation are present.

2.2.1.3 Powder preparation

For the powder samples, high surface area, micro-porous UO_2 beads were produced from uranyl nitrate at the EC-JRC by the sol-gel technique (Fernández *et al.*, 2002; Cologna *et al.*, 2016). About 2.3 g of this powder was weighed and transferred into a 1 ml alumina boat for annealing. In order to achieve stoichiometry, the powder was annealed in a controlled atmosphere, tube furnace attached to a glove box where ingress and egress of the sample into the furnace occurs inside the glovebox with an argon atmosphere (0.1 O_2 ppm). It was annealed at 800 °C for three hours with a reducing gas mixture of 5 vol% H_2 in 95 vol% Ar, after an initial hour of pre-heating to the requisite temperature. There was no pre-wash carried out for this set of experiments.

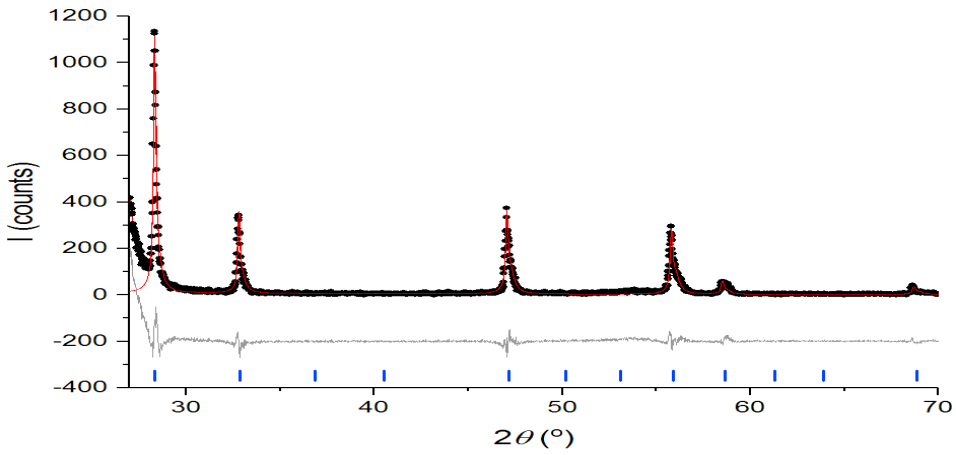

Figure 2-3 Rietveld refinement plot showing experimental (black dots), calculated (red line) and difference (grey line) patterns. UO_2 peak positions are indicated in blue.

Due to the long-term air-exposure and high surface area of the uranium dioxide powder, it was important to ensure that the powder have been reduced to stoichiometric UO_2. XRD data of powder samples were collected in capillary on a Bruker D8 Advance diffractometer (Cu Kα radiation, λ = 1.541 Å, parallel primary beam, Vantec position sensitive detector) for a total of 16 hours each over an angular range $20° \leq 2\theta \leq 90°$ ($\Delta 2\theta = 0.02°$). A full Rietveld refinement (Figure 2-3) was carried out of the acquired capillary diffraction patterns. The background was fitted with a 6 parameter Chebyshev function and the peak shape was modelled using a pseudo-Voigt function for the micro-porous uranium dioxide powder pre- and post-annealing. Based on the lattice parameter obtained of 5.4656(5) Å (Fig. 2-3 shows a plot of the final refinement after convergence with $\chi 2$ and Rwp equal to 1.22 and 8.44% respectively), and the equation $ax = 5.4690 - 0.12x$ (Maslakov *et al.*, 2018), a bulk stoichiometric ratio prior to dissolution of $UO_{2.03}$ was found for the UO_2 powder.

2.2.2 Solid Pellet Dissolution Experiment

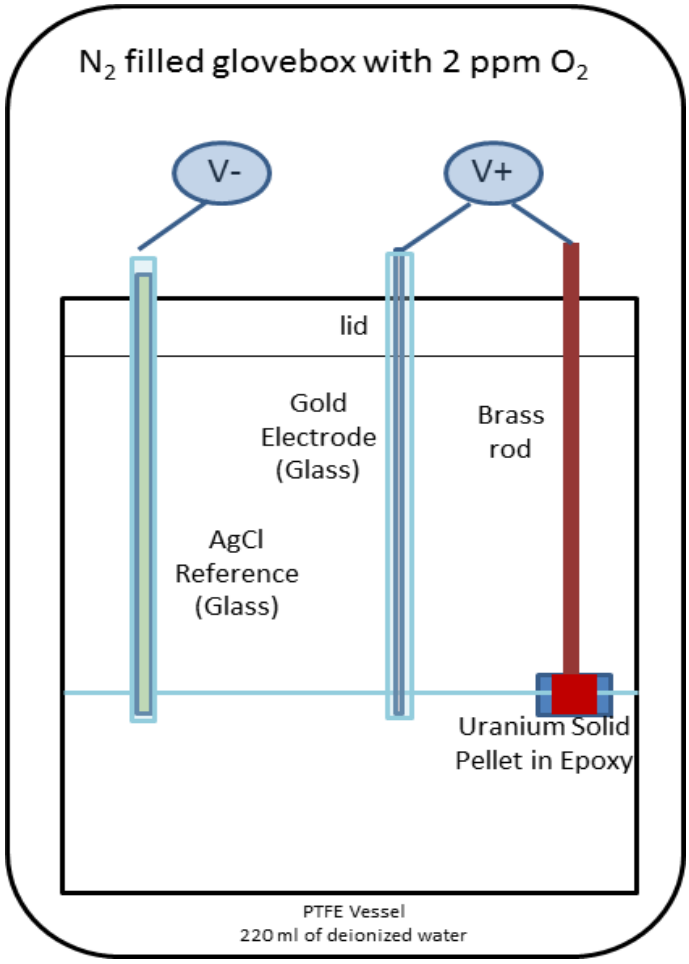

Figure 2-4 Schematics of Solid Pellet Dissolution Experiment

After a 21-hour prewash and drying for 1 hour in the glovebox atmosphere, UO_2 electrodes were immersed in 220 ml of sparged, deionized water in a sealed (screw top) 480 ml Fisherbrand® PTFE dissolution vessel. Dissolution measurements were performed in triplicates.

To determine the electrochemical evolution of both the uranium dioxide electrode and the solution potential, open circuit potentiometry was used (Wilbraham *et al.*, 2015). Solution potential was measured using 500 µm Au disk electrodes, and the UO_2 electrodes were polished using 600 and 1200 grit SiC papers and rinsed with deoxygenated, deionized water inside the glovebox prior to immersion. Through the use of a simple switch box, the open circuit potential of both electrodes was measured vs. one reference electrode. In order to avoid chloride contamination, an ammonium nitrate saturated agar double junction was used with an Ag|AgCl reference electrode (RE-5B, BASi, Indiana, USA). All vessels were tightly closed to prevent

water evaporation, with gaps around electrodes sealed using parafilm®. One vessel filled with 250 ml of deionized water and an Au electrode only (no UO_2 electrode) was used as a control. During dissolution, batch replenishment tests were conducted, where ~1 ml aliquots of the solution sample were extracted and ~1 ml of the deionized water was replenished at defined time intervals after the start of the experiment, namely 2 hours, 6 hours, 1 day, 5 days, 12 days, 30 days, 61 days and 100 days. The amount of solution in the aliquots was monitored by weighing empty and filled vials on a balance. The dissolution of all samples was performed at an ambient temperature of ~25 °C for 100 days. After completion, the PTFE vessels were acid-washed using 3 M HNO_3. 5 ml of each acid wash was used for ICP-MS analysis in order to determine the presence of any uranium sorption or precipitation on the walls of the leaching vessel.

2.2.3 Thin Film Dissolution Experiment

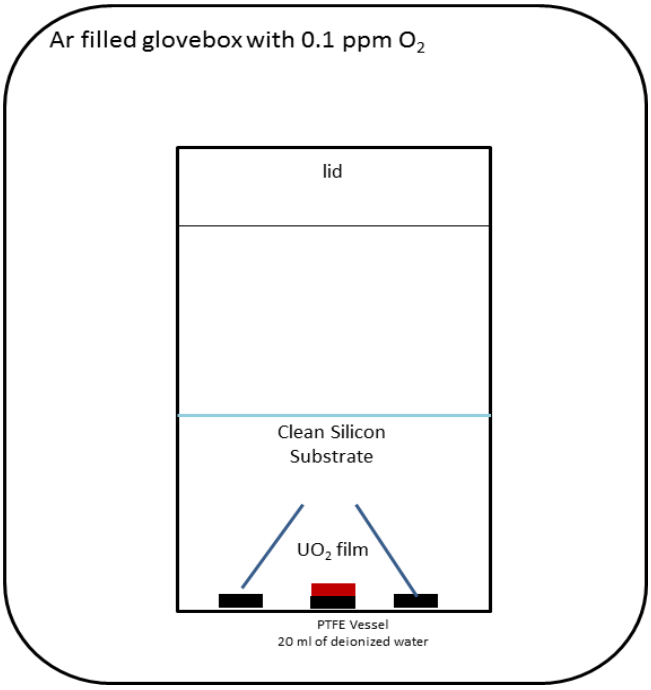

Figure 2-5 Schematics of Thin Film Dissolution Experiment

After a 12-hour prewash and drying for an hour, the UO_2 thin film sample was rinsed with sparged, deionized water and placed into a 60 mL Fisherbrand® PTFE dissolution vessel containing 20 ml of the deionized water and two blank Si substrates (to detect any U precipitation/nucleation from the solution) (Tan *et al.*, 2019).

Static batch replenishment tests were run where ~1 ml aliquots were extracted at various intervals and ~1 ml of the deionized water was replenished. One vessel, filled with 20 ml of the deionized water and two blank Si substrates, was used as a control blank. All vessels were tightly closed to prevent water evaporation. The amount of the solution transferred from the dissolution vessels into the vials was monitored by weighting empty and filled vials. The dissolution experiment was performed at an ambient temperature of ~25 °C for 140 days.

2.2.4: Variable Temperature powder dissolution experiments

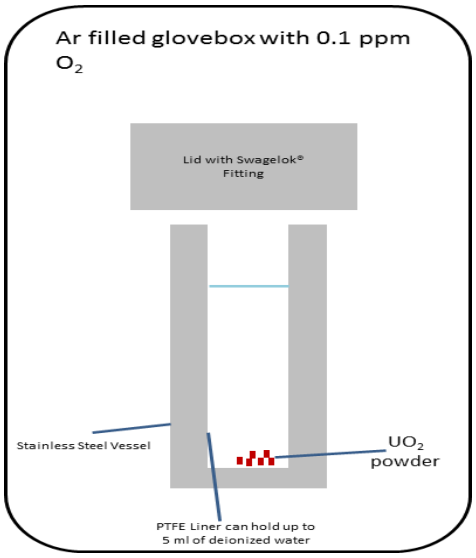

Figure 2-6 Schematics of Swagelok reacting vessels subjected to various temperature

After annealing, 100 mg of reduced UO_2 powder was weighed out carefully with a Mettler Toledo XS-104 mass balance and placed into each of twelve stainless steel leaching vessels with a PTFE liner and a Swagelok seal. Upon the addition of 4 ml of sparged, deionized water to each leaching vessel, the leaching vessel was tightly sealed and transferred to another glove box under double containment. The dissolution experiment was performed at 4 different temperatures ambient (~25 °C), 40 °C, 90 °C and 140 °C with deoxygenated water (<2.5 ppb O_2) within an Ar atmosphere glovebox (0.1 ppm O_2). All vessels were kept in the glove box for the duration of the experiment and tightly sealed. The extraction was carried out on the 390th day with a syringe through a 0.45 µm pore size disposable filter.

2.3 Selected Minerals for Synthesis and Enrichment

To investigate the alteration of spent nuclear fuel in repository conditions, attempts were made to synthesize the potential products of anoxic dissolution and study them through XRD and NMR. Since the formation of amorphous forms may precede crystalline formation, NMR will be used primarily in Chapter 6 to characterise them.

Samples to be fabricated were chosen based on their pervasiveness in nuclear waste disposal or formation potential when groundwater intrudes. Given the simple chemical equipment in our laboratory, ease of fabrication is an important factor.

Majority of uranyl-containing minerals have similar structures with layers or chains containing uranyl groups coordinating to anions held together either by interlayer hydrogen bonding, or by coordination to additional cations lying between the uranyl sheets, which in most cases are accompanied by water. At the core of these structures is the uranyl ion, UO_2^{2+}, in which two oxygen ions form partial triple bonds of ~ 1.8 Å to U^{6+} to make a near- linear ion (Burns, Ewing and Miller, 1997). The sheets or chains that form the backbone of these structures are formed by anionic groups, almost always O^{2-}, coordinating to multiple uranyl uranium atoms.

2.3.1 Studtite $(UO_2)(O_2)(H_2O)_2.2(H_2O)[UO_4.4(H_2O)]$ and Metastudtite $(UO_2)(O_2)(H_2O)_2[UO_4.2(H_2O)]$

Studtite is the only known peroxide mineral, and has been found occurring in Chernobyl lavas and in wastes at the Hanford Site, as well as during leach tests on spent nuclear fuel. This gives a strong indication of its potential to form on geologically disposed spent nuclear fuel (Clarens et al. 2004, Forbes 2011). As discussed previously in this introduction, the radiolysis of water by alpha radiation is expected to produce significant quantities of hydrogen peroxide even at the long timescales expected for water contact to SNF. However there remains a significant question over the likelihood of hydrogen peroxide solutions of significant concentration forming, as its natural instability makes the expected concentration dependent on the rate of its degradation as well as production. Whilst most work on studtite does not consider the degradation of hydrogen peroxide it is surely a concern: The degradation can be catalysed by species such as CO_3^{2-} that have the potential to feature in groundwaters (Seuss and Janik), the dissolution of UO_2 itself (Lousada et al. 2013) as well as corrosion products of a stainless steel or zircalloy clad (Solvay Interox, Lousada and Jonsson 2010).

The combination of these factors will need modelling for a specific repository to determine the potential for studtite formation, however it remains of interest due to its potential relevance and its unusual structure.

Studtite consists of chains of uranium centred hexagonal bipyramids sharing edges, whose boundaries are demarcated by O1, O2, O3, O3','','''' in Figure 2-7. Shared edges are between peroxide O-O groups that lie equatorial to the uranyl group (e.g. O3 and O3' with O3'' and O3''') . In the plane of the peroxide group, two water groups also lie equatorial to the uranium. Chains are held together by water lying between them in a complex network of hydrogen bonding. Studtite and metastudtite are structurally distinct from other uranyl minerals as they contain the peroxide group and having a chain rather than a sheet structure.

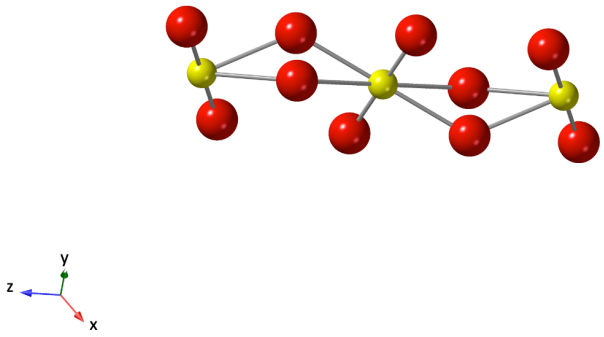

Figure 2-7 Studtite chains consists of peroxide groups coordinating equatorially to uranyl ions. Water coordinates to the uranyl ion. Red atoms represent oxygen, yellow uranium. Structure from Burns and Hughes (2003)

The structure of metastudtite has not been refined, however it is a partially dehydrated form of studtite. Burns and Hughes proposed that, in line with dehydrated forms of other uranyl minerals, the linear component of the structure remains, whilst the water lying between chains is lost in metastudtite. Recent modelling of metastudtite by (Weck *et al.*, 2012) shows different uranyl bond lengths of metastudtite which will be discussed in 7.3 Analysis of NMR data.

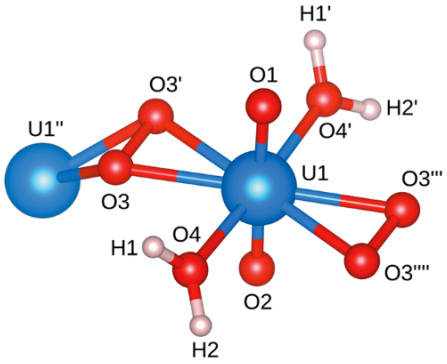

Figure 2-1 Ball-and-stick representation of the $(UO_2)(O_2)(H_2O)$ complex composing studtite and metastudtite, with the only difference speculated to be the removal of half of the coordinating water molecules and a probable change in the uranyl bond lengths because of that.

2.3.2 Dehydrated schoepite ($UO_3.1H_2O$) and metaschoepite ($UO_3.1\text{-}2H_2O$).

Dehydrated schoepite was long known as a dehydration product of schoepite, but has recently been discovered naturally and named paulscherrerite (Brugger *et al.*, 2011). The structure of dehydrated schoepite is similar to that of metaschoepite and schoepite but with the absence of interlayer water, and a simplified layer structure based around hexagonal bipyramids rather than the pentagonal uranyl bipyramids of metaschoepite and schoepite.

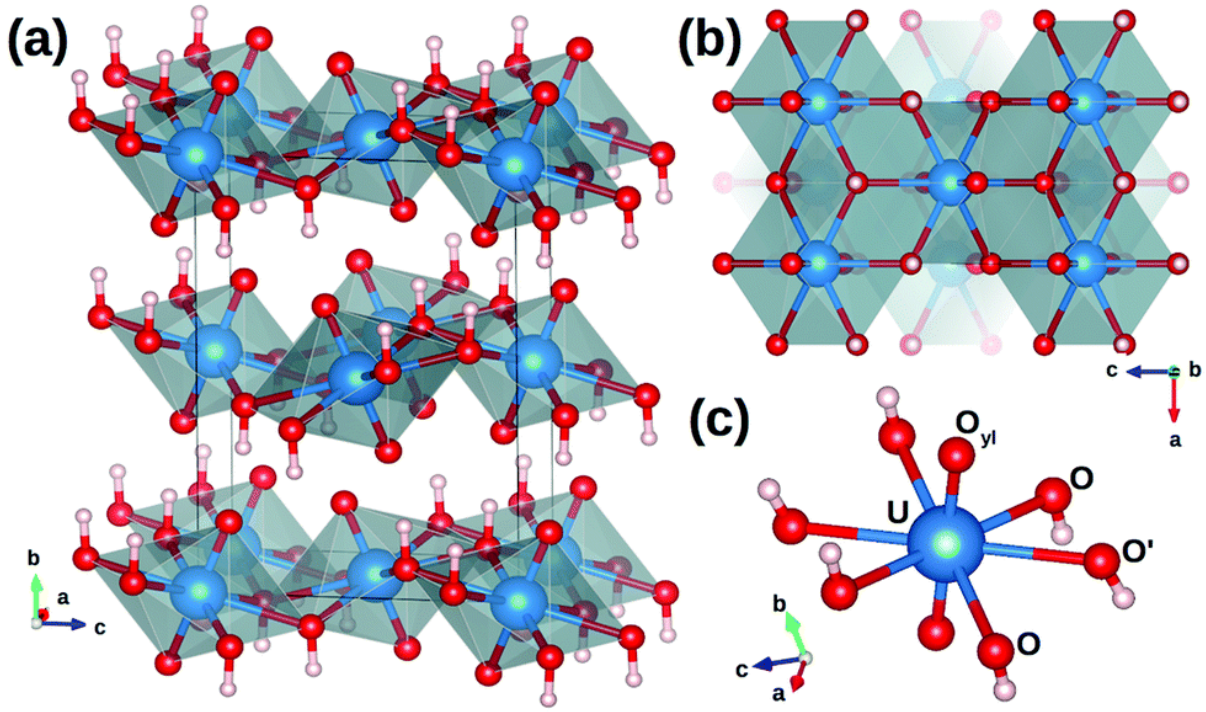

Figure 2-9 Crystal unit cell of dehydrated schoepite α-$UO_2(OH)_2$ (space group Cmca, Z = 4) relaxed with DFT at the GGA/PBE level of theory. (a) Side view of the stacking of $UO_2(OH)_2$ sheets showing the uranium coordination polyhedral; (b) Top view along the [010] direction; (c) $UO_2(OH)_6$ hexagonal-bipyramid unit. Color legend: U, blue; O, red; H, white. Adapted from (Weck and Kim, 2014)

The crystal structures of most uranyl oxide hydrates are based on sheets of polyhedral of the form $[(UO_2)_xO_y(OH)_z]^{(2x-2y-z)}$.(Weck and Kim, 2014) This includes three closely related uranyl oxide hydrates/hydroxides without interlayer cations that form the schoepite subgroup of the fourmarierite group: schoepite ($UO_3.2H_2O$), metaschoepite ($UO_3.1\text{-}2H_2O$) and dehydrated schoepite ($UO_3.1H_2O$). Schoepite and metaschoepite consist of $(UO_2)_4O(OH)_6$ sheets formed by edge-sharing UO_7 **pentagonal** bipyramids (see Figure 2-10 and Figure 2-11), with only differences related to the orientation of uranyl groups relative to the layers. The structure of the stoichiometric α-phase of de-hydrated schoepite (also often referred to as "monohydrate"), due

to its generic formula $UO_3(H_2O)$ consists of $UO_2(OH)_2$ sheets made of edge-sharing UO_8 **hexagonal** bipyramids.

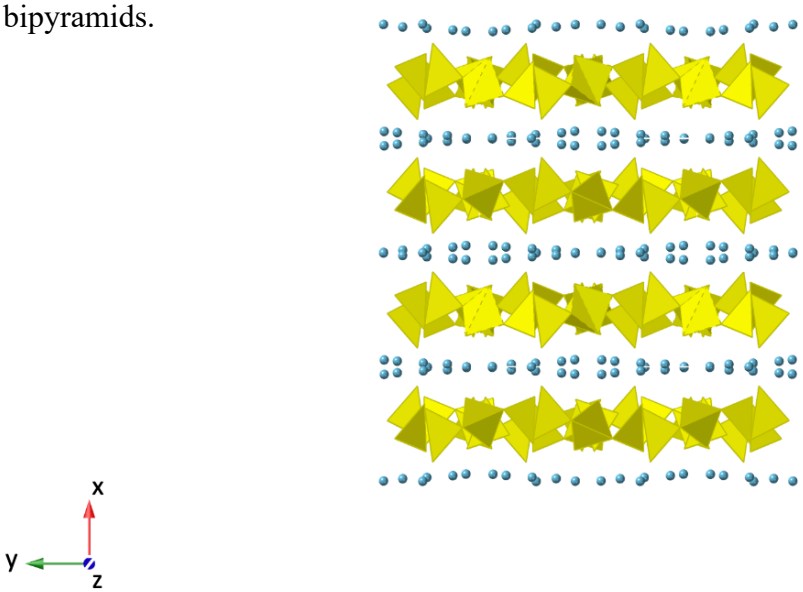

Figure 2-10 Structure of metaschoepite from Weller et al. (2000). Uranium lies at the centre of oxygen coordination polyhedron (yellow) in a uranyl group lying normal to the sheet. Equatorially it is coordinated by oxygen coordinated to two other uranium sites, or hydroxide coordinating to one other uranium atom. Blue spheres mark the position of interlayer water.

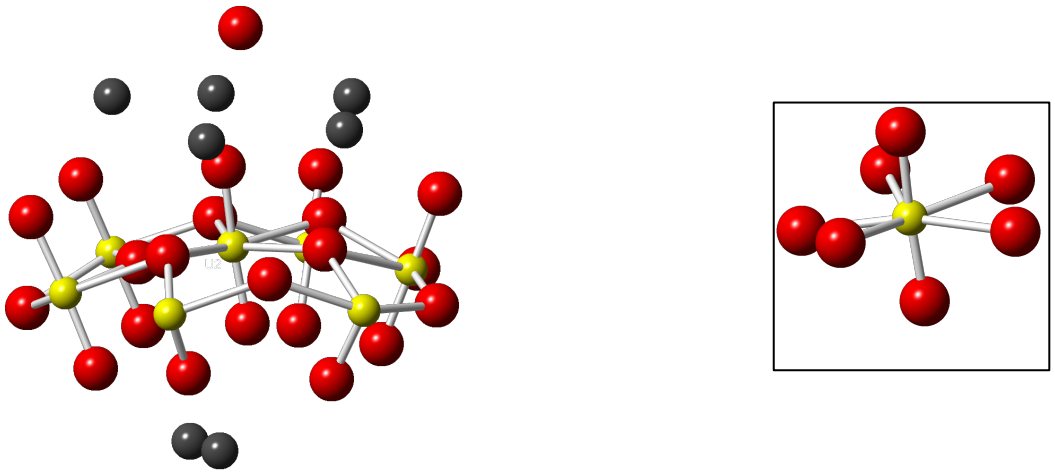

Figure 2-11 shows the coordination of the uranium atom with two 'yl' oxygen forming a linear uranyl ion that is coordinated with 5 oxygen atoms to form a pentagonal bipyramid structure. Inset shows the pentagonal bipyramid. The black spheres represent water.

A topological relation exists between uranyl sheets in schoepite/metaschoepite and α-$UO_2(OH)_2$ via the substitution

$$\boldsymbol{2(OH)^- = H_2 + O^{2-} + vacancy}.$$

Equation 2—1

Previous studies (Finch and Hawthorne, 1998) suggested that the excess strain energy resulting from the incomplete conversion of schoepite into metaschoepite might be used to transform the remaining schoepite to dehydrated schoepite. Details of such inter-conversions between the α -phase of dehydrated schoepite, metaschoepite, and schoepite have been extensively discussed by Finch and co-workers.

Dehydrated schoepite takes the orthorhombic α-uranium hydroxide structure, but with some XRD peak splitting. This suggests a slight loss of symmetry compared to the ideal structure (Brugger *et al*. 2011, Finch *et al*. 1998). The structure is comprised of sheets of uranium centred hexagonal bipyramids, with uranyl groups lying normal to the sheet, and hydroxide groups coordinating equatorially. These hydroxide groups are shared between two uranyl groups to form the sheet network. From crystal XRD, there are only two distinct oxygen environments, uranyl, and equatorial hydroxide.

Dehydrated schoepite with a formula $(UO_2)O_{0.25-x}(OH)_{1.5+2x}(0\leq x\leq 0.25)$ [or $UO_3\cdot xH_2O$ $(0.75\leq x\leq 1)$] was identified as a corrosion product of UO_2 from spent nuclear fuel (SNF) reacted in water vapour experiments and in low and high drip-rate experiments. In the presence of moisture and hydrogen peroxide (H_2O_2) generated by α-radiolysis of water near the SNF surface, dehydrated schoepite can eventually lead to the formation of studtite, $(UO_2)O_2(H_2O)_4$, another important corrosion phase of SNF exposed to water. Assuming an ideal stoichiometry of $UO_2(OH)_2$ for simplicity, the experiments conducted so far (Forbes *et al.*, 2011) have shown that dehydrated schoepite is rapidly converted to studtite upon contact with hydrogen peroxide and moisture according to the reaction:

$$\boldsymbol{UO_2(OH)_2 + H_2O_2 + 2\,H_2O \rightarrow UO_2(O_2)(H_2O)_4}$$

Equation 2—2

This reaction brings about minerals who are composed from uranium, oxygen and hydrogen however, lab fabrications indicate stringent conditions (such as pH) for acceptable levels of crystallinity for XRD analysis (see Figure 2-16) which will probably remain true in the real world, rendering the need for other techniques to study such amorphous samples. Fortunately, unique oxygen and hydrogen sites in these structure can be analysed with NMR-active isotopes, such as ^{17}O and ^{1}H. It is hence important to study the NMR spectra of dehydrated schoepite, metaschoepite and studtite [Section 6.5 NMR of uranium minerals] where these information

can be employed to decipher real life problems of corrosion of nuclear fuel and the extent of subsequent conversion upon water ingress and alpha radiolysis.

2.3.3 Becquerelite $Ca[(UO_2)_6O_4(OH)_6].(H_2O)_8$

In addition to the compositionally simple schoepite group minerals, uranyl minerals may also form structures containing other cations. A simpler example will be orthorhombic becquerelite (see Figure 2-12), containing water and the cation species of Ca^{2+} within the interlayer, with the structure of the sheets being very similar to those of schoepite group. Ca^{2+} cation coordinates to oxygen in the sheets above and below it as well as to interlayer water (Burns and Li 2002). In this case, a sheet is maintained with uranyl ions normal to the sheet coordinating equatorially to bridging oxygen groups. It does however have an overall negative charge due to a lower level of protonation compared to schoepite. Becquerelite has been observed in natural analogues where it results from the dissolution and reprecipitation of metaschoepite that initially forms on the surface of uraninite during its weathering (Finch *et al.*, 1996).It is intended that a bentonite clay will be used to backfill UK HLW and SNF geological disposal facility, providing a potential source of aqueous calcium (NDA, 2010). In Figure 2-12, Uranyl polyhedral are shown shaded yellow and calcium polyhedral are shaded blue, and connecting oxygen atom and H_2O groups are indicated with red and black dots respectively.

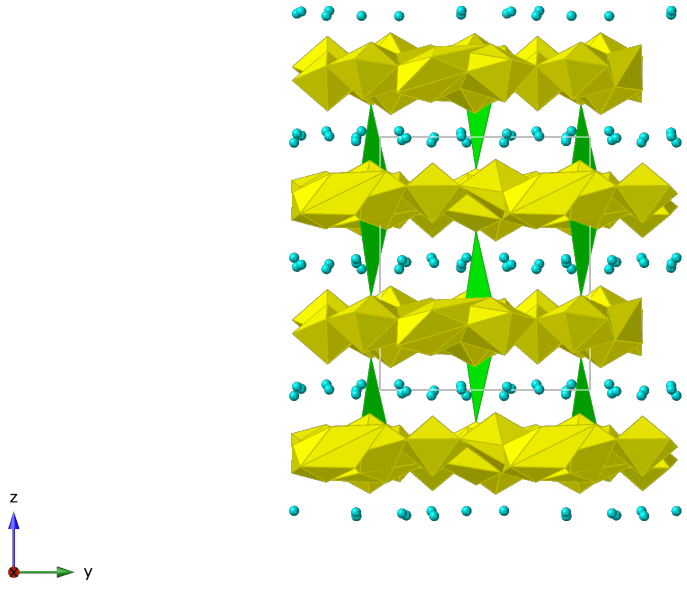

Figure 2-12 Polyhedral representations of the structure of becquerelite projected along [100] showing sheets of uranyl polyhedral (yellow) and the interlayer constituents of water (blue spheres) and Ca^{2+} polyhedrons (green).

2.3.4 Andersonite, $Na_2Ca[UO_2(CO_3)_3].x(H_2O)$ and Grimselite, $K_3Na(UO_2)(CO_3)_3 \cdot (H_2O)$

Andersonite and Grimselite were also selected as fabrication candidates because of the ubiquity of carbonate in ground water with possible traces of sodium and potassium. Their fabrication procedure has also been established in previous literature. As such, they are ideal targets for us to probe the uranyl bond differences in potential minerals that may be formed in repository storage when groundwater ingresses. The synthesis process involves fabricating them and enriching them with ^{17}O for NMR studies. Figure 2-14 shows the crystal structure of Andersonite (Coda *et al.*, 1981). This is a trigonal $R\bar{3}m$ structure, with a = 17.902 (4) Å, c = 23.734(4) Å and Z =18.

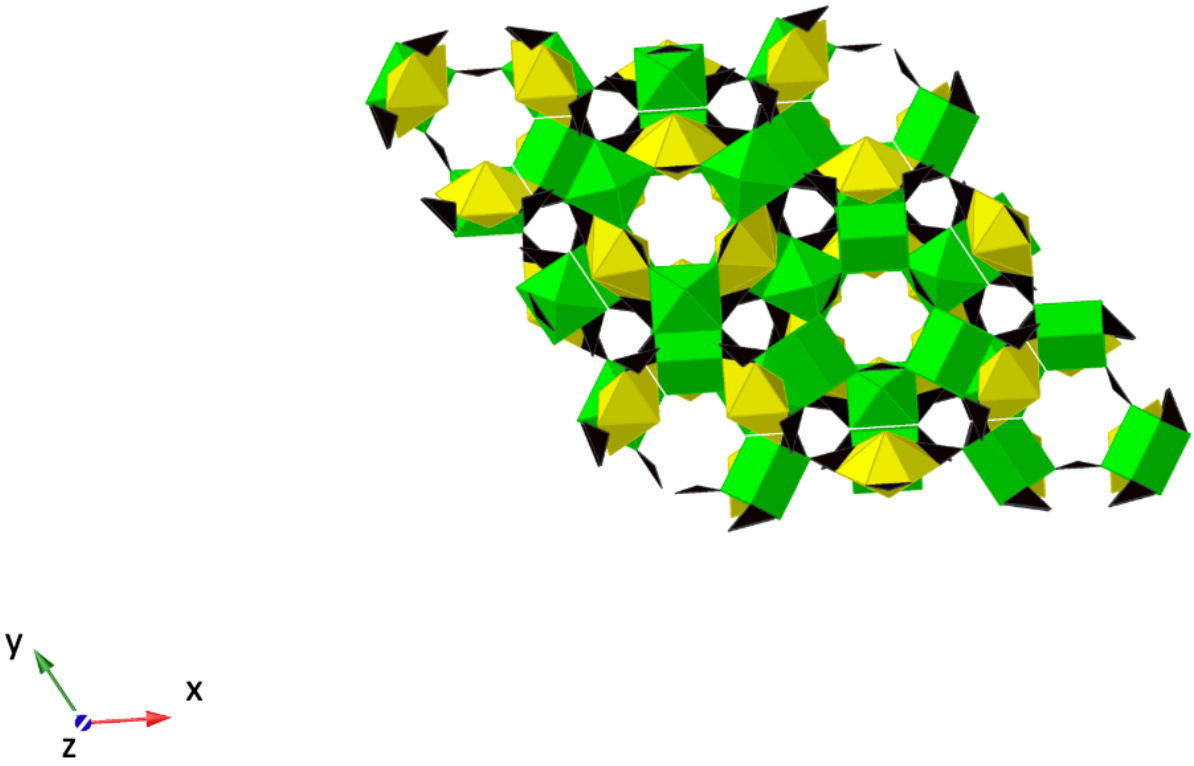

Figure 2-13 The framework structure of andersonite viewed along z direction. Framework is built from uranyl tricarbonate cluster (UO_8 polyhedral are yellow, CO_3 groups black) and CaO_7 polyhedral (green). The channels, running parallel to c, are occupied by H_2O (omitted for clarity). Na atoms are not displayed.(Plášil and Čejka, 2015)

The characteristic anionic unit is the $UO_2(CO_3)^{4-}$ with the U having a coordination number of 8; U is surrounded by a hexagonal-bipyramidal polyhedron, with two uranyl O atoms having U-O bond lengths of 1.7763Å and 1.8078 Å. The six equatorial oxygen come from equatorial coordination by three bidentate CO^{2-} anions.

Figure 2-14 shows this characteristic ionic group where the yellow, red and black spheres represents the uranium, oxygen and carbon atoms respectively. Three equatorial CO^{2-} anions are found about the UO_2^{2+} uranyl ion.

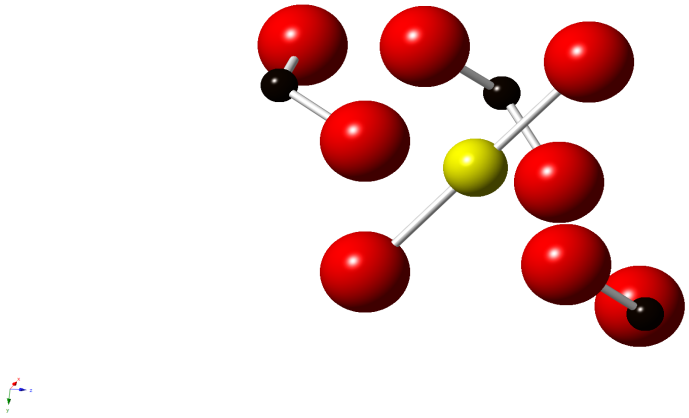

Figure 2-14 The crystal structure of synthetic Andersonite from XRD literature. (Coda *et al.*, 1981)

Figure 2-15 shows the crystal structure of Grimselite (Li and Burns, 2001). This is a hexagonal structure with a = 9.302 (2) Å, c = 8.260(3) Å, V 618.9 (3) $Å^3$, spacegroup $P\bar{6}2c$ and Z = 2.

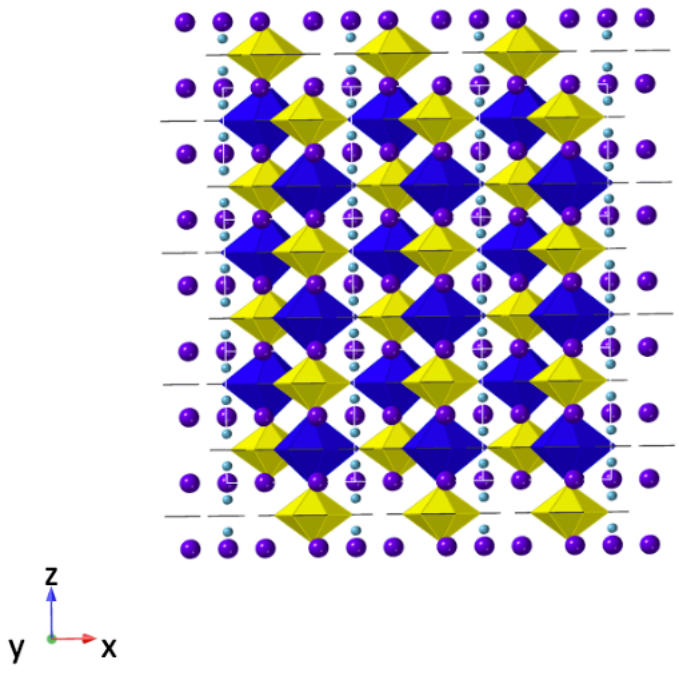

Figure 2-15 The yellow polyhedral in Grimselite represents the uranyl tricarbonate cluster $[(UO_2)(CO_3)_3]$, which comprises of a uranyl hexagonal bipyramid that shares three equatorial edges with CO_3 triangles. The uranyl tricarbonate clusters are interconnected to the NaO_8 hexagonal bipyramids (navy blue) in adjacent sheets, with purple and blue circles representing potassium cations and H_2O groups, respectively.

2.4 Synthesis procedure

2.4.1 Studtite $UO_4.4(H_2O)$ and Metastudtite $UO_4.2(H_2O)$

Synthetic studtite analysed using ^{17}O NMR was produced by 2 different methods, both yielding studtite easily from pXRD measurements taken at 150 K for verification purpose.

Uranyl acetate was added to hydrogen peroxide, washed with deionized water and left to dry over a few days, yielding studtite of crystallinity of 48% as determined from pXRD. Another method was a fast reaction between uranyl acetate and hydrogen peroxide which was then filtered and dried immediately, yielding a crystallinity of 60%. The better method used for our final samples was the addition of 0.45ml of 1M of uranyl nitrate to a solution of H_2O_2 (formed by 0.12 g of H_2O_2 in 2 ml of 35-40% ^{17}O enriched water). After some iteration, maximum crystallinity of 70% was observed in Figure 2-16 at a pH of 6.0 by acidifying with HNO_3.

$$UO_2(NO_3)_2 + H_2O_2 + 4\,H_2O \rightarrow (UO_2)(O_2)(H_2O)_2.\,2(H_2O) + 2HNO_3$$

Equation 2—3

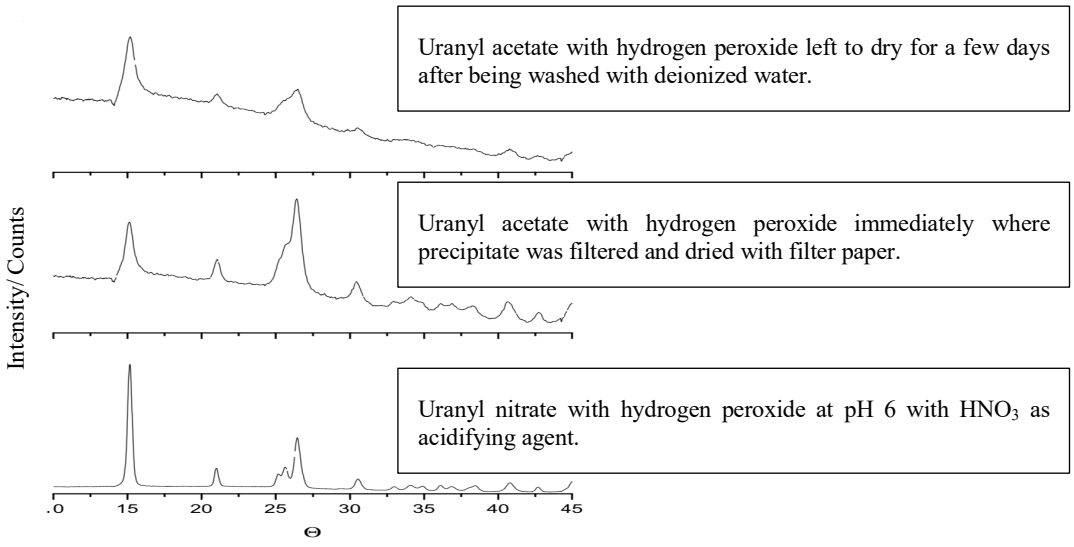

Figure 2-16 XRD studies for different crystallinity of studtite produced by the different methods.

Two batches of studtite were produced with the above method; one with ^{17}O enriched water and the other with isotopically normal deionized water. The primary intention is to compare the spectral differences. A secondary aim is to enrich the equatorial oxygens of normal studtite by steeping it in ^{17}O water (Chapter 6.7.1), which was unsuccessful with the synthesis here.

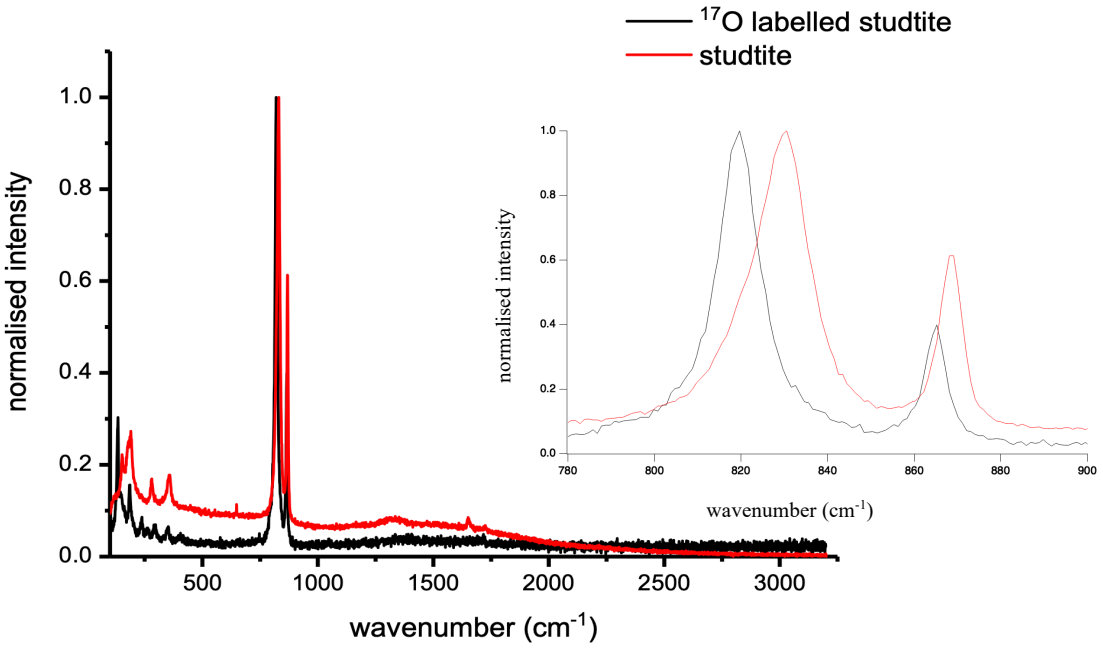

Figure 2-17 Raman spectroscopy of enriched studtite and normal studtite with 785 nm laser. Inset shows zoomed in region between 780 to 900 cm^{-1}. Peroxo peak was shifted by 5 cm^{-1} vs calculated value of 8 cm^{-1} and an 11 cm^{-1} shift was seen against a calculated value of 15 cm^{-1} in the uranyl bond. The values are in agreement as the enrichment factor was 35-40% ^{17}O.

Isotopic enrichment was successful as seen from Raman spectroscopy with 785 nm laser. Figure 2-17 shows that there was a small peroxo peak shift of 5 cm^{-1} from 863 cm^{-1} to 868 cm^{-1} and a larger uranyl peak shift of 11 cm^{-1} from 819 cm^{-1} to 830 cm^{-1} which is in agreement with calculated values for the Raman spectroscopy due to the slightly heavier mass of ^{17}O atom. This does not imply enrichment in both the peroxo and uranyl bond as discussed in page 141. Despite two different isotopes of oxygen in nearly even ratio in the enriched sample (35% ^{17}O and 65 % ^{16}O) due to the 35%-40% isotopically-enriched water, two peaks were not detected in the Raman signal, presumably due to a lack of resolution. This subtle difference could however be seen with NMR as discussed later in Figure 3-2. Another observation was despite a slight 5 cm^{-1} shifting of the peroxo bond detected here implying isotopic enrichment of these oxygen, the NMR-active ^{17}O in the equatorial peroxo positions was not detected during NMR experiments. This is another potential limitation with Raman spectroscopy where the signal differences from the slight polarizability of the bond in very similar structure is less pronounced than NMR where different isotropic ^{17}O peak positions (especially in uranyl compounds) have large differences and can be detected easily.

2.4.2 Dehydrated schoepite and metaschoepite

Dehydrated metaschoepite and metaschoepite samples were precipitated from uranyl nitrate solution. They were produced by the dropwise addition of 0.5 ml of 40% mass concentration tetrabutylammonium hydroxide (TBAOH) to 2.6 ml of 0.2 M uranyl nitrate solution. The uranyl nitrate solution was formed by dilution of a 1 M stock solution with 1 ml 35 – 40% ^{17}O water, and the remainder deionised water.

For dehydrated schoepite, the solution was heated for 5 days at 95°C before drying on a filter for two days without rinsing and subsequently loaded into a PTFE NMR liner.

For the metaschoepite sample produced from uranyl nitrate solution was made using the same method used for dehydrated schoepite however it was heated at 55°C rather than 95°C.

According to the safety requirements, different XRD methods were employed as seen in Figure 2-18 and Figure 2-19.

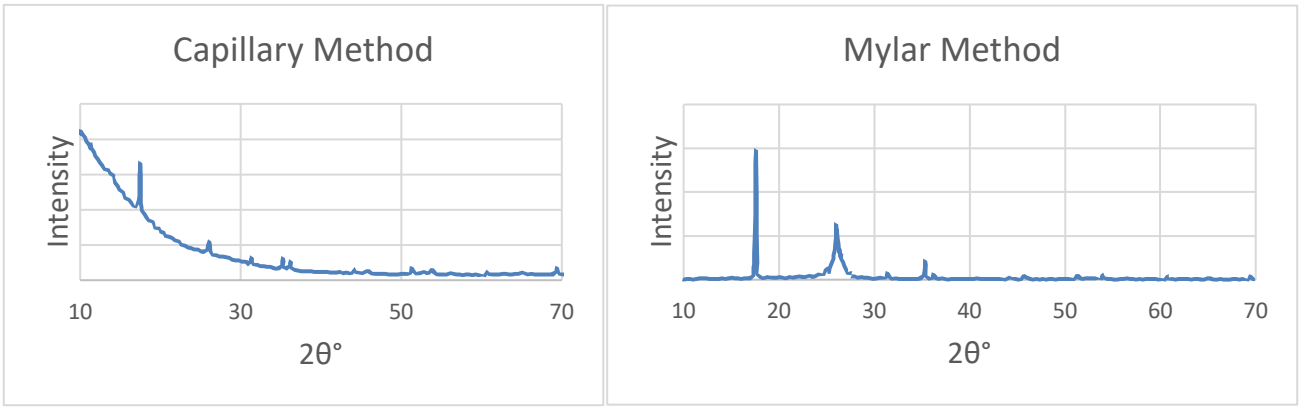

Figure 2-18 Diffraction patterns of dehydrated schoepite collected using the capillary method, and on the Bragg-Brentano stage whilst encapsulated in Mylar.

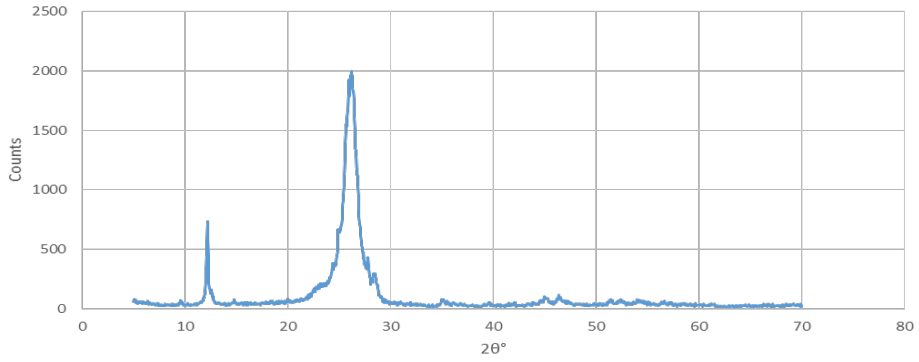

Figure 2-19 Diffraction pattern of synthetic metaschoepite collected using a Mylar mount. The large, broad peak around 27° is due to the Mylar.

2.4.3 Becquerelite $Ca[(UO_2)_6O_4(OH)_6].(H_2O)_8$

Becquerelite, Andersonite and Grimselite were synthesized during a visit to Trinity College, Dublin. Due to the high costs of isotopically enriched water, approximately 1 ml was used for each synthesis. Verification was carried out with 4.4 Raman Spectroscopy and 4.5 Emission Spectroscopy with their working principles explained later in this thesis.

106 mg of uranyl hydroxide was dissolved in 0.8 ml of 35-40% ^{17}O enriched water. 6 mg of calcium carbonate was then dissolved in 0.2 ml of enriched water. They were then heated in a hot oil bath at 300 ^{0}C for a few days to dry the sample and vaporise the unstable carbonic acid which was not entirely removed as seen in Figure 2-21.

$$6\ UO_2(OH)_{2\ (aq)} + Ca(CO_3)_{\ (aq)} + 6\ (H_2O)_{\ (l)} \rightarrow Ca[(UO_2)_6O_4(OH)_6].(H_2O)_{8\ (s)} + H_2CO_{3\ (aq)}$$

Equation 2—4

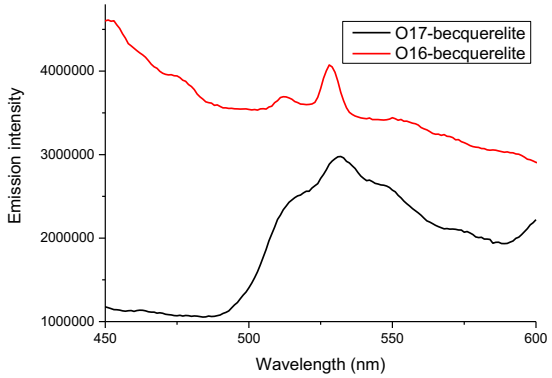

Figure 2-20 Emission spectroscopy of Becquerelite after synthesis with ^{17}O water.

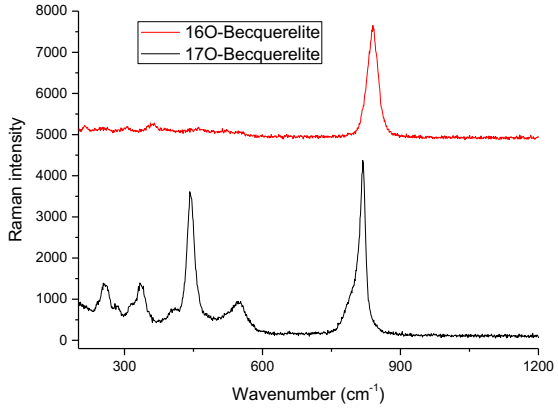

Figure 2-21 Raman spectroscopy of Becquerelite after synthesis with ^{17}O Water.

2.4.4 Andersonite $Na_2Ca[UO_2(CO_3)_3].x(H_2O)$

150 mg of uranyl nitrate was added to 95 mg of sodium carbonate and dissolved in 0.7 ml of 35-40% ^{17}O enriched water. 70 mg of calcium nitrate was added to 0.3 ml of enriched water. The resulting solution is left to dry under a fume hood after filtration. The successful enrichment was seen from Figure 2-22 and Figure 2-23.

$$UO_2(NO_3)_{2\,(aq)} + Ca(NO_3)_{2\,(aq)} + 3\ Na_2(CO_3)_{\,(aq)} \rightarrow Na_2Ca[UO_2(CO_3)_3]_{(s)} + 4\ Na(NO_3)_{\,(aq)}$$

Equation 2—5

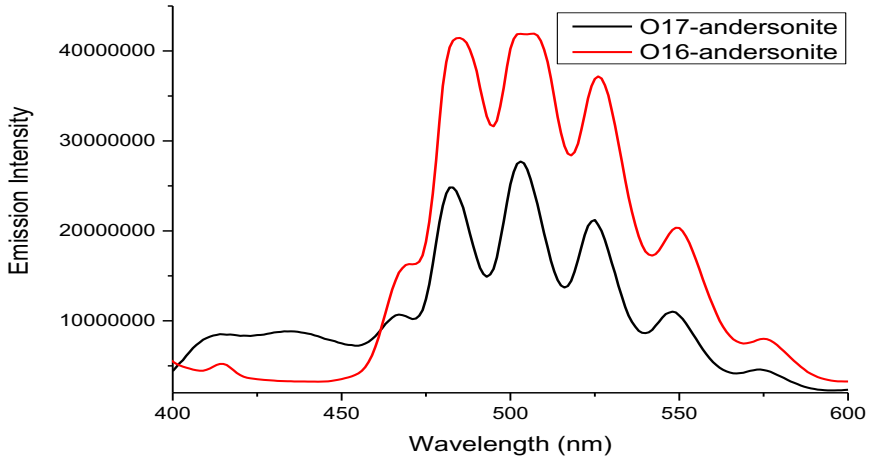

Figure 2-22 Emission spectroscopy of Andersonite after synthesis with ^{17}O water.

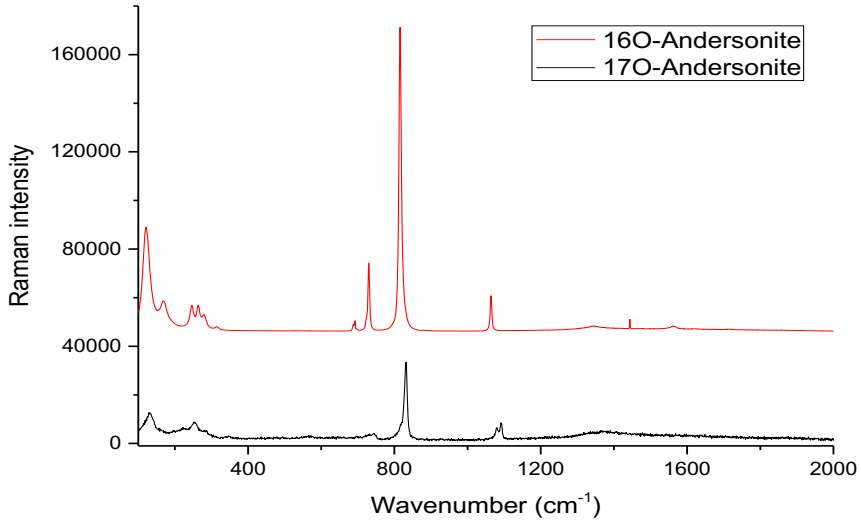

Figure 2-23 Raman spectroscopy of Andersonite after synthesis with ^{17}O water.

2.4.5 Grimselite, $K_3Na(UO_2)(CO_3)_3 \bullet (H_2O)$

150 mg of uranyl nitrate was dissolved in 0.6 ml of 35-40% ^{17}O enriched water. 63 mg of potassium carbonate was added to 17 mg of sodium carbonate and dissolved in 0.4 ml of enriched water as the ratio of U: K: Na are to be maintained at 1:3:1. The resulting precipitate is left to dry under a fume hood after filtration.

$$2\ UO_2(NO_3)_{2\ (aq)} + 3\ K_2(CO_3)_{(aq)} + Na_2(CO_3)_{(aq)} + 2CO_3^{2-} \rightarrow 2\ K_3Na(UO_2)(CO_3)_3 \bullet (H_2O)_{(s)} + 4NO_3^-{}_{(aq)}$$

Equation 2—6

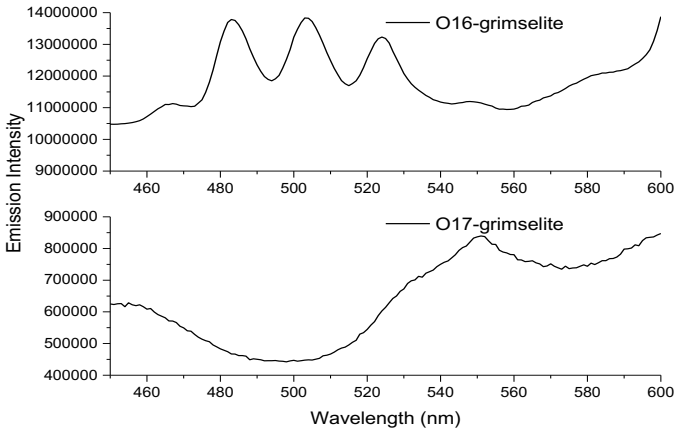

Figure 2-24 Emission spectroscopy of Grimselite after synthesis with ^{17}O water.

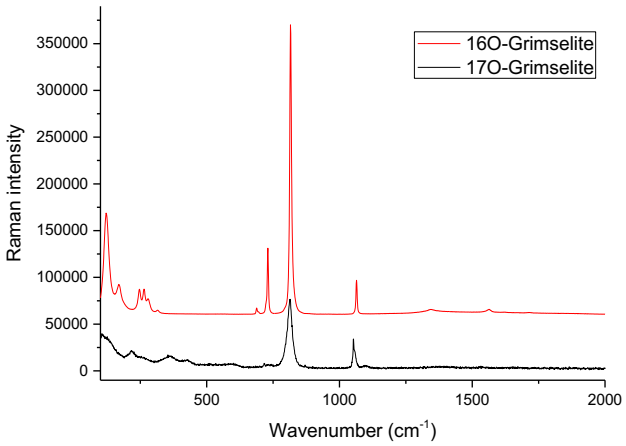

Figure 2-25 Raman spectroscopy of Grimselite after Synthesis with ^{17}O Water

It can be seen from the spectroscopies that single phase enriched grimselite was not produced. The amount of grimselite produced could be inferred from NMR intensities shown later at Figure 6-34 (see Chapter 6).

Chapter 3 Nuclear Magnetic Resonance (NMR) Techniques

3.1 NMR Advantages

The migration of radionuclides from underground nuclear waste repositories will potentially involve formation of uranium secondary minerals when groundwater reacts with the spent nuclear fuel in dissolution and precipitation reactions (Costin *et al.*, 2011). Such underground repositories, as described in Chapter 2, are anoxic environments, under which long-term equilibrium concentrations of uranium ions are low with concentrations of less than 10^{-9} mol / L (Neck and Kim, 2001). Such conditions are in contrast with oxic dissolution that may occur above ground during spent fuel interim storage at spent nuclear fuel pools with higher dissolved uranium concentrations of 10^{-6} mol / L (Shoesmith, 2000). Dissolution experiments here have detected the presence of uranium-containing precipitates even at 10^{-9} mol / L of uranium (Tan *et al.*, 2019). Nuclear Magnetic Resonance will be a good technique to identify chemical environment of oxygen and other NMR-active elements in amorphous phases, which can precede the development of well-defined crystalline mineral phases during spent fuel dissolution. Several strengths of NMR technique are detailed below:

a) Absence of long- range translational order in amorphous phases limit conventional analytical techniques based on diffraction and superposition principles due to incoherence of scattered electrons or photons. Hence, NMR spectroscopy stands out as a technique that is sensitive to subtle changes on elemental coordination that can be used to analyse chemical environments of both crystalline and amorphous samples. In this technique, nuclei with their unique combinations of protons and neutrons act as structural probes, thus the crystallinity of solid samples is not a consideration. Regardless of crystallinity, NMR's sensitivity to local chemical environments reveals structural features such as bond length and coordination parameters. Hence, it is useful for analysing amorphous materials that lack the long- range order required for diffraction.

b) A key strength of NMR spectroscopy is element or rather isotope specificity. Each element/ isotope has a unique number of fermions (protons and neutrons with half-integer spin) in its nucleus, resulting in unique resonant frequencies. Differences in resonant frequencies between different elements are in the order of megahertz (MHz),

where resonant frequencies within different chemical environments for a particular element lie in a narrow range of kilohertz (kHz). The large differences between these ranges enable the accurate detection and differentiation between the chemical environments of a particular isotope/ elements with a frequency accuracy ranging to a few hertz (Hz) or parts per millions (ppm) of the spectrum which shows more information than other non-destructive spectroscopic techniques like Raman spectroscopy, as shown below in Fig 4.1 and Fig 4.2.

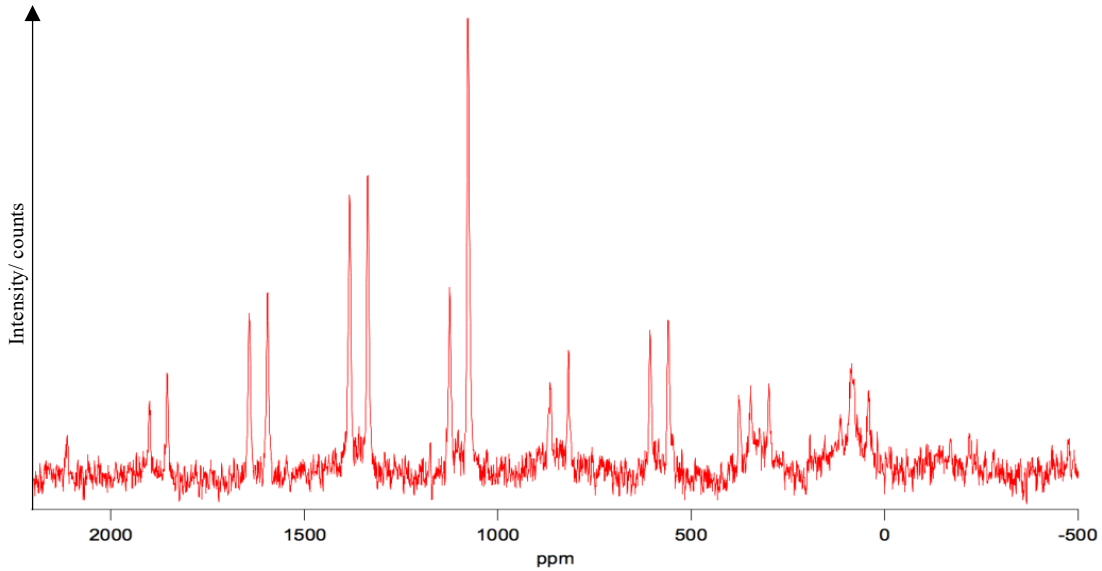

Figure 3-1 NMR spectrum of Andersonite, where the two different uranyl peaks corresponds to two uranyl bond lengths of 1.7763 A and 1.8078 A separated by a chemical shift of 47.3 parts- per- million (ppm)

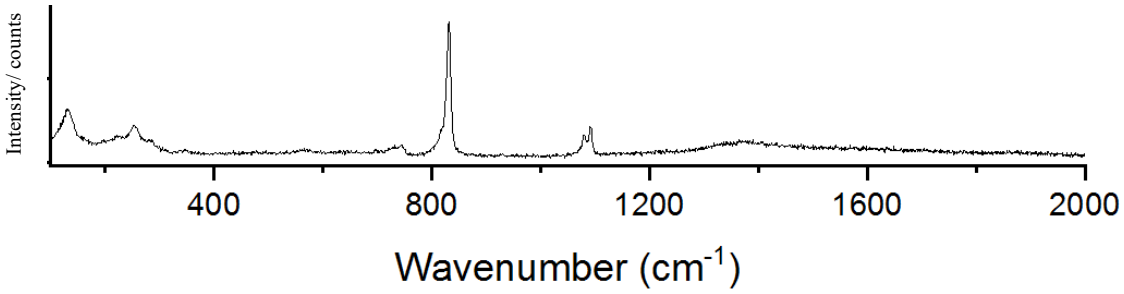

Figure 3-2 Raman spectrum of Andersonite, where the uranyl peaks are represented by 832 cm^{-1}, and the two different uranyl bond length cannot be resolved.

c) Another advantage of NMR is that its signal is directly proportional to the abundance of the nucleus being probed. NMR is based on permanent nuclear dipole instead of induced dipoles from various spectroscopies, such as ultraviolet, infrared or Raman spectroscopy where Beer- Lambert law is obeyed, and NMR reduce confounding variables such as transition cross-sections and chemical transparency.

Beer- Lambert's Law

$$\boldsymbol{I = \varepsilon \times c \times l}$$

Equation 3—1

where I denotes signal intensity, ε denotes extinction coefficient (which is dependent on properties such as cross-section and chemical transparency), c denotes the concentration of the species and l is the path length through the sample.

It is clear the intensity in an IR or UV spectroscopy experiments depends on multiple variables and analysis is more complicated than NMR where the abundance of the distinct chemical environments is reflected directly by intensity variations.

d) To complement the experiments, density functional theory (DFT) calculations with the use of the Gauge Including Projector Augmented Wave (GIPAW) by (Pickard and Mauri, 2001) will be used to verify our experimental data and elucidate the relationship between the chemical environments and the spectra obtained.

3.2 Interpretation of NMR spectra

Two models exist to explain the phenomenon of NMR. Firstly, the classical model which works generally for spin – ½ nuclei and extend to the higher spin nuclei and secondly, the quantum- mechanical model, which is consistent for all NMR- active nuclei (nuclei with non-zero spin).

3.2.1 Classical Model

NMR spectroscopy is the measurement of the precession frequencies of magnetic nuclei in a given magnetic field.

The magnetic moment $\vec{\mu}$ of a nucleus arises from its spin angular momentum $\vec{J}$ which in turn stems from its intrinsic spin, I, $\vec{\mu}$ and $\vec{J}$ are related via the gyromagnetic ratio γ , which is unique for each nuclide, by

$$\vec{\mu} = \gamma\vec{J}$$

Equation 3—2

When a magnetic field $\vec{B}$ (T) is present, a dipole with its own angular momentum like a magnetic nucleus would precess around the field at a frequency ω (rad s^{-1}) where

$$\omega = -\gamma|\vec{B}|$$

Equation 3—3

This frequency is referred to as the nuclear Larmor frequency. The overall motion could be comprehensively described by

$$\frac{d\vec{\mu}}{dt} = \gamma\vec{J} \times \vec{B}$$

Equation 3—4

In a macroscopic sample, the total magnetisation $\vec{M}$ is made up of all the individual magnetic moments as their vector sum $\sum_n \mu_n$. The presence of an external magnetic field $\vec{B}$ would induce an anisotropic net macroscopic $\vec{M}$ in its direction from originally randomly distributed (isotropic) nuclear magnetic moments resulting in a paramagnetic ensemble (Apperley, Harris and Hodgkinson, 2012).

3.2.2 Quantum mechanical aspects of NMR

Nuclear magnetic moment is derived from nuclear spin which is a quantum mechanical property that many nuclides possess. Nuclear spin results from combined individual angular momentum states of protons and neutrons, which are fermions with half- integer spins and constrained by the Pauli exclusion principle. Nuclear spin is characterised by a spin number I from which the magnitude of the total angular momentum J could be calculated by

$$\mathbf{J=\hbar\sqrt{I(I+1)}, \text{ where } \hbar=\frac{h}{2\pi}}$$

Equation 3—5

I could be either integer or half integer positive numbers.

Unlike classical angular momentum of a rotating object, nuclear spin and angular momentum are quantised. Nuclides with a spin number I have $2I + 1$ discreet energy levels, each of which could be assigned a quantum number m. m takes increasing values with unit increments from $–I$ to I. In the absence of a magnetic field, these energy levels are degenerate (identical). In the presence of an external magnetic field, these energy levels split. This is known as the Zeeman effect and is illustrated in Figure 3-3 for $I = ½$.

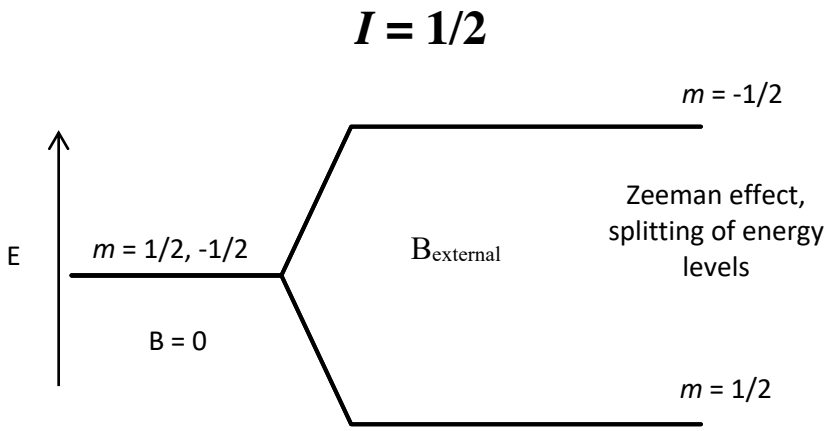

Figure 3-3 The degeneracy of energy levels m = -1/2 and m = 1/2 when no magnetic field is present and the Zeeman effect in the presence of an external magnetic field. Note that m = 1/2 is at a lower energy level.

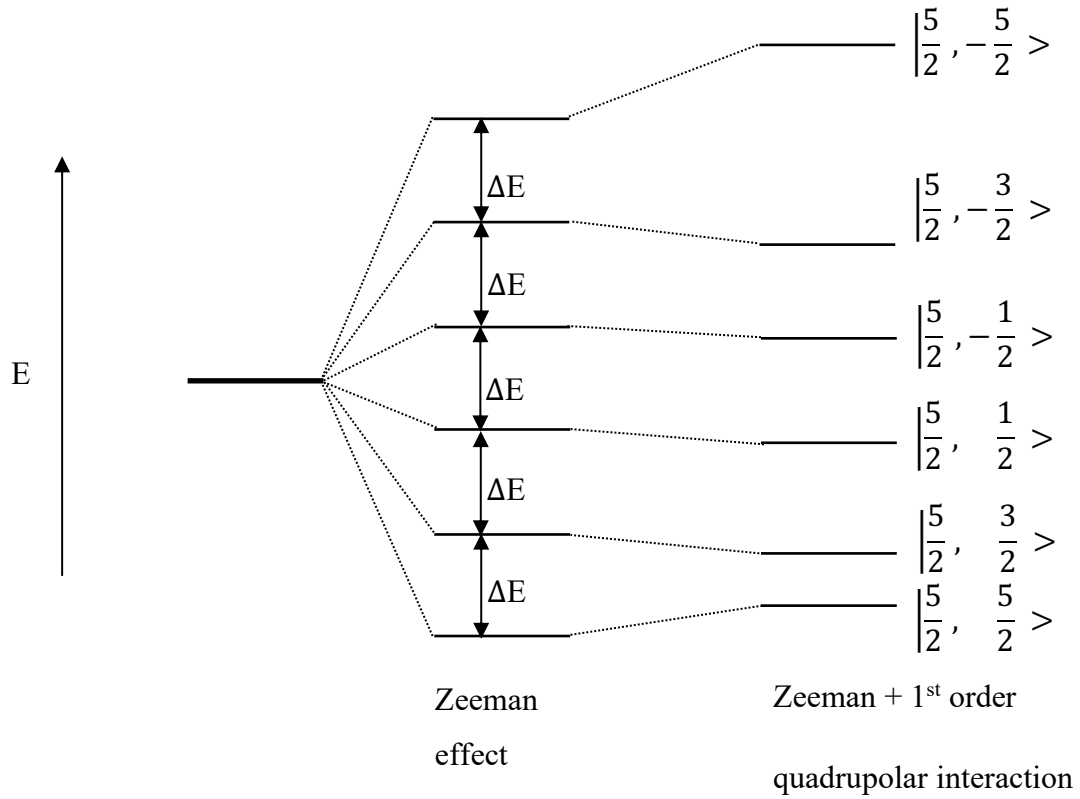

Figure 3-3 1st order quadrupole interaction for I =5/2. We see that the Zeeman effect undergoes a perturbation due to quadrupolar interaction.

Figure 3-4 shows the typical degeneracy for nuclides with spin I=5/2. It is important for this thesis as the work revolves primarily around ^{17}O nuclei, which have a natural abundance of 0.04%. Enriching our samples with ^{17}O allows the clear observation of changes that are not due to environmental contamination and endows greater confidence in the results.

In quantum mechanics, the state of any particular system is probabilistic and described by a wavefunction, ψ. As seen in Figure 3-4, there are multiple eigenstates $|I, m>$, each of which is described by a unique wavefunction $\psi_{I,m}$. The wavefunction of a system at any point of space is represented by a linear combination of these wavefunctions.

To determine certain properties of such a system, the corresponding operations can be conducted on the wavefunction (eigenfunctions) that describe the system. For example, by applying the particular spin operator $\hat{I}$ on the eigenfunction $\psi_{I, m,}$ the square of the magnitude of spin angular momentum is obtained by

$$\hat{I}^2 \, \psi_{I,\,m} = \hbar^2 \, I(I+1) \, \psi_{I,\,m}.$$

Equation 3—6

Similarly, the energy values of the non-degenerate energy levels can be obtained, each of which is an eigenstate of the spin system, in a magnetic field. The energy operator (Hamiltonian) $\hat{H}$ for an isolated (i.e. not perturbed by other interactions) nuclear spin in a magnetic field B_0 is represented by

$$\hat{\boldsymbol{H}} = -\hat{\boldsymbol{\mu}}.\boldsymbol{B_0}$$

Equation 3—7

where $\hat{\mu}.$ is the nuclear magnetic moment operator, $\hat{\mu}$, in turn, is related to the spin operator $\hat{I}$ by

$$\hat{\boldsymbol{\mu}} = \boldsymbol{\gamma}\hbar\hat{\boldsymbol{I}}$$

Equation 3—8

The direction of applied B field is defined to be in the $\vec{Z}$ direction, hence nuclear spin quantisation would be along this $\vec{Z}$ direction and so will be the Zeeman splitting. By applying the z component of the nuclear spin operator $\hat{I_Z}$ on the eigenfunction $\psi_{I,\,m,}$ the corresponding quantum number m can be obtained as follows

$$\hat{\mathbf{I}}_{\mathbf{z}}\,\boldsymbol{\psi}_{\mathbf{I,\,m}} = \mathbf{m}\,\boldsymbol{\psi}_{\mathbf{I,\,m}}.$$

Equation 3—9

Eventually, the energy of each eigenstate $E_{I,\,m}$ can be evaluated by comparing Equation 3—7, 8 and 9

$$\mathbf{E_{I,\,m} = -\gamma\hbar\, B_0 m.}$$

Equation 3—10

A simple consideration of the $I = ½$ spin, the energies of the two eigenstates $\psi_{1/2,\,-1/2}$ and $\psi_{1/2,\,1/2}$ are $½\gamma\hbar B_0$ and $-½\gamma\hbar B_0$, respectively with the energy gap between these two energy levels is $\gamma\hbar B_0$. In quantum mechanics, the Planck equation $E = h\nu$ states that energy of a photon is proportional to its frequency. Comparing the energy gap with Equation 3—3 for the classical model, it is clear that the photon absorbed/emitted associated with the transitions between the two Zeeman states has the same precession frequency as that in a classical model.

The macroscopic magnetisation $\vec{M}$ also finds its extension in quantum mechanics. In a nuclear spin ensemble at equilibrium, the Zeeman states are populated following a Boltzmann distribution as

$$\frac{N_{-\frac{1}{2}}}{N_{+\frac{1}{2}}} = e^{\frac{-\gamma\hbar B0}{kT}}$$

Equation 3—11

where N represents the population of spins, k_B is the Boltzmann constant and T is the absolute temperature. In the case of $I = ½$, according to the population distribution law, the state m = ½ is more populated than its counterpart m = -1/2 as it is a lower energy state. The larger distribution of spins in the lower energy state results in a net magnetisation $\vec{M}$.

3.2.3 Pulsed NMR experiments

The direction of the applied external magnetic field B_0 has been defined as $\vec{Z}$. The classical model of signal acquisition involves the tipping of the net macroscopic magnetisation towards the X-Y plane (X-Y-Z forms the laboratory frame (LAB) where $\vec{X} \times \vec{Y} = \vec{Z}$) and determining its precession frequency within the plane. To tip the magnetisation, an electromagnetic radiation is applied to perturb the equilibrium. This radiation is typically in the radio frequency region of the electromagnetic spectrum and usually only turned on for a few microseconds, it is commonly referred to as a rf pulse and the direction of this magnetic field is conventionally named B_1. This process is schematically shown Figure 3-5.

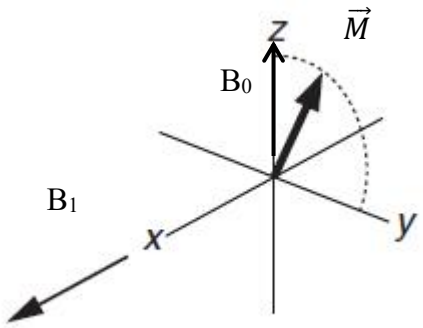

Figure 3-5 Application of a rf pulse tipping the magnetisation from the Z direction to X-Y plane.

The rf pulses in an NMR experiment are applied at a frequency near to the precession frequency. In this case, the coordination frame that is rotating close to the precession frequency of the net magnetisation so that $\vec{M}$ will be "static" in that frame as it does not precess as in Figure 3-5. A uniform excitation profile is required so that high experimental efficiency and quantification could be achieved for detection of multiple resonant frequencies. After excitation, the rf pulse is switched off and $\vec{M}$ is allowed to precess freely during which time it decays in the X-Y plane

and builds up again in the Z direction. The decay of $\vec{M}$ against time is known as free induction decay (FID) which contains all the information from an NMR experiment. Information in the time domain is hard to read, therefore FIDs need to be Fourier transformed to produce spectra in the frequency domain that can be interpreted and analysed.

3.2.4 Chemical shifts

NMR spectroscopy is useful as the nuclei in a sample interacts not only with the external magnetic field, but also the surrounding electrons, other nuclei and electric field gradients (for nuclei with I > ½ with quadrupolar interactions as seen in Figure 3-4) etc. These internal interactions generate magnetic fields at the nuclear site in addition to B_0 so that the total magnetic field experienced by nuclei in different chemical environments are slightly different. By measuring the resonance frequency resulting from a summation of all these interactions, one can obtain atomistic-level information, rendering NMR a powerful tool in materials structure studies.

Chemical bonds are formed by electrons delocalising between nuclei and they account for a large part of the structural and chemical properties of a material. When placed in a magnetic field, the electrons that surround a nucleus do not remain passive but react to the external field to create a secondary field by Lenz's law: chemical shielding, which generally reduces the effect of the magnetic field B_0 on the nucleus. The secondary field is typically ~10^{-6} to 10^{-4} of B_0 which are significant to cause measurable shifts in frequency as the sensitivity of NMR is in terms of parts per million (ppm) (Levitt, 2000). The corresponding Hamiltonian operator $\widehat{H_{cs}}$ of this secondary field can be represented (similar to Equation 3—7, 8)

$$\widehat{\mathbf{H}_{\mathbf{cs}}} = -\hbar\hat{\mathbf{I}}.\boldsymbol{\sigma}_{\mathbf{cs}}.\mathbf{B}_{\mathbf{o}}$$

Equation 3—12

where σ_{cs} is the chemical shielding tensor and the other terms have their prior descriptions. In the laboratory frame (X-Y-Z), this tensor can be represented as a 3 × 3 matrix

$$\begin{pmatrix} \sigma_{xx} & \sigma_{xy} & \sigma_{xz} \\ \sigma_{yx} & \sigma_{yy} & \sigma_{yz} \\ \sigma_{zx} & \sigma_{zy} & \sigma_{zz} \end{pmatrix}$$

Due to the chemical shielding effect, the total field B_{tot} experienced by a nucleus is

$$\boldsymbol{B_{tot} = (1 - \sigma_{cs}).B_0.}$$

Equation 3—13

Since B_0 is applied in the Z (or "zz") direction, only the σ_{xz}, σ_{yz} and σ_{zz} components are left after multiplication with the column vector, $\boldsymbol{B_0} = \begin{pmatrix} 0 \\ 0 \\ B_0 \end{pmatrix}$. Furthermore, only the 'zz' component matters as it is the component which aligns with B_0, which lies in the direction of the quantization axis, while "xz" and "yz" parts only make contributions of the second order (Duer, 2008). As a result of this simplification, Equation 3—12 becomes

$$\widehat{\mathbf{H}_{\mathbf{cs}}} = -\hbar\hat{\mathbf{I}}.\boldsymbol{\sigma}_{\mathbf{zz}}.\mathbf{B_o}$$

Equation 3—14

From Equation 3—3, the Larmor frequency ω_0 of a bare nucleus is γB_0, therefore, the deviation due to chemical shielding ω_{cs} can be simply expressed as

$$\boldsymbol{\omega_{cs} = \gamma B_0 \sigma_{zz}}$$

Equation 3—15

and the magnitude of σ_{zz} determines how much the frequency is going to be shifted.

In reality, the frequency shift was measured relative to a standard compound (reference) and represent the spectrum in a relative manner in parts-per-million (ppm) i.e. chemical shift δ as

$$\delta = \frac{\omega - \omega_{ref}}{\omega_{ref}} \times 10^6$$

$$= \frac{\gamma(1-\sigma_{zz})B_0 - \gamma\left(1-\sigma_{zz}^{ref}\right)B_0}{\gamma\left(1-\sigma_{zz}^{ref}\right)B_0} \times 10^6$$

$$\approx \frac{\sigma_{zz}^{ref} - \sigma_{zz}}{1-\sigma_{zz}^{ref}} \times 10^6 \approx \left(\sigma_{zz}^{ref} - \sigma_{zz}\right) \times 10^6$$

Equation 3—16

3.2.5 The two frames: Laboratory and principle axis

Being interested in the secondary contributions, it is possible to represent the shielding tensor in a frame that all the off-diagonal components of the tensor matrix are zero as

$$\begin{pmatrix} {\sigma_{xx}}^{PAF} & 0 & 0 \\ 0 & {\sigma_{yy}}^{PAF} & 0 \\ 0 & 0 & {\sigma_{zz}}^{PAF} \end{pmatrix}$$

and this frame is called the principle axis frame (PAF). This can be done by performing matrix rotations on the original shielding tensor shown in Equation 3—13.

$$\begin{pmatrix} \sigma_{xx} & \sigma_{xy} & \sigma_{xz} \\ \sigma_{yx} & \sigma_{yy} & \sigma_{yz} \\ \sigma_{zx} & \sigma_{zy} & \sigma_{zz} \end{pmatrix} \rightarrow \begin{pmatrix} \sigma_{xx}^{PAF} & 0 & 0 \\ 0 & \sigma_{yy}^{PAF} & 0 \\ 0 & 0 & \sigma_{zz}^{PAF} \end{pmatrix}$$

Equation 3—17

The important implication of this is shown below and will be used in Chapter 3.3 NMR parameters calculation. As with the chemical shielding, the chemical shift should be regarded as a tensor in both frames. In the LAB, based on Equation 3—16 each component of the matrix is

$$\delta_{\alpha\beta} = \frac{\sigma_{\alpha\beta}^{ref} - \sigma_{\alpha\beta}}{1 - \sigma_{\alpha\beta}^{ref}} \text{ where}$$

$$\alpha\beta \text{ are combinations of } x, y \text{ and } z \text{ depending on position in tensor.}$$

Equation 3—18

and in the PAF, this is obtained $\begin{pmatrix} \delta_{xx} & 0 & 0 \\ 0 & \delta_{yy} & 0 \\ 0 & 0 & \delta_{zz} \end{pmatrix}$

The isotropic chemical shift δ_{iso} is defined as the average of the three principal values i.e.

$$\delta_{iso} = \frac{\delta_{xx} + \delta_{yy} + \delta_{zz}}{3}$$

Equation 3—19

The exact allocation of axes x, y and z differs in the literature. In this thesis, the Haeberlen notation is adopted.(Haeberlen, 1976):

$|\delta_{zz} - \delta_{iso}| \geq |\delta_{xx} - \delta_{iso}| \geq |\delta_{yy} - \delta_{iso}|$ with anisotropy Δ_{cs} and asymmetry η_{cs} being

$$\Delta_{cs} = \delta_{zz} - \delta_{iso}$$

$$\eta_{cs} = \frac{\delta_{xx} - \delta_{yy}}{\delta_{zz} - \delta_{iso}} \quad .$$

Equation 3—20

and these three parameters are required to fully describe a chemical shield tensor, in terms of its shape and width.

With all these tools in the toolbox, and based on derivations from literature (Duer, 2001; MacKenzie and Smith, 2002; Apperley, Harris and Hodgkinson, 2012 etc.), this is deduced

$$\delta = \delta_{iso} + \frac{\Delta_{cs}}{2}\,(3\cos\,^2\theta - 1) + \eta_{cs}\sin\,^2\theta(\cos 2\phi)$$

Equation 3—21

where θ and ϕ are the two polar angles describing the orientation of B_0 relative to the PAF[1]. As shown, the exact frequency shift, δ is orientation dependent.

3.2.6 Magic angle spinning solid-state NMR

Fundamental differences impose challenges in solid state NMR when contrasting with solution NMR because of the rigid network structures and the associated anisotropies, which are shown in the interaction tensors in the earlier chapter.

Chemical shielding as seen in Equation 3—21 is anisotropic, that is orientation- dependent. In liquid NMR, the natural tumbling of molecules occurs at a sufficiently high speed and is randomly averaged over the surface of a sphere such that these anisotropies are averaged to a **single sharp line** (high resolution) at the isotropic shift position as all molecules experience the field in all orientations. The work set out in this thesis are conducted solely on powder samples where such tumbling cannot occur, broad lines are formed as the differently orientated sites resonate over a range of frequencies. Each crystallite in a powder-form sample would have their PAF in all possible orientations with respect to the external magnetic field direction. Therefore, the orientation-dependent (anisotropic) interactions would alter the energy levels to different extent in a powder-form sample for different crystallites. Consequently, different frequencies (shifts) was observed even from a chemically identical site and the resulting **broad lines** are termed the powder-pattern line shapes with its associated poor resolution.

Magic angle spinning (MAS) is an effective technique in the removal of the effects of chemical shift anisotropy. By spinning rapidly at the magic angle of 54.736° chemical shift anisotropy

[1] Technically, the relative orientation between LAB and PAF needed to be expressed with three Euler angles. However, the z axis of LAB i.e. the B_0 direction is a symmetry axis for all tensors in their PAF so that the two polar angles suffice.

and at sufficient speeds, heteronuclear coupling can be removed (Duer, 2008) leaving a resonance at the isotropic shift position, as in liquids.

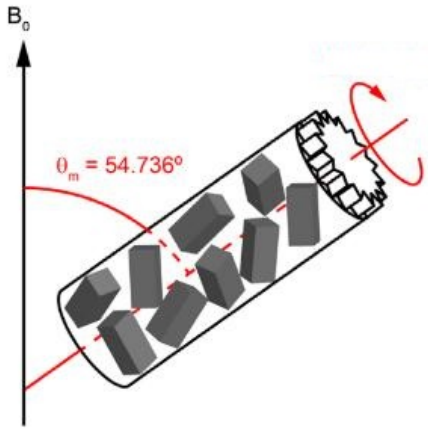

Figure 3-6 An illustration of magic angle spinning where the rotating axis is tilted from B_0 by 54.736º

The reason is because the anisotropic part is modulated by term $(3\cos^2\theta - 1)$ where θ is the angle between rotor axis and B_0 (Mackenzie and Smith, 2002) and this magic angle, 54.736° causes the term $3\cos^2\theta - 1$ to be equal to 0. Physically speaking, when a powder is spun at the magic angle all orientations of the crystal experience the same time-averaged orientation, generating a sharp peak at the isotropic shift. In the process of spinning (see Figure 3-7), the crystallites are rotated away from their initial position with respect to the magnetic field. This leads to them sampling a set of fields before the process is reversed during the second half of the rotor period due to the 2-fold symmetry of the magnetic field, and the same fields are experienced by the spins but with the opposite sign. This symmetry means that moments that are dephasing in the x-y plane in the first half of the rotation converge in the second half. As the rotor returns to its starting point the spins are all aligned in their starting position. This refocusing causes a peak in the magnetisation once every rotor period, these so-called rotational echoes can be observed in the FID of sample being spun (see Figure 3-8). Fourier transformation of such a signal results in spinning sidebands emanating from the isotropic shift with intensities dependent on the chemical shift anisotropy of the site in question (Herzfeld and Berger 1980).

a)

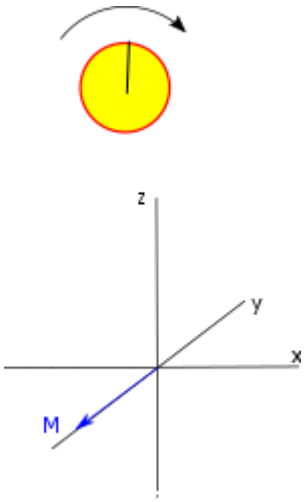

The rotor in its initial position with the magnetisation aligned on y-axis.

b)

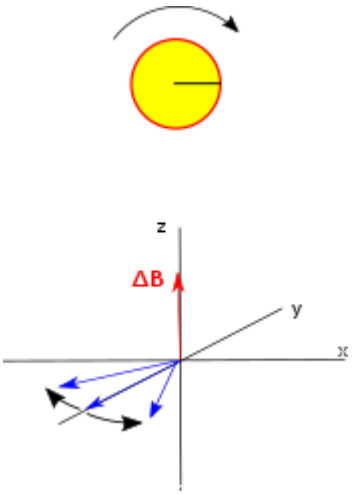

As the rotor rotates an apparent reduced field develops, and the moments disperse due chemical shift anisotropy.

c)

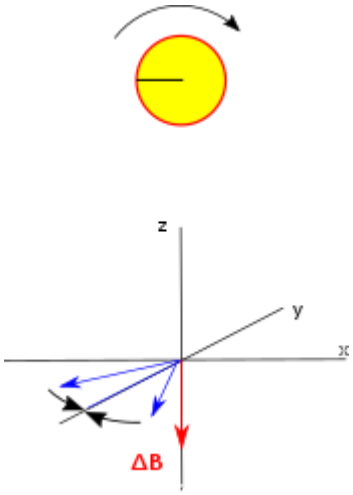

With the rotor mirrored in the z-axis compared to b, the apparent reduced field is reduced so, by symmetry the spins converge as they were dispersing.

d)

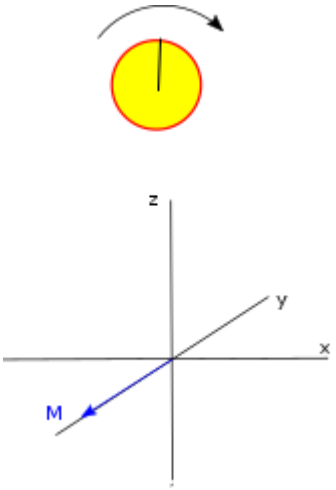

When the rotor returns to its starting position the moments have refocused generating an echo.

Figure 3-7 Simplified illustration of the formation of a rotational echo in MAS NMR.

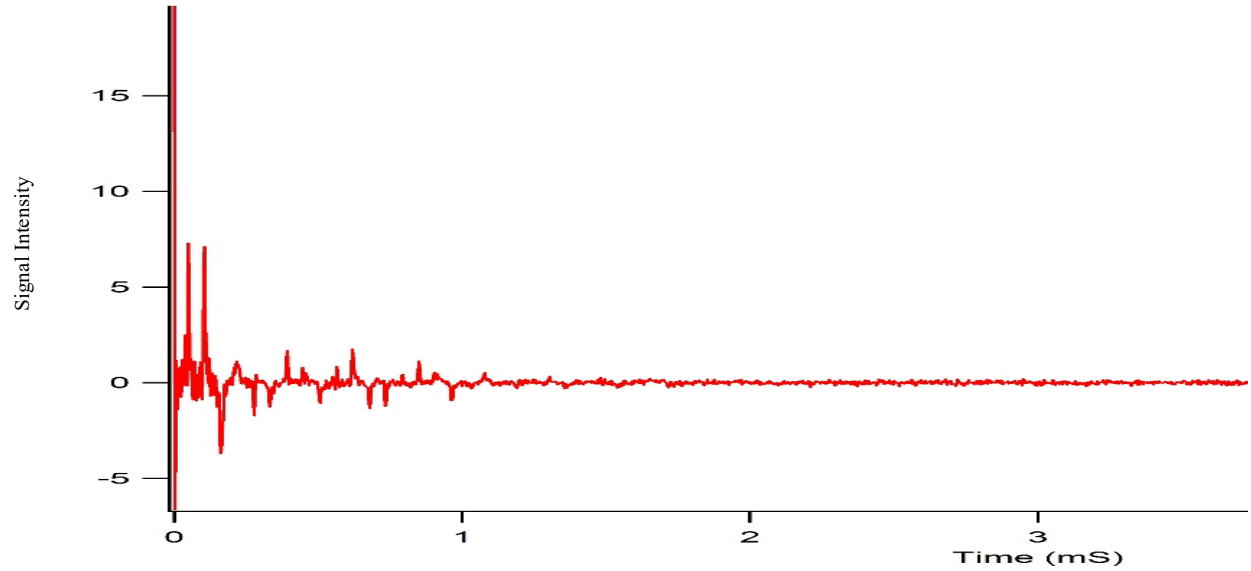

Figure 3-8 Untransformed free induction decay signal from ^{17}O spectrum of metaschoepite with rotational echoes clearly visible in the first millisecond.

3.2.7 Spinning speed

In order to fully remove the broadening associated with anisotropy, the spinning speed must be fast with respect to the anisotropy. That is the sample must be spun at a frequency higher than the width of the range frequencies seen due to the anisotropy. Should this not be achieved, spinning sidebands will result. These sidebands radiate from the isotropic line and are separated by the spinning speed; faster spinning results in greater separation between the isotropic line and its sidebands. The isotropic line is not necessarily the most intense line, as is the case for most of the minerals studied as part of this work where the first two sidebands at higher shifts are more intense than the peak at the isotropic shift (see Figure 3-9). The isotropic line can be simplified by conducting experiments with the sample spun at different speeds. As the spinning frequency determines the sideband spacing, sidebands will appear in different positions when spun at different speeds whilst the isotropic shift is invariant.

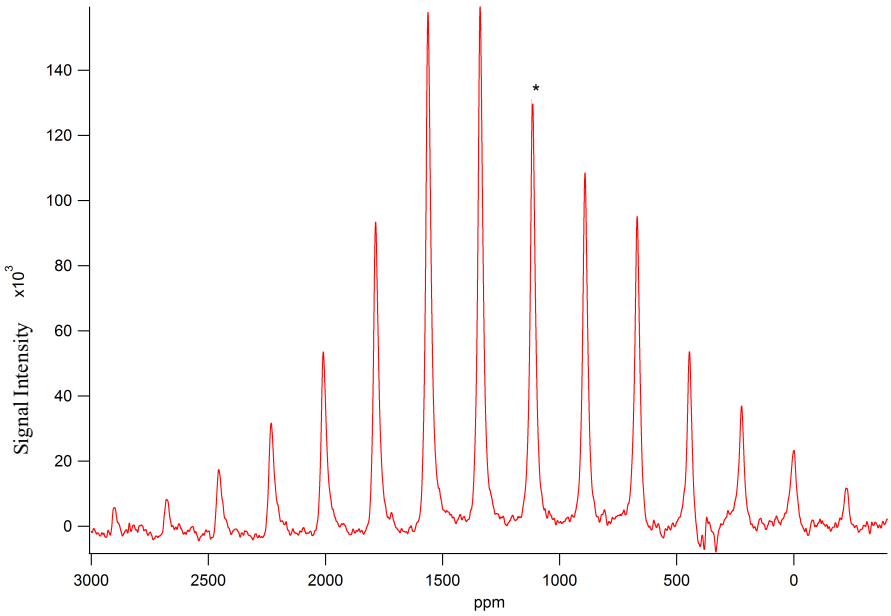

Figure 3-9 ^{17}O spectrum of a single uranyl environment. Spinning at 15.1 kHz produces sidebands of the isotropic peak at 1114.8 ppm (marked with a star). The sideband separation of 223 ppm corresponds to 15.1 kHz.

The degree to which sidebands are observed is a function of the level of chemical shift anisotropy, greater chemical shift anisotropy corresponds to the asymmetry of the local bonding environment which is proportional to the number of electrons (Duer, 2008). As this work is focused on uranium minerals, the large number of electrons of the uranium neighbour is commensurate with the high chemical shift anisotropy of the ^{17}O nuclei that leads to a large number of sidebands.

3.2.8 Spin echo experiment

Due to short lived resonances in the circuitry of the probe (ringdown), the first part of the FID could not be collected. Transforming the signal from any rotational echo (i.e. discarding data collected before that point) can give a full spectrum, but it leads to some signal losses as the beginning signal is not usable. Nonetheless, it has proven useful in the collection of ^{17}O spectra of uranium minerals (see Figure 3-9) where transforming the FID from zero time resulted in large distortion.

An improvement is to use the spin echo procedure instead of the single pulse procedure, which was used to produce most of the spectra in Chapter 6.

.

The spin echo experiment involves

1) Application of a 90° pulse which will tip the magnetisation into the x-y plane.

Inhomogeneous dephasing (due to magnetic field inhomogeneities or anisotropy) will occur subsequently, causing different spins in the samples to precess at different rates, some spins will slow down whereas others speed up, causing the signal to decay.

2) After a short time interval, t, a 180° pulse is applied to invert the magnetisation and the echo is collected after another identical short time interval.

Upon inversion, it was noted that the slower spins will lead the faster spin. Nonetheless, in the same interval, t, they will all travel back to the main moment as spins of different speeds travel their respectively similar distances after the 90° and 180° pulse.

This procedure helps to completely refocus the spins and an accurate T_2 echo can be collected. Practically, this approach helps to get signals that can be phased easily and reduces the ringdown effect of the coil in the spectra due to the echo delay before collection of the signal.

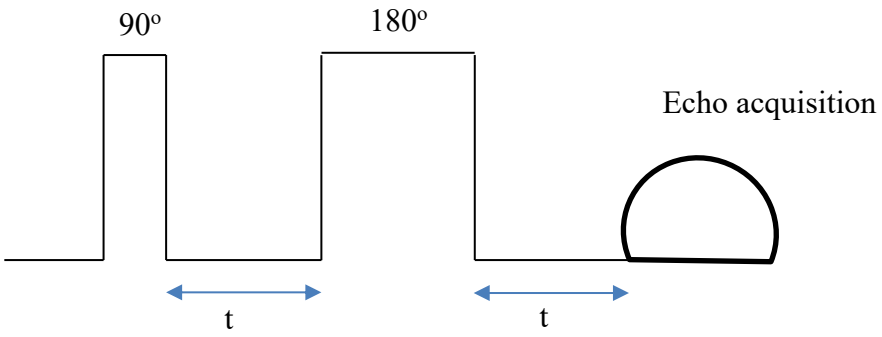

Figure 3-4: Schematics of Spin echo experiment

3.3 NMR parameters calculation

3.3.1 CASTEP

Cambridge Serial Total Energy Package (CASTEP) is a first-principle quantum mechanical code for calculating electronic structure related materials properties, designed based on density function theory (DFT) plane-wave pseudopotential methods (Segall and Probert, 2002). As a first-principle method, CASTEP does not rely on any empirical data but calculate the electronic structure solely from the fundamental assumptions of quantum mechanics. That being said, it is still impossible to exactly solve many-body Schrödinger equations without making sensible approximations. Since its new modular redevelopment since 1999, CASTEP code is now capable of calculating a series of physical properties of materials including total energy, electronic charge density, phonons, NMR parameters and performing geometry optimisation and molecular dynamics tasks (Clark *et al.*, 2005). For more accurate simulation of highly correlated materials, the Hubbard model known as DFT + U scheme was built (where U is often known as the Hubbard's term or on-site Coulomb parameter) which is computationally convenient for accurate calculations of electronic structures. The CASTEP implementation of DFT+U adopts a simplified, rotationally invariant approach where the only external parameter is the effective value of the on-site Coulomb parameter, U, for each affected orbital. This parameter can be calculated theoretically but experience shows that the best results are achieved when the U parameter is allowed to vary. CASTEP does not calculate the value of U but uses it as an input parameter for DFT + U calculations.

3.3.2 DFT and plane-wave pseudopotential

First of all, CASTEP adopts the Born-Oppenheimer (BO) approximation (Kohn and Sham, 1965) such that nuclei and electrons in a system could be treated separately because of the drastically different mass of these two kinds of particles. Since nuclei are massive and slow relative to electrons, the necessity of solving time-dependent Schrödinger equations for electrons is reduced to time-independence in nuclear coordinates. Even with this simplification, solving many-electron time-independent Schrödinger equations is still an unfeasible undertaking. The idea of DFT is to deviate from solving the many-electron Schrödinger equation directly but to build up a model in which each single electron can be feasibly treated by solving a single-particle Schrödinger equation. The real situation thus can be well simulated by integration/summation of each individual state providing good approximations are made.

In the Kohn-Sham scheme, at ground state, an interacting many-electron system can be equivalently represented by a set of non-interacting single electrons, each of which experiences an effective potential that results from the charge density ρ(ρ is a function of position r). If ρ(r) is identical to that in the true system, one only needs to solve the single-particle Schrödinger equation even though this is needed for all the electrons in question as each one has its own energy state.

Atoms are periodically arranged and the charge density should hence vary periodically. This phenomenon can be employed to apply Bloch's theorem. According to Bloch's theorem, the wavefunction can be represented as

$$\psi_k(r) = e^{ikr}\, u_k(r)$$

Equation 3—22

where $u_{\mathbf{k}}$ is a periodic function with respect to the lattice. i.e. $u_{\mathbf{k}}(\mathbf{r}) = u_{\mathbf{k}}(\mathbf{r} + \mathbf{L})$ with $\mathbf{L}$ being an arbitrary lattice vector.

A basis set of plane-waves are adopted in CASTEP as the choice for the periodic function $u_{\mathbf{k}}$ in the form

$$u_k(r) = \sum_G c_k(G) e^{iGr}$$

Equation 3—23

Therefore, this leads to

$$\psi_k(r) = \sum_G c_k(G) e^{i(k+G)r}$$

Equation 3—24

where c_k are

the Fourier coefficients and the exponential term is the plane-wave of wavenumber $\boldsymbol{k}$ while $\boldsymbol{G}$ is the reciprocal lattice vectors ($\boldsymbol{G}$-vectors). The quality of electronic state calculations then depends on the number of $\boldsymbol{k}$ sampled in the first Brillouin zone (k-points sampling) and the number of $\boldsymbol{G}$-vectors included for representing the plane-wave functions (Moran, Dawson and

Ashbrook, 2017). Therefore, all calculated results must be convergence tested against these two parameters[2] to achieve accuracy.

One of the disadvantages of using plane-waves is that the number of plane-waves needed, hence number of ***G***-vectors, is determined by the greatest curvature of the wavefunction (Segall and Probert, 2002) i.e. very large ***G*** components are required for the area close to nuclei where there is very attractive Coulomb potentials. Two approximations have been made in order to increase calculation efficiency with very little loss in accuracy (Kohanoff, 2006). Firstly, "core" electrons within a defined atomic region close to nucleus are "frozen" so that only valence electrons are explicitly calculated. Secondly, the rapid oscillations of valence electron waves close to the nucleus are "smoothed" out. Both simplifications are valid because tightly bonded "core" electrons are largely unaffected in different chemical environments and electron waves in the near-nucleus region are not directly relevant to chemical bonding. Therefore, a smooth effective potential can be defined in the near-nucleus region to achieve the two goals of replacement of the strong nuclear Coulomb potential and the provision of the same screening effects of "core" electrons on the valence ones. Such a potential is called a pseudopotential and this methodology is adopted in CASTEP code.

3.3.3 Calculating NMR parameters using CASTEP

Despite the success in increasing calculation efficiency by adopting pseudopotentials, the high sensitivity of NMR parameters, especially chemical shielding, to the near-nucleus electrons requires a full treatment of all electrons. The so-called Projector Augmented Wave (PAW) method (Van De Walle and Blöchl, 1993) treats this inconvenience explicitly by applying a linear transformation operator on the pseudo- wave functions, the functionality of which is to map it onto the corresponding all-electron wave functions so that the latter is reconstructed. The breakthrough in the calculation of the magnetic response of all-electron wave functions reconstructed from PAW came about with the integration of a field-dependent transformation operator to account for the gauge origin problem (Bonhomme *et al.*, 2012). Such an approach is called the Gauge Including PAW (GIPAW) method (Pickard and Mauri, 2001). The

[2] In setting up a CASTEP calculation, the exact number and grid of k points can be specified; the number of G-vectors is manifested in the cut-off energy *E*cut which sets the highest kinetic energy of the plane-waves in the basis set.

"pseudopotential + GIPAW" method is adopted in CASTEP *Magres* modules for calculating NMR parameters including isotropic chemical shift, chemical shielding, J-coupling and electric field gradient (EFG) tensors. In some cases, it has provided exceptionally good agreements with experimental results (Profeta, Mauri and Pickard, 2003; Ashbrook *et al.*, 2007).

3.3.4 Interpreting CASTEP simulations

Using CASTEP MAGRES, the eigenvalues and eigenvectors of the quadrupolar tensor and the chemical shielding tensor can be calculated. From these tensors, the orthonormal basis can be constructed which will then be tested by two steps, the multiplication of itself by its transpose and the calculation of its determinant.

If the two bases are orthonormal, the multiplication by its transpose will yield the identity matrix. And to make sure that the mapping occurs in the right-hand screw coordination system, the determinant should give one. By convention, the largest component of the quadrupolar and the chemical shield tensor is the V_{zz} direction and σ_{zz}, however the mapping of x and y component may be reverse. This is the best way to ensure that the orthonormal bases are selected correctly and the rotational matrix will also give a determinant of one, hence it will be a true rotational matrix instead of a reflection from left hand coordinate system to right hand coordinate system.

Subsequently, MagresView can be used. It is a viewer funded by EPSRC research in 2016 to look at our simulation output visually (Sturniolo *et al.*, 2016). This is an open source tool to aid the processing and visualisation of ab-initio computed solid-state NMR parameters with the Magresfile format for computed NMR parameters (as implemented in CASTEP v 8.0). MagresView is built on the Jmolcrystal viewer, and provides an intuitive environment to display computed NMR parameters. It allows the visualisation of the relative sizes and orientations of chemical shift and quadrupolar tensor principal values onto atomic sites.

Chapter 4 Non- NMR Experimental techniques

4.1 X-Ray Diffraction

X-ray diffraction (XRD) was used in characterisation of the uranium dioxide thin film and powder for the dissolution experiments and studtite and metastudtite minerals for the temperature-dependence experiment. It is a powerful tool for studying periodic structures and is able to obtain useful information such as lattice parameter and crystallinity. Powder XRD patterns collected from samples were used in this project to confirm the synthetic starting minerals produced as well as to refine their structure. This section gives an introduction to the basic theory of XRD and a discussion of the adaptations to the procedure needed to allow the use of uranium minerals on existing equipment.

4.1.1 Physics of XRD

The diffraction of electromagnetic radiation (X-rays in this case) with a lattice of atoms in a crystalline material leads to multiple light rays that undergo constructive interference at certain angles as described by Bragg's Law. This relates the integer number, n, of wavelengths, λ, of X-rays interference from a plane with Miller indices, *hkl, and* interplanar spacing d and the angle of incidence, θ, as in Equation 4—1 and illustrated in Figure 4-1.

$$\mathbf{n\lambda = 2d_{hkl} \sin \theta}$$

Equation 4—1

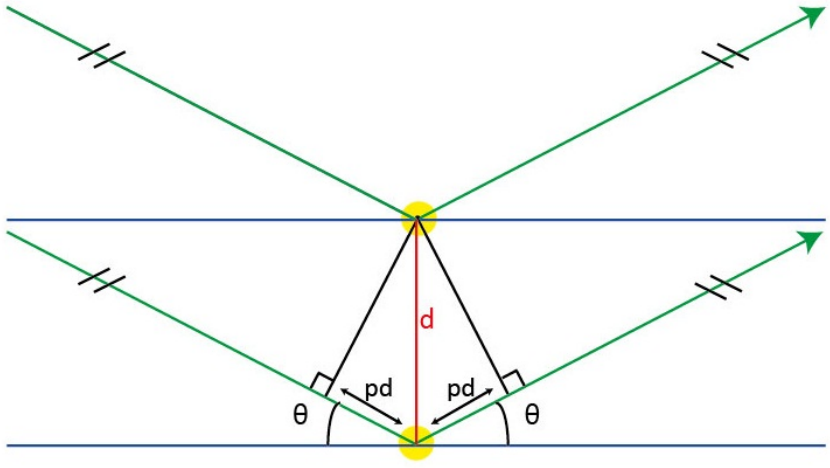

Figure 4-1: Diffraction of X-rays (green) from planes in a crystal lattice, where 2pd is the path difference and constructive interference results when the path difference is an integer number of the wavelength

The path difference between waves scattered from the upper and the lower planes in Figure 4-1 differs by twice the length *pd*, which by simple trigonometry equates to $2d\sin\theta$. When the path difference is equivalent to integer wavelengths, constructive interference occurs giving rise to an intense spot in a diffraction pattern. Thus, in powder diffraction with a random distribution of powder crystallites, cones of X-rays are scattered from the sample with angles that correspond to the spacing of the planes from which they have been diffracted (see Figure 4-2). In powder XRD, the source and detector sweep through an arc in one dimension to build up a picture of the diffraction pattern. The sample is generally rotated to ensure that all orientations are being sampled so that no diffraction planes are omitted.

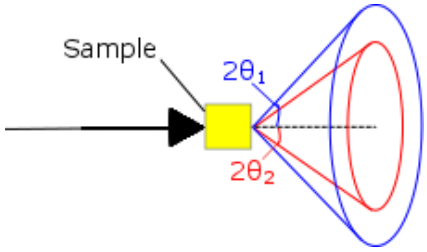

Figure 4-2 Diffraction cones formed from diffraction at angles θ_1 and θ_2.

The resultant diffraction pattern contains intensity peaks at values of 2θ where the Bragg condition is met with each peak corresponding to diffraction from the spacings between adjacent lattice planes with the angle of the peak dependent on the spacing of the planes. In simple cases, or where knowledge of the sample allows, the spacing of the planes combined with their Miller indices allows the lattice parameters of the phase to be determined.

The intensity of peaks is affected by several factors, such as the structure factor and the atomic scattering factor. Figure 4-3 illustrates diffraction from the same scenario as in Figure 4-1, but with the presence of an additional atom at position B. Here the observed intensity from atoms at position C from adjacent layers will be affected by interference with rays with the other atom in its motif located at B. The rays diffracted by the two atoms in the motif will have a phase difference of CD – AB. This leads to structure factors which account for the effect of such interference and for a motif is given by;

$$\mathbf{F_{hkl}} = \sum_{\mathbf{n=1}}^{\mathbf{N}} \mathbf{f_n exp}\left(\mathbf{hx_n} + \mathbf{ky_n} + \mathbf{lz_n}\right)$$

Equation 4—2

where $\boldsymbol{F}_{hkl}$ is the structure factor for the reflection with Miller index (h k l) off a motif with N atoms at coordinates (x, y, z) and atomic scattering factors f_n. (Clearfield *et al*. 2008)

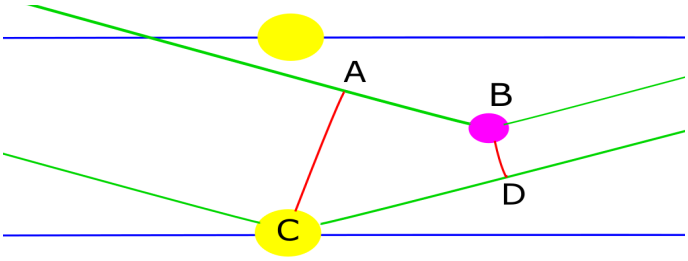

Figure 4-3: Diffraction from a motif, where an additional purple atom is present. Green lines represent parallel X-rays, and red lines serve as guide to the eye perpendicular to these.

Scattered intensity is also dependent on the atom responsible for the scattering, this is described by the atomic scattering factor. Atomic scattering factors are dependent on the element that is scattering the X-rays as well its oxidation state, the angle of scattering, and temperature. X-rays are scattered by electrons which, as charged particles, oscillate with the applied electric field of the incoming electromagnetic radiation. This oscillation causes the electron to absorb energy from the incident wave which it re-emits coherently. Thus if atoms are represented as a point source the atomic scattering factor could be approximated as the number of electrons per atom multiplied by the effect for one electron. The effect is however complicated by the similarity of the wavelength of the x-ray radiation (e.g. Cu Kα = 0.15 nm) to the diameter of the atom in which the scattering electrons lie (e.g. uranium at 0.35 nm). Thus phase differences in the radiation scattered by different electrons in the same atom occur and this affect the resultant intensity of the scattering. This is represented by the atomic scattering factor which is also angle dependent. Nevertheless, the interaction between atoms and X-rays is stronger with heavier atoms, as represented by a larger atomic scattering factor which is not monotonous due to absorption edges (Yager, 2014).

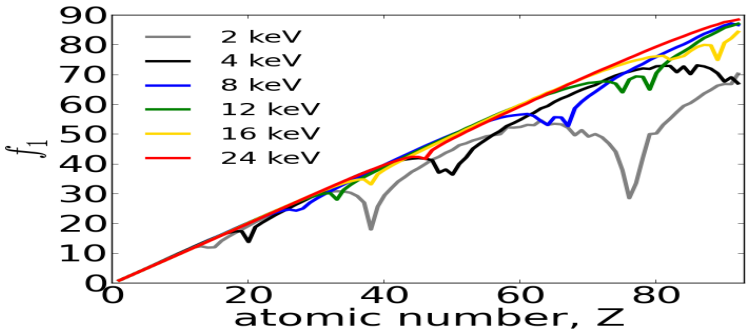

Figure 4-4 The graph of the dispersive component of the atomic scattering factor , $f1$, against atomic number, Z where the non-monotonous trend is due to absorption edges, which is less apparent at higher energy of X rays.

The large disparity in number of electrons between uranium and lighter elements such as oxygen and hydrogen that make up uranium minerals meant that the uranium positions can be readily resolved, however the large diffraction intensity due to uranium atoms results in difficulty in discerning of the lighter atoms. Since uranium atoms are usually bonded with oxygen and water molecules, problems ensue. Oxygen can be difficult to place, and the location of protons only inferred by geometric and bond valence considerations (Cejka 1998).

In the case of more complex structures where the phase being measured is not known it may be more difficult to assign Miller indices to all peaks. Indeed one of the main uses of XRD in this project was the identification of the produced phases for which an approach of fingerprinting against reference patterns was used. In addition to their angles, the intensities of peaks diffracting from a plane is dependent on geometric factors, as well as on the atom they are being diffracted from. This allows unknown phases to be identified by comparison of peak positions and intensities to those of reference patterns.

4.1.2 Rietveld refinement of powder XRD

Full structural refinement from a diffraction pattern of an unknown material works best with a single crystal sample for isolation of all crystal orientation. In dissolution studies and uranium mineral synthesis, no sufficiently large single crystal samples could be identified and isolated so powder X-Ray diffraction was used. This allows a one-dimensional X-ray pattern to be compared to a reference or calculated pattern in order to identify a structure.

In powder diffraction, the lack of information regarding orientation of diffracting planes makes ab-initio structural refinements difficult. However, refining the structure can be completed when a candidate structure has been identified (for instance by fingerprinting against reference patterns). A least squares Rietveld refinement is then conducted: A pattern is calculated based on a postulated structure and instrumental parameters. A fitting routine then alters the structure to optimise the match between the measured and calculated patterns. This approach is versatile allowing for factors such as broadening due to strain, and crystallite size to be refined, as well as determining the proportions of multiple phases present, in addition to refining the individual structures (B. Toby, 2006).

Care is required in the analysis of powder diffraction data. Due to many convoluting factors affecting the peak shapes and intensities, an erroneous structure may be fitted, i.e. by the use

of unrealistic orientations. Consideration of past literature and possible bond lengths are vital in interpreting a fit of powder diffraction data.

Use of single crystal diffraction can provide significantly more information, eliminating a lot of the uncertainty encountered in the fitting of powder data when the structure cannot be easily deduced. Single crystal data was, however, not available for the materials studied in this work as equipment to allow the isolation and mounting of the relatively fine crystals whilst working inside a glovebox was not available.

4.1.3 Quantitative Analysis

As part of this project, powder X-ray diffraction was used to determine the extent to which UO_2 could be (chemically) reduced in our laboratory and determine the structures of some secondary minerals, such as studtite. The simplest yet still robust method to determine the composition of a two-phase system is by comparison of peak intensities of a multi-component sample with intensities attained for reference samples of each individual component and mixed phase samples of known composition to calibrate them.

This method was not practical for this work due to the difficulty in isolating alteration products to produce calibration samples. This led to the use of Rietveld refinement for the quantification of the level of alteration of UO_2 to its secondary minerals in the experiments.

Whilst the refinement software used for this work, TOPAS 4, is proprietary and so the exact algorithms used cannot be known, the underlying theory of quantitative Rietveld analysis is briefly outlined. The aim of the Rietveld refinement is the minimisation of the differences between the square of the intensities of a calculated pattern and the experimental data. Thus in the following equation R is minimised where,

$$\mathbf{R} = \sum_{\mathbf{n}} \frac{\mathbf{1}}{\mathbf{I_n}} \left[\mathbf{I_{exp_n}} - \mathbf{I_{cal_n}}\right]^{\mathbf{2}}$$

Equation 4—3

I_{exp} and I_{cal} are the experimental and observed intensities of n^{th} peak. The weighting factor $1/I_n$ is applied to prevent high intensity peaks from dominating R and hence, ignoring areas of low intensity from being fitted (Clearfield, 2008). The calculation are summed up in the following equation

$$\mathbf{I_n = \sum_p s_p \sum_{K_p} LP_{K_p} m_{K_p} |F_p|^2 G(\theta)_{n,p} Or_{K_p} + I_{bg_n}}$$

Equation 4—4

s_p is the scale factor of phase p. It is by comparison of the values of the scale parameters for the phases present.

K_p signifies the Kth peak of phase p.

LP_K is the Lorentz polarisation factor of the Kth peak. This is a geometric factor that accounts for the polarisation of X-rays during scattering, and geometric considerations.

I_{bg} the background intensity, which in this work has been modelled with a Chebyshev function,

Or_{Kp} is the orientation factor of phase p, and

$G(\theta)_p$ is the peak profile function which is angle dependent and discussed below.

The peak profile function accounts for the peak broadenings, instrumental and sample effects. Whilst monochromatic X-ray sources were used, the emission profile is not infinitely narrow. This slight variation in wavelength effectively broadens the values of θ for which the Bragg condition is met, resulting in broadened peaks. Additionally the diffractometer will have some limitations to its resolution which causes peak broadening. Some of these effects will be constant with angle, and others angle dependent and these dependencies are modelled within the refinement software to calculate their contribution to G at each point. Parameters describing the instrumental line broadening were characterised for the diffractometers used in this work based on highly crystalline reference samples of corundum. The instrumental parameters were then not refined whilst fitting the pattern of samples undergoing characterisation.

Whilst crystallite size and residual strains were not a focus of this study, their effect on the line width nevertheless requires fitting in a realistic manner. Strain due to the presence of dislocations within the sample creates differences in the inter-planar spacing and thus the Bragg angle. Assuming the strain, ε, is pure tensile or compressive (In thin film dissolution experiment, tensile stress resulting from lattice parameters mismatch between the substrate and thin film), the average value of an increase in the full width at half maximum is

$$\mathbf{\beta = -4\varepsilon \tan \theta}$$

Equation 4—5

For crystallites smaller or around 500 nm, broadening occurs dependent on the crystallite size, as described by the Scherrer Equation;

$$\beta_{hkl} = \frac{K\lambda}{L_{hkl}\cos\theta}$$

Equation 4—6

β is the broadening in the peak and is known as the integral breadth and is converted from the full width at half maximum intensity (FWHM) with the Bragg profile where for a Gaussian distribution,

$$\beta_{hkl} = \frac{H}{2}\left(\frac{\pi}{ln2}\right)^{\frac{1}{2}}$$

Equation 4—7

L is the mean size of the crystallites, and K a shape factor with a value between 0.89 and 1 whose value is dependent on the geometry of the diffracting crystallites. Care must however be taken when determining crystallite sizes and strains using this method as other crystal imperfections such as stacking faults and twins may give rise to broadening.

4.1.4 Adaptations for Radioactive Work

Powder X-ray diffraction is typically conducted with samples mounted in one of two ways: In the Bragg-Brentano geometry the sample rests on top of a flat mount which it has been transferred to in suspension (see Figure 4-6). Alternately the sample can be loaded into a glass capillary mounted perpendicular to the beam and detector such that at 0° the beam can pass straight through the sample (see Figure 4-5).

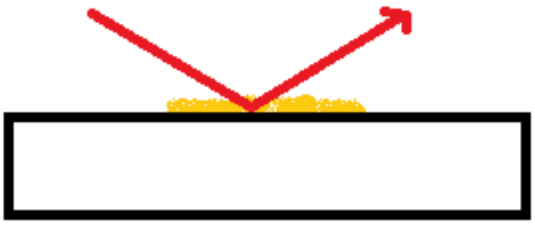

Figure 4-6 Cross section of Bragg-Brentano sample geometry.

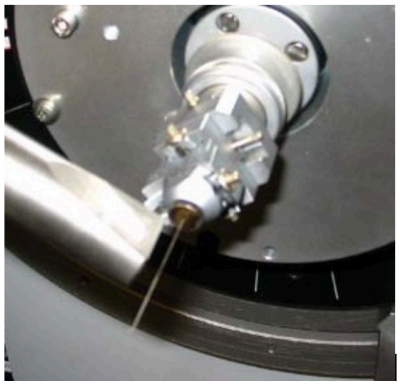

Figure 4-1: Glass capillary mounted for XRD. Goniometer head allows the sample to be rotated in the beam, with the detector to the left of the image.

The typical Bragg-Brentano setup is not ideal for the purpose of preventing exposure to radionuclide powder with the powder free to disperse as a dust when disturbed, resulting in a significant inhalation risk. The capillary setup was deemed to present acceptable health risks due to the robustness of the capillary (whilst glass, at 0.5 mm diameter is flexible), the very small quantity of material that would be present (< 50 Becquerels at few milligrams). Testing with talcum powder showed that it was difficult to disperse more than 20% of the sample mass from a broken capillary.

Concerns, however remained about the use of the capillary stage in its normal form due to potential issues with the maintenance and repair of the diffractometer by external service engineers should it become contaminated with uranium. Both the Bragg-Brentano and the capillary sample mounting methods were adapted for use with radionuclides with the adaptations presenting further difficulties as outlined below. All measurements conducted in our laboratory were made using one of these adapted mounting methods.

Figure 4-7 and Figure 4-8 show the adapted mount used for XRD of uranium powders on the Bragg-Brentano stage. Mounts supplied with the diffractometer for transmission XRD were used as they had a central hole, as well as a clip for holding two Mylar sheets in tension with the sample held between them. The mount was loaded inside a glovebox, and the Mylar around the sample bonded to the other sheet using impact adhesive so that even if the clip failed, the sample would still be contained.

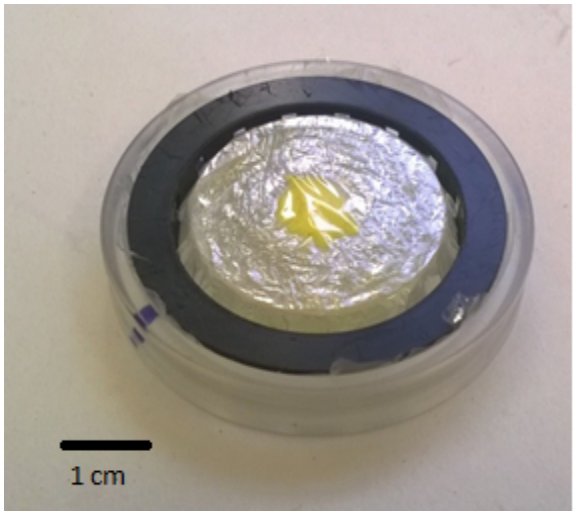

Figure 4-7: Metaschoepite contained in Mylar for XRD.

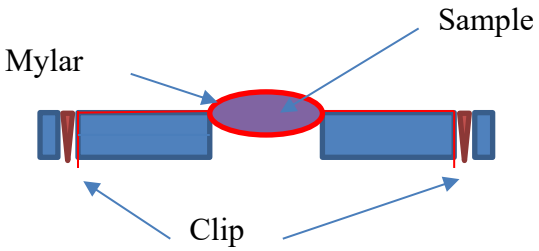

Figure 4-8: Cross section of Mylar Bragg-Brentano XRD mount.

The need to glue the sheets together presented the biggest limitation to this method. The design of the mount for transmission experiments relies on the clip tensioning the Mylar, pulling the sheets together to bring the sample into a thin layer at the correct height. The glue prevents tension being put into the central area in which the sample is held, as can be seen in Figure 4-7. This leads to the height of the sample being different from that intended. This difference is inconsistent between samples, which introduces errors into measurements as illustrated in Figure 4-9. In practice, the height differences between the top and bottom of the sample were too small for this effect to cause any obvious broadening and structural refinement software was able to account for the shift.

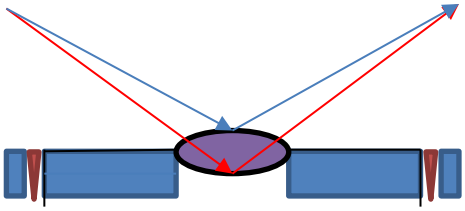

Figure 4-9: Illustration of the differences in measured diffraction angle as a factor of sample height.

More troublesome was the presence of the broad signal from the Mylar sheets from around 23° to 29° (see Figure 4-10). In cases where it was desired to conduct a comprehensive structural refinement, especially of metaschoepite which has numerous peaks in the affected region, this presented a significant difficulty. Where refinements were of samples with fewer peaks in this area, for instance dehydrated schoepite, or where the focus was on quantification of mixed phases, this method presented a viable option. To overcome these difficulties, adaptations were made to allow the use of the capillary stage which are discussed in the next section.

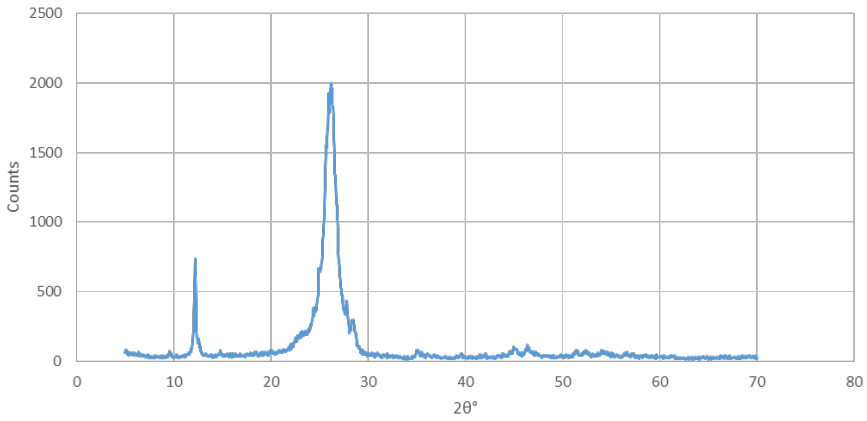

Figure 4-10: Diffraction pattern of synthetic metaschoepite collected using a Mylar mount. The large, broad peak around 27° is due to the Mylar.

The capillary stage was desired to eliminate the broad Mylar peak present in Bragg-Brentano measurements, allowing the inclusion of peaks in the region 20° – 30° in structural refinements.

The sample is held in a glass capillary that is mounted on a goniometer used to align it with the X-ray beam whilst it is rotated around its axis (see Figure 4-12). Capillaries used has an outer diameter of 0.5 mm, which results in small samples being contained but required painstaking amount of capillary rotation to allow the fine grains to settle into the capillaries. This minimised the activity of sample present (~ 50 Bq) and led to a degree of robustness due to the flexibility commensurate with their thin walls. To investigate the safety of possible accidental breakages of capillaries, tests were conducted where capillaries filled with non-radioactive powders were broken over a balance and the mass loss recorded. This indicated that, even with significant agitation of the capillary after its breakage, no more than 20% of the mass contained could be lost from the capillary. The potential doses associated with such a small release were deemed acceptable, allowing the use of capillaries from a radiological safety point of view. This allowed for handling of sealed capillaries outside of a glovebox but in designated work areas where they could be mounted into a bespoke guard to protect them whilst in the diffractometer.

Figure 4-11 Guard made to mount on the goniometer and protect the capillary which was to align with the windows. In use these were sealed with Kapton film.

Figure 4-12 Capillary sample shown mounted on goniometer used to align the capillary with the beam. The lower circular part allows the goniometer to be screwed to the diffractometer.

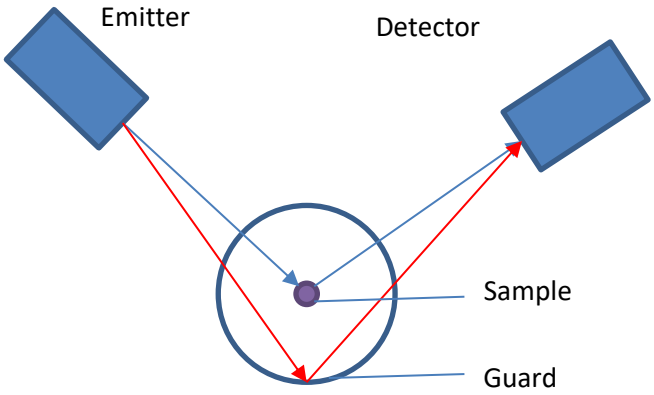

Figure 4-13 Red arrows show beam from the guard entering the detector despite their divergence from the in focus path (blue) occupied by the sample.

The design assumed that as the struts of the guard that passed by the capillary were separated from the capillary by around 1.5 cm they would be out of focus and hence not be detected by the diffractometer. However the detector on the diffractometer used was sensitive to signals from broader angles than is typical, and the collimation of the beam was less than expected meaning that whilst out of focus (Figure 4-13), the supports still produced a signal (Figure 4-14).

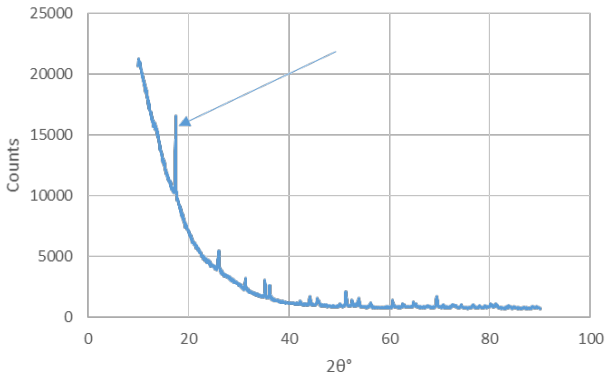

Figure 4-14 Diffraction pattern of corundum with guard in place. The large peak at 17° is due to guard.

To remove the signal from the spectrum, the width separation of the guard from the sample was increased. To minimise the cost of having the guard fabricated, and to allow it to be as easy to handle as possible it was necessary to determine the minimum diameter that would give no signal from the struts.

Tests to establish this diameter were conducted by cutting off the supports leaving only the part that connected to the goniometer. A cardboard "collar" was then attached through which wooden studding was passed and used to support the Kapton. The distance of the wooden struts was from the capillary was increased until no signal was detected above 10°, as the lowest angle peak of any material of interest was at 12°. This corresponded with a radius from the capillaries to the supports of 5 cm.

Using these measurements, a new guard was designed (Figure 4-15). The design incorporated holes to allow the plastic struts to be replaced with wood should a signal arise due to the use of plastic instead of wood. This did not occur, with no signals being detected from the guard above 8°.

This device allowed the use of capillary stage XRD. This was used relatively infrequently due to the difficulty of filling capillaries in a glovebox; however it was vital to confirm that the expected peaks were present in the region inaccessible to Bragg-Brentano stage XRD. This chapter concludes with images of the final guard. (See Figure 4-15 and 4-16). The improved diffraction patterns are shown in Figure 4-18.

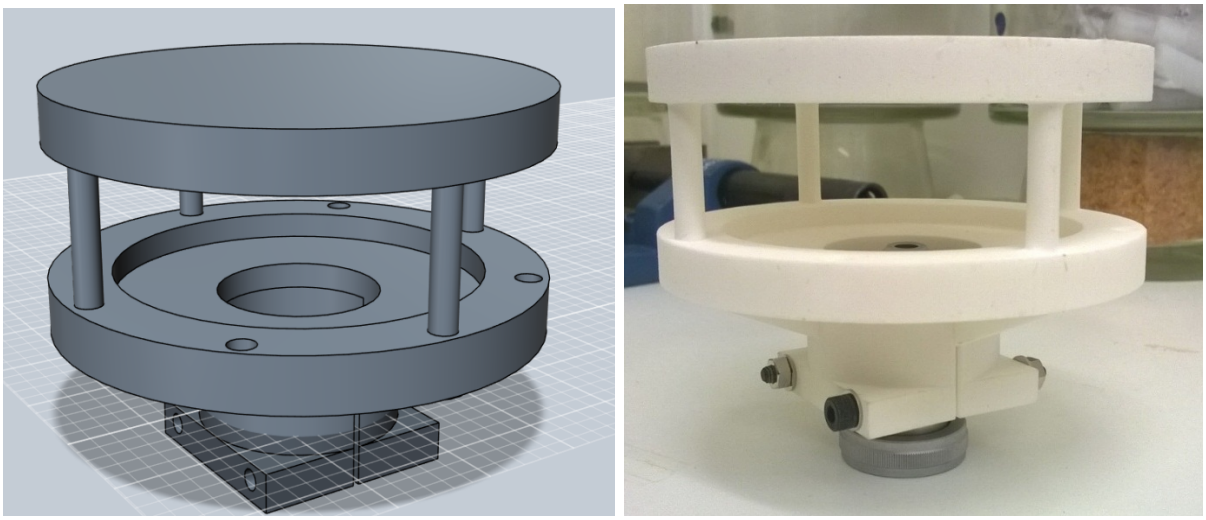

Figure 4-15: Final guard: Design image, left, and mounted to the goniometer, right.

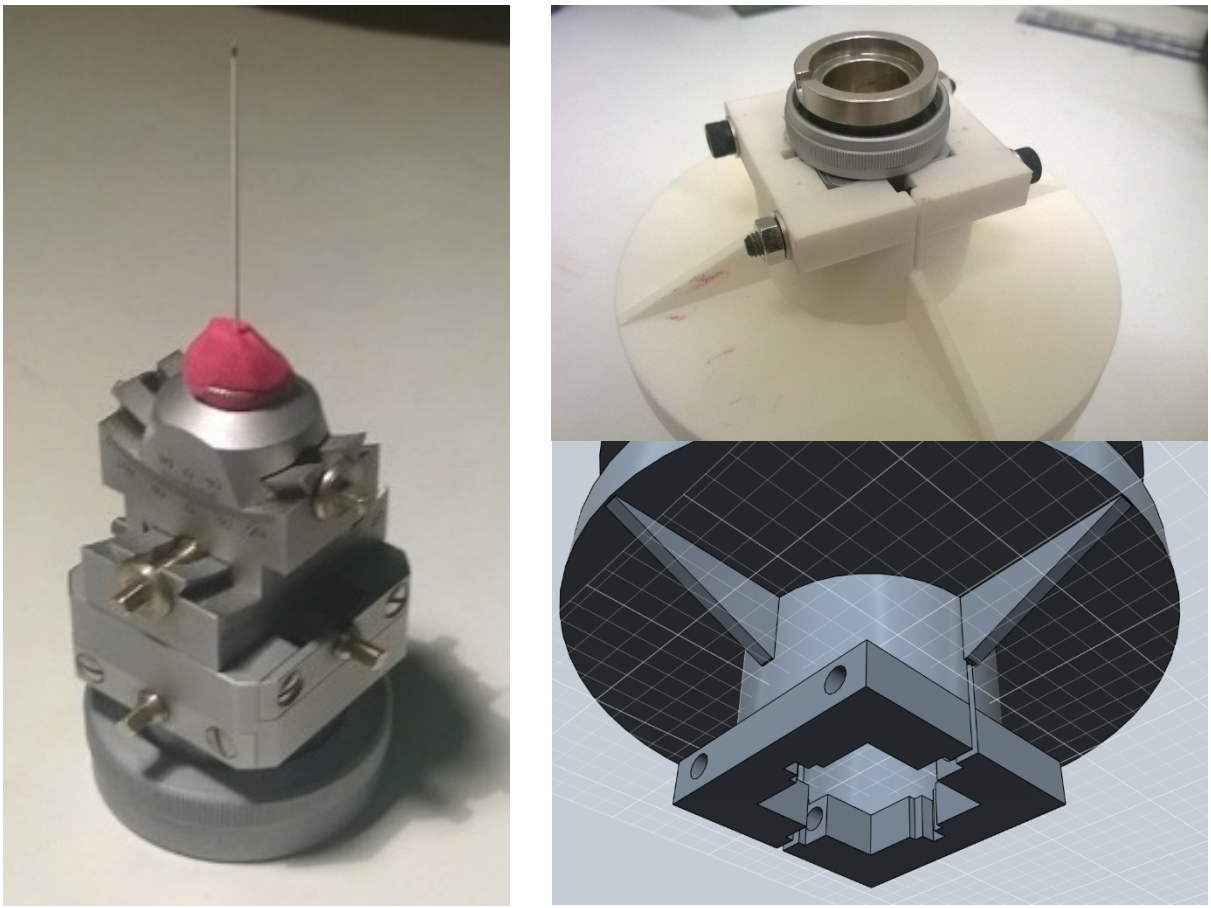

Figure 4-16 Top right shows detail of the design that allows the goniometer, left, to tightly interlock with the guard, bottom right. This minimises the possibility of spillage, however procedures require this entrance never to be below a mounted capillary.

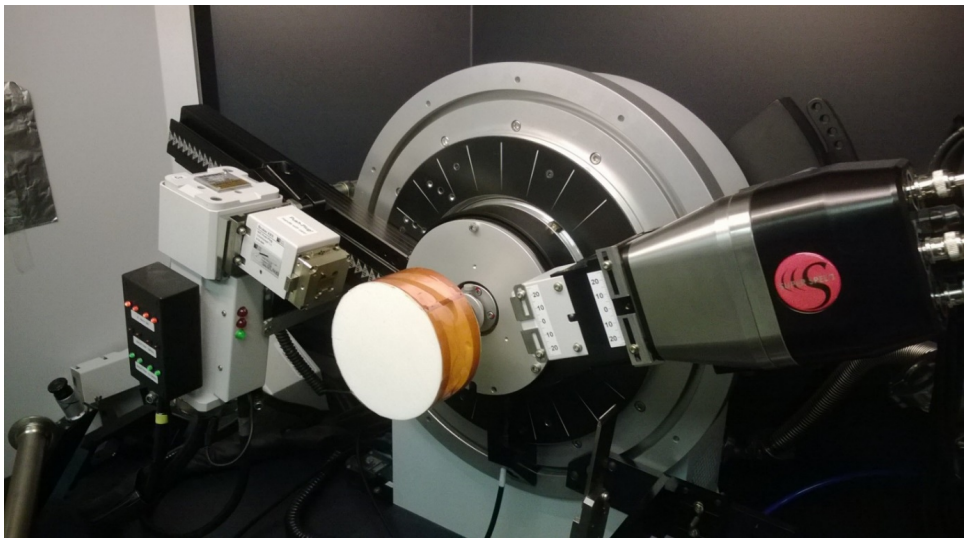

Figure 4-17: Guard mounted in diffractometer with Kapton tape in place for secondary containment of radioactive capillary mounted samples.

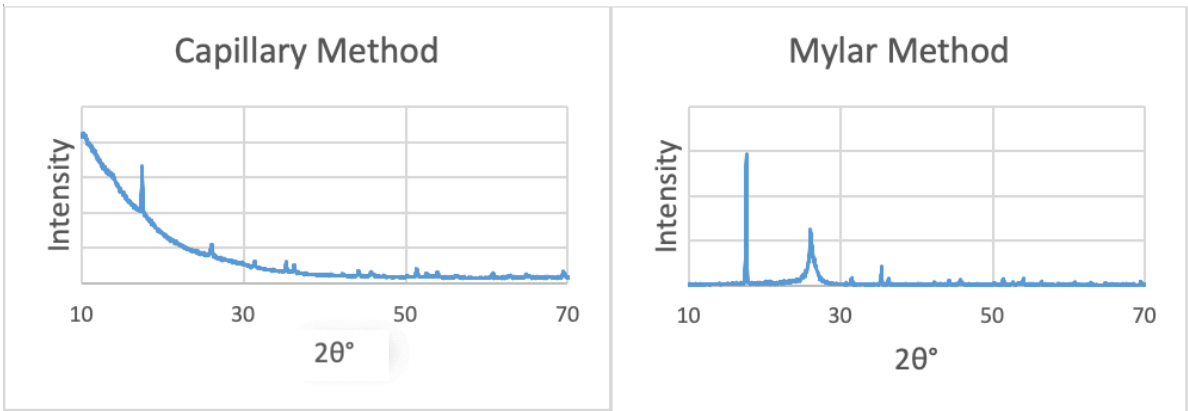

Figure 4-18: Improved diffraction patterns of dehydrated schoepite collected using the capillary method, and on the Bragg-Brentano stage whilst encapsulated in Mylar.

4.1.5 Technical specifications

XRD of thin films were conducted with a Bruker D8 Advance diffractometer in reflection geometry (Cu Kα radiation, λ = 1.541 Å , Ge monochromator and Sol- XE energy dispersive detector) for a total of 12 hours over an angular range $20° \leq 2\theta \leq 130°$ ($\Delta 2\theta = 0.01°$).

XRD data of powder samples were collected in capillary on a Bruker D8 Advance diffractometer (Cu Kα radiation, λ = 1.541 Å, parallel primary beam, Vantec position sensitive detector) for a total of 16 hours each over an angular range $20° \leq 2\theta \leq 90°$ ($\Delta 2\theta = 0.02°$). A full Rietveld refinement was carried out of the acquired capillary diffraction patterns.

4.2 Inductively Coupled Plasma Mass Spectroscopy (ICP-MS) and Inductively Coupled Plasma Optical Emission Spectroscopy (ICP-OES)

Inductively coupled plasma mass spectroscopy (ICP-MS) is an elemental analytical technique that is able to detect most of the periodic table of elements at parts per billions (ppb) to parts per trillion (ppt) accuracy. It was used extensively in this work to characterise aliquots obtained from the dissolution experiments, particularly to determine dissolved uranium concentration and deduce how various conditions affect the leaching of uranium into the solution.

4.2.1 Function of ICP-MS

To determine dissolved uranium dioxide concentration, the leachate was pipetted into centrifuge tubes and acidified with HNO_3. This serves to reduce reprecipitation of dissolved uranium and in some experiments reduce the concentration of ions to reduce the matrix levels, as excessive concentrations may result in deposition on the interface cone orifices, leading to signal loss and instability.

For our set up, the aqueous samples are introduced by an adjustable peristaltic pump. A nebuliser generates an aerosol in a spray chamber that allows fine aerosol droplets to pass to a high-power argon plasma which rapidly desolvates, atomises, and ionises the sample creating a beam of singly charged positive ions.

These ions are rapidly accelerated into the vacuum of a mass spectrometer via a triple cone system involving sampler, skimmer, and hyper skimmer cones. Ion focusing is achieved by a Quadrupole Ion Deflector, followed by mass filtering in a quadrupole. The ions are sequentially detected in a single channel electron multiplier. The ion beam pathway is shown below in Figure 4-19.

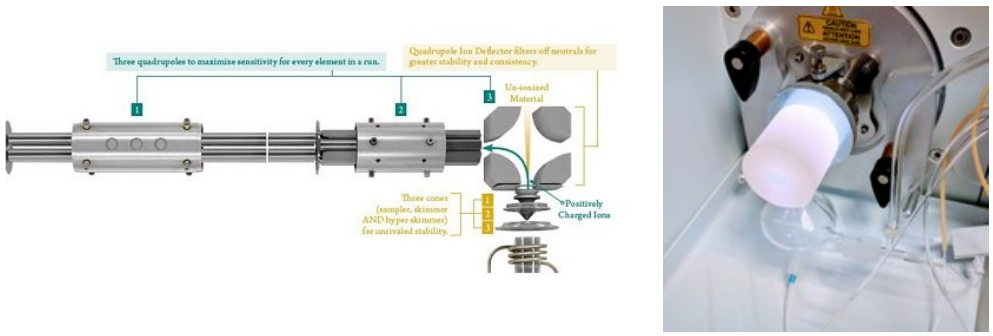

Figure 4-19 The left figure shows the schematic of the flow of ions and the right figure shows the argon plasma generated to ionise the aqueous sample.

4.2.2 Technical specifications and standards

For our samples, the acquired 1 ml aliquots were acidified with another 1 ml of 1 wt% HNO_3 and all samples were analysed on a Perkin Elmer Nexion 350D ICP-MS instrument. The uranium calibration standards were prepared as an external calibration using serial dilutions of standards (blank, 0.001, 0.01, 0.10, 1.0, 10 ppb, mass basis) prepared from single element high purity standard (CPI, California, USA) in high purity 1 wt % HNO_3 (quartz distilled in house). The ICP-MS internal standards were 10 ppb Rh, In and Re and each sample was prepared in 1 wt % HNO_3, added online with a t-piece and mixing tube prior to the nebuliser. Two different independently prepared quality control standards (SPS-SW2, LGC Standards, UK and SCP Science, Canada, ICP-MS Verification Mix) were repeatedly analysed throughout the run to check for calibration accuracy (~5%) with a similar precision. Instrumental drift was less than 10% measured for the raw intensity of the internal standards during the entire analytical run (50 or more solutions per batch). Solutions were analysed using a Micromist FM05 microconcentric nebuliser using a pumped flow rate of 80 µl/min (Glass Expansion, Australia) and a quartz cyclonic baffled spray chamber with nickel sampler and skimmer cones. ICP-MS sensitivity in this configuration was 4.5×10^5 cps/ppb In with CeO/Ce ratios = 2.8%. Concentration results were calculated using the Syngistix 1.1 software with a simple linear calibration line and intercept set to zero. The raw intensities were blank subtracted and internal standard normalised before calibration calculations were performed. All results (unknowns and standards) were accurately corrected for dilutions by mass by performing all dilutions with calibrated pipettes on a four-place analytical balance.

4.2.3 Function of ICP-OES

Compared to atomic absorption spectroscopy, ICP-MS has greater speed, precision, and sensitivity. However, ICP-MS introduces many interfering species: argon from the plasma, component gases of air that leak through the cone orifices, and contamination from glassware and the cones. In order to observe the low concentration of silicon in one set of dissolution experiment, it was not possible to observe this through ICPMS and inductively coupled plasma optical emission spectrometry (ICP-OES) was used to determine silicon concentration.

In ICP-OES, identification is based on the electronic energy levels of the ions, rather than their mass and charge ratio. At the high temperature plasma, atomization and ionizations of the sample takes place. The electrons are thermally excited and releases photons corresponding to

their discrete energy gaps upon deexcitation. Each element has an own characteristic emission spectrum that is measured with a spectrometer. The light intensity on the wavelength is measured and with the calibration calculated into a concentration.

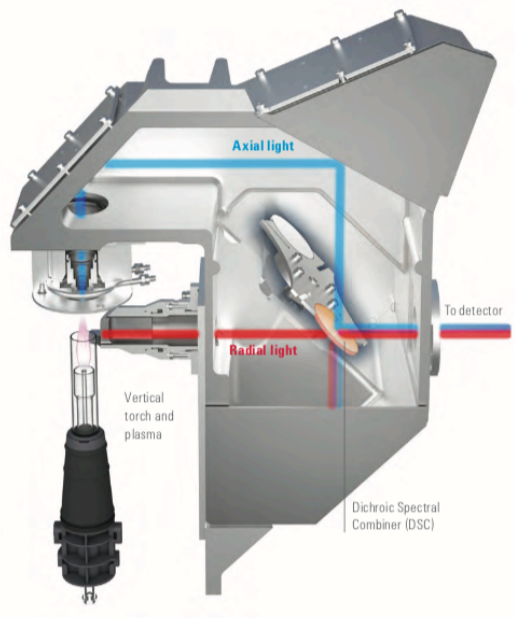

Figure 4-20 The Agilent 5100 Synchronous Vertical Dual View enable axial and radial view analysis at the same time with its dichroic spectral combiner.

For the leachate from the uranium dioxide thin film experiment, the acquired 1 ml aliquots were acidified with another 1 ml of 1 wt% HNO_3 and all samples were analysed on an Agilent 5100 ICP-OES instrument, capable of determining the concentration of silicon ions to ppb accuracy. Inductively coupled plasma atomic emission spectroscopy (ICP-AES) of this leachate found the concentration of dissolved silicon in that experiment to be in the range of 15–25 ppb. Dynamic light scattering was employed to confirm the absence of colloids greater than 5 nm.

4.3 Scanning Electron Microscopy (SEM), Electron Backscattered Diffraction (EBSD) and Elemental Dispersal X- ray Spectroscopy / EDS

Figure 4-21 Thermo Scientific Quanta-650F at University of Cambridge Earth Science department was instrumental for imaging of my uranium dioxide thin film samples.

Close proximity to scanning electron microscopy made it an essential tool among the limited equipment that can be used for radioactive work. The essential vacuum however meant that it cannot be used for powder samples, which formed the bulk of this work. It is however very useful for thin film of uranium oxides coated on silicon substrate. With its range of installed techniques, a thorough investigation of our thin film sample was conducted.

4.3.1 Function of FEG SEM/ EDX

This Field Emission Gun Scanning Electron Microscope (FEG SEM) is a fully equipped instrument that can be run at high vacuum, low vacuum or environmental mode. This allows for imaging/chemically analysing samples with or without a conductive coat. At higher vacuum, imaging at higher magnifications is possible due to the reduction of scattering of incoming electrons by air molecules. The data was collected from the secondary electrons (SE), back-scattered electrons (BSE), and X- rays. These enable us to analyse the chemical composition

and phases with energy dispersive x-ray spectroscopy (EDS) and electron back-scattered diffraction (EBSD) respectively.

The scanning electron microscope (SEM) produces images by scanning the sample with a high-energy beam of electrons. As the electrons interact with the sample, they produce secondary electrons, backscattered electrons, and characteristic X-rays. These signals are collected by detectors to form images. This field emission sources uses a fine, sharp single crystal tungsten tip instead of a filament to produce a more coherent electron beam with larger intensity, which is subsequently accelerated by the anode and focused by the magnetic lenses and interacts with the sample as seen in Figure 4-22.

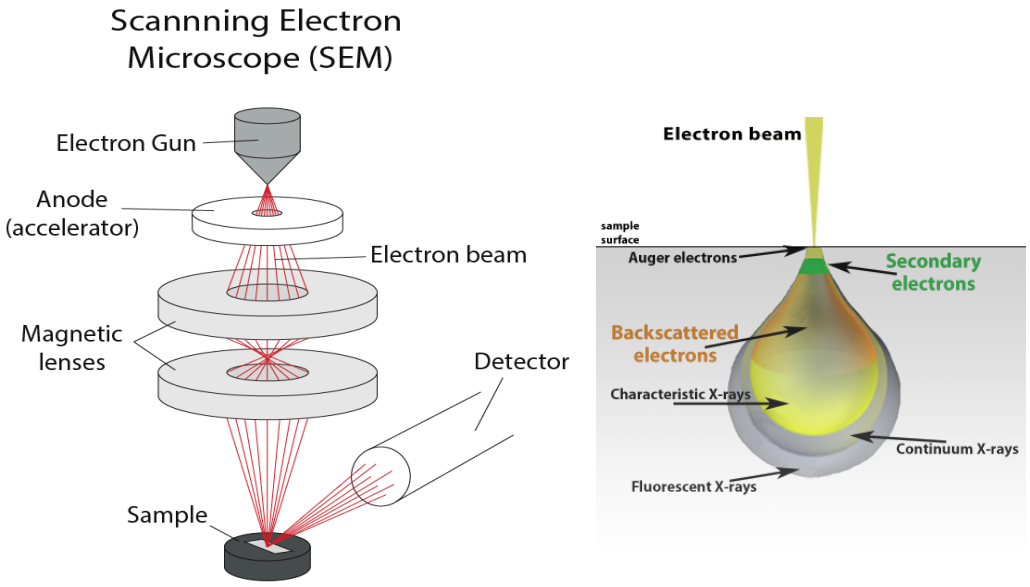

Figure 4-22 Schematics of a Scanning Electron Microscope and the type of electrons and photons produced at the sample.

Upon interaction of the incident electron beam, **secondary electrons** are ejected from the k-shell in the sample by **inelastic** scattering interactions with the incident beam electrons. These low energy electrons (< 50 eV) originate from within a few nanometres from the sample surface, thus providing an excellent, high resolution, depth of field image. They are typically used for imaging structures and topography of samples due to their origins. In the cases when the angle of incidence between the incoming electron and the sample atoms is near 90^0 (a head- on collision) , "rebounding" or backscattering occurs. **Backscattered electrons** vary directly as a function of sample's composition by virtue of the atomic number (Z) through **elastic**

interactions in the specimen and possess higher energy than secondary electrons, however, they are not as surface sensitive as secondary electrons. Nonetheless, they provide an invaluable imaging tool to rapidly discriminate phases that have different mean atomic (Z) values. Figure 4-23 serves to illustrate the different roles of these two techniques in this work and how they complement each other. From (a), a 200-nm wide strip and a 1-μm droplet were observed on the left and right. As secondary electrons are surface sensitive, it is clear that the higher intensity, relating to a higher number of secondary electrons, implies that these two features are situated above the relatively flat surface. From (b), the back-scattered electrons support that the surface is relatively flat and gave additional information of the relative compositional uniformity of the strip and drop. Since the silicon ($^{28}_{14}Si$) substrate led to more backscattered electrons, this implies that the features have a lower Z number and fit in with our conclusions that they must be carbon contaminants from the carbon tape when attaching the sample to the SEM apparatus.

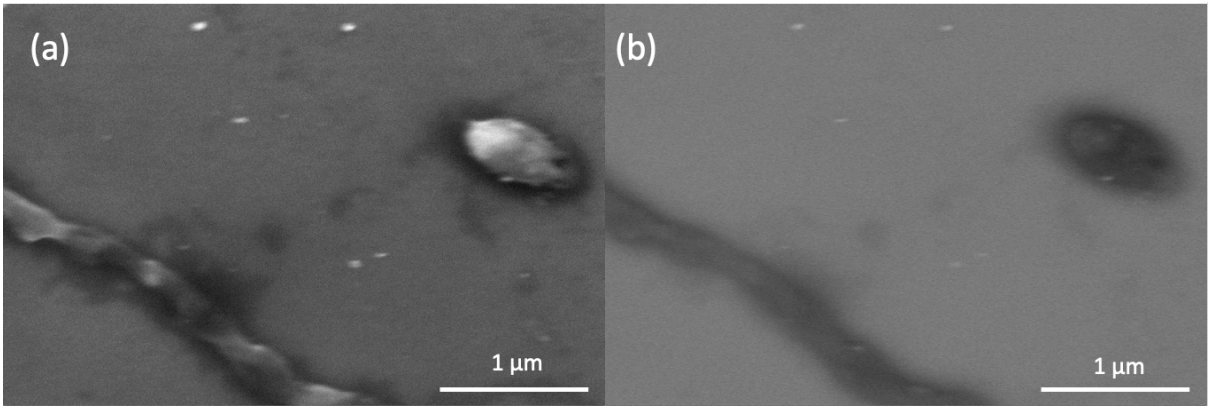

Figure 4-23 100,000× magnification secondary electron and (b) backscattered electron micrographs of carbon contaminants on a silicon substrate.

Apart from electrons emission, the interaction of the high- speed incoming electrons with the sample can happen in the form of knocking out electrons from inner shells of the sample atoms. When this happens, electrons from outer shell will move to the more stable shells, emitting electromagnetic radiation with energy corresponding to the energy difference between the unique electronic energy levels of the atoms. Based on this principle of using characteristic X-rays, Energy-dispersive X-ray spectroscopy (EDX) can be used for elemental analysis or chemical characterisation of a given sample, unfortunately, this technique is not that useful for our thin film samples, which is only ~ 100 nm thick and the penetrative depth of EDS is ~1-2 micrometres. It was used for our solid pellet samples and discussed lightly in 5.3 Solid Pellet-Raman spectra where the small degree of oxidation resulted in a small difference.

4.3.2 Function of EBSD

The SEM was also equipped with electron back scattered diffraction capability; which is a microstructural-crystallographic characterization technique commonly used in the study of crystalline materials such as our single crystal UO_2 thin film. Accelerated electrons in the incoming beam can be diffracted by atomic layers in crystalline materials. These diffracted electrons can be detected as Kikuchi bands (electron backscattered patterns (EBSPs). These patterns are effectively projections of the geometry of the lattice planes in the crystal, and they give direct information about the crystalline structure and crystallographic orientation of the grain from which they originate (See Figure 4-24). When used in conjunction with a data base that includes crystallographic structure information for phases of interest and with software for processing the EBSPs and indexing the lines, the data can be used to identify phases, to index the pattern, and to determine the orientation of the crystal from which the pattern was generated. Individual mineral grains can be selected for identification and determination of crystal orientation. Mapping may also be conducted where data is acquired over a selected area of the surface of the sample to determine the identity, orientations, and spatial relations between a large number of grains.

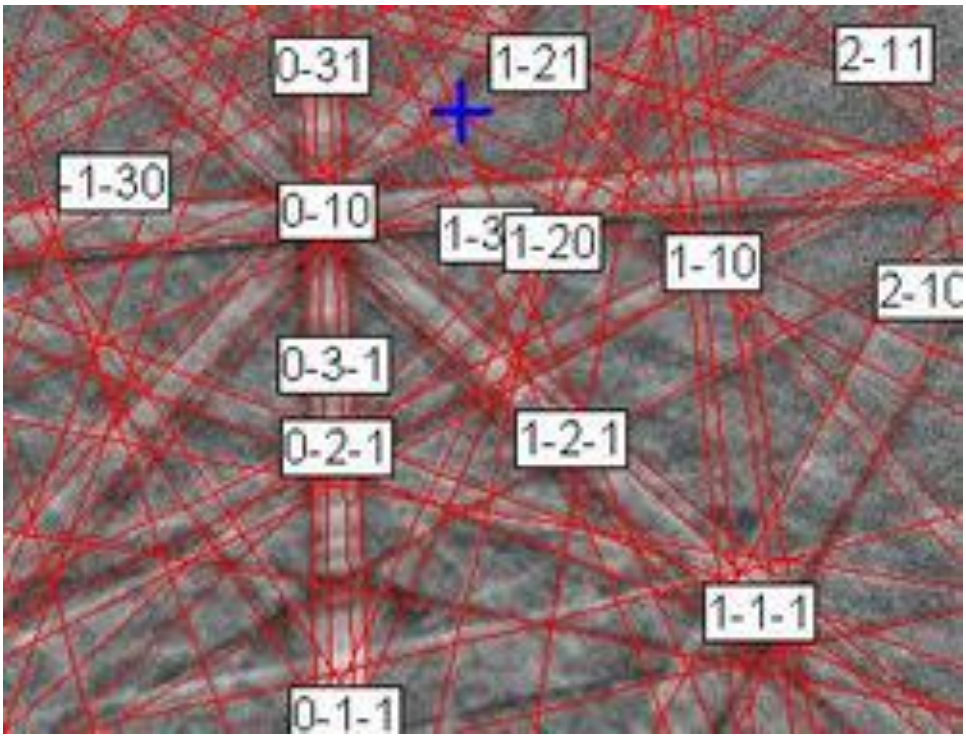

Figure 4-24 Typical electron backscattered patterns (EBSPs)

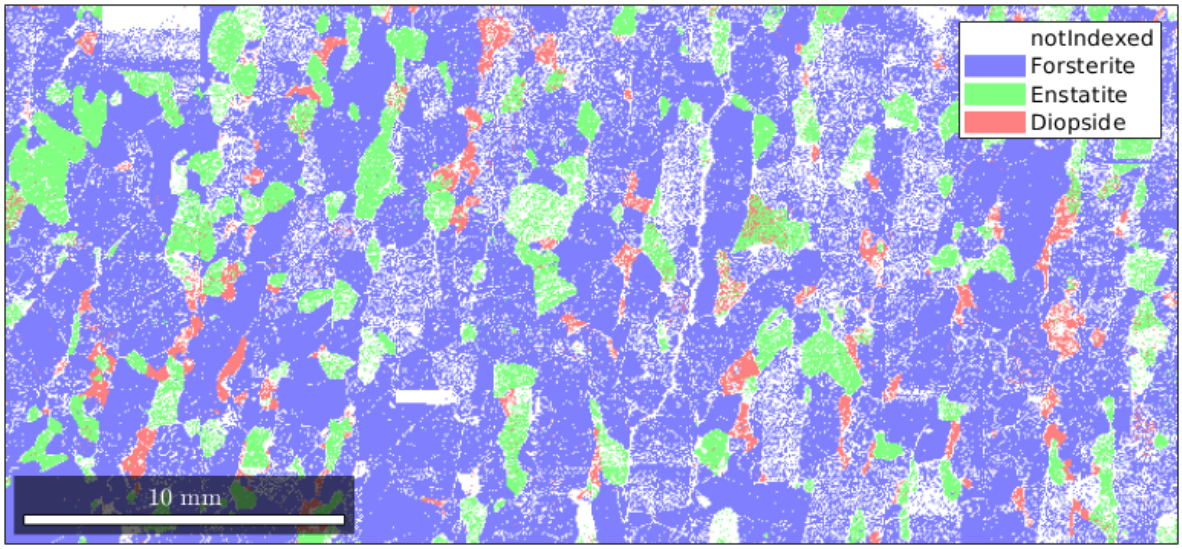

Figure 4-25 Thresholded EBSD map showing the misorientation angle of every pixel with respect to the average orientation.

With the use of Matlab program and MTEX toolbox (Bachmann, Hielscher and Schaeben, 2010; The MathWorks, 2016), it was possible to generate graphical displays of the distribution of even individual pixels (see Figure 4-25) and pole figures for displaying statistical distributions of orientations of individual pixels. It is a novel technique used in geological studies of rocks, which was extended in this thesis for thin film analysis where the smaller changes in misorientation are more subtle at smaller and need greater scrutiny.

MTEX is a MatLab- based method for the estimation of an orientation density function from either diffraction pole figure intensities or from EBSD phase data. An orientation density function is approximated by a non-negative linear combination of non-negative kernels, which are sufficiently well localized in spatial and frequency domain, more specifically with functions which are unimodal radially symmetric in spatial domain and with Fourier coefficients which vanish smoothly and sufficiently fast.

For the resolution of the inverse problem to determine an orientation density function from given experimental pole figure data this approach is justified by the general solution of the Darboux differential equation (Nikolayev and Schaeben, 1999) governing the pole density function corresponding to an orientation density function. The pole density function has been recognized as mean of the totally geodesic Radon transform of the orientation density function (Bernstein, Hielscher and Schaeben, 2009), experimental pole figure data may be seen as its discrete values. Since the Radon transform is a linear integral transformation, it is applied to each term in the linear combination individually. Thus, experimental pole figure data are fitted

by a non- negative linear combination of means of totally geodesic Radon transforms of the kernels.

The best fit is determined as a solution of a constrained non-linear minimization problem and numerically found by a version of the conjugate gradient method. The algorithm which MTEX is based on applies discretisation with radially symmetric basis functions centered at a given grid which may be irregular. The kernel itself is approximated by a finite Fourier series expansion.

MTEX offers functions to compute a wide range of texture characteristics like the modal orientation, mean orientation, entropy, texture index, Fourier coefficients, and volume portion in the neighbourhood of a given orientation for any mathematical model orientation density function or any computed orientation density function. Furthermore, arbitrary orientation density functions can quantitatively be compared independently of being model orientation density functions, orientation density functions estimated from pole figure data or estimated from EBSD data.

4.3.3 Technical specifications

The solid pellet samples were analysed before and after the dissolution experiment by SEM with EDX. SEM-EDX was carried out at 20 kV using a JSM-6010PLUS (Jeol, Japan).

The thin film sample was analysed before and after the dissolution experiment by SEM, EDX, X-ray diffraction (XRD) and electron backscatter diffraction (EBSD) techniques with a FEI Quanta 650F instrument operating at 5 kV with beam spot size 3 under high vacuum was used to acquire SEM images with a Bruker 6130 XFlash EDX detector. EBSD instrumentation from Bruker with an e-Flash$_{HD}$ detector associated with the FEI Quanta 650F SEM was used to obtain EBSD data; the resolution of each square pixel of 97 nm. The operating voltage was 20 kV and the beam spot size 5.5. The detector resolution was 320 × 240 pixels, while working distance and sample to detector distance was 26 mm and 15.5 mm respectively. Data collection and indexing was performed with Bruker QUANTAX CrystalAlign software(Bruker Nano GmbH, Berlin, 2010).

4.4 Raman Spectroscopy

Raman spectroscopy is based on inelastic scattering of monochromatic laser light upon impinging a sample. Inelastic scattering results in a change in energy and frequency of the scattered light as opposed to the main scattering interaction of elastic Rayleigh scattering. By filtering out the original frequencies with a notch filter (with a cut-off spectral range of 80-120 cm^{-1} from the laser line), the Raman signals, above the cut-off range, will be detected. The filter is essential as these inelastically-scattered photons only corresponds for ~ 0.001% of the total scattering, however this small percentage provides invaluable information on the vibrational, rotational and other low frequency transitions in our samples(Princeton Instruments, 2012).

4.4.1 Physics of Raman spectroscopy

Raman effect stems from molecular deformations when the atom is subjected to an electric field, E with the extent of deformation being determined by its molecular polarizability α. The laser beam can be considered as an oscillating electromagnetic wave with electric field component, E. Upon interaction with a sample, it induces an electric dipole moment

$$\boldsymbol{P = \alpha E}$$

Equation 4—8

which deforms molecules. The oscillating field results in periodic deformation, molecules start vibrating with their characteristic frequency υ_m.

When a laser light of frequency impinges on a molecule, three scenarios can occur.

1. A Raman-inactive molecule absorbs a photon with the frequency υ_0. The excited molecule returns back to the same basic vibrational state and emits light with the same frequency υ_0 as an excitation source. This type of interaction is called an elastic Rayleigh scattering.

2. A photon with frequency υ_0 is absorbed by Raman-active molecule which at the time of interaction is in the basic vibrational state. Part of the photon's energy is transferred to the Raman-active mode with frequency υ_m and the resulting frequency of scattered light is reduced to $\upsilon_0 - \upsilon_m$. This **reduced** Raman frequency is the **Stokes** frequency. (See Figure 4-26)

3. A photon with frequency υ_0 is absorbed by a Raman-active molecule, which, at the time of interaction, is already in the excited vibrational state. Excessive energy of excited Raman active mode is released, molecule returns to the basic vibrational state and the resulting frequency of scattered light goes up to $\upsilon_0 + \upsilon_m$. This Raman frequency is the Anti- Stokes frequency.

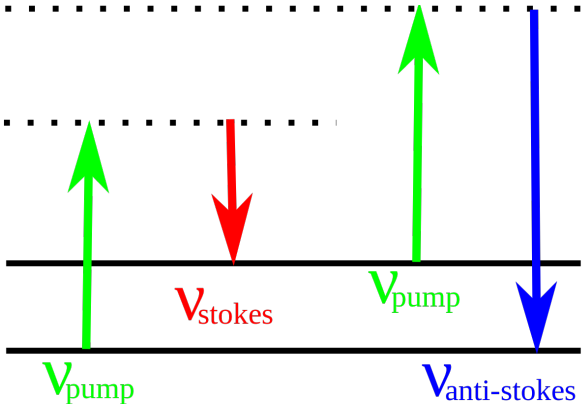

Figure 4-26 Formation of Stokes and anti-Stokes signal with a Raman active molecule where the green line represent the energy absorbed from the incoming laser photon.

4.4.2 Instrumentation

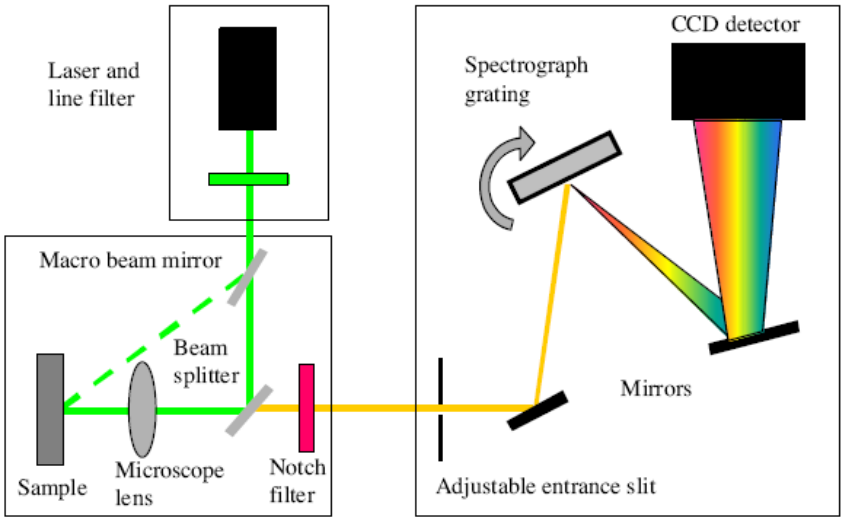

Figure 4-27 The workings of a typical Raman spectrometer.

A Raman spectrometer consists of a laser source to excite the target species with a filter to collect the Raman scattered Stokes signal and filter out the Rayleigh and Anti Stokes signals, which is then split up with a diffraction grating and the data is collected by a charge-coupled detector which has a large number of light sensitive pixels, which can be used to consider the Raman shift in cm^{-1}.

Raman, being a non-destructive technique and the high polarizability of the uranyl bond, was used extensively in this experiment to identify synthesized uranium secondary phases of becquerelite, andersonite and grimselite. It was also employed to detect the extent of oxidation in anoxic dissolution of uranium pellet in 5.3 Solid Pellet- Raman spectra.

4.4.3 Technical specifications

Raman microscopy measurements were taken using a Voyage confocal Raman microscope system (B&WTek, Newark, USA). All Raman spectra were acquired with an excitation wavelength of 785 nm. The sample was focussed using a 50× objective lens before taking spectra with an integration time of 40 seconds over a wavenumber range from 190 to 3000 cm^{-1}. Before analysis, the laser power was adjusted to < 5 mW using neutral density filters in order to avoid any thermal oxidation of UO_2 to U_3O_8 (Elorrieta *et al.*, 2018). In order to account for surface roughness and surface inhomogeneity, 10 spectra were taken at random locations across the sample with the highest and lowest outliers removed to produce a sample average.

4.5 Emission Spectroscopy

Emission spectroscopy was used in tandem with Raman spectroscopy to verify enriched synthesized minerals have identical spectra as synthesized minerals to demonstrate successful enrichment in 2.3 Selected Minerals for Synthesis and Enrichment.

It works by the excitation of the sample by an external laser source. The typical wavelength ranges covered in the experiment are 350- 700 nm for hydrogen and 300- 900 nm for oxygen spectrum. Light from the external light source is guide through an optical fiber onto the monochromator of spectrophotometer placed in the single-beam mode. Depending on the chemical composition of the sample, different wavelengths of light will be emitted after excitation by the external light source subjected to quantum mechanical principles and the relation between the electronic structure and spectral observations. (Minas da Piedade, Manuel E. and Berberan-Santosm, Mario N., 1998)

4.6 Electrochemistry with PHREEQC

The dissolution of uranium involves exchange of electrons between uranium oxide and the solution to form soluble ions, hence reduction potential is an important variable. This has been investigated at lengths with cyclic voltammetry experiment and X-ray photoelectron spectroscopy (XPS) by Shoesmith *et al.* (Shoesmith, 2000; He, Qin and Shoesmith, 2010; He *et al.*, 2012) as shown in Figure 4-28. Due to limitations of equipment access to XPS studies under anoxic conditions, hence a study of the surface potential is used to estimate the surface oxidation state.

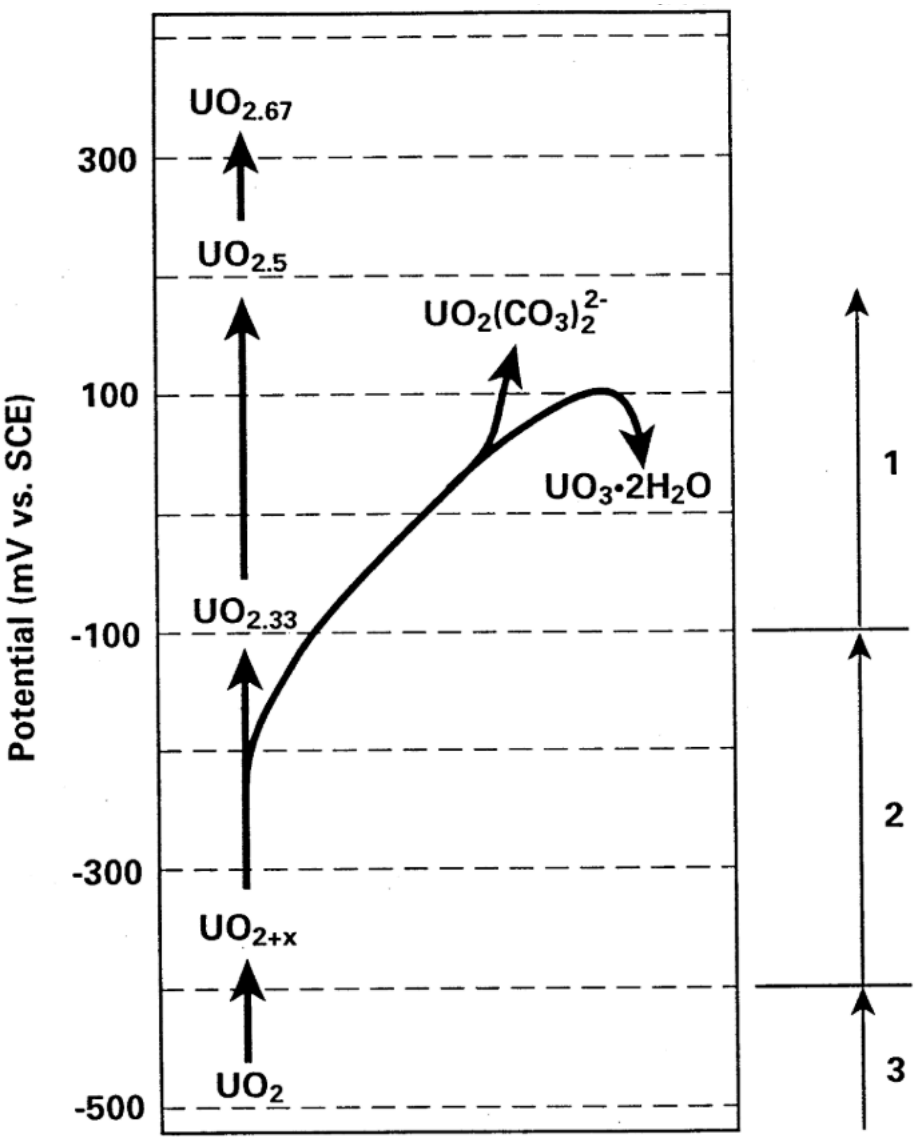

Figure 4-28 Electrochemistry of UO_2 oxidation and dissolution as a function of electrochemically applied potential.

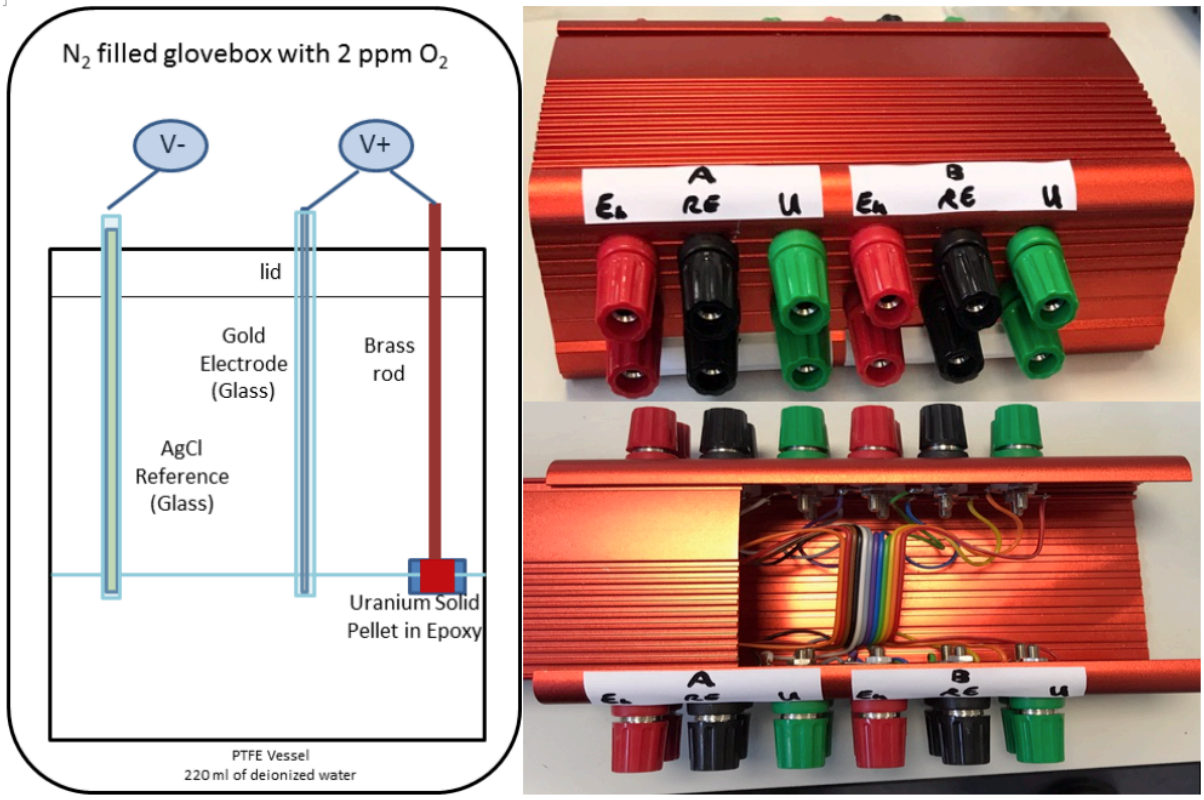

Figure 4-29 Self-created device for dexterity in potential measurements when working in a glovebox.

PHREEQC is an aqueous geochemical modelling program that allows for speciation calculations and equilibration of systems with phase assemblages using an iterative approach to determining the equilibrium state of a system by minimising its free energy. Additionally it has features such as one-dimensional transport, kinetic and surface complexation calculations which were not used as part of this project (Parkhurst and Appelo (2013)).

PHREEQC is frequently used to provide an estimate of the equilibrium uranium concentration of a solution in the context of dissolution experiments to give confidence that equilibrium has been approached (e.g. Guilbert et al. (2000), Riba et al. (2005)), and for comparison with simple thermodynamic models (e.g. Trocellier et al. (1998)).

In this project PHREEQC has been used for simulating our actual experiment of anoxic uranium dioxide dissolution where the detected reducing potential, Eh of solution and dissolved oxygen concentration after three months of dissolution experiments was used to calculate the concentration of dissolved uranium dioxide. This provide a close fit with our experiment in the next chapter.

Chapter 5 Dissolution Results and Discussions

5.1 Rationale for anoxic dissolution experiments

The relative abundance of uranium as an energy resource, coupled with the high costs of spent nuclear fuel reprocessing and the associated risks of nuclear proliferation, make a strong case for direct disposal of SNF in deep underground geological disposal facilities (GDF)(Cui *et al.*, 2008). An important consideration in implementation of GDF is the projected radionuclide release rates from the spent fuel in the case of groundwater intrusion and secondary containment failure(He *et al.*, 2012). Extensive work had been devoted to the analysis of the different aspects of spent nuclear fuel dissolution under geological disposal conditions. Depending on burn-up and local position in the rod (the linear power rating), spent fuel is comprised of ~96 at% uranium dioxide (UO_2) matrix with ~3 at% of fission products and ~1 at% of transuranium elements. As such, previous studies have shown that the release of radionuclides (apart from instant release fractions (Lemmens *et al.*, 2017) of several percent of total inventory for some radionuclides), is mainly dependent on dissolution of the UO_2 matrix under the oxygen-free environment of deep geological facilities (Shoesmith, 2000)

However, there has been no consensus on the proposed mechanisms of anoxic UO_2 dissolution in the literature. Ulrich et al. (Ulrich *et al.*, 2009) initially suggested that anoxic dissolution of UO_2 proceeds via Equation 5—1:

$$\boldsymbol{UO_2(s) + 4H^+ \rightleftharpoons U^{4+} + 2H_2O}$$

Equation 5—1

Based on an XPS analysis of leached UO_2 samples consisting of bulk and surface U(IV), Ulrich *et al*. noted surface oxidation to 7–10% U(VI) and ~20% U(V) under reducing dissolution conditions (5 vol% H_2, 95 vol% N_2 atmosphere) which was explained by a sequential oxidation mechanism of U(IV) to U(V) to U(VI) by water molecules, similar to that proposed by He *et al*. (He *et al.*, 2012) for UO_2 dissolution below the oxidative threshold potential (–400 mV versus saturated calomel electrode on the UO_2 surface).

$$\boldsymbol{UO_2 + H_2O \rightarrow (U^VO_2OH)_{ads} + H^+ + e^-_{(aq)}}$$

Equation 5—2

$$(U^{V}O_2OH)_{ads} + H_2O \rightarrow (U^{VI}O_2(OH)_2)_{ads} + H^+ + e^-_{(aq)}$$

Equation 5—3

A caveat to the applicability of these equations is the absence of detectable U(VI) in the sample solutions with a kinetic phosphorescence analyzer (KPA), although U(VI) is a few orders of magnitude more soluble than U(IV) (Altmaier *et al.*, 2017). Ulrich *et al*. concluded that the anoxic UO_2 dissolution was primarily driven by hydrolysis of U(IV) and not by oxidation to U(VI) (Ulrich *et al.*, 2009). However, it is possible that, although the sample transfer to the XPS instrument occurred with minimal exposure to oxygen in this work, a short exposure was enough to induce surface oxidation, which led to the observed U(V) and U(VI) at the surface. In addition, Ollila *et al*. (Ollila, Olin and Lipponen, 1996) reported that after anoxic (N_2 atmosphere) dissolution of UO_2 in deionized water, the uranium oxidation state in the solution was U^{6+} as determined by anion exchange methods in an HCl medium within an inert atmosphere glove box (N_2). However, there was no information on the characterization of UO_2 samples in contact with the solution. In view of the above literature, it is important to investigate the anoxic dissolution mechanism of uranium dioxide with respect to the anoxic conditions pertaining in a GDF.

Considering the long timeline for SNF storage and disposal, this study focuses on the long-term surface changes and products due to dissolution of spent nuclear fuel. Three anoxic experiments with near stoichiometric uranium dioxide were conducted with different aims.

1) The dissolution of uranium dioxide in solid pellet electrode form to determine electrochemical variation of both solution and surface and subsequent analysis of surface oxidation with Raman spectroscopy, Scanning Electron Microscopy (SEM) and Energy Dispersive X-ray (EDX) analysis techniques.

2) The dissolution of a single crystal uranium dioxide thin film (~100 nm thickness) deposited epitaxially on a (001) silicon substrate, to ascertain uranium dissolution and potential secondary phase precipitation (Popel *et al.*, 2017, 2018) on a topographically flat surface with high surface sensitivity.

3) High-surface area UO_2 powder in steel heating vessels with PTFE (polytetrafluoroethylene) liners to analyse differences in dissolved uranium concentrations at different temperatures, simulating decay heat at different disposal ages.

A summary of the experiment's preparation and conditions is listed in the table below for easy reference.

Table 5-1 Summary of UO_2 dissolution experiments conducted in this thesis.

Forms	Annealing	Polishing	Prewashing	Oxygen content	Leaching test conditions
Pellet	No	Yes (SiC paper + deionized water)	Yes (21 hours) – 10mL	2 ppm glovebox <2.5 ppb dissolved O_2	100 days 220 mL deionized water
Thin film	Yes (5% H_2 in Ar at 800^0C for 2 hours)	No.	Yes (12 hours) – 20mL	0.1 ppm <2.5ppb dissolved O_2	140 days 20 mL deionized water
Powder	Yes (5% H_2 in Ar at 800^0C for 2 hours)	Not applicable	No	0.1 ppm <2.5 ppb dissolved O_2	390 days 4 mL deionized water Filtration 0.45 µm

5.2 Solid Pellet- ICP-MS results

ICP-MS results, represented in Figure 5-1, show a uranium concentration increase from 1×10^{-9} mol L^{-1} to ~6×10^{-9} mol L^{-1} being leached from the solid uranium pellet. Such a low level of uranium release is indicative of anoxic dissolution, which has a reduced rate of uranium ion release compared to oxic leaching (Cera *et al.*, 2001). This also agrees with the end solution potential of the uranium containing pots (-56 mV, -52 mV, -52 mV vs. SCE, respectively) and the control pot (-55 mV vs SCE). There is no significantly measurable difference in the solution potential between the leaching and control pots. Such a negligible change in potential is consistent with the Nernst equation, as the dissolved uranium ion release into the solution is so small (10^{-9} mol L^{-1}).

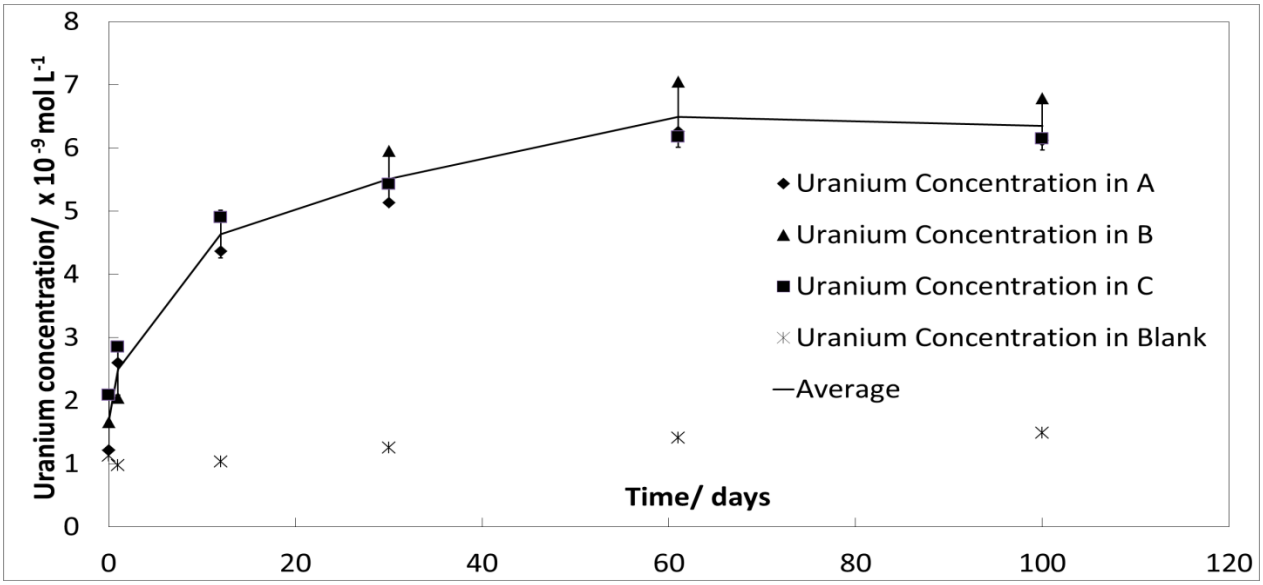

Figure 5-1 Uranium concentration in aliquots obtained from three vessels, A, B and C containing a uranium pellet each and a control vessel labelled as blank with the same set up without a uranium pellet.

The concentration of uranium reaches a maximum value of 6×10^{-9} mol L^{-1} after 60 days. This may be attributed to the uranium reaching its solubility limit under anoxic condition, hence there was a decrease in the driving force for further dissolution. Under such a scenario, re-precipitation can occur, which was confirmed by the detection of uranium-based compounds which had precipitated on the surface container during the dissolution experiment as dissolved uranium was observed in the acid washout fraction after the experiment. This effect is more pronounced in the uranium concentration data of the thin film experiment shown in Figure 5-6. ICP-MS of acid washes of the vessels after completion of the dissolution experiment show a

dissolved uranium concentration of ~3 × 10^{-9} mol L^{-1} in 250 cm^3 of 3 mol L^{-1} nitric acid, which is significantly higher than that in the blank pot (1 x 10^{-9} mol L^{-1}). Such an observation supports the presence of precipitated uranium phases within the dissolution vessel.

Figure 5-2 shows the recorded open circuit potential of the uranium dioxide electrodes at the beginning and end of this experiment. These measurements indicate some evolution (Shoesmith and Sunder, 1992) of the oxidation state at the uranium dioxide surface. Referencing with a standard calomel electrode, Shoesmith and Sunder (Shoesmith and Sunder, 1992) reported potential readings between -150 to -270 mV for near stoichiometric uranium dioxide in argon-purged solutions, containing surface UO_{2+x}. This correlates reasonably well with our data with an average initial reading of -150 mV shown in Figure 5-2. With increased oxidation of the uranium surface, He *et al*. reported that the potential reading would increase correspondingly, and surface conversion to U(VI) occurs at a threshold of -50 to -100 mV, where the surface composition approaches a thin layer (2–5 nm) of $UO_{2.33}$ as detected from angular-dependent XPS studies (He *et al.*, 2012). Our experimental reading reaches an average of -70 mV after 100 days of dissolution. This is due to oxidation arising from trace amount of ~2 ppm O_2 present in the glovebox atmosphere as determined from the 20 ppb detected at the end.

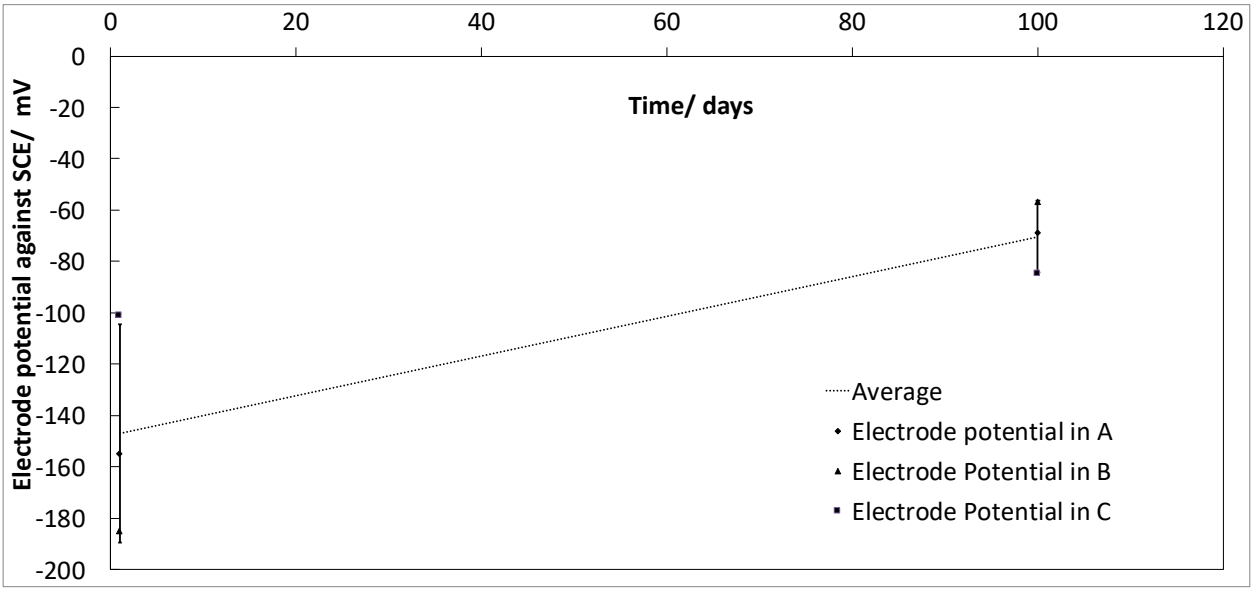

Figure 5-2 Open circuit potential of the uranium dioxide electrodes recorded at the beginning and end of this leaching experiment. Note values are plotted vs. the standard calomel electrode (SCE) for ease of comparison with data from (Shoesmith and Sunder, 1992).

5.3 Solid Pellet- Raman spectra

Area averaged Raman spectra of a freshly polished UO_2 electrode and three UO_2 electrodes after 100 days dissolution is shown in Figure 5-3, which is a magnification of the Raman shift range 350 to 750 cm^{-1}, a region previously reported as being the most important with regards to the degree of oxidation of the UO_2 lattice (He and Shoesmith, 2010; Elorrieta *et al.*, 2016). There are two distinct differences between a freshly polished electrode and that leached in deionized water under anoxic conditions. Firstly, there is a decrease in the large vibration at 440 cm^{-1}, although it should be noted that this intensity difference is only significant for Electrode C after accounting for the measurement's standard deviation as function of measured area. Secondly, there is a small increase in the broad band from ~550 to ~650 cm^{-1}.

Considering the former 440 cm^{-1} vibration first, group theory predicts that a perfect fluorite structure would be expected to give a triply degenerate Raman active mode (T2g) (Allen, Butler and Nguyen Anh Tuan, 1987), typically defined as the fundamental U-O symmetric stretching mode (He, Qin and Shoesmith, 2010; Razdan and Shoesmith, 2013). This intense vibration has been reported at ~445 cm^{-1} and in the UO_2 pellet samples of Fig. 5-3 is very close to this value at 440 cm^{-1}. A decrease in the intensity of this peak has been reported as being indicative of deviation from a perfect fluorite lattice structure, caused by either dopant effects or changes in UO_2 stoichiometry (He and Shoesmith, 2010; Razdan and Shoesmith, 2013).

Turning now to the broad band from ~550 to ~650 cm^{-1}, this band has been ascribed to various vibrations that may occur as a result of increasing lattice defectiveness (He and Shoesmith, 2010). In the absence of dopants, this region is composed of three overlapping peaks at 550, 575 and 630 cm^{-1}, respectively. The peak at 550 cm^{-1} has only recently been considered and is tentatively assigned to UO_2 grain boundaries (Guimbretière *et al.*, 2013; Elorrieta *et al.*, 2016; Maslova *et al.*, 2017). The other two peaks are of more interest with regards to the degree of oxidation of the leached samples. The first at 575 cm^{-1} has been assigned to a longitudinal optical (LO) phonon (He and Shoesmith, 2010). Usually, this phonon is forbidden under the selection rule imposed due to lattice symmetry, this peak can appear as a result of changes in translational symmetry at oxygen vacancy sites, leading to lattice disorder and the consequential breakdown in selection rules. These changes in symmetry are caused by either the incorporation of interstitial oxygens or dopant ions. The second peak at 630 cm^{-1} has been

attributed to clustering of interstitial oxygens to form higher oxidation state cuboctahedrons associated with a transition to a defective U_4O_9 structure (Desgranges *et al.*, 2012).

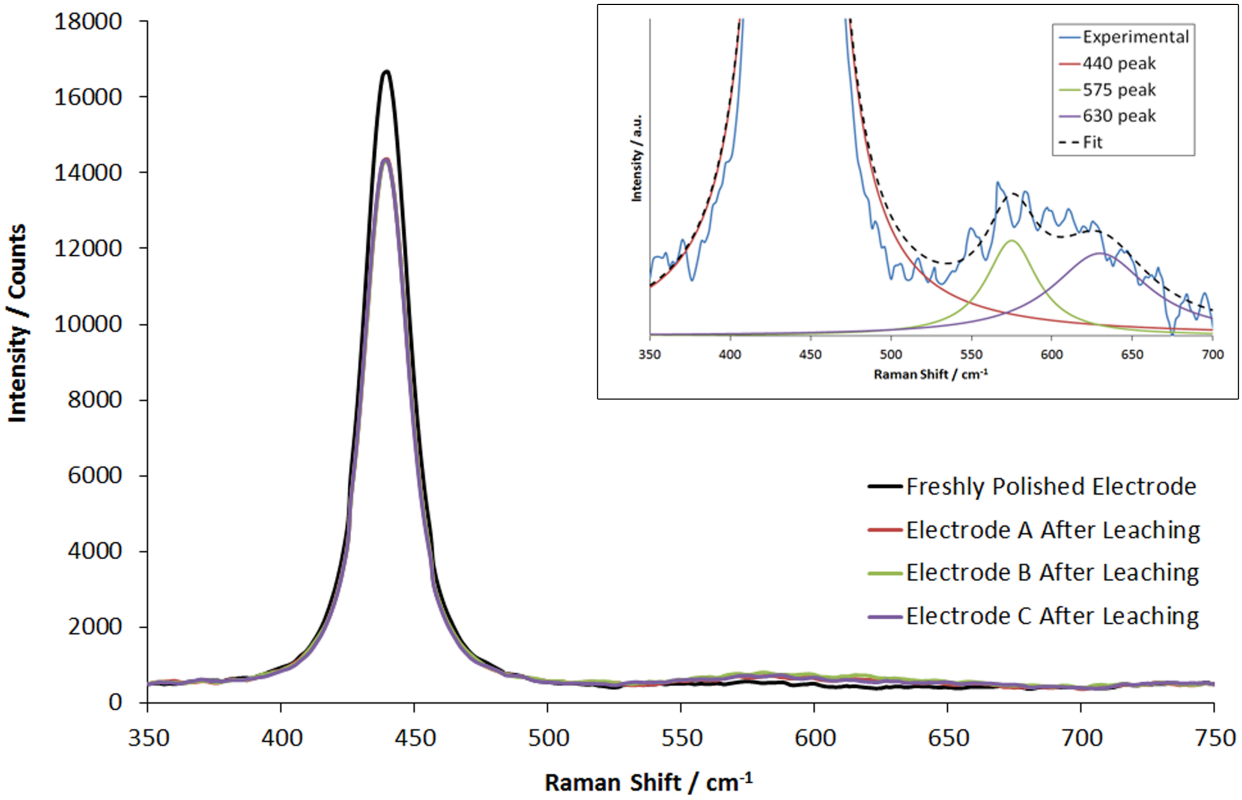

Figure 5-3 Main: Linear baseline subtracted, area averaged Raman spectra of a freshly polished UO_2 electrode and three UO_2 electrodes after 100 days dissolution over the Raman shift range 350 to 750 cm^{-1}. Inset: Example Lorentzian fit of defect bands at 575 cm^{-1} and 630 cm^{-1} from a single measurement point from electrode A after leaching.

Thus, the ratio of either the 575 cm^{-1} or 624 cm^{-1} peak to the 440 cm^{-1} UO fundamental stretch is indicative of the degree of surface hyperstoichiometry (oxidation) of UO_2 (Elorrieta *et al.*, 2016). In order to determine the contributions of each peak to the broad band of Fig. 5-3, a Lorentzian peak fit was performed for the data of Fig. 5-3, assuming peak maxima at 440, 575 and 630 cm^{-1}. An example fit for data from electrode A is shown in Figure 5-3 – inset. The analysis of this peak expressed as a ratio to the 440 cm^{-1} peak are shown in Figure 5-4A for the 575 cm^{-1} and Figure 5-4B for the 630 cm^{-1} peak.

For both the 575 cm^{-1} and 630 cm^{-1} peak, there is a significant increase in surface oxidation heterogeneity as shown by the increase in result standard deviation after electrode leaching in deionized water. However, with the exception of the 575 cm^{-1} peak for Electrode B, the results show a significant increase in the 575/440 and 630/440 peak ratio after dissolution compared to a freshly polished electrode. This suggests there is an increase in the degree of surface

oxidation of the electrodes after leaching for 100 days, corroborating the change in the measured open circuit potentials of the uranium dioxide electrodes discussed above. Finally, despite the observed increase in surface oxidation, no new peaks were observed in the region 800–830 cm^{-1} (Elorrieta *et al.*, 2018) in any of the acquired spectra, suggesting that there was no detectable highly-oxidised uranium dioxide (such as U_3O_8 and above) phases formed during the leaching process.

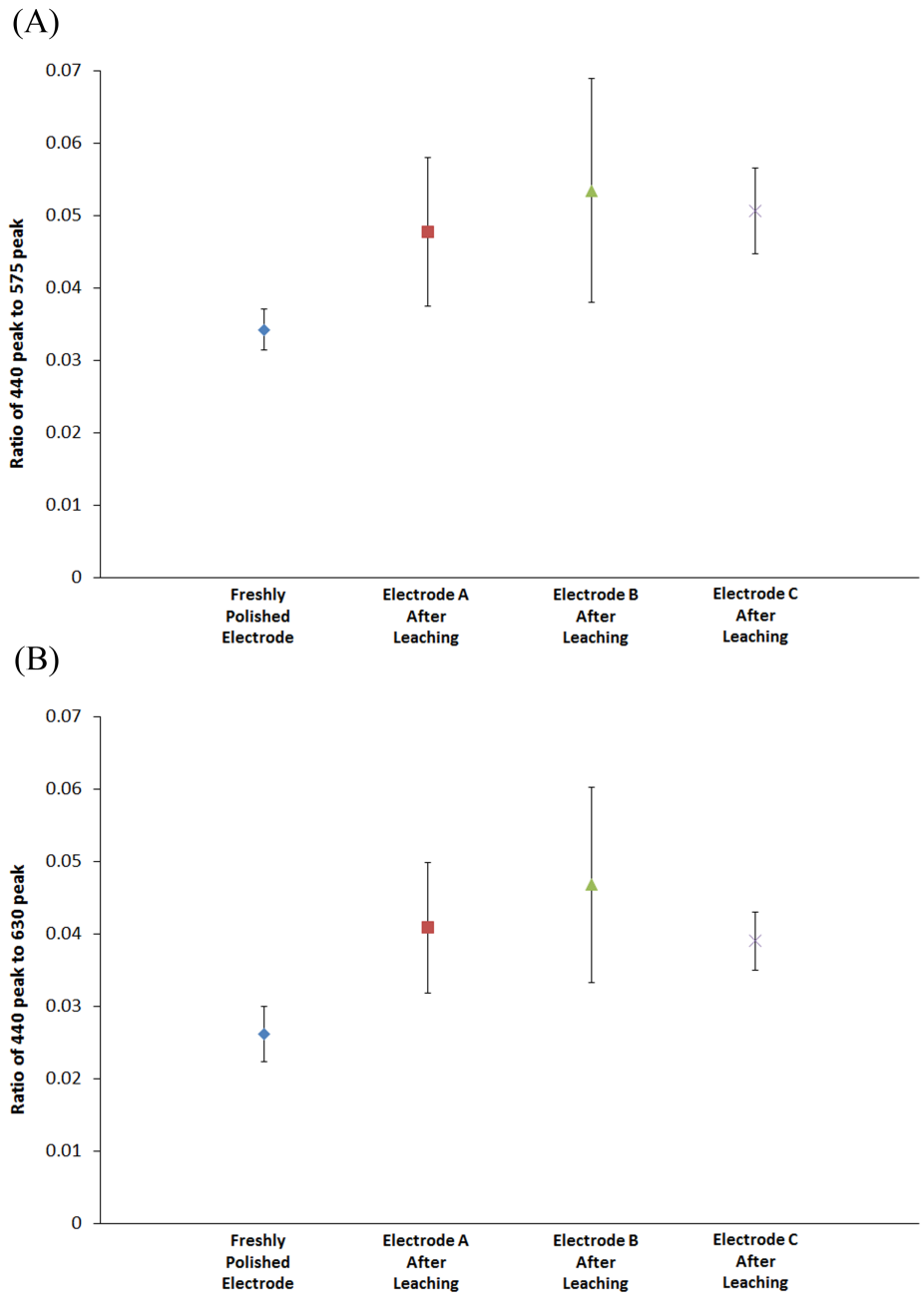

Figure 5-4 Lorentzian peak fit results for the data of Fig. 3, assuming peak maxima at 440, 575 and 630 cm^{-1}. Results are expressed as a ratio of (A) the 575 cm^{-1} peak and (B) the 630 cm^{-1} peak to the 440 cm^{-1} peak.

Scanning electron microscopy and EDX studies of the UO_2 electrode surfaces were carried out pre- (Figure 5-5A) and post-dissolution (Figure 5-5B) to ascertain the presence of any observable surface morphology changes or secondary phases.

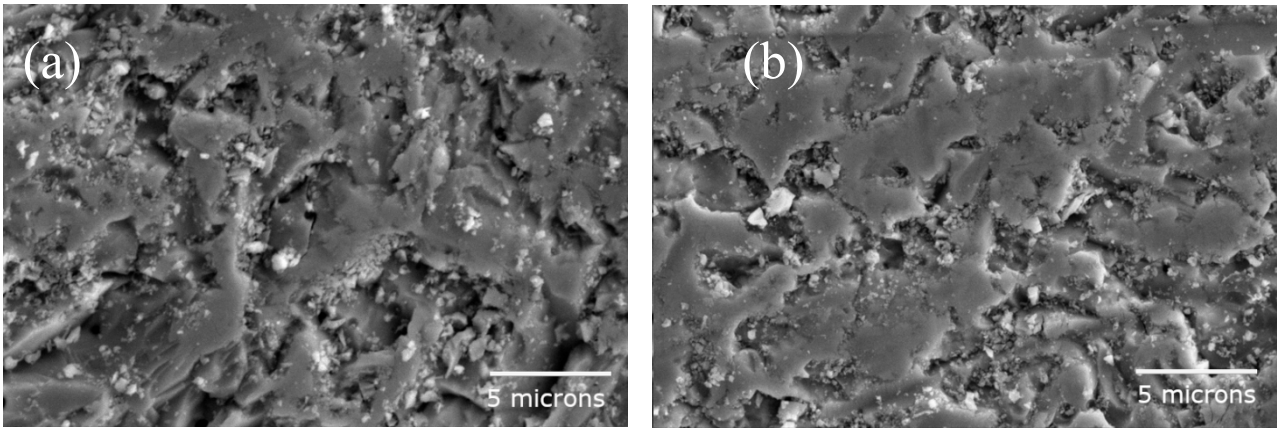

Figure 5-5 SEM at the surface of the (a) pre-leached UO_2 pellet after polishing and (b) the post-leached UO_2 pellet.

Comparison between Fig. 5a and Fig 5b reveals no significant differences before and after the leaching process. Furthermore, the high degree of surface roughness makes the identification of small secondary phases, such as those described for the thin film below, extremely difficult. However, comparison of the area EDX analysis of the electrodes before and after the leaching process reveals a small increase in oxygen atomic % from 45.71 (±0.23) to 46.44 (±0.35) where the uncertainties arose from the fitting. It is interesting to note that the atomic % oxygen should be 66.7 % in the ideal case of UO_2. The reason for the deviation is due to the high electron numbers of uranium atoms interacting more strongly with the incoming electrons than the oxygen atoms, hence less than accurate atomic % of oxygen were "determined". This small detected increase in oxygen % is likely to be insignificant but it is in agreement with both Raman and open circuit potential measurements (Figure 5-3 and Figure 5-4) that there is a small oxidation of the surface occurring due to a trace amount of ~2 ppm O_2 present in the glovebox atmosphere and a small amount of ~ 20 ppb O_2 detected in the solution.

5.4 Thin film sample- ICP-MS, ICP-OES and DLS results

A high-quality single-crystalline thin film (~100 nm) of UO_2 deposited on a (001) silicon single crystal substrate has been subjected to an extended anoxic dissolution test in deoxygenated deionized water of < 2.5 ppb O_2 under anoxic argon (0.1 O_2 ppm) atmosphere at ambient temperature (~25 °C). ICP-MS measurements of both the uranium dissolution vessel and the vessel containing only silicon wafer as a function of time are shown in Figure 5-6.

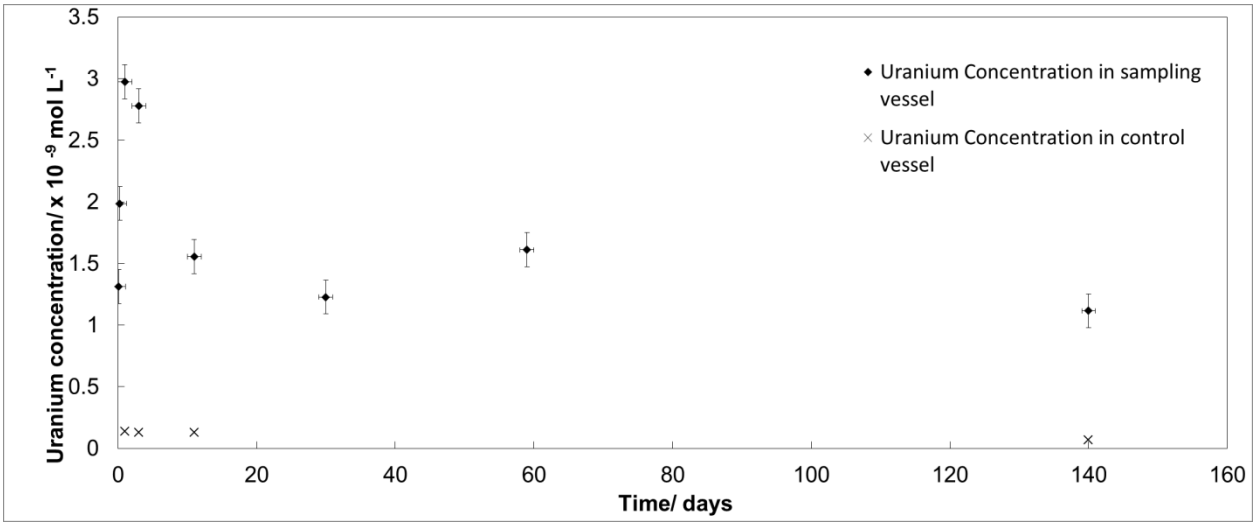

Figure 5-6 Dissolved uranium concentrations of extracted aliquots from both the uranium dioxide thin film dissolution vessel and the silicon wafer only vessel (control), determined by ICP-MS.

Figure 5-6 reveals uranium concentrations in the UO_2 thin film vessel are in the range of 1.2–3.0 × 10^{-9} mol L^{-1}. This is similar in order of magnitude to the uranium concentration from the pellet dissolution experiment shown in Figure 5-1 and believed to be linked to the long- term anoxic solubility of stoichiometric uranium dioxide. The initial increase in uranium concentrations followed by a decrease and plateau concentration at >10 days dissolution time is again indicative of a secondary phase precipitation mechanism. The nature of such deposits is described in more details in Figure 5-9 and Figure 5-10.

For the leachate from the uranium dioxide thin film experiment, dynamic light scattering was used to confirm the absence of colloids greater than 5 nm. Inductively coupled plasma atomic emission spectroscopy (ICP-AES) of this leachate found the concentration of dissolved silicon in that experiment to be in the range of 15–25 ppb.

5.5 Thin film- SEM results

The advantages of UO_2 thin film dissolution over pellets or powders is that the flat morphology of the film facilitates sharper focusing in surface imaging, allowing features that will have gone unnoticed in samples with rougher surfaces to be made more apparent as seen in the next section.

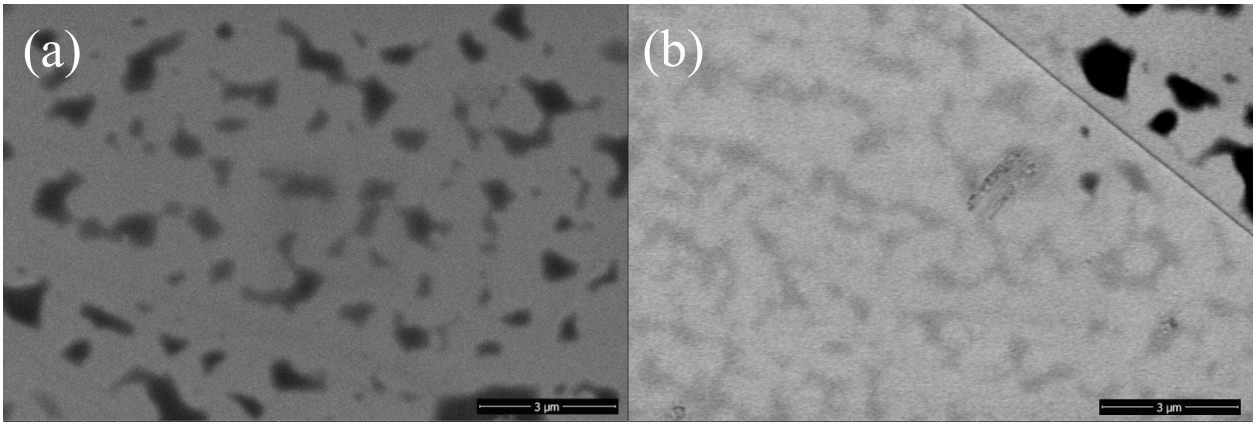

Figure 5-7 (a) 30000× magnified secondary electron and (b) backscattered electron micrographs of the thin film before prewash and heat treatment.

From the pre-leaching SEM micrographs of Figure 5-7, the surface is generally smooth with some trace particulates. Backscattered atomic contrast electron images reveal that the particles are significantly darker than the uranium surface, i.e. they have a significantly lower atomic number, suggesting they are not uranium dioxide particles. A likely cause is carbon particles from the carbon tape used in the mounting. Post-leached SEM images of a UO_2 thin film exposed to anoxic deionized water are shown in Figure 5-8 and Figure 5-9.

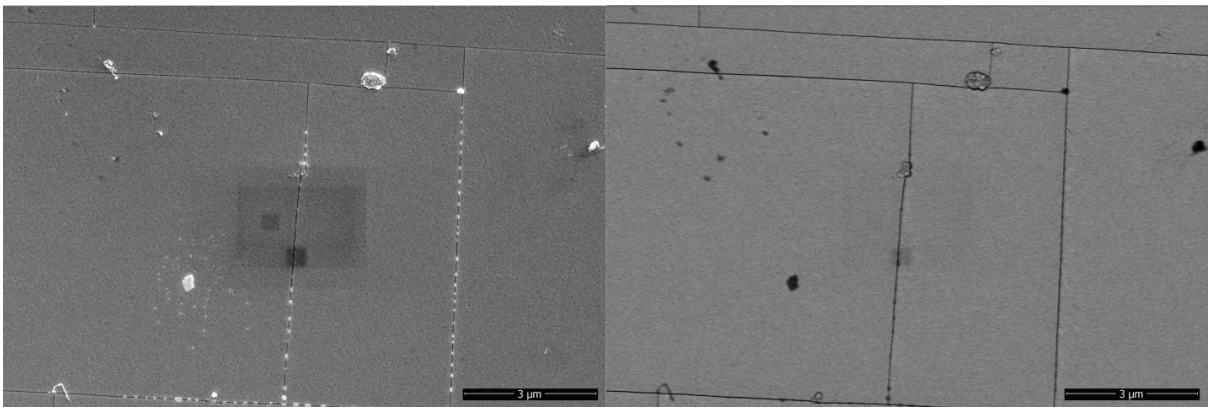

Figure 5-8 (a) 30000× magnified secondary electron and (b) backscattered electron micrographs of the leached thin film surface after 140 days dissolution.

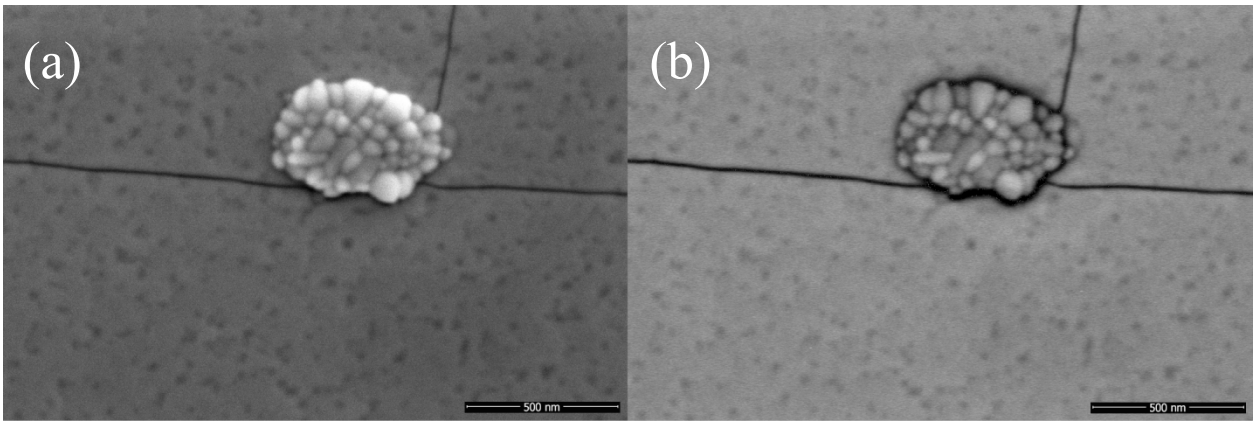

Figure 5-9 (a) 200,000× magnification secondary electron and (b) backscattered electron micrographs on the nucleate with clear growth domains ranging between 20-100 nm.

From Figure 5-8 and Figure 5-9, there are three main differences that can be seen between pre and post leaching. Firstly, more cracks are observed. These cracks are likely due to the relaxation of the stress between the substrate and thin film during the dissolution process. Both structures are based on the face centred cubic structure with slight differences in the lattice parameters, the uranium dioxide (fluorite type lattice) thin film and the underlying silicon (diamond type lattice) substrate having lattice parameters of 5.47 Å (Leinders *et al.*, 2015) and 5.43 Å (Okada and Tokumaru, 1984), respectively.

Secondly, high magnification images at 200,000× magnification (Figure 5-9a) enable the identification of small pits (20–100 nm) where dissolution has occurred. Based on previous studies on cerium oxide (CeO_2), a common analogue for uranium dioxide due to radiation safety considerations, dissolution is known to initiate at energetically reactive sites (Corkhill *et al.*, 2016) such as point defects, dislocations terminating at the surface and so forth (Schwertmann, 1991; Stumm, 1997; Corkhill *et al.*, 2014).

Lastly, Figure 5-9 reveals the presence of circular (d = 20–100 nm) secondary phase formations preferentially nucleated at film cracks. From (a), a 500 nm growth cluster was observed on a flat surface with cracks. Higher intensity of surface- sensitive electrons implies that the cluster is resting on the relatively flat surface. From (b), the back-scattered electrons with the relative uniformity of the cluster and the flat surface meant that these secondary phase have similar Z values. Together, it is clear that there is a cluster on top a flat surface composed of elements with the same atomic numbers. Unfortunately, due to the small size of the individual grains, a reliable EDX analysis could not obtain compositional information on the secondary phase.

To observe possible re-precipitation on the silicon substrates placed in the same vessel as the UO_2 thin film, SEM imaging was also conducted with secondary and backscattered electron images shown in Figure 5-10.

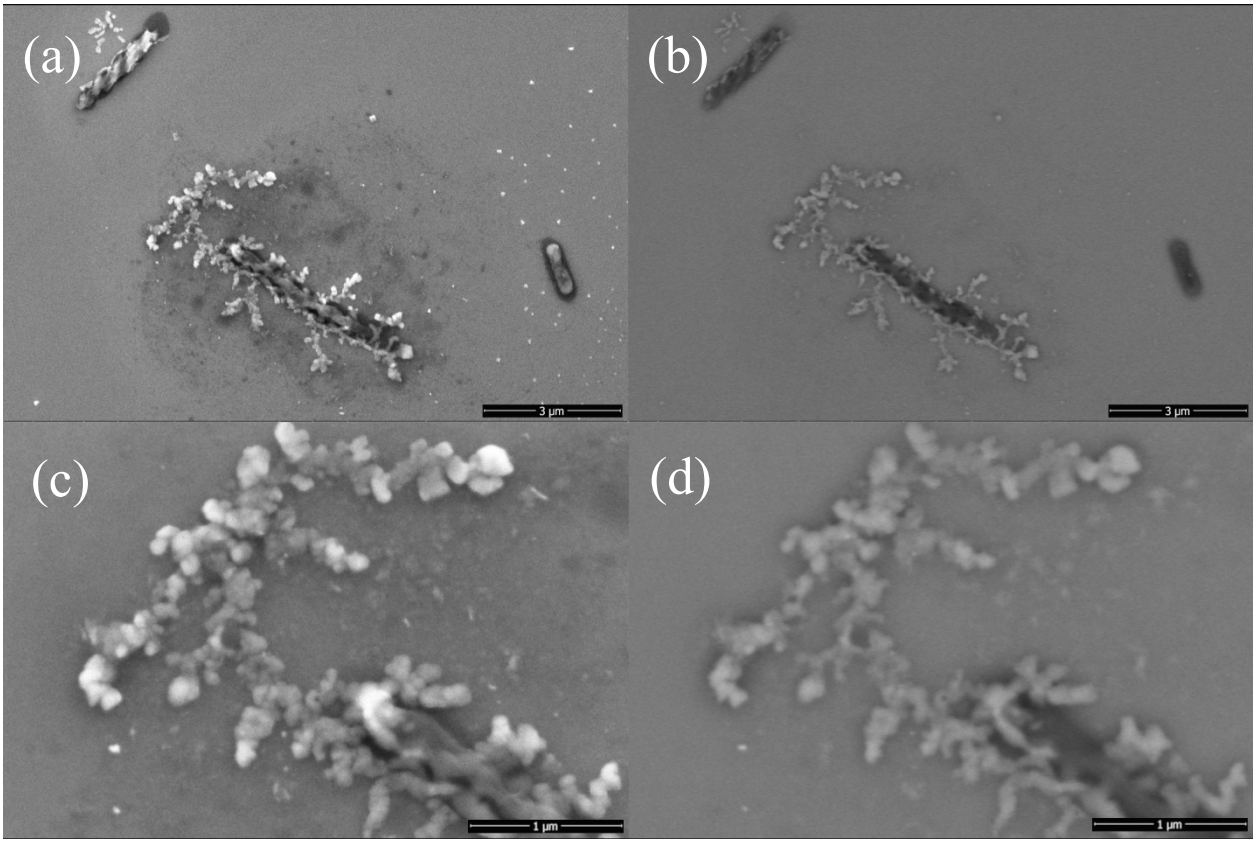

Figure 5-10 Secondary (a) and backscattered electron (b) micrographs of secondary precipitates detected at 30, 000× and secondary (c) and backscattered electron (d) micrographs of secondary precipitates detected on blank silicon substrates at 100, 000× magnifications.

Figure 5-10 shows some precipitates present on the silicon surface. Back-scattered electron image, Figure 5-10b and Figure 5-10d show that the precipitates contrasted significantly against the silicon substrate suggesting the precipitates have higher atomic numbers. Considering the closed system of deionized water, silicon substrates and uranium thin film, this implies that uranium precipitates are not just a local phenomenon found at the uranium thin film surface. However, the mechanism of precipitation is postulated to be different.

The precipitates formed on the silicon substrates differ significantly from the precipitates formed on the UO_2 thin film in terms of topography and morphology. On the flat silicon substrate, Figure 5-10 shows clearly the presence of two types of precipitates, randomly scattered particles and dendritic precipitates at the dissolution trenches and pits, appearing as

agglomerates of many grains (~50 nm) with different heights. Both these precipitates have distinctly different morphologies from those formed on the uranium thin film. Spherical UO_2 colloids have previously been reported in oxygen-starved dissolution of uranium dioxide (Kaminski *et al.*, 2005). The scattered particles might be formed from colloidal agglomeration and precipitation (Zänker and Hennig, 2014) from dissolved uranium in the solution and the dendritic growth are uranium secondary phases formed after interaction with the silicon substrate at dissolution pits/trenches. This precipitates might be better understood in future works with transmission electron microscopy as a possible future techniques.

Despite the low ionic strength of deionized water contributing to a large kinetic barrier against aggregation (Hiemenz and Rajagopalan, 1997), the gravitational force on the colloids coupled with the large difference in density between the dense uranium colloids and the surrounding fluid resulted in their precipitation after formation. Neglecting Brownian motion, Figure 5-11 shows the relationship of colloidal size to settling time using sedimentation velocity calculation based on the Stokes' equation where

$$Sedimentation\ velocity = \frac{g(\rho_{UO_2} - \rho_f)(d_{UO_2})2}{18\mu_f}$$

Equation 5—4

where g represents the gravitational acceleration experienced by the colloid, ρ_{UO_2} represents the density of uranium dioxide, ρ_f represents the density of fluid (water), d_{UO_2} represents the diameter of uranium dioxide colloids and μ_f stands for the dynamic viscosity of water.

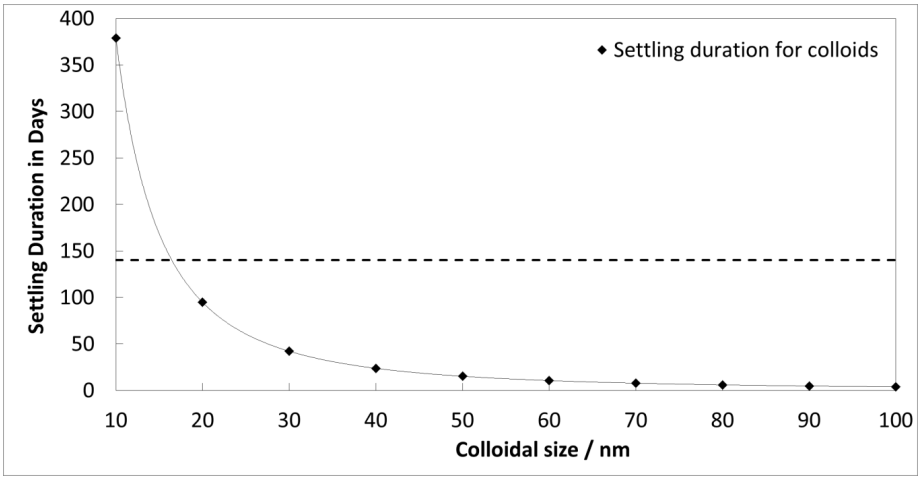

Figure 5-11 Stokes' equation predicts the relationship between the settling/sedimentation duration against colloidal size for colloidal precipitation in 2 cm deep leaching vessel, similar to our set-up.

For 140 days experiments, colloid precipitation is seen to have a colloidal size limit at 15 nm. Smaller colloids will take a much longer time to settle. The velocity of sedimentation was calculated to be 1.53×10^{-8} ms^{-1} for the observed ~50 nm uranium dioxide colloids, achieving sedimentation after 2 cm descent (depth in our experiment) in ~14 days.

Dynamic light scattering experiment at 183 days (40 days after removal of the uranium dioxide thin film) did not reveal colloids greater than 2.3 nm with a full width half maximum of 1.5 nm. Though this may imply that there were no detectable colloids in the solution 40 days after the thin film was removed. They may have been absent or already settled as calculated.

To identify the precipitates, EBSD, EDX and XRD were attempted but no signals were detected that allowed differentiation from the underlying UO_2 thin film. The lack of elemental analysis opens up possible alternative interpretations for these colloids to be uranium silicates, such as coffinite. Given the high solution concentration of silicon ions (25 ppb or 10^{-6} mol L^{-1} Si from ICP-AES measurement of the solution after the experiment), these colloids are possibly uranium silicate colloids that have been formed in the near field of the silicon substrate at near neutral pH (Dreissig *et al.*, 2011) if there is super saturation of silicon ions of a few orders of magnitude. Our concentrations of silicate to uranium concentration is quite close to that reported in the dissolution of coffinite by Szenknect et al (Szenknect *et al.*, 2016). The only caveat to this interpretation is the difficulty in producing coffinite at room temperature in laboratory conditions (Amme *et al.*, 2005; Dreissig *et al.*, 2011; Szenknect *et al.*, 2016) where the concentration of silicon is higher than our measured silicon concentrations at 10^{-4} mol L^{-1}. It is however possible that the precipitates might be precursors of coffinite.

The distinct morphology of the dendritic formation implies a different secondary phase from that observed at the uranium thin film. From the sharp contrast from the underlying silicon substrate at Figure 5-10d, these grains may be preferential uranium precipitation in the dissolution trenches/ pits where super saturation of silicon ions is possible and uranium secondary phases containing silicon, potentially uranium silicates are formed.

5.6 Thin film- XRD and EBSD results

X-ray diffraction analysis of the uranium thin film in standard Bragg-Brentano geometry is shown in Figure 5-12. Unfortunately, this diffractogram does not show any signal from any secondary phases that may be present, most likely due to the low amount of material present versus the bulk UO_2 film and the high penetration depth of XRD.

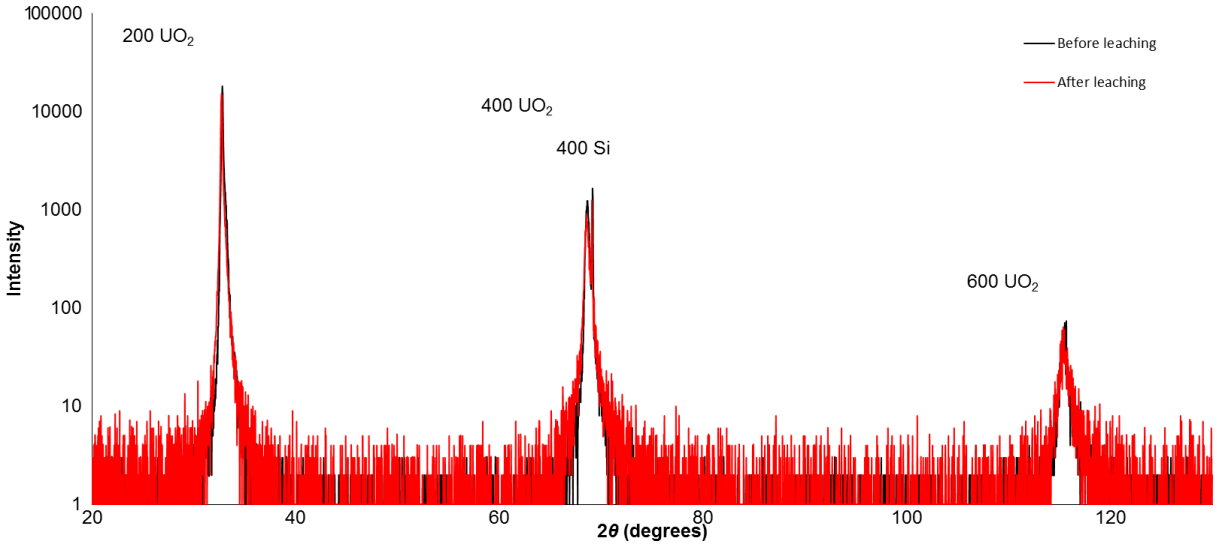

Figure 5-12 XRD diffractogram for the pre-leached and post-leached UO_2 thin film sample on a silicon substrate. Only 200, 400, and 600 UO_2 reflections corresponding to the (001) crystallographic orientation are present.

Neck and Kim (Neck and Kim, 2001) proposed that for actinides in neutral and alkaline solutions, where $An(OH)_{4(aq)}$ are the predominant aqueous species, the solubilities of $AnO_{2(cr)}$ become equal to those of the amorphous solids. Hence, a conclusion was drawn that the crystalline dioxides are covered by amorphous hydroxide layers. Despite this, from X-ray diffraction of the pre and post-leached thin film samples (Figure 5-12) and surface sensitive EBSD measurements (Figure 5-15), the sample of UO_2 did not amorphize during the dissolution duration of 140 days.

Finally, it was observed that dissolution of the uranium dioxide thin film led to micro-crack formations seen in Figure 5-8 and Figure 5-9. These cracks are curiously found to be almost perpendicular to each other and transverse the whole thin film. They were postulated to result from the release of film strain due to lattice-mismatch between the uranium dioxide thin film and the underlying silicon substrate. The misorientation differences between each point of the thin film surface was carefully investigated with EBSD images. MTEX, a MATLAB toolbox for quantitative texture analysis, was used to quantify the misorientation differences between

individual points on the thin film to investigate this dissolution-assisted strain release micro-cracks formation in the compressively stressed thin film. Such crack formation in thin films under tensile stress has been simulated by Zhang *et al.* (Zhang and Zhao, 2002). These micro-cracks are distinct from previously observed, oxidative cracks (Desgranges *et al.*, 2010) as

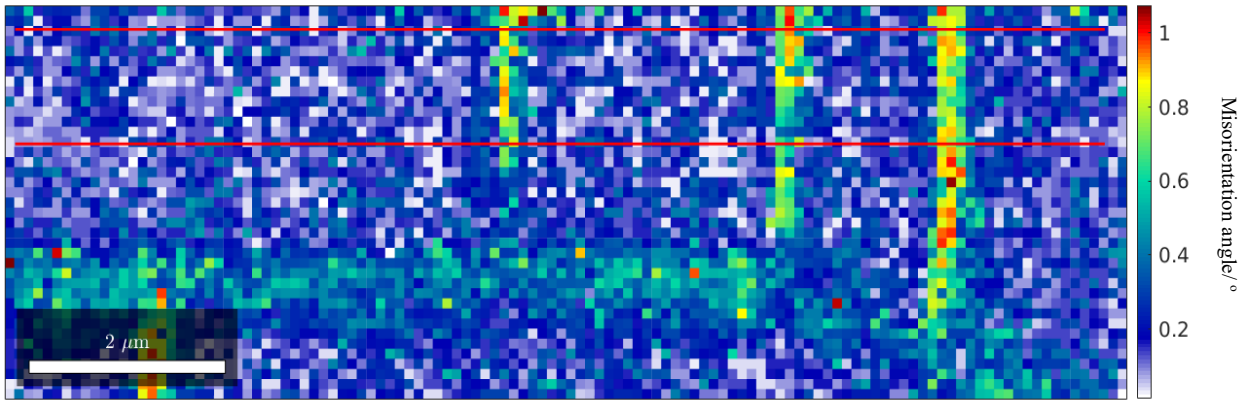

there was no evidence of oxidation of UO_2 to U_3O_7 from our XRD data.

Figure 5-13 Thresholded EBSD map showing the misorientation angle of every pixel with respect to the average orientation. The twelve adjacent misorientation profiles delimited by the two red lines were averaged to obtain the averaged misorientation profile of Figure 5-15.

A thresholded EBSD map, Figure 5-13, shows that the crystal orientation is constant throughout the grain, with virtually the entire area within 1 degree of misorientation. Next, subgrain boundaries were defined with the fast multiscale clustering (FMC) method (McMahon *et al.*, 2013) with a scaling parameter for grouping and segregating pixels into subgrains, (C_Maha of 4.8). Figure 5-13 shows that the subgrain features found reflect the crack morphology. By fitting a misorientation profile with a third order polynomial function a precision error (3σ) smaller than ± 0.3° was calculated in Figure 5-14.

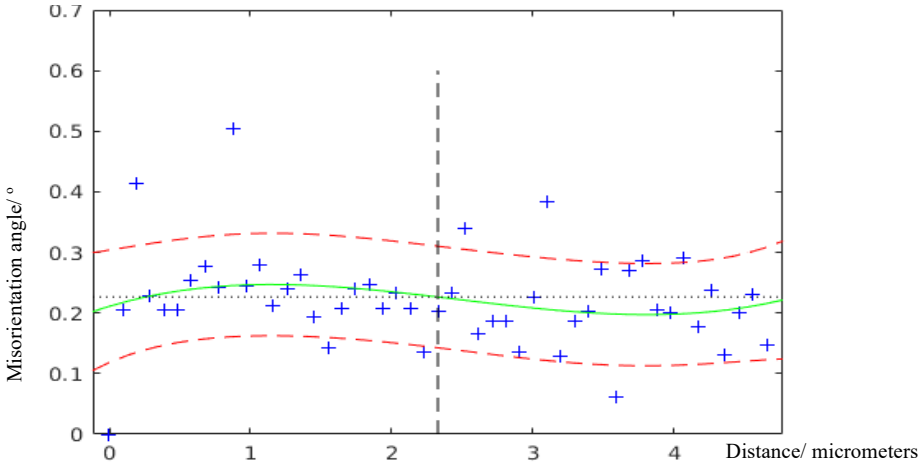

Figure 5-14 Misorientation angle (°) against distance (um) fitting plot of the profile shown in Figure 5-13. The red dashed curves represent the 3rd order polynomial fitting curve plus or minus ± sigma = 0.08°.

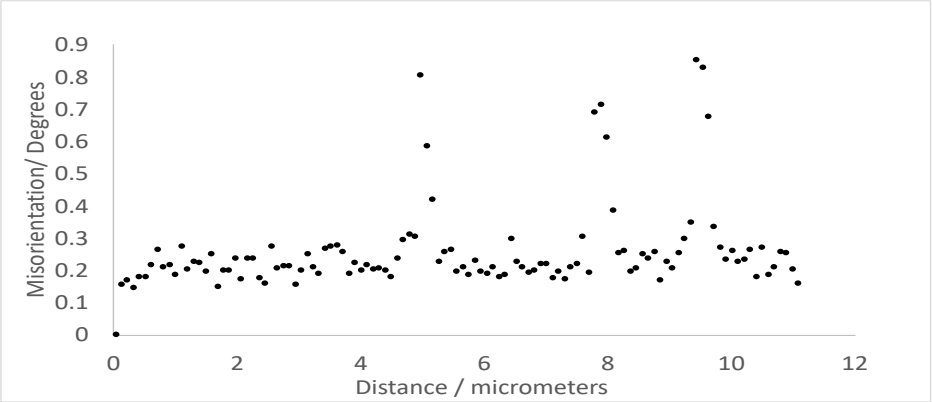

Figure 5-15 Averaged misorientation profile (see Figure 5-13 as a reference)

The resolution of each square pixel shown in Figure 5-13 is 97 nm by 97 nm. Vertical grains with areas of two by ten pixels left and right of each crack were merged and their average misorientation axes were calculated with respect to the immediate adjacent areas to the left. These misorientation axes are plotted in the inverse pole figure shown in Figure 5-16. The data show that the misorientation axis looks relatively similar at both flanks of the cracks. With this averaging approach, it can be shown that the misorientation axes oscillate around <111>, which is the cleavage related direction expected for a cubic fluorite structure (Whittaker, 1982). Our interpretation is that due to the lattice mismatch between the UO_2 and the silicon substrate crystal structures, the oxide structure is distorted along the <111> cleavage directions throughout the entire thin film. This distortion becomes experimentally significant (i.e. larger than 0.3 º) at the proximity of the cracks: that is, the crack allows for a larger crystal distortion. Such distortion promotes further propagation of the cracks themselves in a positive feedback loop. This can be seen from Fig. 8 where the cracks are seen at 90º to each other, implying a <111> direction of propagation in this (001) oriented uranium dioxide thin film.

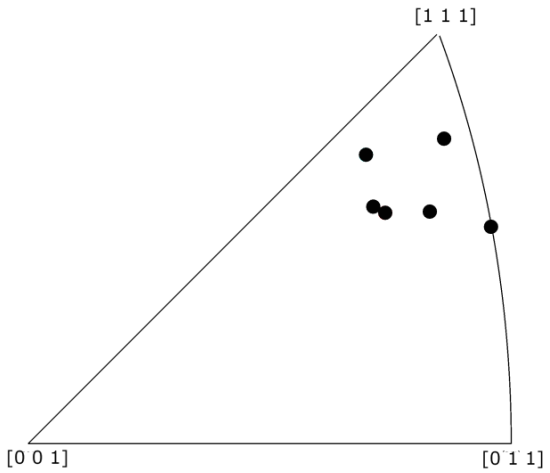

Figure 5-1 Plot of misorientation axes obtained on either side of the three cracks. They have similar misorientation axis with some statistical variation.

5.7 Variable temperature powder- ICP-MS results

This last experiment aims to determine the effect of temperature on uranium dioxide dissolution. High surface area uranium dioxide powder was leached under varying temperatures to determine the effect of temperature on uranium dioxide dissolution. ICP-MS determined uranium solution concentration values from the UO_2 powder leaching vessels held at different temperatures (ambient temperature (~25˚C), 40 ˚C, 90 ˚C and 150 ˚C) are shown in Figure 5-17. It should be noted that the aliquot extraction was done at the ambient glovebox temperature of 25˚C.

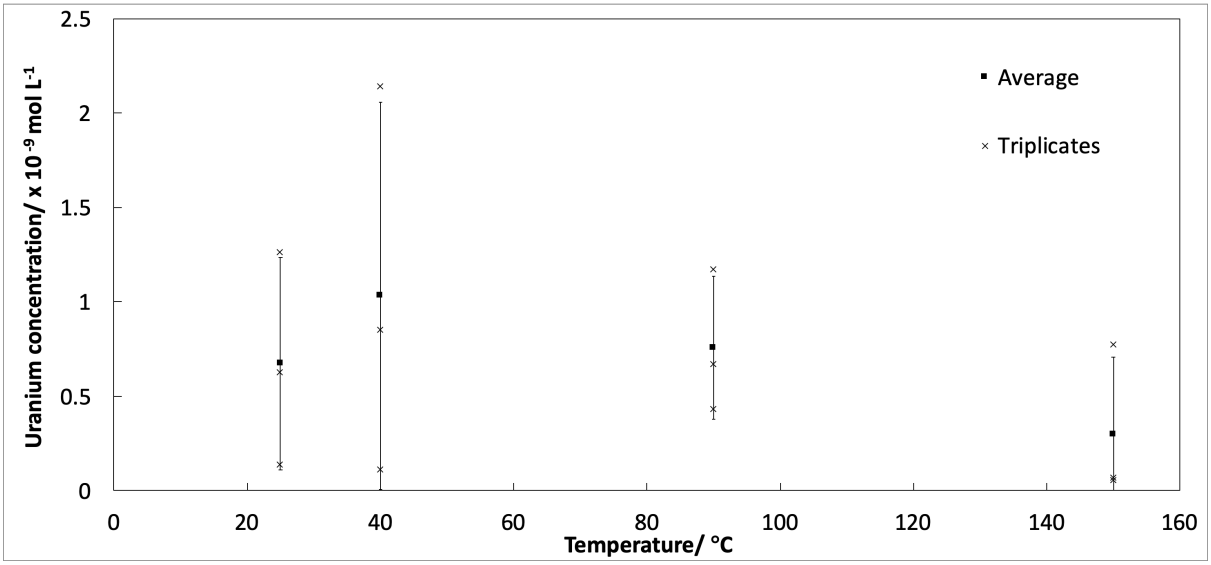

Figure 5-17 ICP-MS determined uranium concentration values after 390 days of dissolution at temperatures from 25 to 140 ˚C.

From Figure 5-17, it can be seen that the concentration of dissolved uranium does not vary significantly despite the different temperatures employed. In fact, the mean U concentration appears to decrease from 40 ˚C to 150 ˚C. It should be noted that the aliquot extraction was done a few minutes after removing the samples from the autoclave and temperatures may have fallen slightly. This observation indicates that increased temperatures do not increase dissolved uranium concentrations for long duration dissolution. It can again be seen that the final concentrations are ~10^{-9} mol L^{-1} consistent with our results on the thin film and bulk dissolution experiments at ambient temperature.

Chapter 6 High-resolution solid-state NMR of uranium minerals

High-resolution nuclear magnetic resonance spectroscopy of solid radioactive materials is in its infancy and much of the work presented here has been involved in developing approaches to obtain quantitatively local structural information on crystalline and amorphous alteration products of UO_2. It is expected that due to the low dissolved uranium concentration in anoxic conditions, the formation of uranium secondary phases will take place over extended period of times, where amorphous forms may precede longer range order; hence NMR will be unique in its ability to characterise these secondary phases, especially from the point of view of ^{17}O NMR. Furthermore, some uranium compounds, such as studtite have been observed to be thermally unstable in a X-ray beam (Guo *et al.*, 2016), often dehydrating and transforming to X-ray amorphous materials as shown for studtite sample in Figure 6-1. Figure 6-1 and Figure 6-2 demonstrate the usefulness of NMR to examine the structure of amorphous phases that are intractable with XRD.

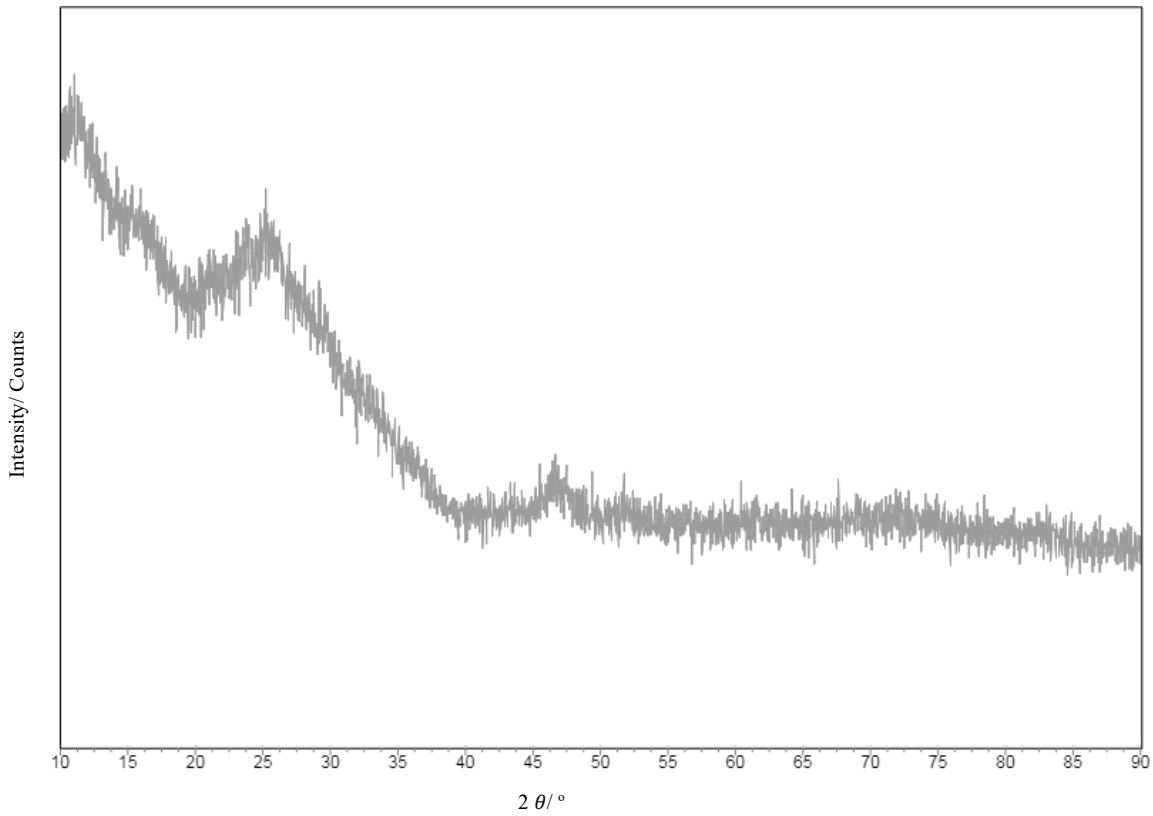

Figure 6-1 XRD pattern of studtite which underwent amorphization with extended X-ray radiation in a capillary pXRD measurement in this work. The absence of long-range order meant no Bragg reflections could be observed after 12 hours.

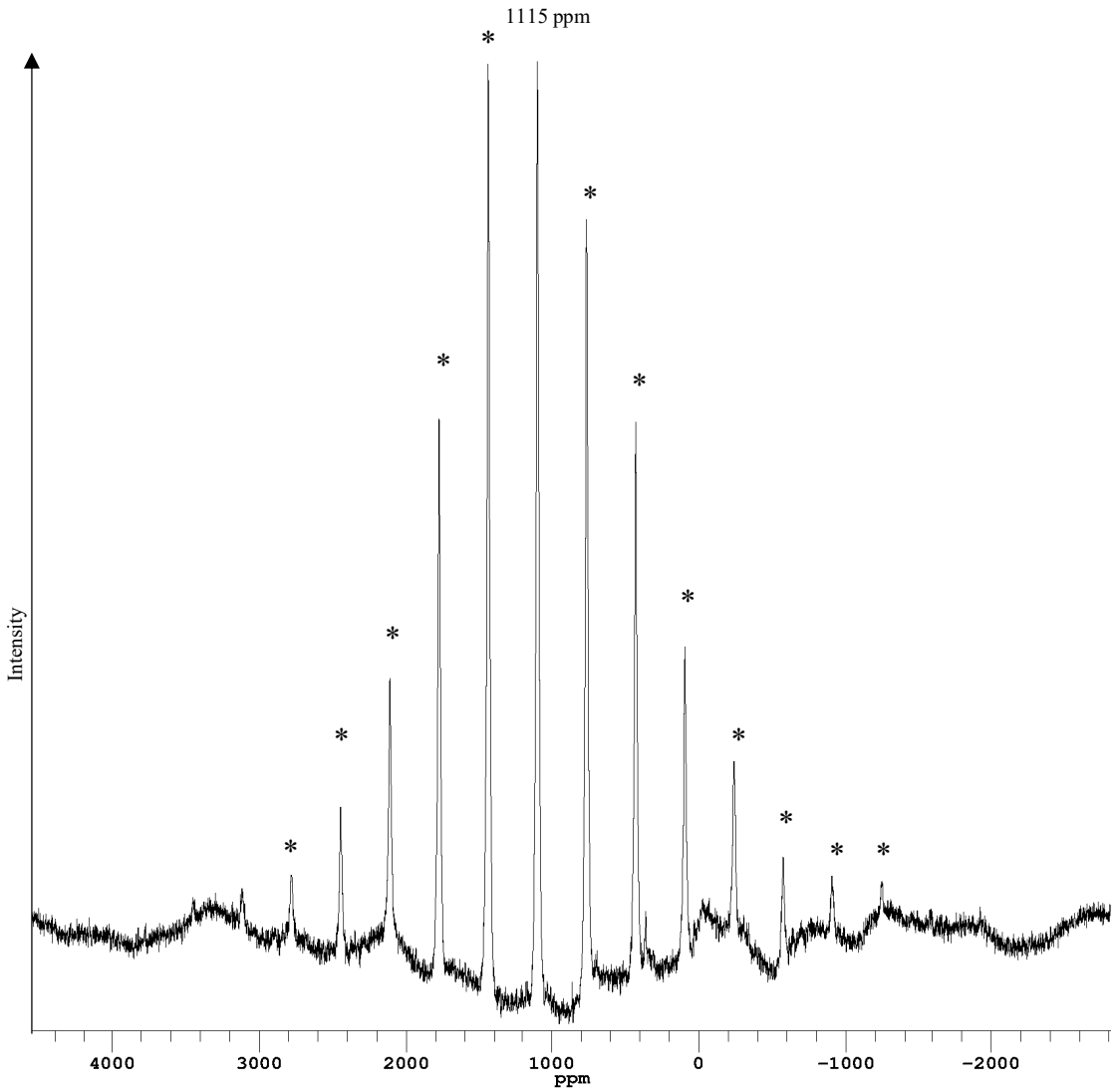

Figure 6-2 A 54.2 MHz ^{17}O NMR spectrum of the same studtite sample. The isotopic uranyl peak is located at 1115 ppm and the remaining peaks are spinning sidebands separated by 240 ppm, which corresponds to the sample rotation frequency of 13 kHz. The baseline distortion is due to the ringing of the coil which is sometimes significant (especially for weaker signals) at the beginning of the signal collection and cannot be eliminated fully without reducing the signal.

Nuclear magnetic resonance frequencies depend on the chemical environment of the resonant nucleus (in particular, the induced magnetic field due to B_0 arising from the electron distribution of its neighbouring atoms). Thus, long range order is not a prerequisite for the detection of a magnetic resonance. Figure 6-2 is a typical resonance observed from a uranyl oxygen. It exhibits a large chemical shift anisotropy resulting in a large number of spinning sidebands (*). These spread over ~ 1500 ppm (~ 80 kHz) and are separated by the sample spinning speed. This results in signal being distributed across a large number of sidebands. The

situation can be remediated by spinning the sample at a higher speed, although the trade-off is a more expensive probe and a smaller volume of sample, which leads to a lower signal.

Due to the 'ringing' of the copper RF coil used in an NMR probe, the first few points from the free induction decay (FID) signal often have to be subtracted before Fourier transformation. In the case of distinct signals from different nuclei, these subtracted points were added back to ensure correct phasing for all the signals (i.e. they started from time 0), however, these result in undulating baseline due to these artificial points. The baseline is then corrected for with the use of a polynomial baseline correction.

6.1 Adaptations for NMR spectroscopy of uranyl-minerals

The ^{17}O nucleus was chosen to probe the uranyl bond rather than using ^{235}U nuclei. Despite the low natural abundance of both of them (0.7% for ^{235}U vs 0.0373% for ^{17}O), it is extremely difficult to obtain material enriched in ^{235}U since it is a *special nuclear material*. In any case, the very large quadrupole moment and low Larmor frequency of ^{235}U make it an unfavourable nucleus for the vast majority of NMR experiments (Farnan and Berthon, 2016).Nevertheless, precautions must be taken when operating with ^{235}U at and below natural abundance (depleted uranium, U_{dep}) and the majority isotope ^{238}U. Both isotopes are α-emitters with half-lives of 4.47×10^9 (^{238}U) and 7×10^8 years (^{235}U). This means that the major radiological hazard associated with them is from transferable contamination and subsequent inhalation or ingestion. Figure 6-3 shows our first adaptation where a PTFE liner was used to double-contain the radioactive samples within the rotor to prevent escape into the environment.

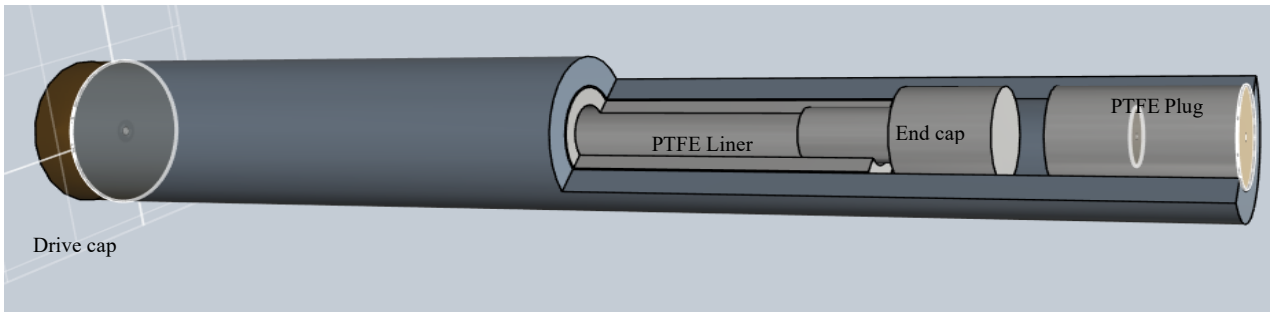

Figure 6-3 Illustration of an NMR rotor with a cut away to show white PTFE liner and end cap. The rotor is sealed at one end by a PTFE plug, and at the other by the Torlon drive cap (brown).

Despite the inherent safety of this double containment method, there are two major drawbacks of this method. The sample volume is hence limited and the distance between the samples to the RF coil has increased, reducing the magnetic coupling between the sample and the coil's

magnetic field. Both drawbacks limit the sensitivity of the experiments, which can be partially remedied by longer acquisition times with more scans. Secondly, the larger rotor size required implies that spinning will be at relatively low speeds. This implies that there will be many spinning sidebands that reduce the amplitude and area of the main isotropic peaks. This will also limit resolution especially in more complicated structures. To address this, the variable temperature exhaust gas tube was adapted to be attached to a vacuum pump system. This will allow the trapping of any escape of radioactivity in the event of a rotor crash as the pump draws the spinning gas through a series of HEPA filters. Figure 6-4 shows the difference in the signal before and after this adaptation. A sharper signal can be obtained and the spectrum will be phased/ processed more accurately.

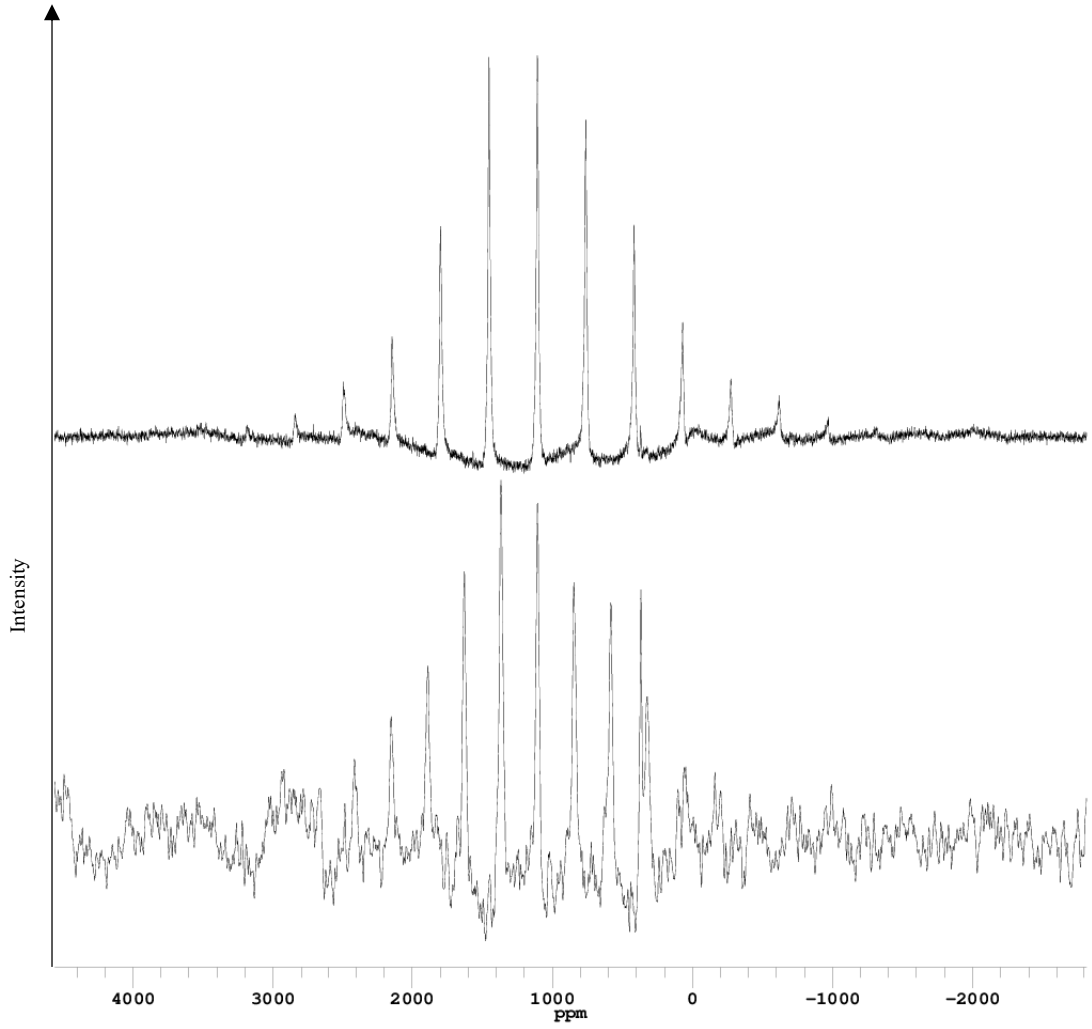

Figure 6-4 The signal improvement with the new NMR adaptation (top) as contrasted with the double containment method with PTFE liner. Both acquisitions were at acquired with low pulse angle with 15, 000 scans with a pulse delay of 10 seconds.

With this modification, smaller rotors that are capable of higher spinning speeds can be used, which reduces the number of spinning sidebands. The fastest spinning speeds that have been achieved are 50 kHz with the use of the 1.3 mm rotors. This is more than three times faster than the 4 mm rotors, hence reducing the area and numbers of spinning sidebands. The signal that would have appeared in those spinning sidebands is not lost, but contributes to the signal resulting in more intense signals that ease peak deconvolution. (See Figure 6-5)

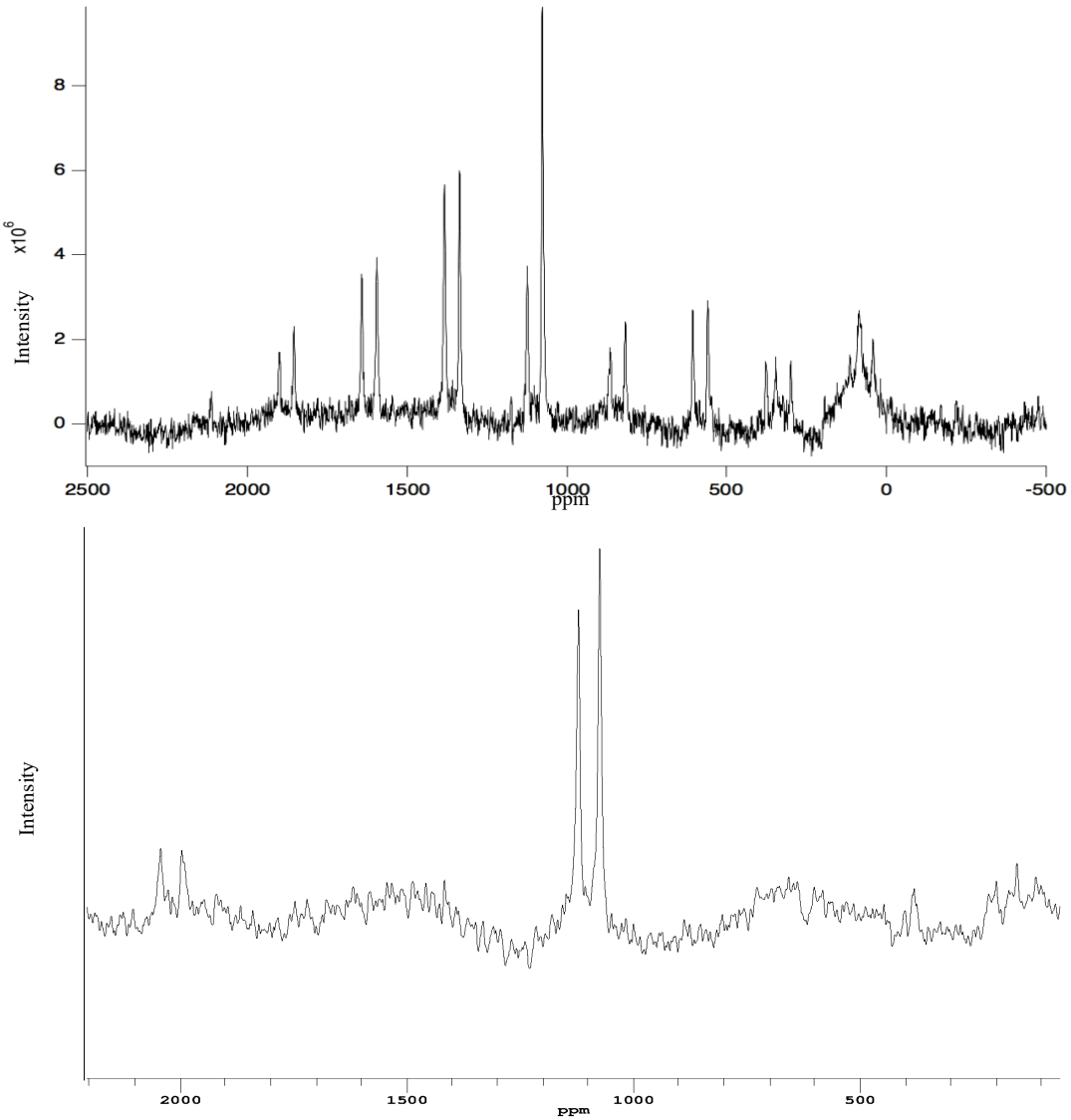

Figure 6-5 shows the single pulse spectra of Andersonite which has isotropic peaks at 1076.8 and 1124.1 ppm. The top spectrum was obtained from a 3.2 mm rotor spinning at 18 kHz, and the bottom spectrum was obtained from a 1.3 mm rotor spinning at 50 kHz. There are fewer spinning sidebands in the lower plot.

With a stronger signal from the higher spinning speed and no extensive sideband manifold, the isotropic uranyl peak in our samples can be studied thoroughly and directly measure the 90° and 180° pulse lengths for the uranyl peaks. This is done in a nutation experiment that is shown in Figure 6-6. This can only be achieved in a reasonable period of time if the signal is strong.

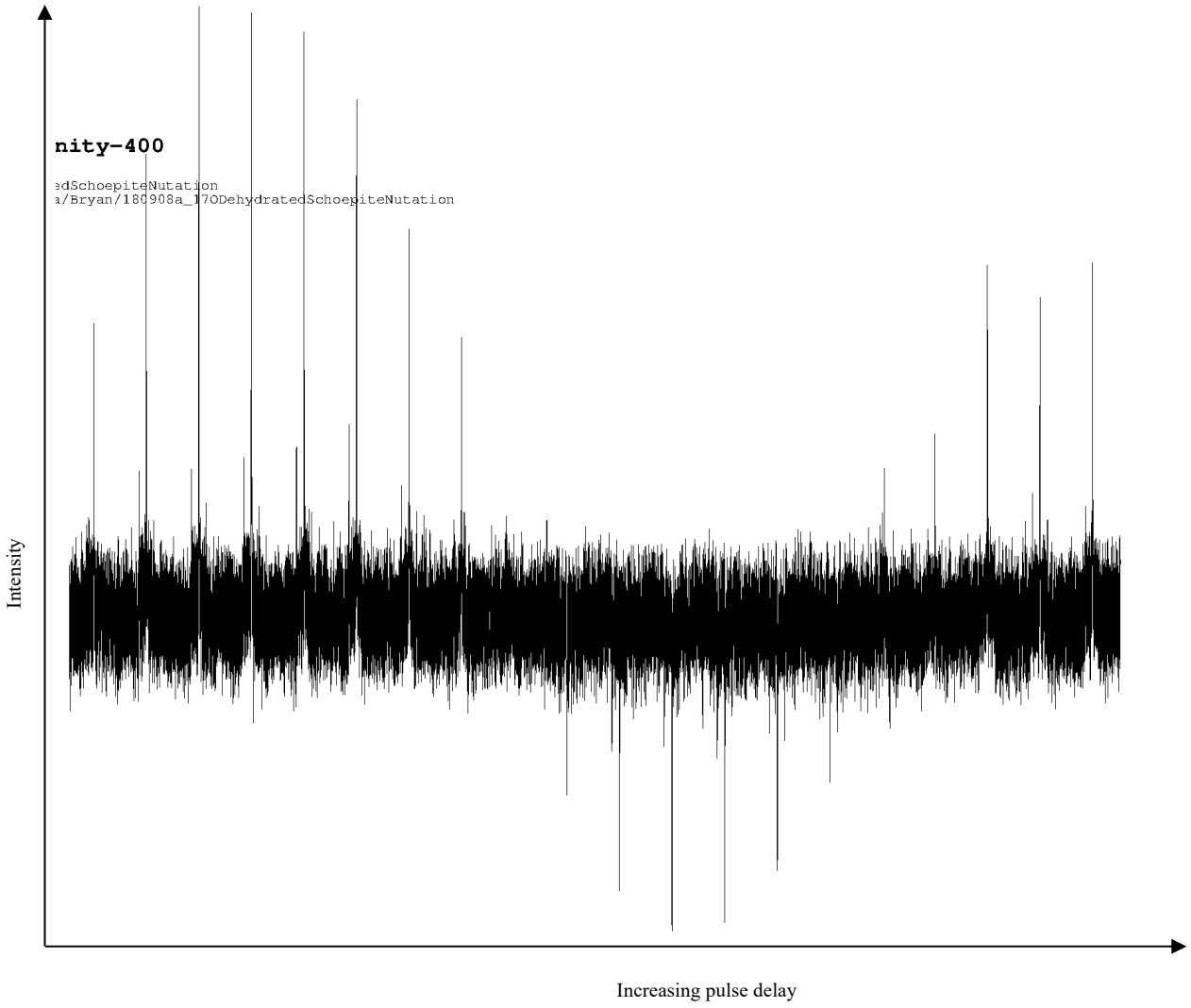

Figure 6-6 shows the nutation signal on the uranyl peak with only 50 acquisitions. The nutation array consists of an initial pulse length of 1 µs and the increment of each pulse is 1 µs. The π pulse (null signal) is 9 µs.

Coincidentally, the uranyl signal (Figure 6-6) shares the same 90° and 180° pulse length as cerium (IV) oxide. 180° or pulse was observed at 9 µs for 111 kHz RF nutation frequency. This implies that the uranyl oxygen exists in an environment with a small electric field gradient (CeO_2 is nominally cubic with Cq = 0). This result agrees with the CASTEP simulations, the Cq value of uranyl are 0.85 MHz, small as typical values range from 0 to 30 MHz, for oxygen, and this yields a small value of ν_q = 64kHz. This value is less than the RF field strength in

frequency units, ν_{RF} = 111 kHz, and hence the nutation frequency is the same for all transitions of the I = $^5/_2$ spin system (Hunger and Brunner, 2004).

6.2 Power Calibration and Sample Referencing with CeO_2 at 877 ppm

6.2.1: ^{17}O Reference: Cerium (IV) oxide at 877 ppm

The small size of the 1.3 mm rotor with an external diameter of 1.3 mm and capacity of 1.5 µL meant that it is difficult to use water as a reference due to insertion uncertainty, surface tension makes it difficult to get water into the rotor. Cerium (IV) oxide fabricated with ^{17}O was used as a ^{17}O reference at 877 ppm. The oxygen environment for ceria is nominally cubic and has negligible electric field gradient, resulting in a sharp peak representing all transitions.

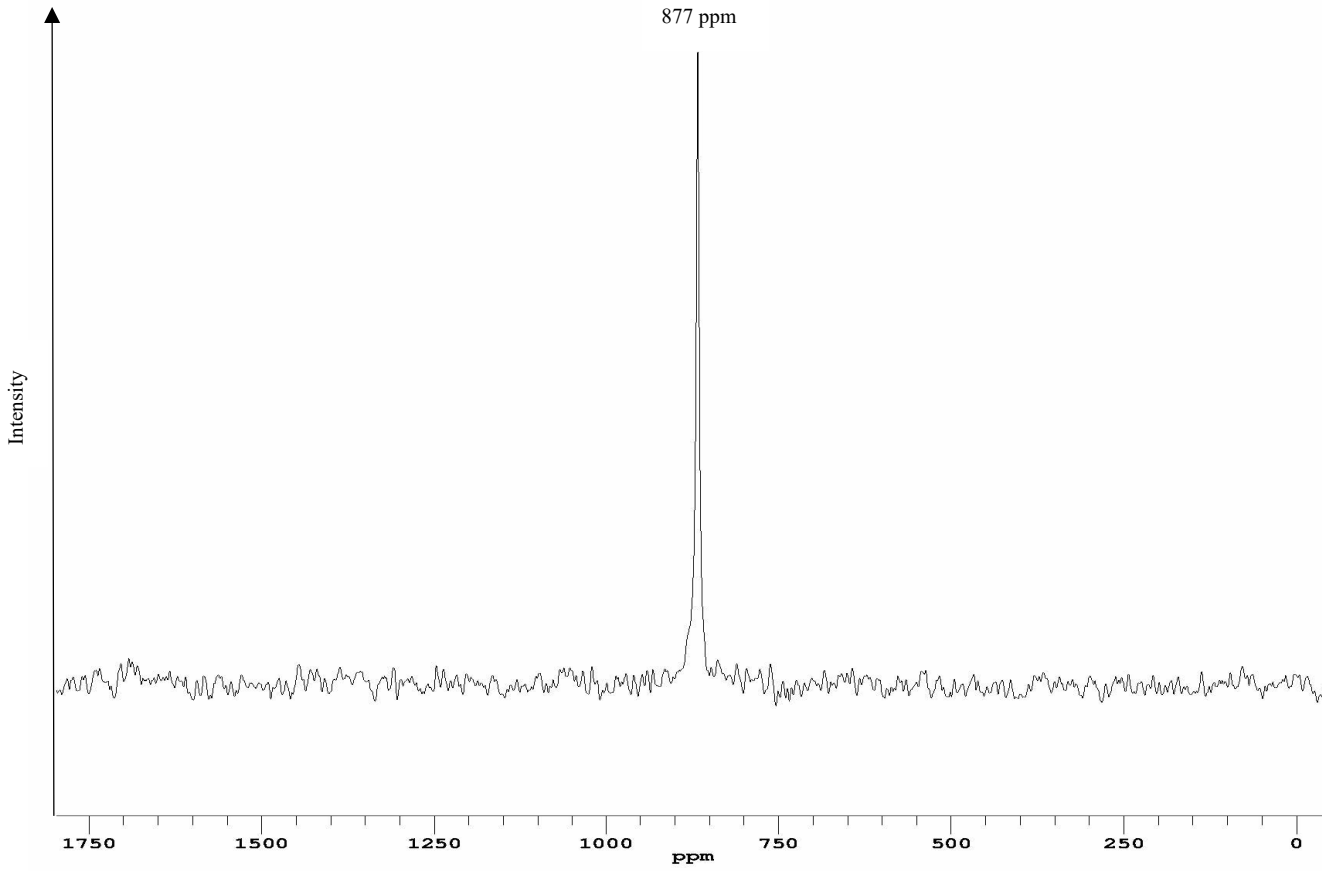

Figure 6-7 ^{17}O reference with Ceria (IV) oxide. There is a sharp characteristic peak at 877 ppm.

For the other probes used in this thesis, predominantly the 3.2 mm probe for variable temperature experiment, liquid water was used as a reference at 0 ppm. Being a liquid, there was no anisotropy and a sharp peak was observed and referenced as 0 ppm. Referencing was done at the start of each experiment.

6.3 Spin Echo experiment

Upon obtaining the uranyl oxygen 90° and 180° pulse characteristics due to the electric field gradient, spin echo experiment can proceed, which will eliminate the ringdown problems of single pulse acquisition. This last step in the experimental iterations enables careful characterization of the different uranyl oxygen environment by comparing the chemical shift and the bond lengths of different uranyl mineral structures. Figure 6-8 shows the spin echo spectrum for the same Andersonite sample and its flat baseline obtained compared with the single pulse acquisition in Figure 6-5.

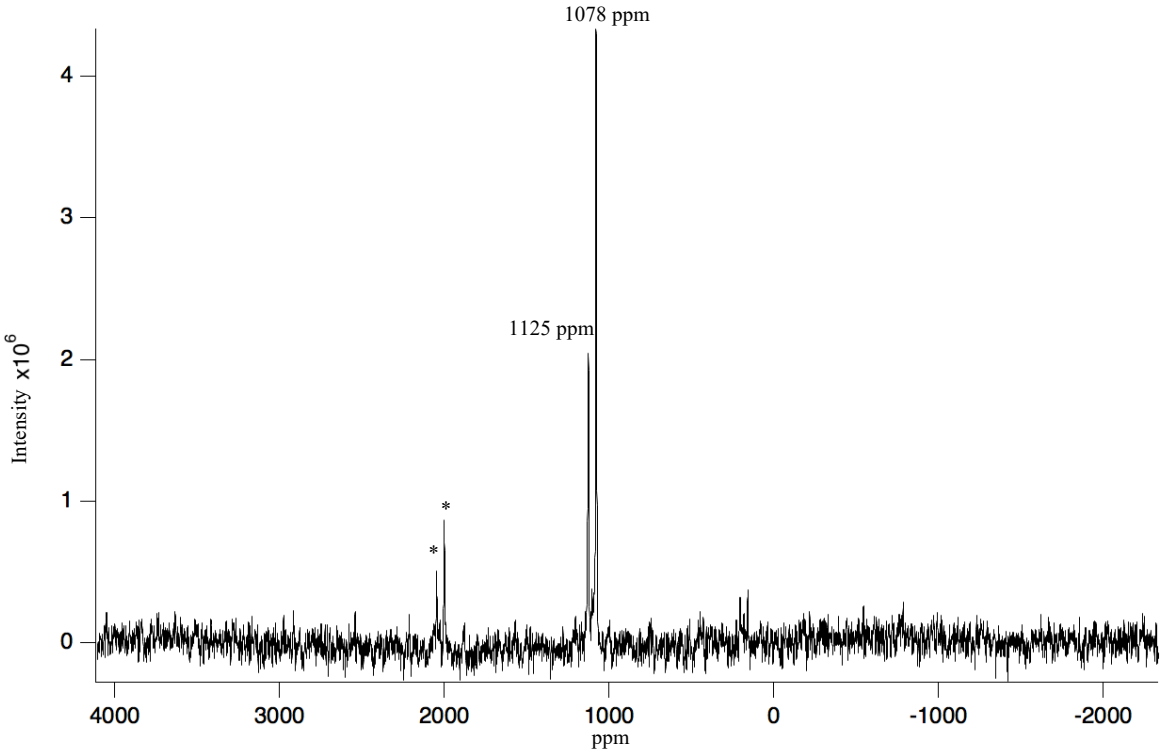

Figure 6-8 The spin echo spectrum of the uranyl oxygen of Andersonite after calibrating pulse angles directly.

Upon completion of the spin echo experiment, the next step is to resolve the peak signal of the uranyl oxygen environments. For more complex structure, such as metaschoepite shown in Figure 6-9, the flat baseline from the spin echo experiment is important and allow us to focus on the main isotropic peak where the signal is now concentrated in as seen from Figure 6-10.

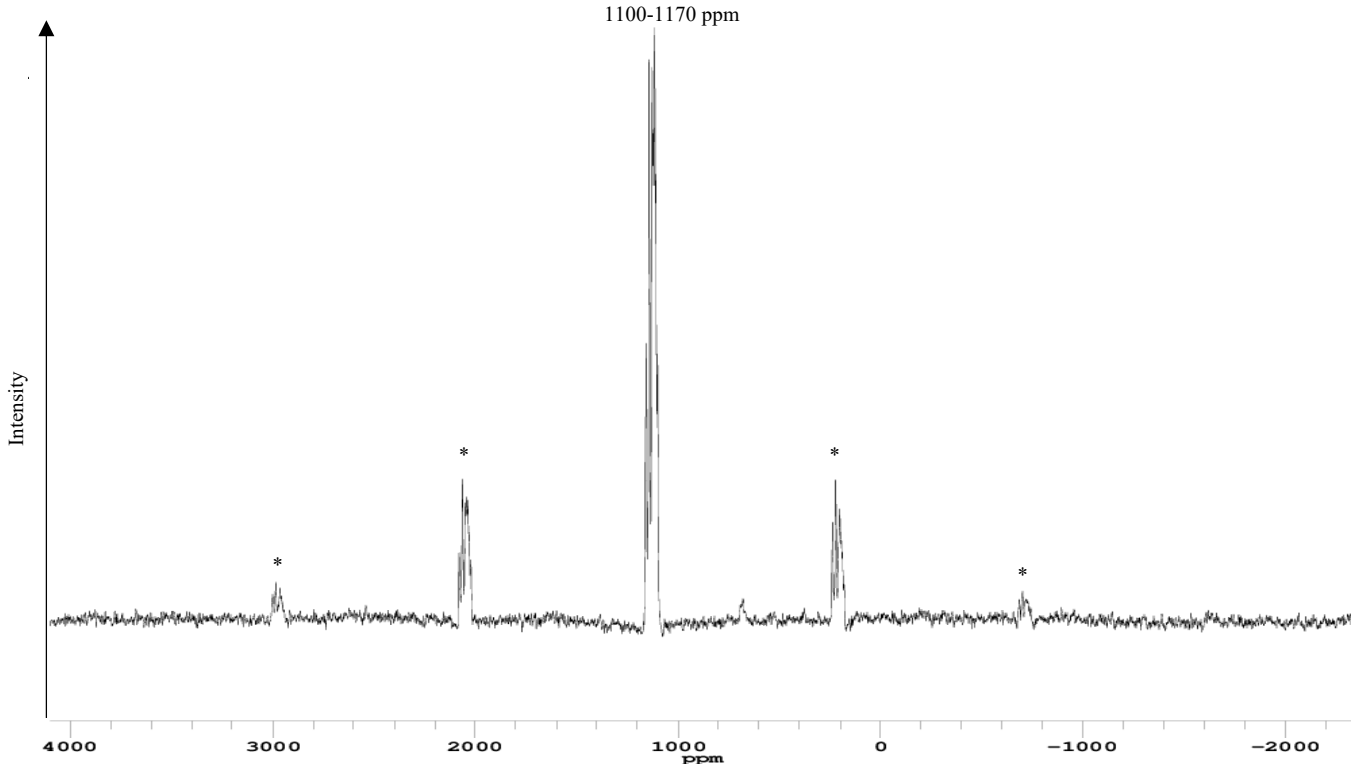

Figure 6-9 ^{17}O NMR spin-echo spectrum of 12 mg of metaschoepite spinning at 50 kHz.

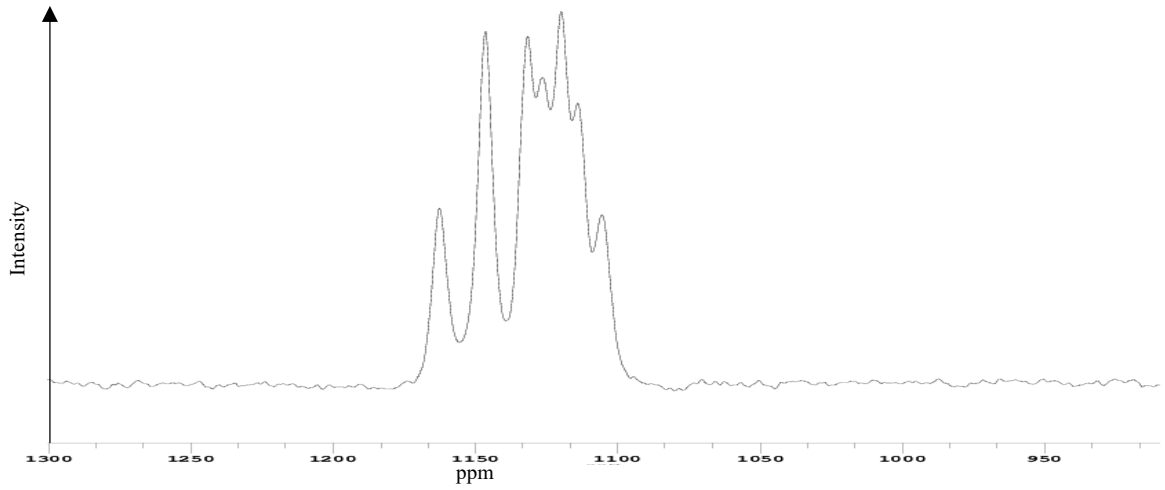

Figure 6-10 Zoomed in spectrum of the centre band of metaschoepite at 50KHz spinning speed.

In a crystal structure with oxygen local environments with large variations in electric field gradient, it is important to calibrate the RF power to ensure uniform excitation (or deliberate preferential excitation). To obtain this, CeO_2 was run at the same power for different pulse lengths (nutation experiment). Increased RF power will increase the flip angle for a constant pulse length. At flip angle of 180° / π, the NMR signal in the z direction should be 0 (with perfect RF homogeneity).

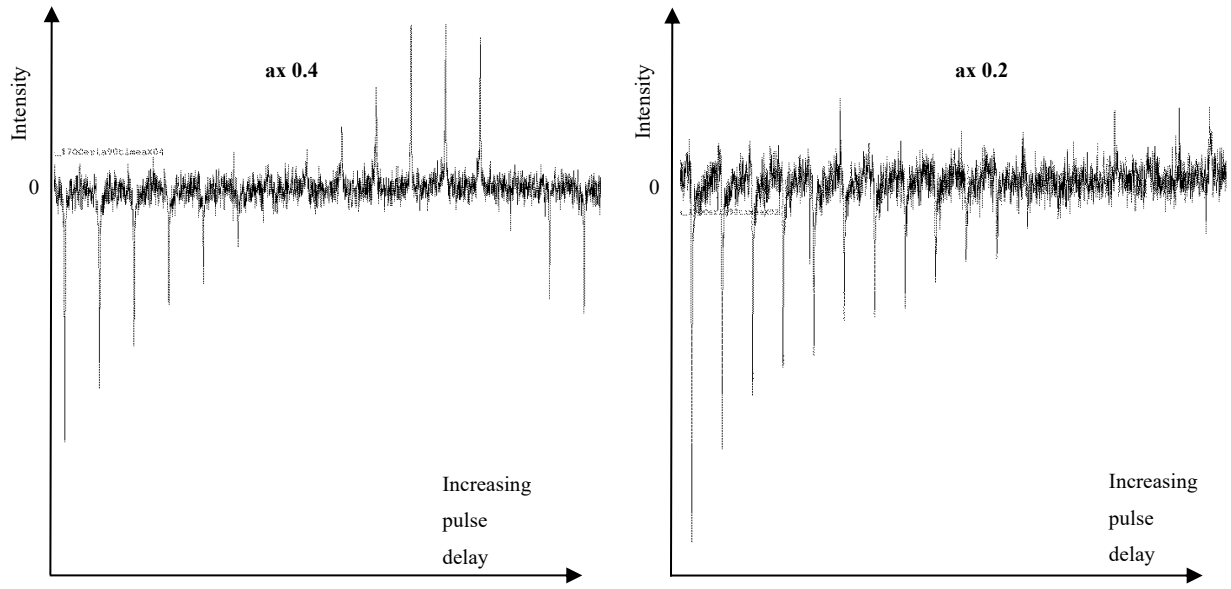

Figure 6-11 These nutation plots of intensity against increasing pulse delays show the different signal strength at pulse length for pulse strength, ax0.4 and ax0.2 respectively. A weaker pulse strength will require a longer duration to obtain a flip angle of π.

180° or π pulse was observed at 4.5 μs for amplification setting ax0.4 and 8.0 μs for setting ax0.2. Power calibration in frequency units are 222 kHz for ax0.4 and 125k Hz for ax0.2 on this probe.

6.4 Characterisation of uranyl bond lengths to NMR chemical shifts

There are competing mechanisms in relating chemical bond lengths to NMR chemical shifts, especially for heavier atoms where the electronic structure can be complex with energy levels that are closely spaced and paramagnetism/ diamagnetism can be exhibited. Generally, atoms/ ions with unpaired electrons exhibit paramagnetism as single electrons are able to align themselves with the magnetic fields whereas atoms/ions with all electrons paired will be weakly diamagnetic due to the Pauli exclusion principle where no electrons have the same state and the spin cancelled out.

However, this become more complicated in NMR studies, as there are three principle effects which control NMR chemical shifts; the relatable diamagnetic term (σ_d), where increased electron "density" results in shielding of the local nucleus, leading to upfield shielding (decreased chemical shift), the neighbouring group anisotropy (σ_n), where asymmetrical local magnetic fields are created by neighbouring atoms/ electrons especially for solid samples (which can be averaged out by MAS at an angle, θ where $3\cos^2\theta - 1 = 0$). Lastly, there is the

paramagnetic term (σ_p), where electronic transition between ground and excited states of orbitals with angular momentum result in downfield deshielding (increased chemical shift) and this forms the principal chemical shift effect resulting in very large shifts (Kong *et al.*, 2015). For this thesis, I am studying a small and relevant subset relating uranyl bond lengths with respect to the chemical shifts, i.e. investigating the magnitude of the impact of the diamagnetic term (σ_d) where the electron density of the nearby uranium atom affects the chemical shift of the 'yl' oxygen in these uranyl- containing compounds.

To link ^{17}O chemical shifts to uranyl bond lengths, six different uranium minerals with different uranyl bond lengths have been synthesized and examined with NMR. From the literature XRD derived lattice parameters and atomic coordinates were also used in CASTEP simulations and compared with NMR ^{17}O chemical shifts. X-ray diffraction literature values were used because some of these compounds are sensitive to X-ray beam exposure and it was difficult to obtain a single-phase material. The aim of setting up these range of measurements enable us to obtain experimentally, a library of uranyl bond lengths to NMR chemical shifts that may be used in forensic applications of uranyl- containing amorphous phases whose formation may precede longer range order, i.e. crystallinity. This is especially true in anoxic conditions for underground nuclear repositories where alteration is projected to occur at longer timescales and long-range order may form over many years. NMR provides a possible alternative to secondary phases detection prior to the development of long range order.

Grouping the different uranyl bond lengths into bins of 0.01Å with the help of a Crystalmaker™ graphing tool, the numerical distribution of bond-lengths is in accord with the ^{17}O NMR spectra. It was observed greater shielding and consequent upfield shifting bond with shorter bond distances. Previous work and modelling with uranium based compounds (Poturaj-Gutniak and Taube, 1968; Gao *et al.*, 2014) shows the transfer of electron from π bond to 5f and 6d orbital of electrons. In order for a diamagnetic shift as seen in this work, the proposition for the uranyl bond is a prior transfer of electrons from the 2p orbital of oxygen to the π bond (resulting in a reduction of the paramagnetic contribution due to the p orbital possessing angular momentum). This may also result in a shorter π bond which strengthen it. More π bonding in a shorter bond would reduce oxygen 2p electron density and result in a diamagnetic shift, thus increasing shielding of the oxygen nucleus from the external magnetic field. The resolution of the fast spinning experiment results in the observation of unique chemical shift

position for each bond length and the ^{17}O uranyl oxygen chemical shift is observed to decrease with decreasing bond length.

6.5 NMR of uranium minerals

6.5.1 Dehydrated schoepite, $UO_3.H_2O$

Dehydrated schoepite described earlier in 2.3.2 Dehydrated schoepite ($UO_3.1H_2O$) and metaschoepite ($UO_3.1\text{-}2H_2O$) has 8 unique uranyl molecules in their crystal structure (Finch, Cooper, *et al*, 1996), which implies that it have 16 unique 'yl' U = O bonds with different bond lengths. A closer inspection of the neighbouring chemical environment of the uranium atom yields complex results. The uranyl bond are highlighted in black.

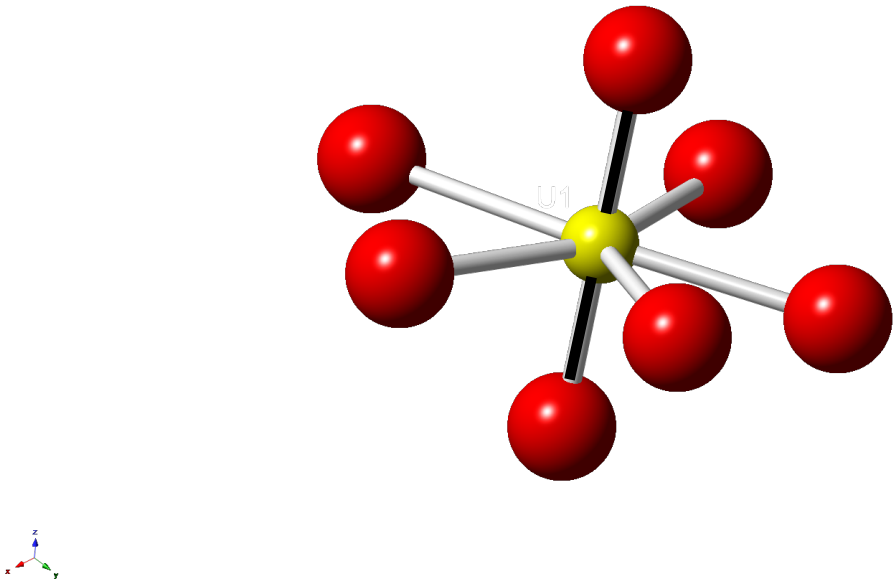

Figure 6-12 shows one of the eight crystalographically distinct uranium atoms with similar configurations. In brief, the unit cell contains eight symmetrically distinct U sites, each of which is occupied by a U^{6+} cation, which is part of a nearly linear $(UO_2)^{2+}$ uranyl ion (designated Ur), with U=O bond lengths ranging from 1.73 to 1.83 Å, Each uranyl ion is coordinated by five additional anions arranged at the equatorial corners of hexagonal bipyramids.

These bond lengths (tabulated below) are extremely close to each other hence they are placed in bins of 0.01 Å for curve fitting purposes in the next figure.

Bins	Bond lengths
1.73-1.74	1.7368, 1.7374
1.74-1.75	
1.75-1.76	1.7541, 1.7566
1.76-1.77	1.7660, 1.7693
1.77-1.78	1.7728, 1.7784
1.78-1.79	1.7840,1.7870
1.79-1.80	1.7913,1.7934,1.7963
1.80-1.81	1.8028,1.8051
1.81-1.83	
1.83-1.84	1.8332

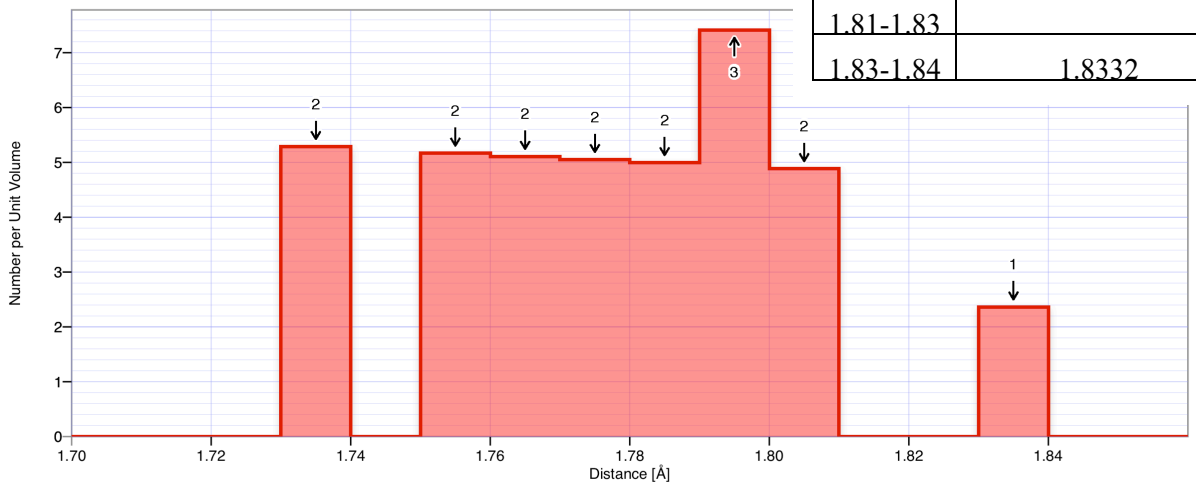

Figure 6-13 By looking at the XRD data, the different uranyl bond lengths were resolved into 0.01 Å bins for a curve fitting guide.

The proximity of these bond distances are reflected in the NMR spectra from the below spectrum (See Figure 6-14) which consists of a broad isotropic peak with a small secondary peak. The small secondary peak (Figure 6-14) at the larger chemical shift (ppm) was subjected to more deshielding. Based on the preceding reasoning on 6.4 Characterisation of uranyl bond lengths to NMR chemical shifts, a longer U=O bond length results in less transfer of electron density from 2p orbital of oxygen to the π bond. This relative increase in the electron density of the 2p orbital result in a paramagnetic effect and hence a larger chemical shift observed. Observing the different full width half maximum (FWHM) of the peaks, it is deduced that the larger peak might be composed of a combination of smaller peaks, hence deconvolution by curve-fitting with IGOR®, a spectra analysis software, was done. (see Figure 6-15).

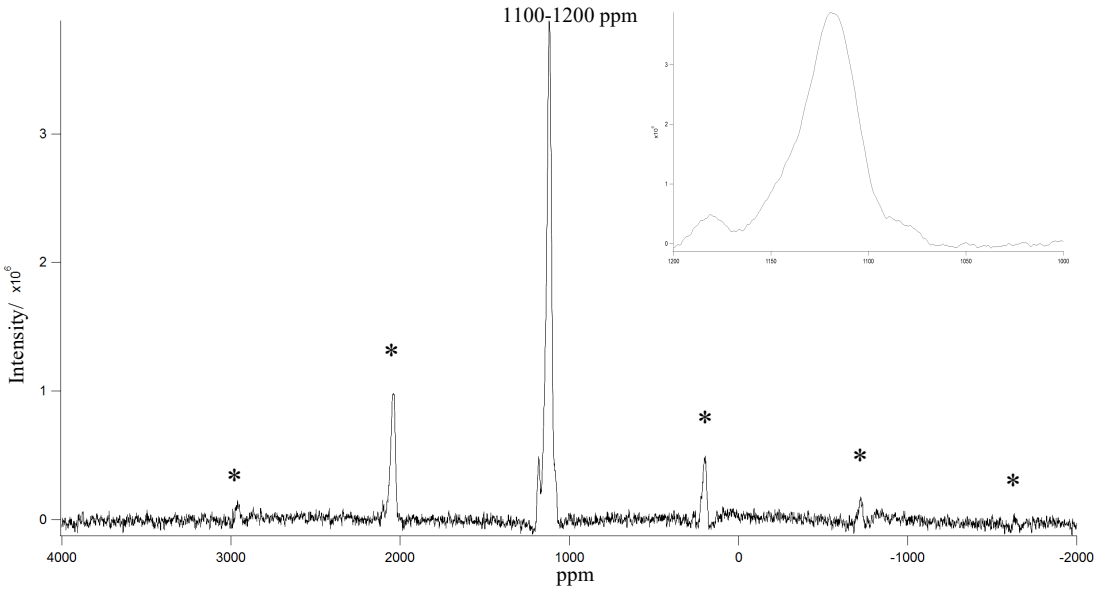

Figure 6-14 ^{17}O MAS NMR spin-echo experiment of dehydrated schoepite with 1.3mm rotor spinning at 50kHz after 100,000 scans with RF pulse lengths calibrated for the 'yl' oxygens. The rotational sidebands are separated by 50 kHz from the central band and each other. Inset shows the zoomed in spectra near the isotropic peak of 1115 ppm.

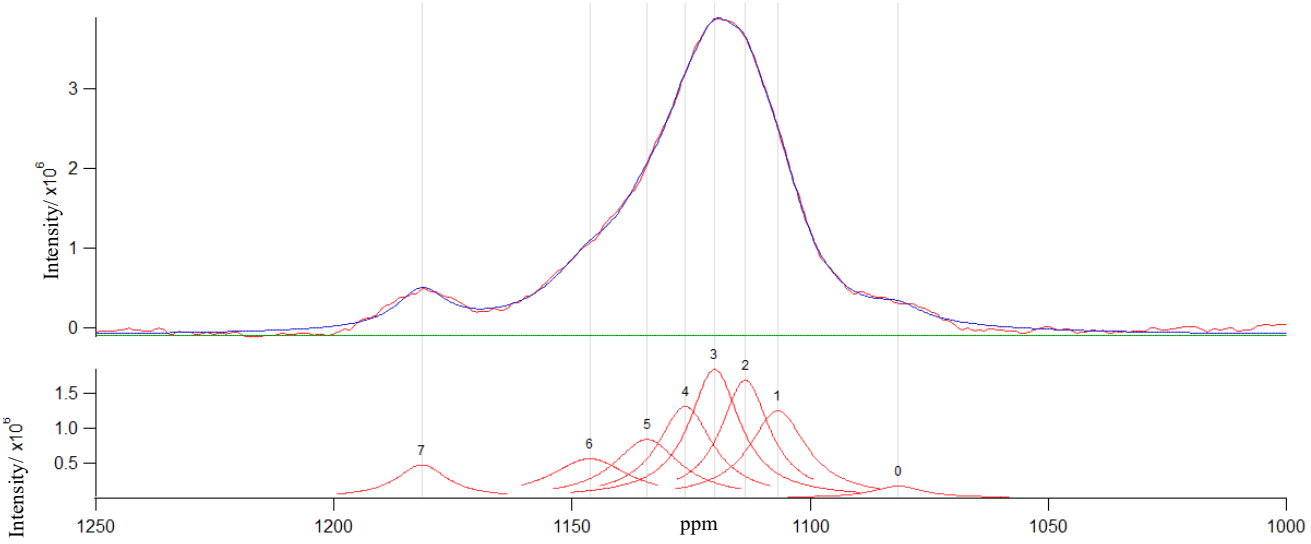

Figure 6-15 Deconvolution of the central band 'yl' oxygen into 8 peaks.

After deconvolution, the peaks was fitted into similar FWHM though some variation exists due to different neighbouring atoms resulting in different electric field gradient to be discussed later. A good match with the different bond lengths shown in Figure 6-13 were achieved and set up in the table below.

Table 6-1 Assignment of different positions for dehydrated schoepite

Peak	Position (ppm)	FWHM	Area	Corresponding Uranyl Bond Length / Å
0	1081.5 +/- 0.5	12 +/- 2	3.3×10^6	1.7368,1.7374
1	1106.8 +/- 0.8	15 +/- 1	2.9×10^7	1.7541,1.7566
2	1113.6 +/- 0.7	12 +/- 4	3.3×10^7	1.7660,1.7693
3	1120.1 +/- 0.9	13 +/- 5	3.7×10^7	1.7728,1.7784
4	1126.2 +/- 1.4	14 +/- 8	2.9×10^7	1.7840,1.7870
5	1134.3 +/- 2.3	17 +/- 8	2.2×10^7	1.7913,1.7934,1.7963
6	1146.3 +/- 1.3	20 +/- 2	1.8×10^7	1.8028, 1.8051
7	1181.6 +/- 0.2	13 +/- 1	9.6×10^6	1.8332

The structure of the centre band is characteristic of different uranyl oxygen environments. However, the uncertainty in peak assignment for deconvolving the broad central peak into six peaks is acknowledged. However it could be justified by the fact that the FWHM for the uranyl oxygens should be similar given the similarly low electric field gradients experienced by these uranyl oxygen atoms. In these convolutions, FWHM of individual peaks was restricted to between 10 and 20 ppm.

By considering older, previous examinations of the crystal structure of dehydrated schoepite from Taylor and co-workers (Taylor and Hurst, 1971; Taylor *et al.*, 1972), it can be seen that the oxygen assignments in their XRD refinement are less precise. It is reasonable to postulate that uranium dominates the X-ray scattering of these materials due to its far greater number of electrons compared to oxygen. This leads to the relatively weak diffraction contribution from oxygen being difficult to accurately resolve against the signal from uranium making refining

oxygen positions inaccurate. In that work, all the resulting uranyl-oxygen bond lengths from XRD were exactly the same at 1.792 Å. In addition, it is also important to get good crystallinity (which is often difficult) for accurate resolution with X- ray diffraction. Later workers (Finch and Hawthorne, 1998) refined the structure of schoepite with varying bond lengths and the curve fitting of the ^{17}O NMR spectra presented here is consistent with that structure. In the next section, (6.5 Discussion of NMR data), the influence of uranyl bond-lengths on chemical shifts is considered in greater detail.

6.5.2 Metaschoepite, $UO_3.1\text{-}2H_2O$

Dehydrated schoepite ($UO_3.H_2O$) or uranium (VI) oxide monohydrate is the most structurally simple of the group, with metaschoepite ($UO_3.1.5\text{-}2H_2O$) and schoepite ($UO_3.2H_2O$) containing more water molecules between their layers, to which the protons on the sheet hydrogen bond. In order to accommodate this, the structure of the sheet in metaschoepite is more complex than in dehydrated schoepite, with uranyl groups coordinating equatorially to five oxygen ions, which are not in all cases part of a hydroxide group. The structure of metaschoepite as refined by Weller *et al*. (2000) can be seen in Figure 2-10 and Figure 2-11, it should be noted that the structure contains no proton positions as these cannot be detected by X-ray diffraction in the presence of the uranium matrix. Decreased sensitivity of this technique to lighter elements also affects refinement of oxygen positions, with inconsistencies in their placement by Weller *et al*. and in several samples refined by Klingensmith *et al*.(Klingensmith *et al.*, 2007) A baseline- corrected spectrum of the metaschoepite under single pulse spectra was acquired with the 3.2 mm probe and shown in Figure 6-16. There were many sidebands and it was not possible to deconvolve the peaks with confidence, as integrations of all the sideband signals with the central peak has to be done before an effective deconvolution, which becomes a difficult task quantitatively when the sidebands are large. There is also an issue as the distributed signals into the many sidebands result in a lower signal to noise ratio at each of these sidebands, which brings large uncertainty into the calculations.

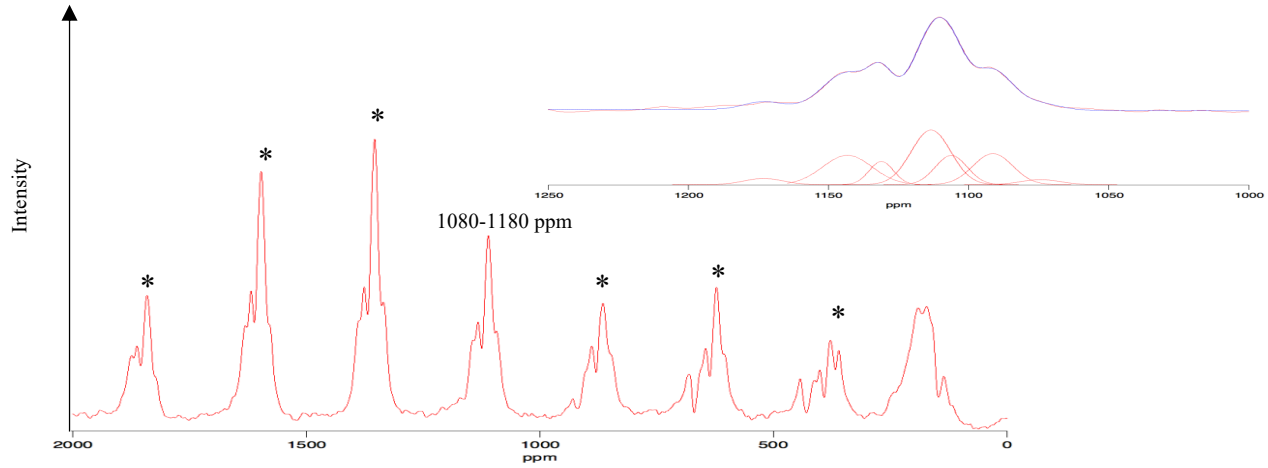

Figure 6-16 ^{17}O NMR spectroscopy of metaschoepite from baseline-corrected single pulse spectroscopy with 3.2mm rotor spinning at 18 kHz after accumulation of 10000000 scans. Inset shows the convolution of the central band for the uranyl oxygen.

From XRD refinement in literature, the distribution of uranyl bond lengths in metaschoepite is more complex than that in dehydrated schoepite. There are eight different bond lengths which have been segregated into seven bins of 0.01 Å.

Faced with the need for higher resolution to deconvolve the peak accurately, the experiment was repeated with a fast spinning probe that takes in a smaller mass of sample of about 8 mg against 35 mg. This is only usable for samples with strong signal.

With the fast spinning probe, the experiment was repeated with a spin echo setting that removes the phasing problem and allows us to deconvolve the spectrum without baseline-correction hence removing an additional step of data processing and its associated uncertainty.

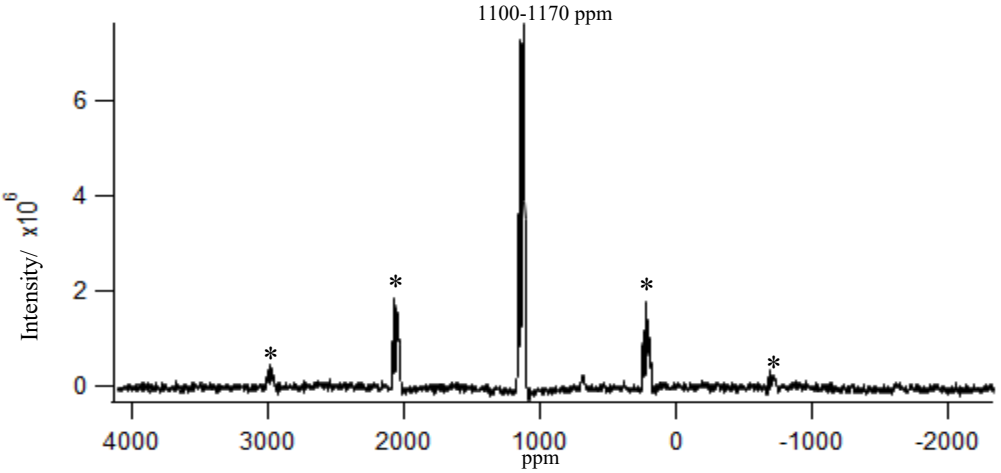

Figure 6-17 Spin echo spectrum of Metaschoepite with the fast spinning 1.3 mm probe, spinning at 50 kHz which shows a relatively flat baseline.

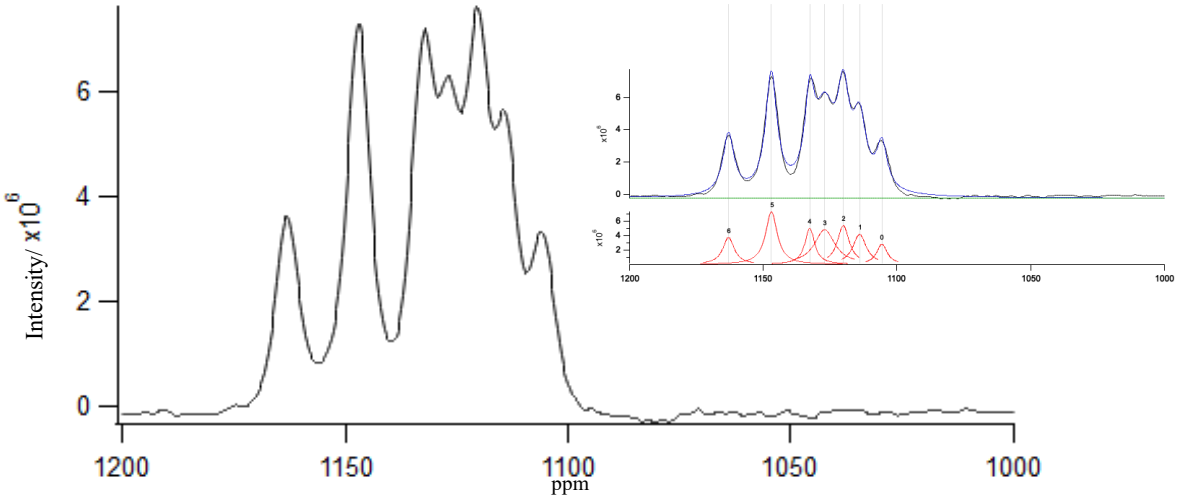

Figure 6-18 Deconvolution of the central band which corresponded to the uranyl oxygen for metaschoepite. Inset shows the convolution of the central band.

Contrasting Figure 6-18 with Figure 6-16, it can be seen that there is enhanced resolution in the peaks. There are two reasons for this; the fast spinning probe concentrates the spinning sidebands into the main peak which improves the sensitivity. Secondly, a longer pulse delay time which can allow more slowly relaxing resonances with narrower linewidths to contribute to each peak. A pulse delay time of 12 seconds was used for this experiment, which allows for the magnetisation to recover completely before sending in the next pulse. This optimized time was obtained by conducting a few experiments at different pulse delay as shown in Figure 6-19 in order to perform this experiment in a reasonable timely fashion. These are signal obtained after a fixed period of time rather than a fixed number of acquisitions. With the same number of acquisitions, the pulse delay of 12 s will undoubtedly give the same signal as the pulse delay of 36s.

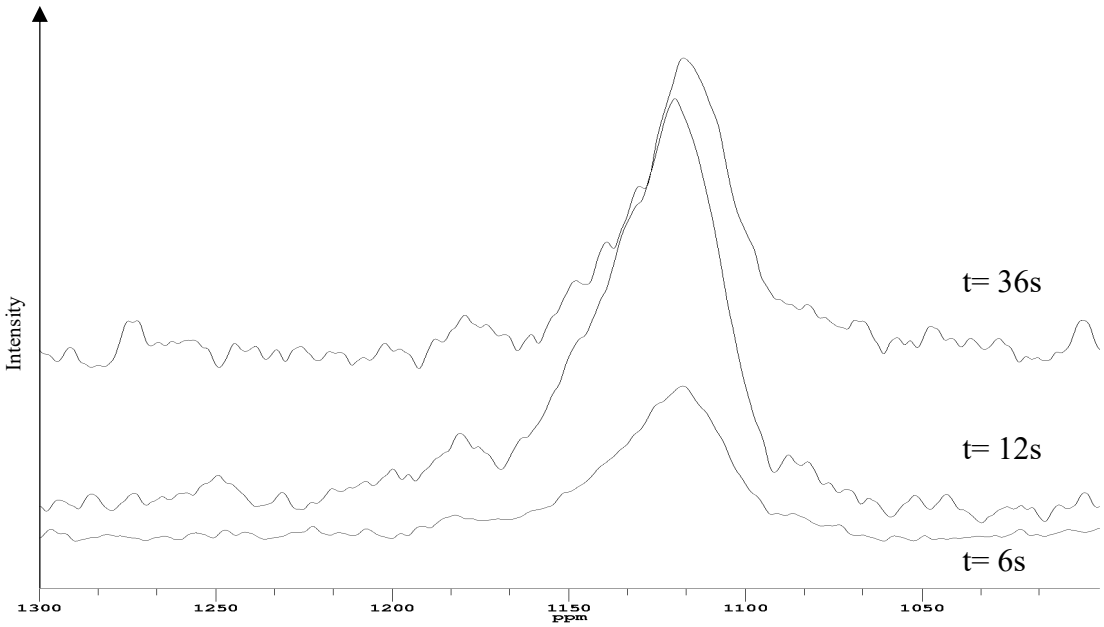

Figure 6-19a Testing for optimum pulse delay for complete dephasing of the magnetic field back to the z direction. The scale has been adjusted for the number of scans.

After deconvoluting the central peak on Figure 6-18, the data on the various peak positions was displayed below in Table 6-2. It appears that the direct fabrication of metaschoepite probably resulted in a more crystalline product than its production from the higher temperature dehydration of schoepite. The increase in crystallinity decreases the electric field gradient and chemical shift inhomogeneity, leading to Lorentzian lines that can be fitted with narrower FWHMs and hence lower uncertainties in peak position. There are eight uranyl bond lengths that can be fitted into seven peaks. Peak 3 has a larger area and peak width due to the presence of two uranyl bond lengths in that vicinity with very similar U-O distances of 1.7723 Å and 1.7767Å.

Table 6-2 Peak position and corresponding bond lengths from deconvolving the central band for metaschoepite.

Peak	Position (ppm)	FWHM	Area	Corresponding Uranyl Bond Length / Å
0	1105.6 +/- 0.1	4.8 +/- 0.3	2.2×10^7	1.7369
1	1113.9 +/- 0.1	5.8 +/- 0.3	3.7×10^7	1.7546
2	1120.2 +/- 0.1	6.3 +/- 0.4	5.9×10^7	1.7658
3	1127.1 +/- 0.2	9.2 +/- 0.7	7×10^7	1.7723,1.7767
4	1132.6 +/- 0.1	4.3 +/- 0.3	3.4×10^7	1.7843
5	1147 +/- 0.1	5.18 +/- 0.09	5.9×10^7	1.8092
6	1163 +/- 0.1	5.1 +/- 0.2	3.0×10^7	1.8198

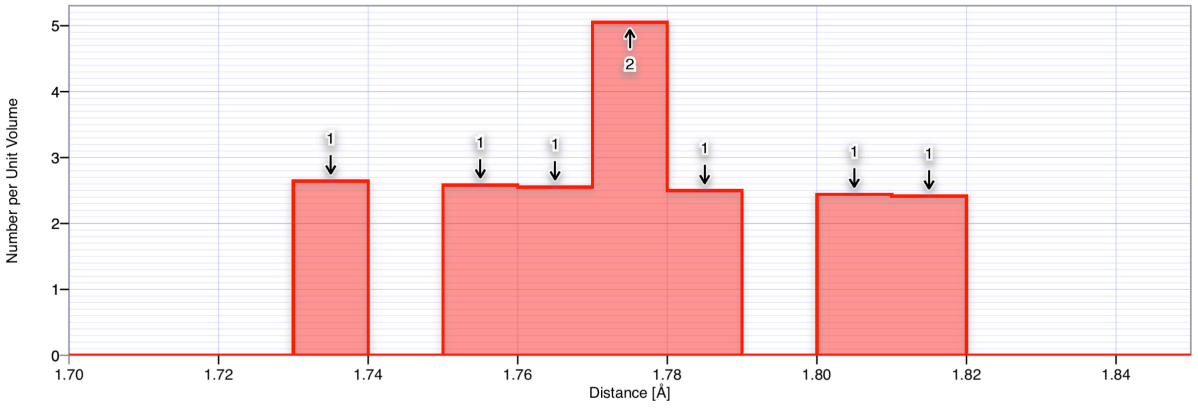

Figure 6-19b Histogram of the uranyl bond lengths in metaschoepite by *Weller* et al.

Strictly, the areas of the central band and the side bands should be integrated in order to get an accurate estimation of the peak areas due to each uranyl. It is conceivable that they might have slightly different anisotropy which will give us relatively different peak area for the central band, however this is not easily achievable because of the signal to noise ratio of the sidebands.

6.5.3 Studtite $UO_4.4(H_2O)$

Studtite is the only known peroxide mineral in the world. Its importance lies in it being formed readily and easily when uranium dioxide in spent nuclear fuel undergoes alpha radiolysis in water which is highly probably with groundwater ingress into a waste repository. Alpha radiolysis in water produces hydrogen peroxide which reacts with uranium dioxide rapidly to form studtite. The crystallographic structure of studtite has been shown earlier (see Figure 2-7 and Figure 2-9)

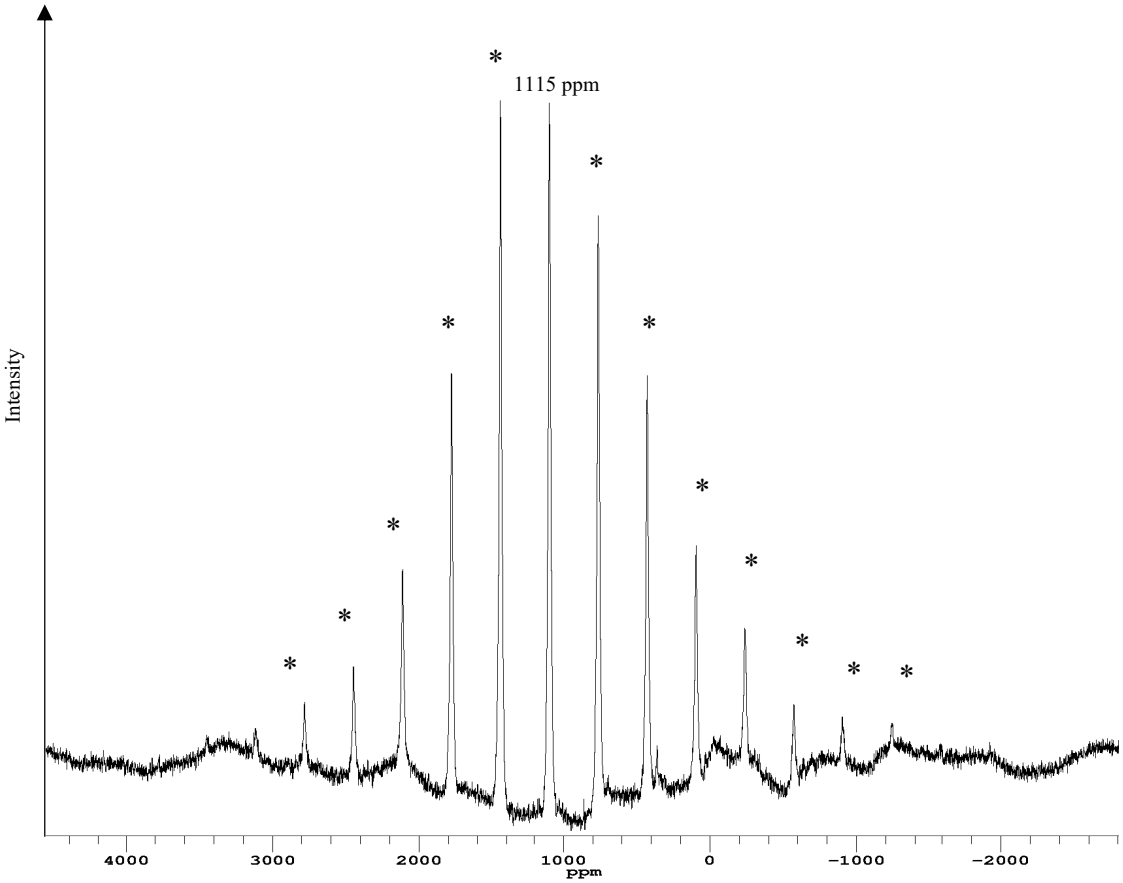

Figure 6-20 Single pulse NMR data of studtite spinning in a 3.2 mm rotor at 18kHz after 500, 000 scans at pulse delay of 0.1 s. The undulating baseline is due to the ringing of the probe for single pulse experiment. The large anisotropy causes the rotational echo to spread over 4000 ppm.

This spectrum was obtained from spinning at 18 kHz in the 3.2 mm probe. Despite the massive improvement from the 4.0 mm probe, there is still a problem with baseline correction. After the baseline correction, the central peak was found at 1115 ppm. Variable temperature

experiments were conducted on this setup which will be shown in the next chapter, Thermal evolution from Studtite $(UO_2)O_2(H_2O)_4$ to Metastudtite $(UO_2)O_2(H_2O)_2$. Briefly, ^{17}O NMR spectra between studtite and metastudtite were largely similar but a closer examination yielded a downfield chemical shift in the uranyl peak, which through this series of experiments here, represents an increase in the bond. As per the other minerals, the quality of the spectrum was improved by spinning it with the fast spinning probe and the better resolution and reduced uncertainty of the spectral parameters was noted.

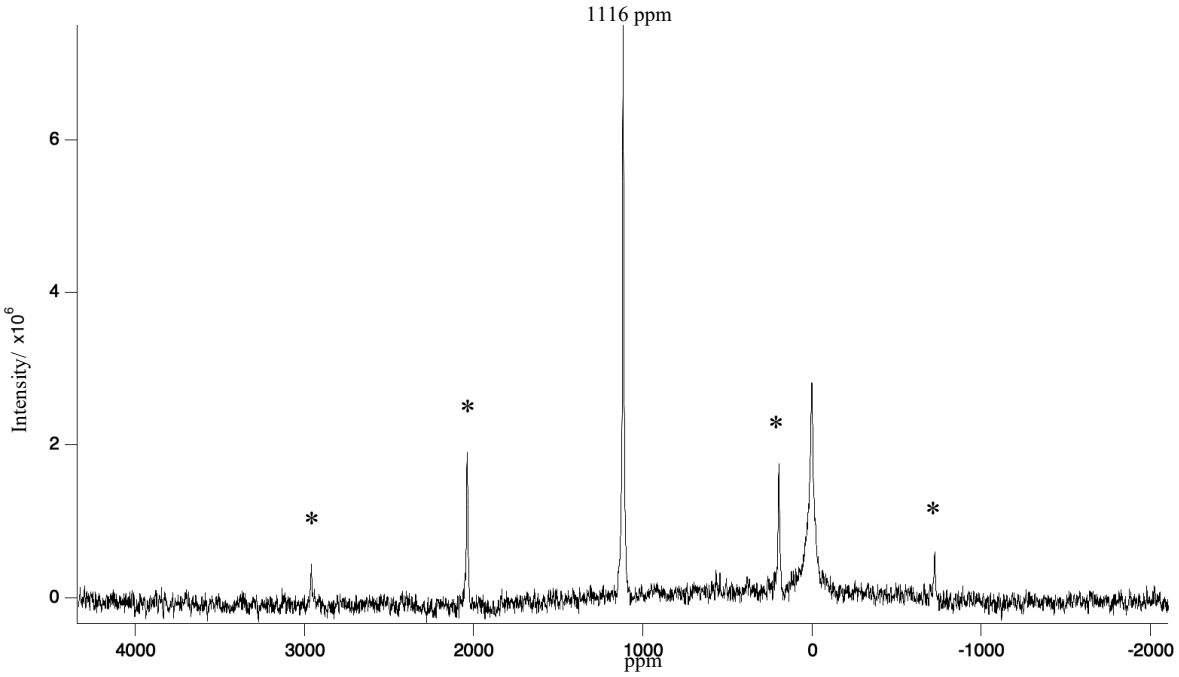

Figure 6-21 Spectrum obtained from fast spinning 1.3 mm probe after 13147 acquisition with a pulse delay of 6 seconds. The spin echo experiment was executed to obtain a relatively flat baseline.

With the improved baseline, the central peak was fitted, showing clearly that it was made up of one distinct peak fitted confidently with the Lorentzian profile and a very narrow FWHM of 9.4 ppm.

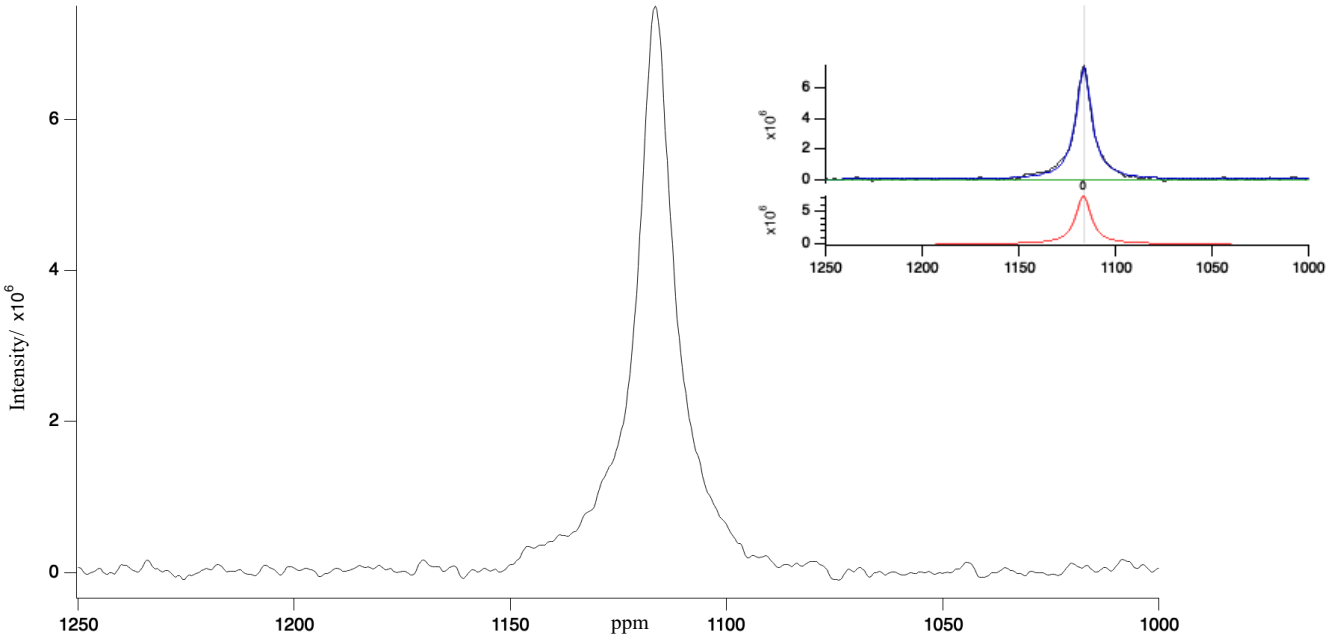

Figure 6-22 Convolution of the uranyl peak signal from studtite. Inset shows the convolution of the central band.

Table 6-3 Peak position and corresponding bond lengths from deconvolving the central band for studtite

Peak	**Position (ppm)**	**FWHM**	**Area**	**Corresponding Uranyl Bond Length / Å**
0	1116.4 +/- 0.02	9.4 +/0.1	1.1×10^8	1.7691

The position of this peak is determined very precisely with curve-fitting.

Besides this peak, it was noticed that the broad ^{17}O peak due to the bound water molecule in studtite. Calibration of 3.2 mm probe for ^{17}O was done with liquid water, with ^{17}O peak being at 0 ppm. One glaring difference between the bound water peak in studtite and liquid water peak lies in the FWHM, which is expected as the oxygen in liquid water are constantly tumbling is isotropic and the linewidth is determined by the T_1 lifetime of the spin-state (lifetime broadening due to quadrupolar relaxation mechanisms), whereas the bound waters are fixed in their orientations and small variations in hydrogen bonding or strain results in a distribution of isotropic quadrupolar and chemical shifts broadening the peak despite the averaging by magical angle spinning.

6.5.4 Becquerelite, $Ca[(UO_2)_6O_4(OH)_6].(H_2O)_8$

In the unit cell for becquerelite, there are six distinct uranium atoms with 12 distinct uranyl bond lengths, that can be arranged in bins of 0.007Å from each other. The large spread in oxygen bond lengths is due to the calcium ions which creates more distinct chemical environments and more unique bond lengths when compared with simpler hydrous uranyl minerals. This mineral composition was chosen due to the ubiquity of calcium in proposed repository groundwaters.

In a 3.2 mm spinning rotor at 18 kHz, the following spectrum was obtained which is more complicated than the previous examples of dehydrated schoepite, metaschoepite and studtite where the isotopic enrichment occurred only in the uranyl oxygens and bound water oxygens. A broad peak was observed at 150-250 ppm and this was an indication of the oxygen in the carbonate reactant, which underwent incident isotopic exchange, during the synthesis process. The resonance at 185 ppm(Clark, Newton, *et al*, 1995) is consistent with free carbonate/bicarbonate ions in solution whereas the other resonance at 225 ppm is consistent with carbonate ligands in the coordination sphere of the uranyl ion. Its sideband was detected at about 780 ppm (which correctly corresponds to a shift of $\frac{1}{18000} = 555\,ppm$). These were postulated to be artefacts from the synthesis process, where the compound was subjected to an oil bath to vaporize the excess carbonic acid but that was evidently not entirely successful.

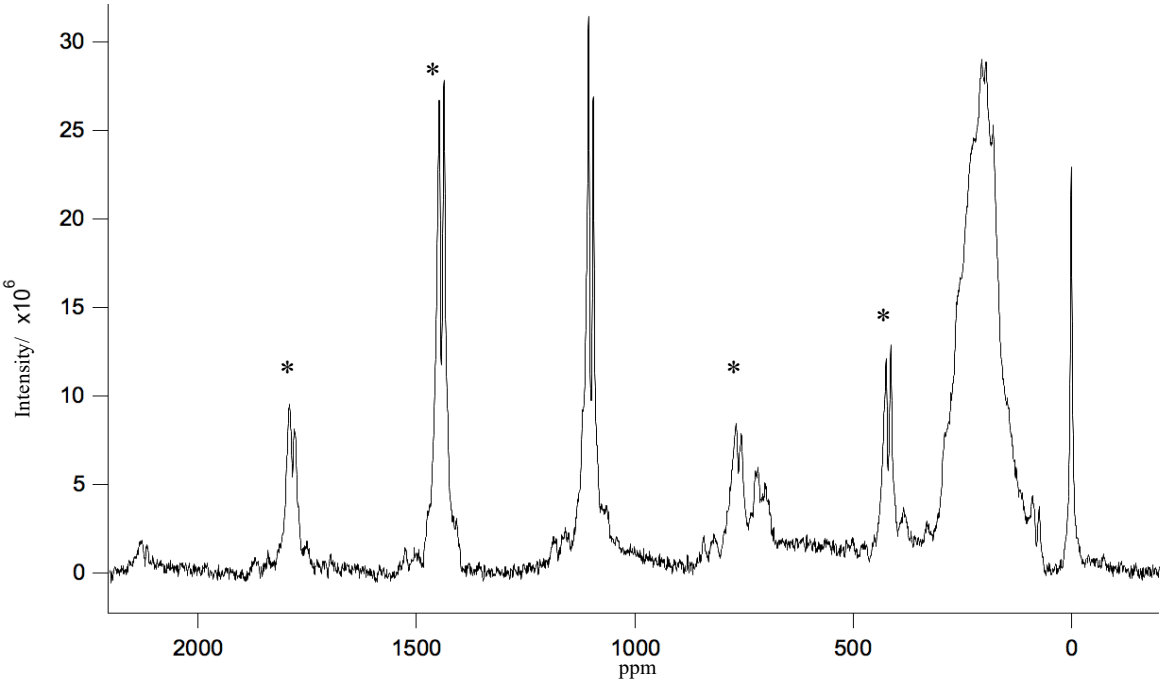

Figure 6-23 Baseline-corrected ^{17}O NMR spectrum from becquerelite spinning at 18 kHz after 500, 000 acquisition.

There were some problems encountered in attempting to deconvolve this. The large number of sidebands despite the moderately fast spinning speed results in the signal being spread out in these sidebands. This can be seen from Figure 6-25, where a peak at 1160 ppm was detectable in the fast spinning probe, but even so, it was indistinguishable in the first sideband. In addition to missing peaks, the rightmost peak is also difficult to resolve given the significant noise to signal ratio.

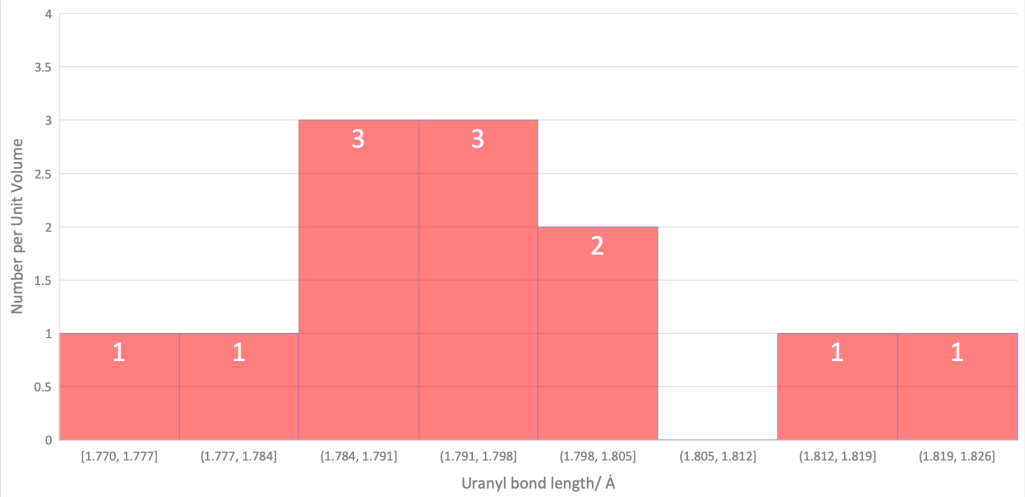

Figure 6-24 A histogram of the different uranyl bond lengths of Becquerelite as refined by Burns.

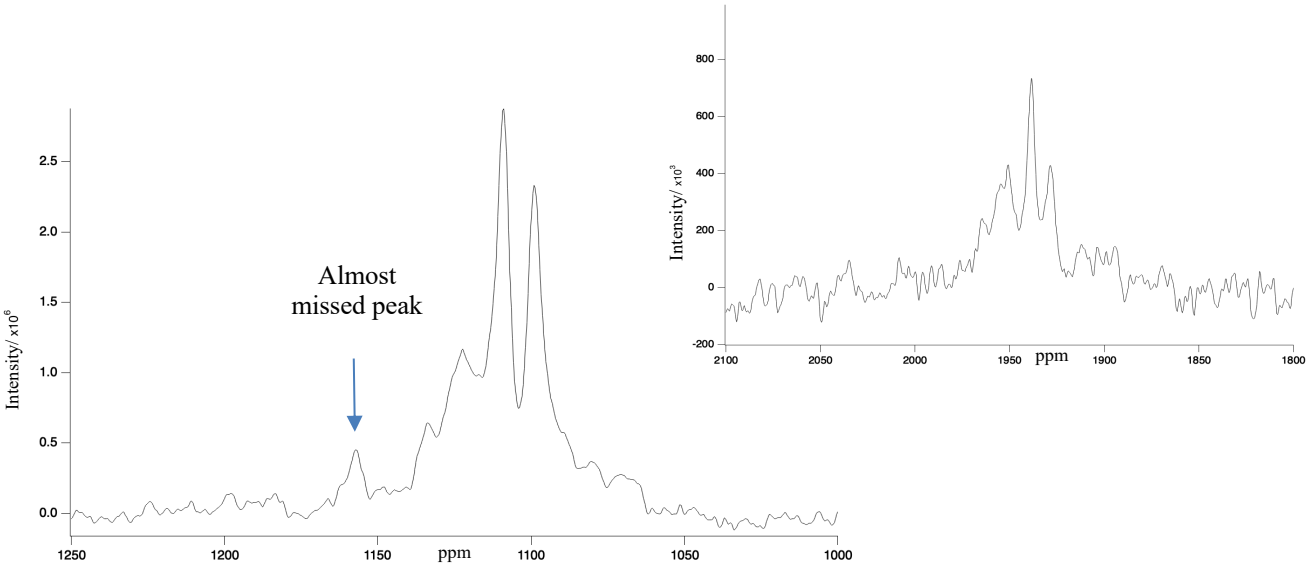

Figure 6-25 Peak at 1160 ppm (blue arrow) is a possible uranyl peak and can only be seen here with the fast spinning probe at 45kHz. Inset show the first sideband which looks similar but the corresponding peak at 2050 ppm is barely distinguishable, hence signal to noise ratio with a fast spinning probe is critical.

For quantitative comparison and to guide the curve fitting, the uranyl bond distances was placed into 0.007Å bins though it should be noted . Because of the easily missed peak, the first set of erroneous deconvolution was done without the 1060 ppm peak and shown in Figure 6-26.

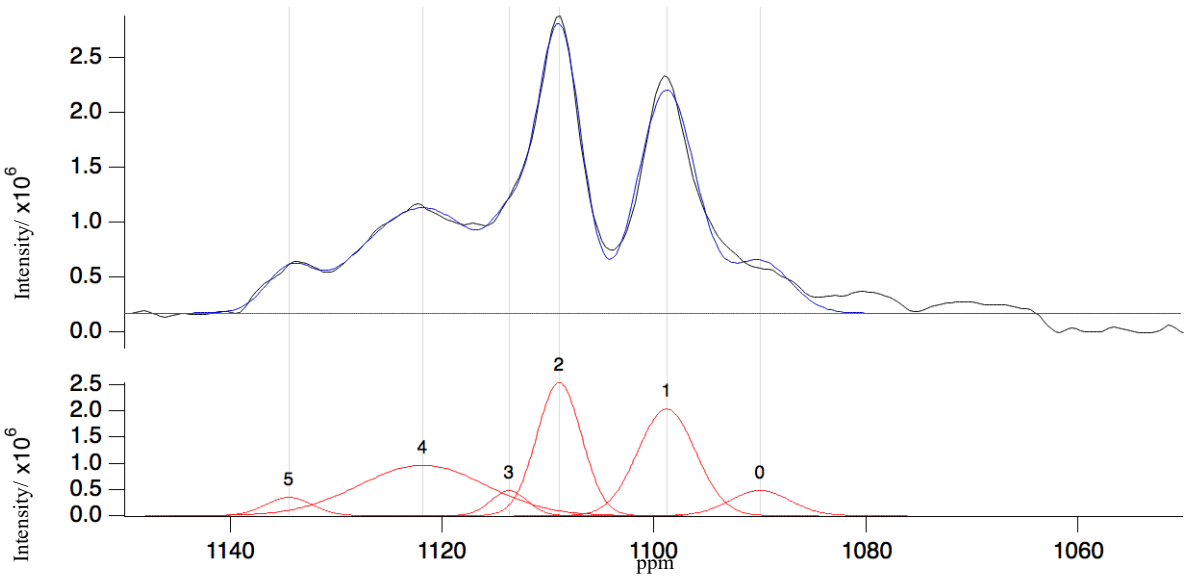

Figure 6-26 First deconvolution without the 1060 ppm peak.

Despite the relatively good fit, this is wrong as it did not include the 1160 ppm peak.

Factoring in the peak at 1160 ppm, the correct deconvolution is shown below.

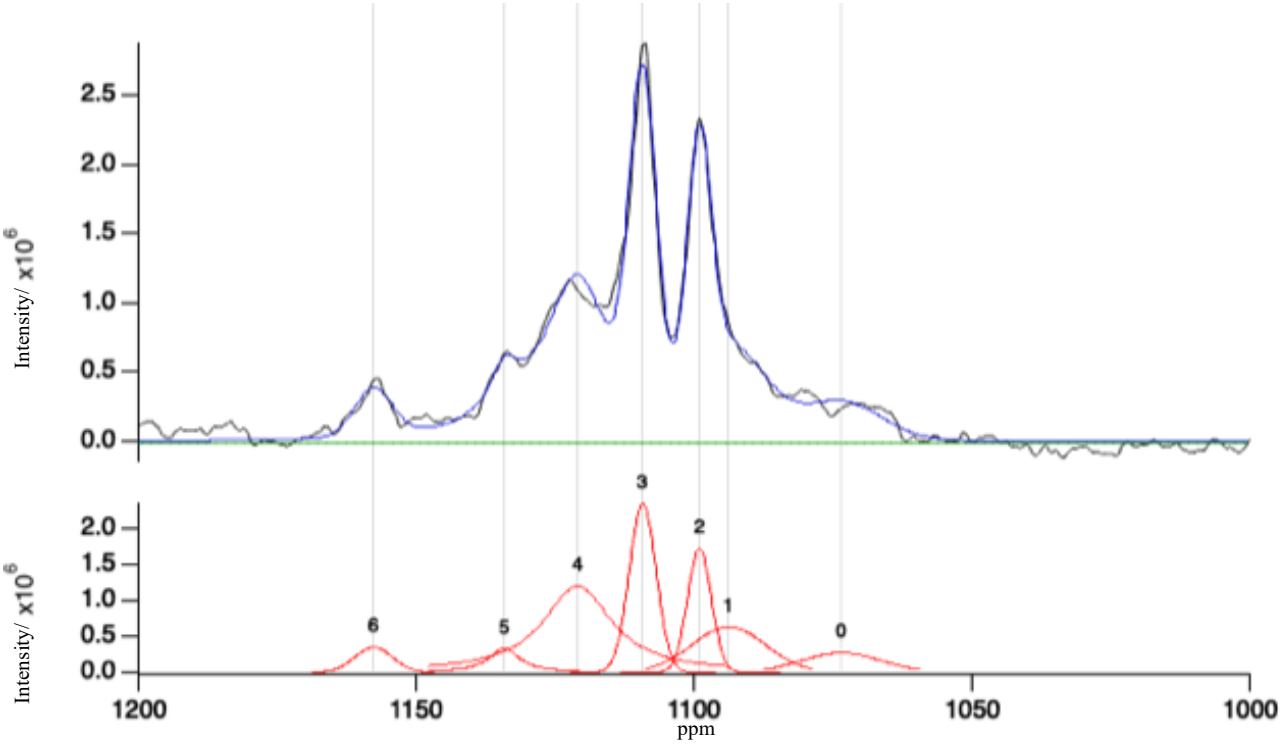

Figure 6-27 Deconvolution of the becquerelite isotropic peak from spectrum from the fast spinning probe at 45 kHz.

Table 6-4 Peak position and corresponding bond lengths from convolving the central band for Becquerelite in the previous figure.

Peak	Position (ppm)	FWHM	Area	Corresponding Uranyl Bond Length / Å
0	1073.4 +/- 0.6	16.7	4.7×10^6	1.7699
1	1093.7 +/- 0.8	9.3	1.0×10^7	1.7803
2	1099.0 +/- 0.1	5.0	9.2×10^6	1.7859, 1.7870, 1.7894
3	1109.2 +/- 0.1	5.6	1.4×10^7	1.7919, 1.7925, 1.7942,
4	1121 +/- 0.2	15	2.8×10^7	1.7993, 1.8036
5	1134.2 +/- 0.3	6.5	3.4×10^6	1.8151
6	1157.7+/- 0.2	7.9	2.9×10^6	1.8225

In the table above, it is clearly shown that most of the peaks are quite well resolved with FWHM of less than 20. Peak 0 has the highest uncertainty due to the noise, however its area is in proportional to the number of bond lengths when compared with the others. The only discrepancy in areas arise for peak 4, which seems to have share the area of peak 5. A longer acquisition time will give us slightly more confidence in this analysis. It appears that peak 0 may be made up of more than one peaks or representative of some slight variation in bond length for becquerelite.

Seeking a rationale for the broad peak of peak 0, calculations was executed in a bid to search for a plausible explanation where the sensitivity of the oxygen positions was investigated by DFT electronic structure calculations of becquerelite. Cell optimization was performed on the becquerelite crystal with the Broyden–Fletcher–Goldfarb–Shanno (BFGS) algorithm, which is an iterative method for unconstrained optimization. This algorithm allows us to relax the structure and test for convergence with the minimum energy for the atoms. This algorithm

yields a more intricate cell structure with more unique oxygen atoms than experimentally shown with XRD. There was a total of 120 different unique oxygen positions, with 48 unique uranyl positions as opposed to 12 unique uranyl position from XRD literature. This explains why peak 0 appear to be made up of more than one peak.

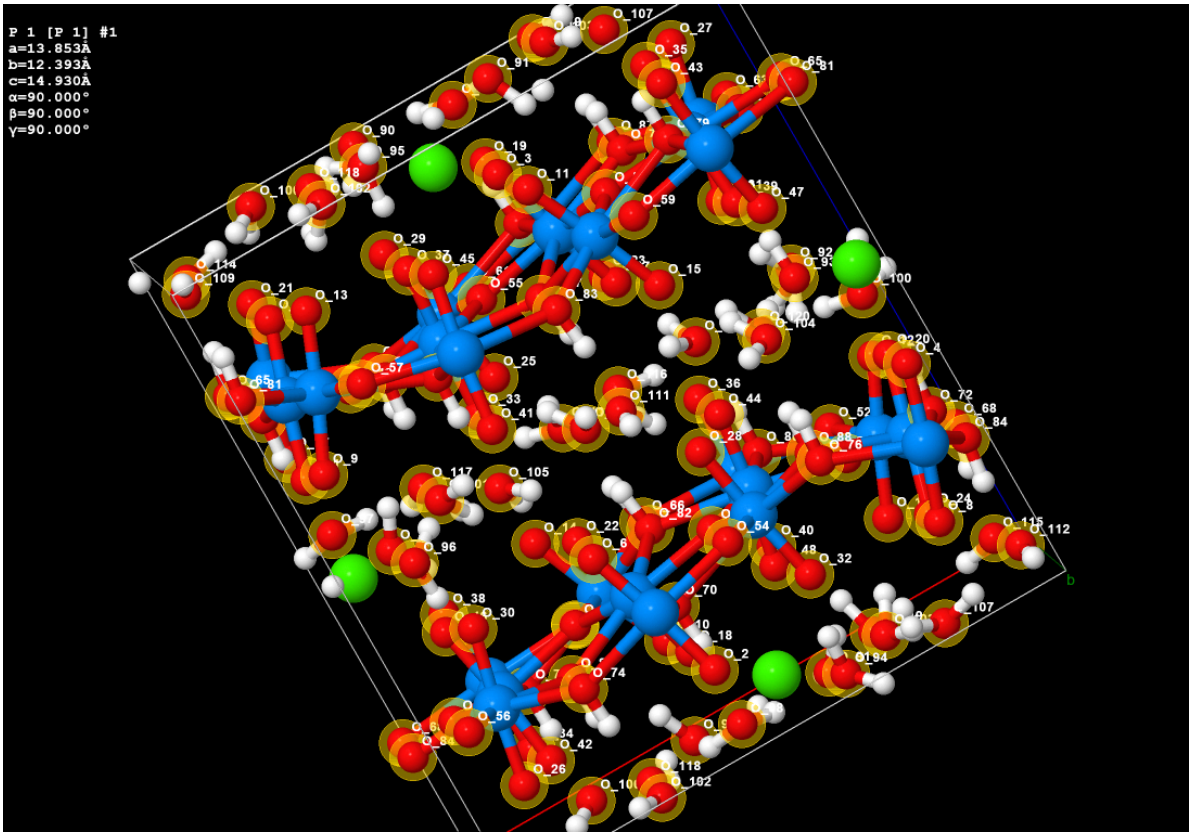

Figure 6-28 The uranyl oxygen as calculated by DFT calculations are shown to have vastly more chemical environments and a large range of chemical shifts.

6.5.5 Andersonite, $Na_2Ca[UO_2(CO_3)_3].x(H_2O)$

The trigonal $R\bar{3}m$ structure of Andersonite was discussed in 2.3.4 Andersonite, $Na_2Ca[UO_2(CO_3)_3].x(H2O)$ and Grimselite, $K_3Na(UO_2)(CO_3)_3 \cdot (H_2O)$ and its ^{17}O NMR spectra will be examined here. The signal was strong even with the signal distributed among spinning sidebands at 18 kHz. A spin echo spectrum of Andersonite was obtained, where the chemical shifts of the two distinct uranyl oxygen environments were detected. These are very sharply defined and can be used to determine the positions of the uranyl peak and the corresponding bond lengths.

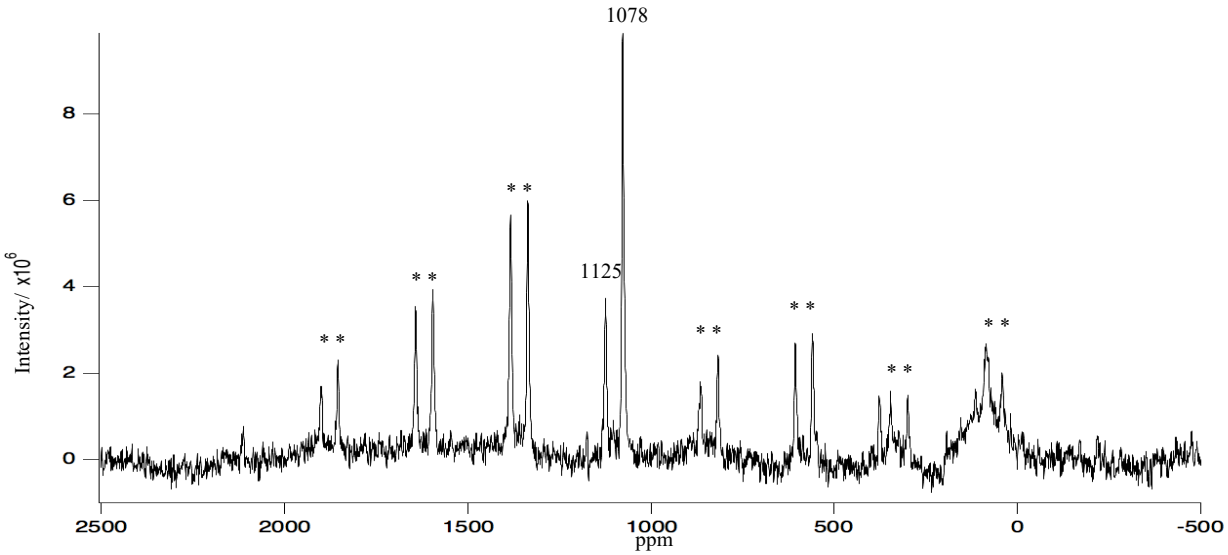

Figure 6-29 Single pulse spectrum of Andersonite as obtained at 18kHz with 3.2 mm rotor holding a sample of ~ 25 mg.

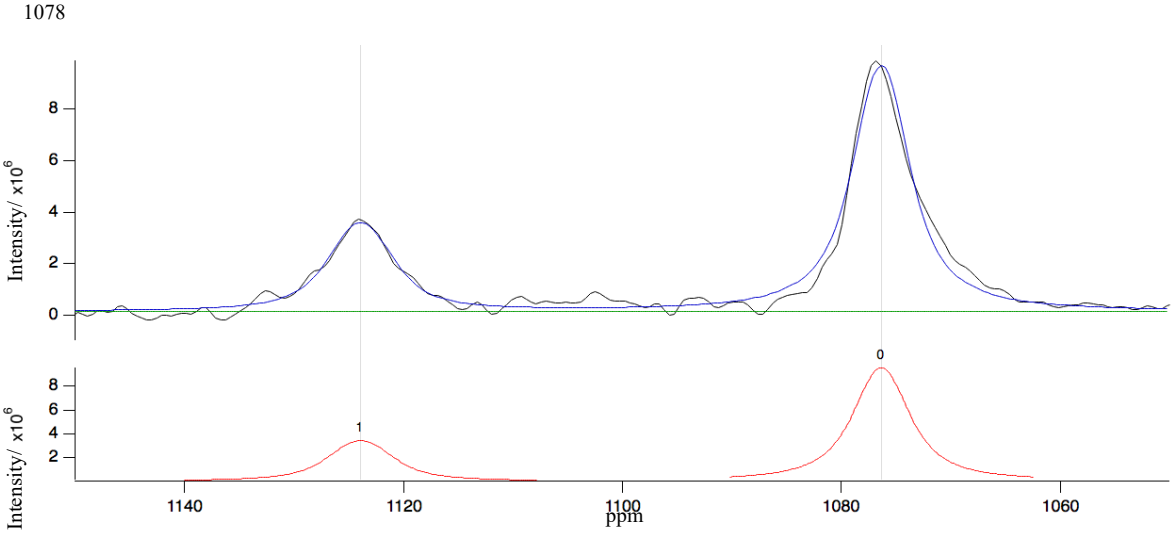

Figure 6-30 Centre band of Andersonite from 18 kHz single pulse MASNMR experiment.

The fast spinning spectrum of andersonite obtained with the 1.3 mm rotor, is shown in the figure below.

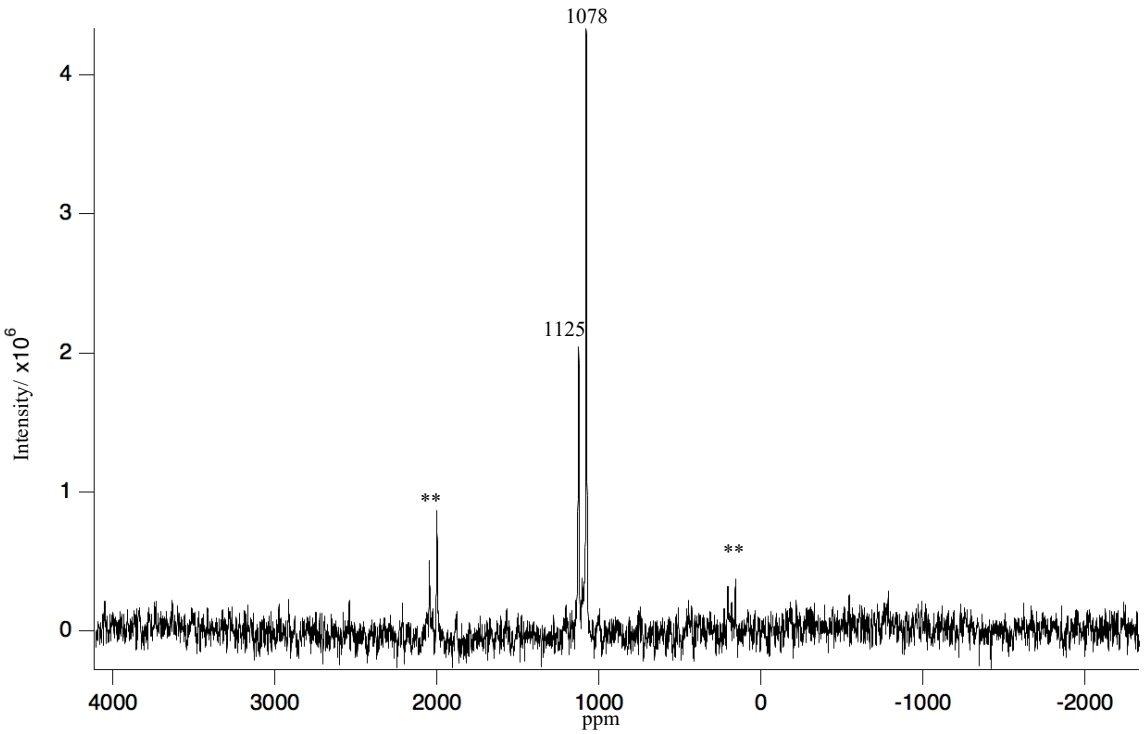

Figure 6-31 Spin echo experiment with 1.3 mm rotor spinning at 50kHz, where intensity of spinning sidebands is concentrated in the centre band.

Due to the high spinning speed, the sidebands are separated from the centre band by about 1000 ppm. This is reasonable as the spinning speed is 50 kHz and the resonant frequency of ^{17}O under a 9.39 T magnet is 54 MHz, and the ratio of these two values is about 1000 parts per million.

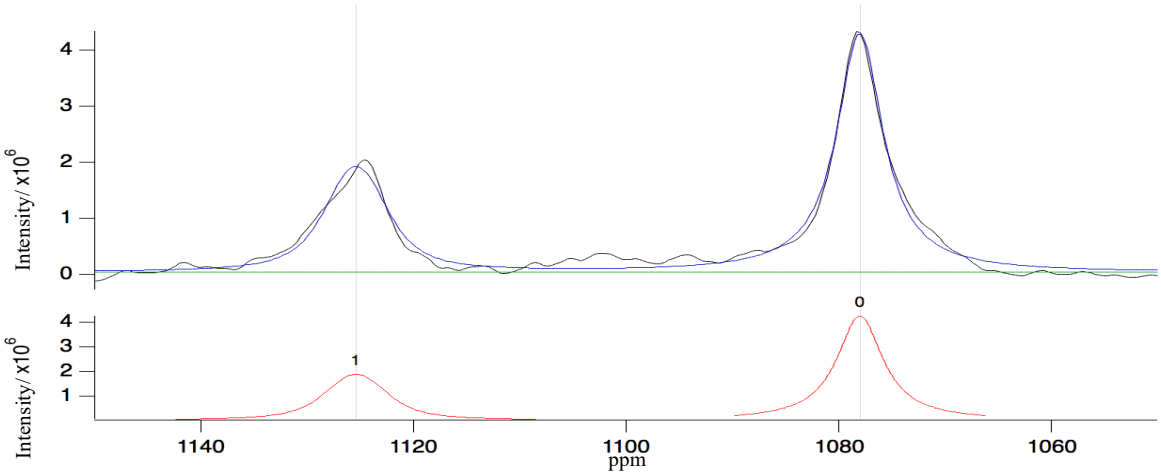

Figure 6-32 Deconvolution of the central peak of spin echo experiment for Andersonite.

Two peaks were fitted at 1076.4 and 1123.9 ppm on the spectrum obtained with the 3.2 mm probe (18 kHz spinning) but the same two peaks were obtained at 1077.5 and 1124.8 ppm at 50 kHz in the 1.3 mm probe. This is most likely largely due to the baseline correction algorithm which introduces a small error in phasing in the slower spinning case. This is why spin echo experiments were utilized instead of single pulse experiments. There could also be the case that spinning at higher speed with the smaller probe introduces greater sample temperature resulting in differences observed.

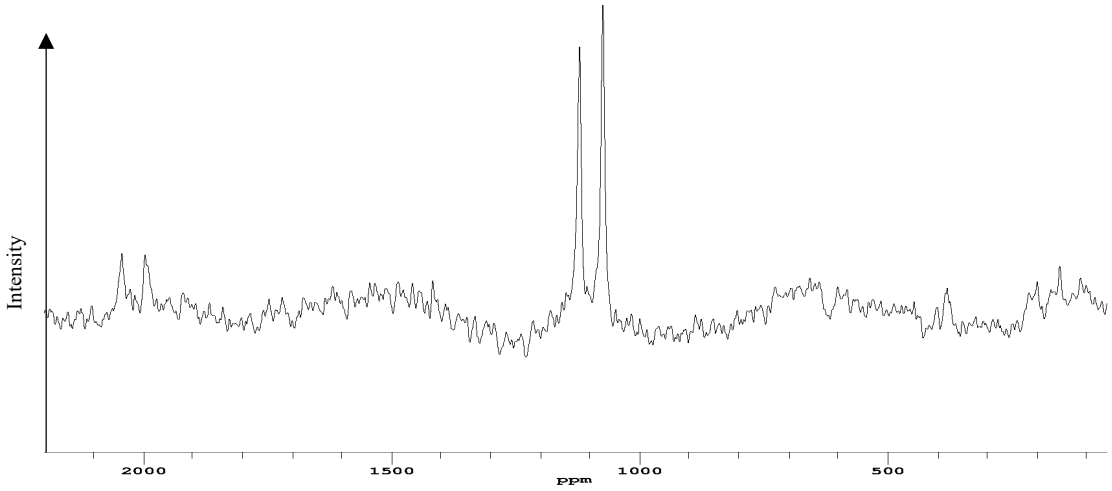

Figure 6-33a Undulating baseline due to ringing from a single pulse experiment, which need to be baseline corrected.

Another possibility might be due to the magnet decaying very slowly over time, at ~ 0.5 ppm per month but experiments runs for 4-5 days because of the low isotopic abundance of ^{17}O. Hence, after referencing, the true reading for the two uranyl peaks are 1077.5 and 1124.8 ppm. Referencing before and after an experiment is important for chemical accuracy at the <1 ppm level.

It is interesting to see that the ratio of the two peaks are roughly the same in a single pulse experiment at Figure 6-33 but they are markedly different in a spin echo experiment. The spin echo experiment is not necessarily quantitative as it depends on the dephasing time of the oxygen nuclei. Since there are two different 'yl' oxygen of different bond lengths at each side of the uranium atom in this case, the dephasing time is different and can be seen from this experiment.

For a quantitative assessment, both nuclei must have the same dephasing time (T_2) and all the sidebands of the spin echo experiment must be summed up. Nonetheless, the peak position is accurate.

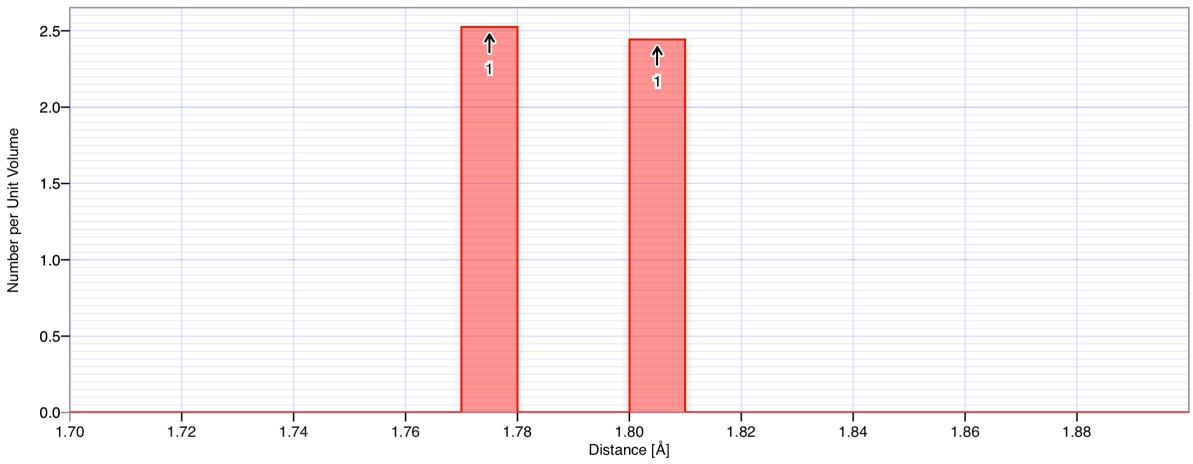

Figure 6-33b Histogram of the uranyl bond lengths in andersonite by *Coda* et al.

Table 6-5 Peak position and corresponding bond lengths from deconvolving the central band for Andersonite. Take note that this is not quantitative.

Peak	Position (ppm)	FWHM	Area	Corresponding Uranyl Bond Length / Å
0	1078.0 +/- 0.1	5.3 +/- 0.1	3.6×10^7	1.776
1	1125.3 +/- 0.1	6.4 +/- 0.3	2.0×10^7	1.808

6.5.6 Grimselite, $K_3Na(UO_2)(CO_3)_3 \bullet (H_2O)$

Despite the synthesized Grimselite not being successful from Raman and emission spectroscopy, it was analysed under ^{17}O NMR with the 3.2 mm probe under the single pulse setting in an attempt to identify if some small amount might be synthesized and oxygen might have been taken into these uranyl bonds formed during the synthesis.

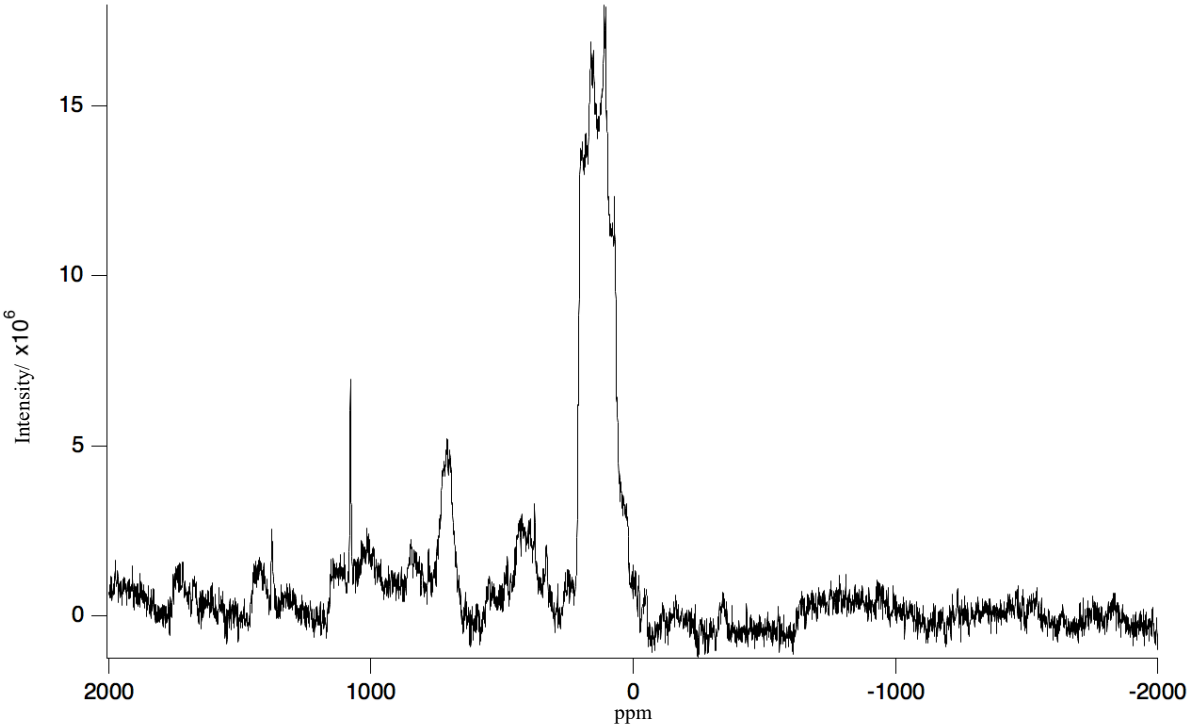

Figure 6-34 Single pulse ^{17}O NMR spectrum of grimselite with a 3.2 mm probe. A small uranyl peak is detected.

One sharply defined uranyl ^{17}O signal was observed, which implies that there was an exchange in the heavier ^{17}O atoms with the uranyl oxygen atoms. This implies that a small amount of grimselite or another uranyl containing mineral was formed. As the area of this is much smaller when compared with the other ^{17}O peaks, where the bulk signal seems to come from oxygen positions from carbonate ions due to incidental isotopic enrichment.

Since the synthesis involved the equation below

$$2\ UO_2(NO_3)_{2\,(aq)} + 3\ K_2(CO_3)_{(aq)} + Na_2(CO_3)_{(aq)} + 2CO_3^{2-} \rightarrow 2\ K_3Na(UO_2)(CO_3)_3 \bullet (H2O)_{(s)} + 4NO_3^-{}_{(aq)}$$

Equation 6—1

It is apparent that the broad carbonate signal comes from three main carbonate groups of potassium carbonates, sodium carbonates and Grimselite. With the fast spinning probe, it was

initially thought there was 2 uranyl peaks but it turned out to be the rotational sidebands of the oxygen in bound carbonate. This demonstrated that the oxygen in these bound carbonates has a larger anisotropy that spreads further than oxygen in free carbonates. The large anisotropy due to the large influence of the uranium atom might be explained by the synthesis of Grimselite (albeit in small amounts) or an intermediate uranium secondary phase was produced.

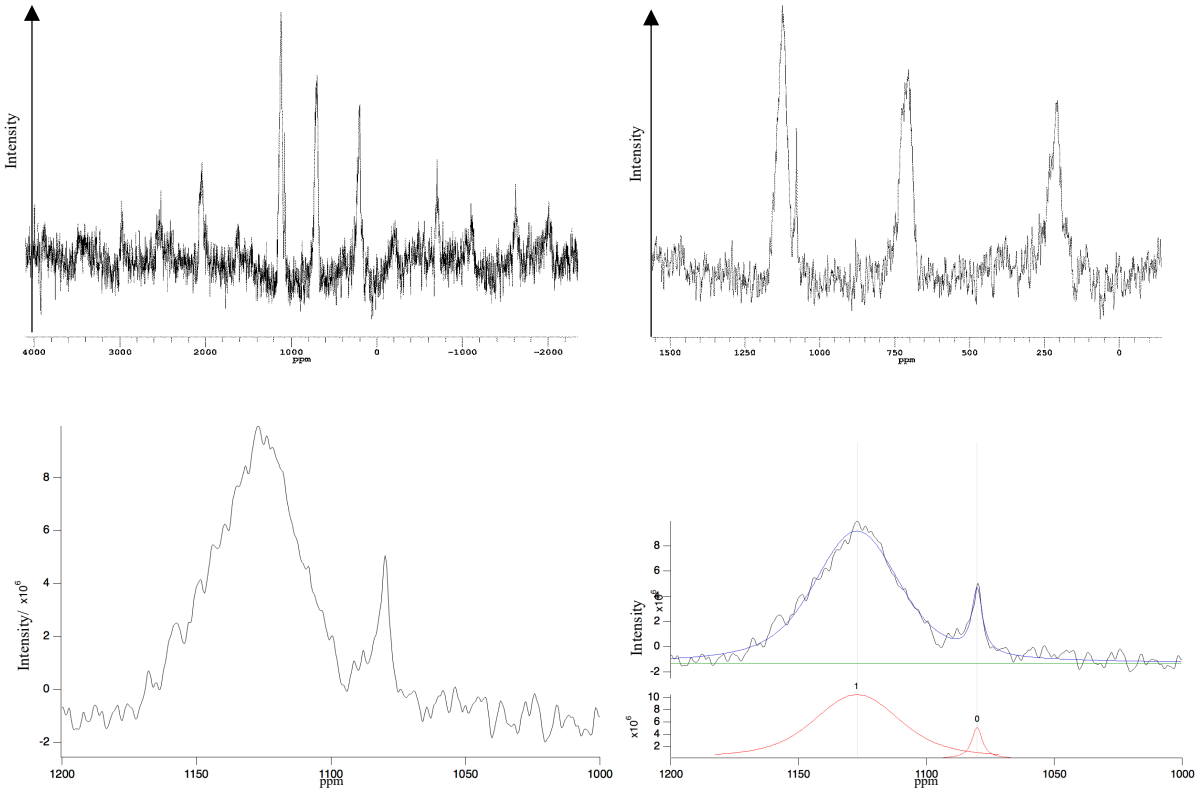

Figure 6-35 Resolution of the single uranyl peak in Grimselite overlaid with the sharp rotational sideband of carbonate.

From Figure 6-35, two peaks were obtained with shifts of 1080 ppm and 1127 ppm. The ratio of the area of the primary peak to the small secondary peak is more than an order of a magnitude. It might be enticing to conclude that there are two uranyl peaks. However, from the uranyl peak's symmetrical and sharp shape (implying a small electric field gradient) and the 3.2 mm single pulse spectrum, there was only one uranyl peak at 1080 ppm. Without a proper understanding of the structure and multiple experiments, the conclusion will be misguided. The peak at 1127 ppm is a spinning sideband from the carbonate peak.

Despite the fact that there is only one unique uranyl bond length from XRD of Grimselite, there is possibility of a secondary peak here due to a phenomenon observed in natural Grimselite (Plášil *et al.*, 2012), where additional Na substitution is $(K_{2.43}Na_{0.57})_3Na[(UO_2)(CO_3)_3](H_2O)$

however the conclusion of this set of experiments (see 6.7.2 Uranyl bond length and corresponding ^{17}O chemical shift) implies that a chemical shift of 70 to 150 ppm for 0.1 Å meant that the FWHM for the peak 1 (37.6 ppm) will mean a spread of 0.05 to 0.1 Å for the peak 1 which is considered to be too wide a range for a single bond. The large numbers of uniquely orientated water molecules will result in large range of chemical shifts that span over 200 ppm in Grimselite, whose rotational sideband can be observed near the small uranyl isotopic peak at 1080 ppm.

Table 6-8 Peak position and corresponding bond lengths from deconvolving the central band for Grimselite.

Peak	Position (ppm)	FWHM	Area	Corresponding Uranyl Bond Length / Å
0	1080.1 +/- 0.1	4.1 +/- 0.3	3.2×10^7	1.7832
1	1126.8 +/- 0.1	37.6 +/- 0.5	6.6×10^8	Sideband of bound oxygen in carbonate group

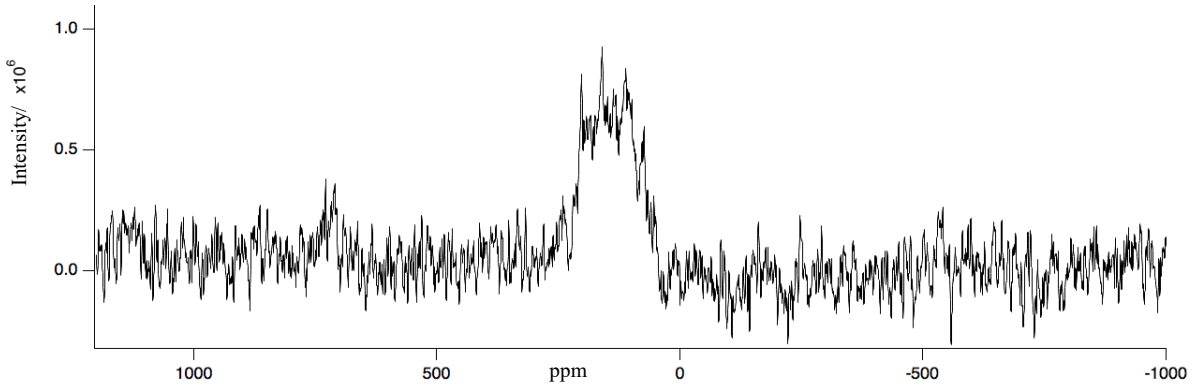

Figure 6-36 This peak belonged to the oxygen to the bound water but it spread over 200 ppm implying a large difference in chemical environments.

6.6 Density Functional Theory calculations of mineral structures

6.6.1 Cell- Optimization

Due to the availability of instruments, synthesized materials were verified with the use of Raman and emission spectroscopy as shown in 2.4 Synthesis procedure. Crystallographic information file (CIF) of the minerals were obtained from online literature and transformed into CELL format for the CASTEP density functional code. Prior to magnetic resonance calculations, all atoms in the structure were relaxed to a stress-zero configuration which is known as a geometrically optimised structure . To optimise the structure, Broyden–Fletcher–Goldfarb–Shanno (BFGS) algorithm was employed. It is a module in the CASTEP code that performs cell optimization by systematically moving atoms through many iterations to find the minimum energy or the stress-zero point which is important for CASTEP NMR calculations (*Task: Magres*) by the Gauge Including Projector-Augmented Wave (GIPAW) method.

A typical geometry optimisation parameter set is attached in the Appendix 3: Studtite Geometric Optimisation Parameters. Here, the structure was optimized after a maximum number of geometric iterations of 400 steps (*geom_max_iter = 400*) or a convergence to energies below 0.01 eV/ atom (*basis_precision : extreme*), whichever arrives first. The resulting report could not be attached to the appendix as it is 600 pages long, but even for the relatively simpler structure of studtite, $UO_4.4H_2O$, this calculation took about a day to complete (56, 000 s) and had a 24 GB peak memory usage. For the more complicated structures, cell optimization often cannot be achieved as the geometric optimisation can run for months with available computing capability

6.6.2 k- points selection

For density functional theory, an accurate calculation requires the Brillouin zone to be sampled as an infinite continuum. However, given that DFT calculations are computational in nature, it is not possible to consider an infinite set of points in *k*-space for the Brillouin zone sampling. Likewise, it is not possible to consider an arbitrarily large finite number of *k*-points, given the limitations of computational resources and time.

Since this ideal case is not achievable, it is necessary to choose a set of *k*-points for Brillouin zone sampling in an expedient manner. To achieve this, the method used is the Monkhorst–

Pack grid, where a sampling density, or a maximum separation of *k*-points can be specified in order to create a fair distribution of *k*-points at the desired density and separation.

Furthermore, for the exchange-correlation functionals considered in this investigation, the computational cost increases linearly with the number of *k*-points sampled, hence the smallest possible number of k- points will aid calculation efficiency, especially of systems with many atoms. For selection of k points in the fastest way to ensure convergence, the fastest task "Single Point" was used and the CASTEP simulations was run at the smallest k points where the energy converges. For easier representation, k matrix was given in terms of k points (i.e. (3 3 3) was represented as 14 k-points and (4 4 4) 32 k-points). The becquerelite simulation manage to converge barely as the change in corrected energy converges to 0 eV.

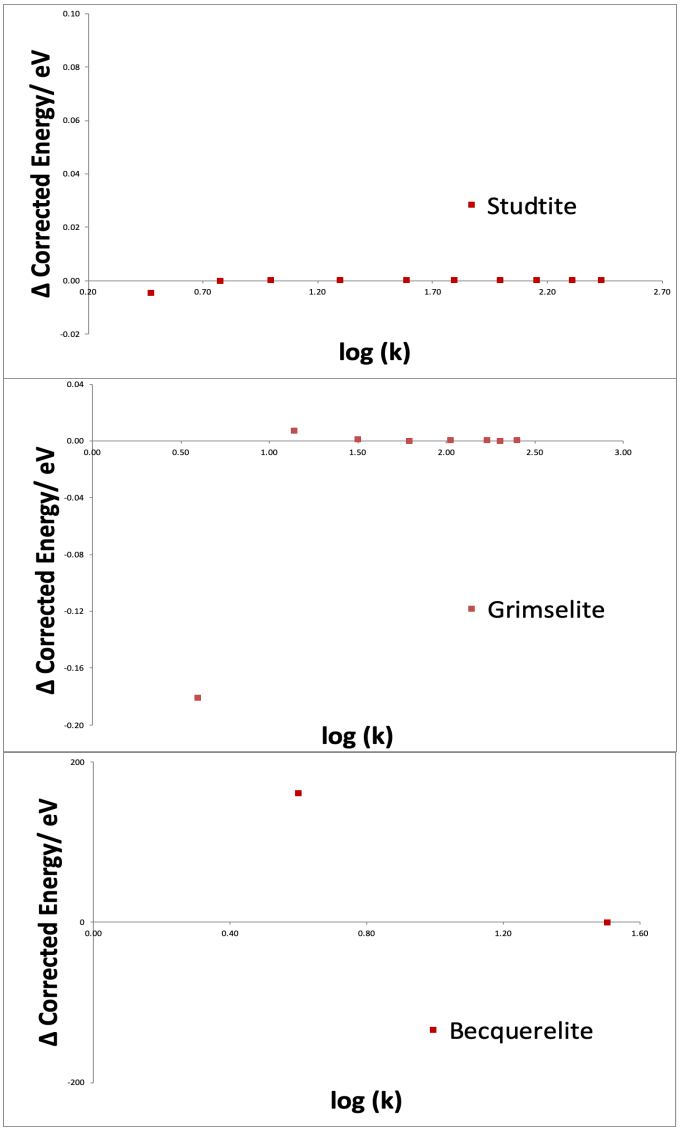

Figure 6-37 k- point convergence for the different minerals.

6.6.3 Magnetic Resonance (MagRes) Results

NMR calculations were conducted as a magnetic resonance (Magres) task in the CASTEP code with an additional zero order relativistic approach (ZORA) parameter (for uranium). An example is attached in the Appendix 4: Studtite Magres Parameters. Due to the large computing requirements and the short period of time before the end of the PhD program, only 2 minerals were calculated, these were studtite and becquerelite which are presented here with the MagRes viewer.

6.6.3.1 Studtite simulation

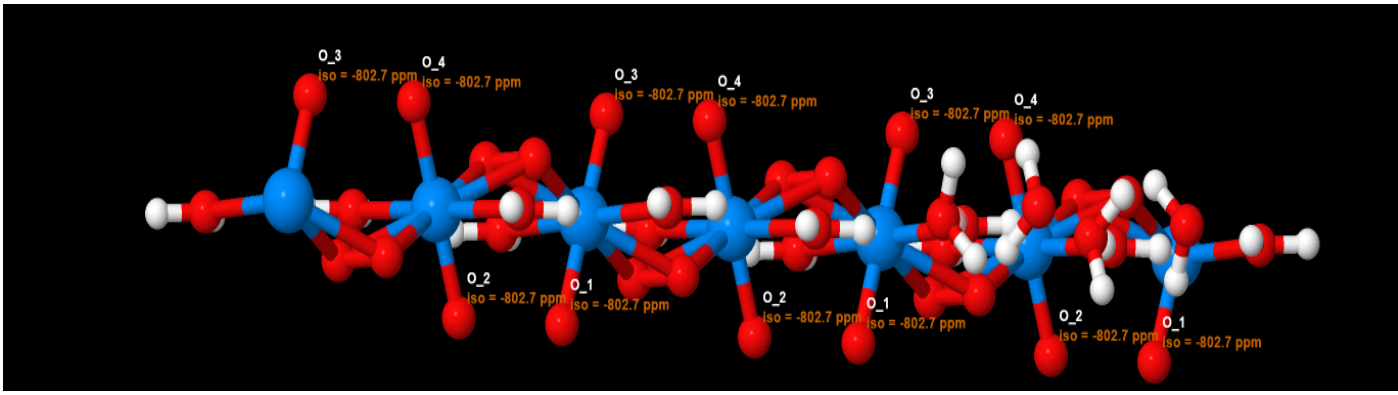

Figure 6-38 Calculation of chemical shift of studtite with CASTEP.

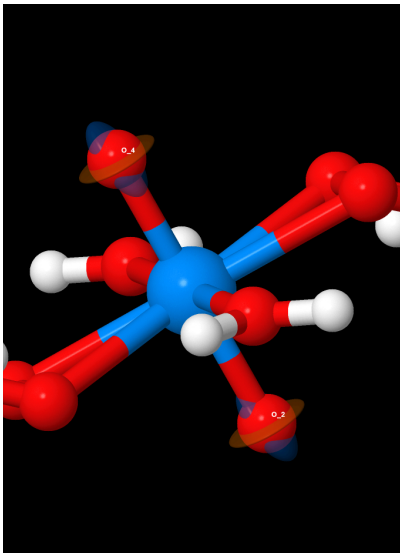

An interesting observation for all the uranyl oxygen atom is that they have a large magnetic shielding component (orange), compared to the other oxygen atoms. This is perpendicular to the small electric field gradients, V_{zz} (blue) that lie along the 'yl' direction. Since all the uranium atoms are shielded uniformly from this simulations, this help to explain the high-intensity peak observed experimentally.

Figure 6-39 The orange shaded region corresponds to the magnetic shielding component and the blue shaded region corresponding to the electric field gradient, V_{zz}.

An interesting observation was observed. Since the electric field gradient is small, the expected anisotropy should be small (Celebre, 2007), however this was not the case as experimentally, the spinning side bands spread out over a few thousand ppm.

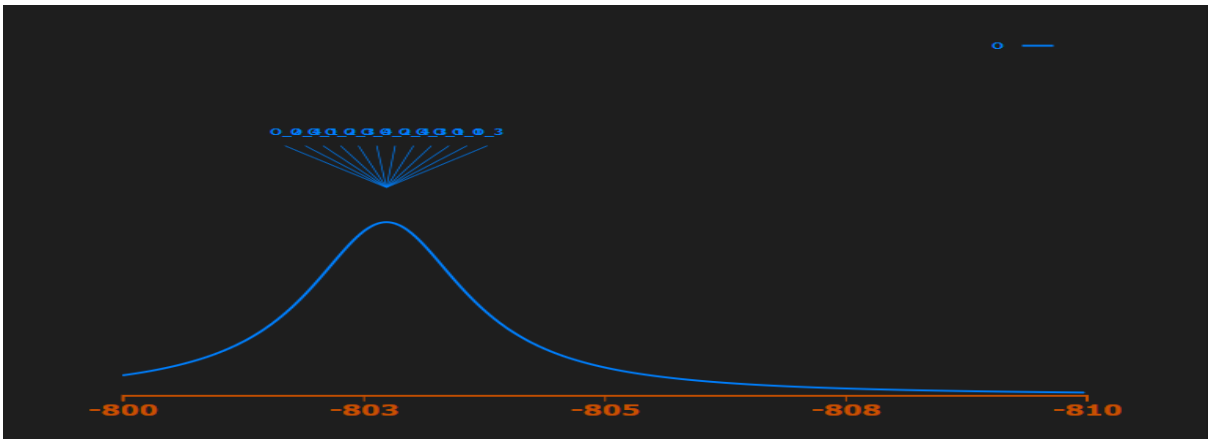

Figure 6-40 Simulation data shows the convergence of isotropic magnetic shielding at -802.7 ppm for all uranyl oxygens.

Calculation and theory concur for the uranyl oxygen, as the experimentally observed chemical shift of the uranyl bond at 1116.4 ± 9.4 ppm, shown in Figure 6-21 is a sharp and narrow peak. This small FWHM is in line with calculations shown in Figure 6-40 which shows that all uranyl oxygen atoms experience uniform magnetic shielding at -802.7 ppm.

Chemical shift, δ is related to magnetic shielding, σ (Widdifield and Schurko, 2008)

$$\delta \equiv \frac{\sigma_{ref} - \sigma}{1 - \sigma_{ref}}$$

Equation 6—2

where σ_{ref} is the shielding value associated with a nucleus for an arbitrarily chosen reference sample. With this relationship, the other expected oxygen signals were calculated.

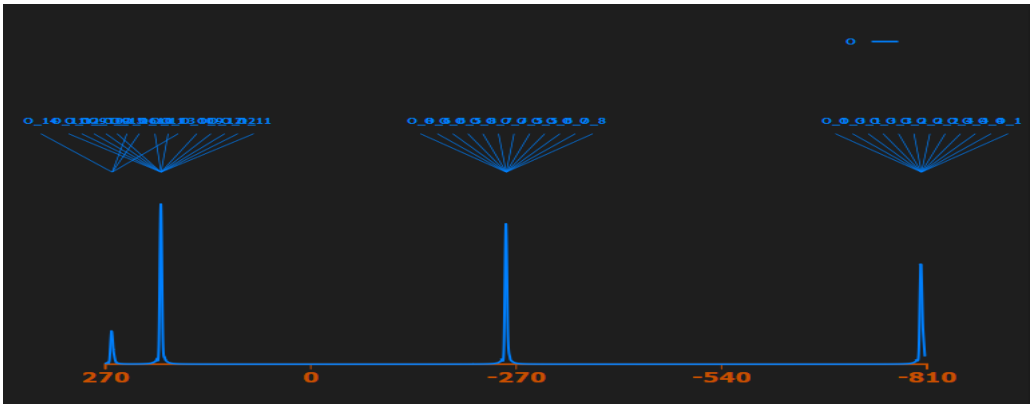

Figure 6-41 Calculated magnetic resonance of other oxygen peaks as seen from MagRes Viewer

From Figure 6-41, there should be four oxygen sites from these calculations and four distinct signal will be obtained experimentally if ^{17}O was substituted in all possible positions.

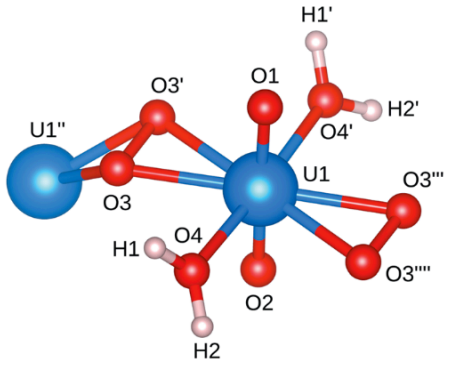

Figure 6-42 Structure of studtite as shown in Fig 2-7

O_1 and O_2 are shown earlier having the same magnetic shielding (-802.7ppm) from both calculations and experimental chemical shift of 1164.4 ppm. O_3 and O_3' are calculated to have the same magnetic shielding of -256.9 ppm whereas O_4 and O_4' from water in the simulation was split into water that are closer to and further away from the uranium atom with the closer one having a magnetic shielding of 196.9 ppm to 261.1 ppm. By simple calculations from the uranyl oxygen chemical shift and magnetic shielding (Equation 6—2), σ_{ref} was determined to be 0.0003613 and the table below was obtained.

Table 6-6 Calculated chemical shift from CASTEP

Oxygen position	Calculated Magnetic shielding/ ppm	Calculated Chemical Shift	Calculated Chemical Shift/ ppm
O_1, O_2	-802.7	0.0011644	1164.42
O_3, O_3'	-256.9	0.0006184	618.42
O_4	196.9	0.0001645	164.46
O_4'	261.1	0.0001002	100.24

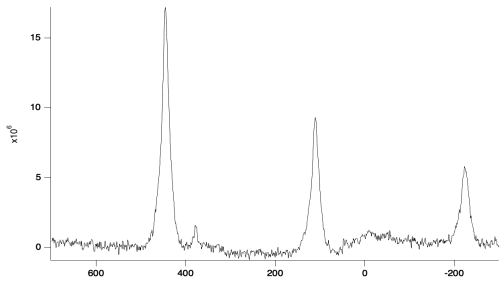

Figure 6-43 Zoomed in of studtite spectra

Zooming in on studtite spectra (left), no equatorial oxygen peak was observed at 618 ppm. This is an important observation that will be discussed in the next section.

The peak at 380 ppm corresponds to the zirconium (ZrO_2)rotor peak.

Oxygen peaks from the bound water were calculated to be broad and, depending on orientation, fluctuating between a range of 60 ppm from *+160 ppm* to *+100 ppm*. It was however observed to span a range of 130 ppm between *+50 ppm* to *-80 ppm* however the discrepancy may be in part due to the low intensity and broad FWHM of the bound water-oxygen peaks.

6.6.3.2 Becquerelite simulation

After geometric optimization, becquerelite ended up with 236 unique atomic positions.

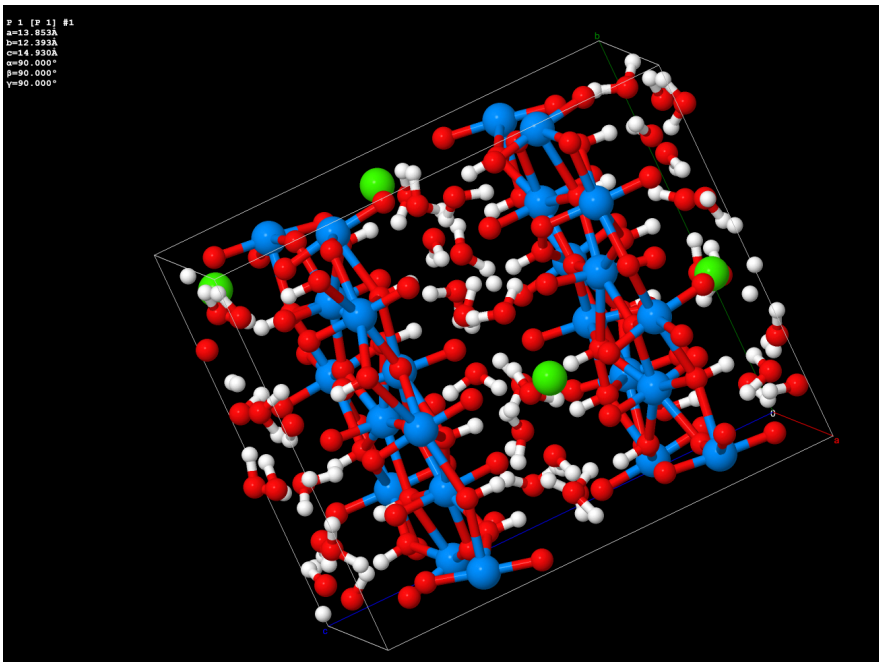

Figure 6-44 Geometrically optimised becquerelite structure

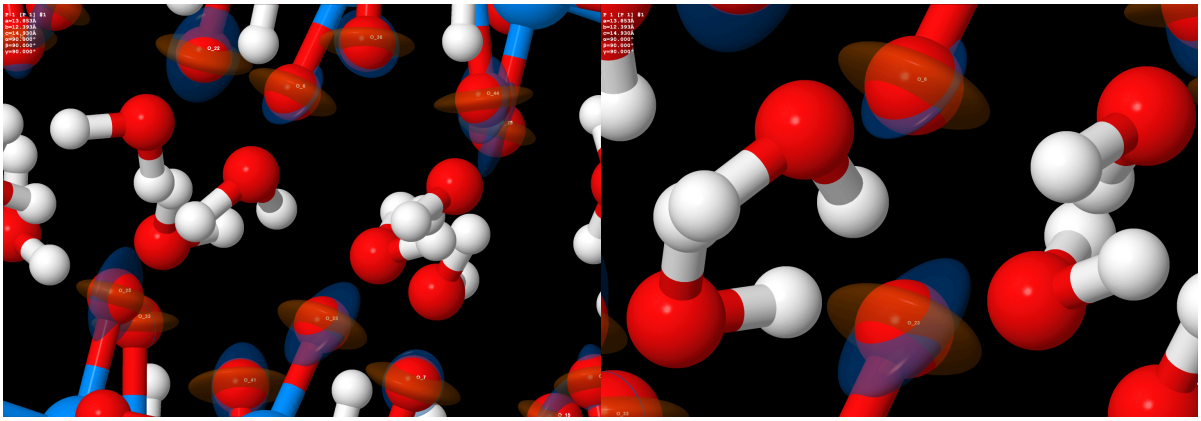

Figure 6-45 The orange region corresponds to the magnetic shielding and the blue region the electric field gradient, V_{zz}.

As seen earlier in studtite, the uranyl oxygens have a very small electric field gradient yet a very large anisotropy. Their electric field gradient is perpendicular to the magnetic shielding and lies along the direction of the uranyl bond.

However, the simulation of this complicated structure with CASTEP yields results that differ greatly from the experiment. Becquerelite has a complicated structure as seen from the ^{17}O NMR spectra in 6.5.4 Becquerelite, $Ca[(UO_2)_6O_4(OH)_6].(H_2O)_8$ where the spectra spans over 50 ppm, which is the largest range for the uranium minerals investigated here, but the calculation shows an equally complicated structure with a wider range of 150 ppm seen in Figure 6-46 Magnetic resonance calculations of Becquerelite uranyl oxygen. This might be resolved if there was time to adjust the pseudopotentials with a wide range of minerals to refine the CASTEP calculations for complicated uranium minerals. This problem may also lie with the NMR limitations of not being able to resolve as finely as the differences of these bond variations are too subtle at less than 0.01Å, where the limitations of scientific measurements lie at ambient temperatures.

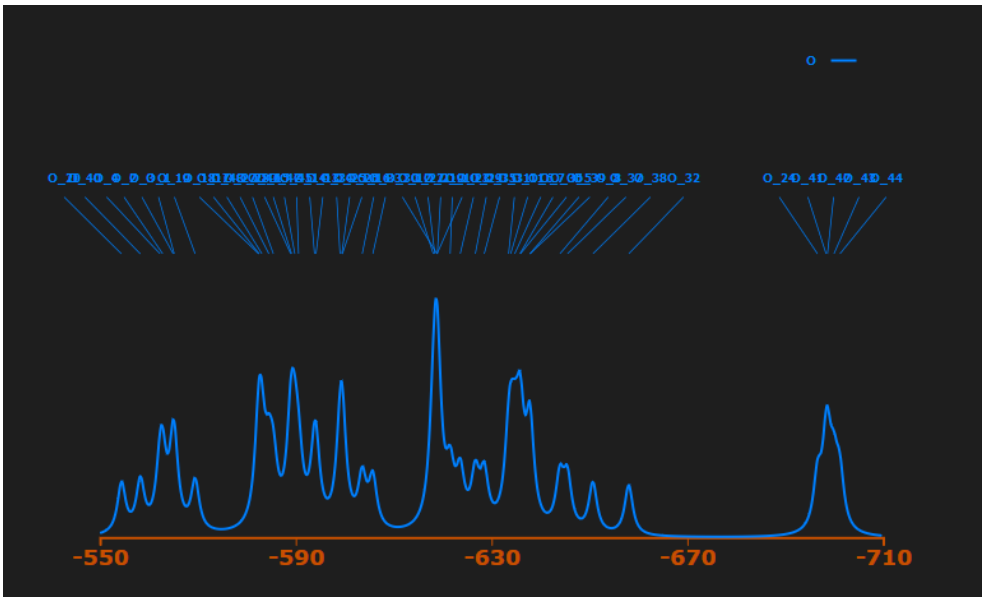

Figure 6-46 Magnetic resonance calculations of Becquerelite uranyl oxygen

6.7 Discussion of ^{17}O NMR preparation, data and simulations

This section is focused on four main conclusions that were obtained from NMR experiments executed. This section will discuss the equatorial oxygen enrichment of studtite, the trend of uranyl bond length to chemical shift, insights from simulation results with CASTEP and experimental development in the technique of in-situ thermal NMR studies.

6.7.1 Studtite ($UO_2(O_2).4H_2O$) Equatorial Oxygen Enrichment Attempt

In the many iterations of isotopic enrichment of studtite by reacting uranyl nitrate (and even uranyl acetate) with hydrogen peroxide in 35-40% ^{17}O water, ^{17}O signal clearly only came from the uranyl oxygen and bound water molecules in the crystal structure. Hence, it is interesting to note that no equatorial (peroxide) oxygen signal was detected with ^{17}O NMR. This implies that the equatorial oxygen atoms do not undergo exchange and enrichment with the oxygen during sample preparation.

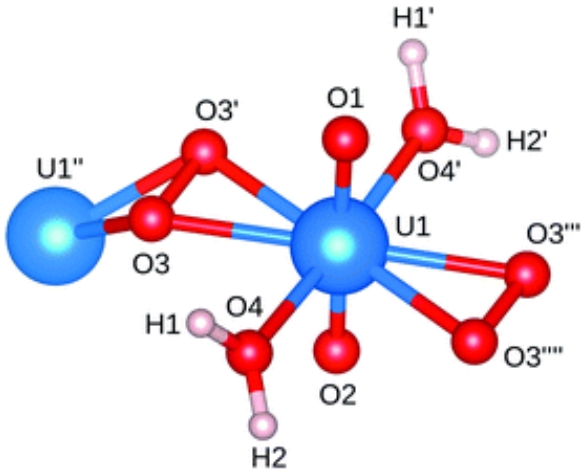

Figure 6-47 Attempts to substitute in ^{17}O with the equatorial oxygen at O3, O3', O3'', O3'''

Attempts was made to enrich the equatorial oxygen atoms in studtite by the following two methods.

1) Uranyl nitrate was reacted with hydrogen peroxide in 1 ml of ~ 40 % ^{17}O water

2) Uranyl nitrate was reacted with hydrogen peroxide then submerged in 40 % ^{17}O water for 150 days (for passive isotopic oxygen exchange). 0.25 mL of ^{17}O water was added to 20 mg of studtite and the mixture was left for 150 days in a tightly sealed container kept in argon atmosphere. 8 mg of these samples were then extracted for ^{17}O NMR spectroscopy.

Passive isotopic oxygen exchange calculations

Molecular mass of non-enriched studtite $UO_2(O)_2.4H_2O$	$238.03+6(16.0)+4(1.01)$	374.09 u
Fraction of oxygen in studtite	$\frac{6 \times 16.0}{374.09}$	0.257
Mass of ^{17}O to be inserted into 20 mg of crystalline studtite	0.257×20	5.14 mg
Mass of 40% ^{17}O water required	$5.14 \times \frac{17+2}{16+2} \div 40\%$	13.5 mg
Volume of water required	$13.5\ mg \div 1 \frac{mg}{\mu l}$	13.5µl
Isotopic transfer probability of 5-10 %	$13.5\ \mu l \div (5-10)\%$	135- 270µl 0.135-0.270 ml

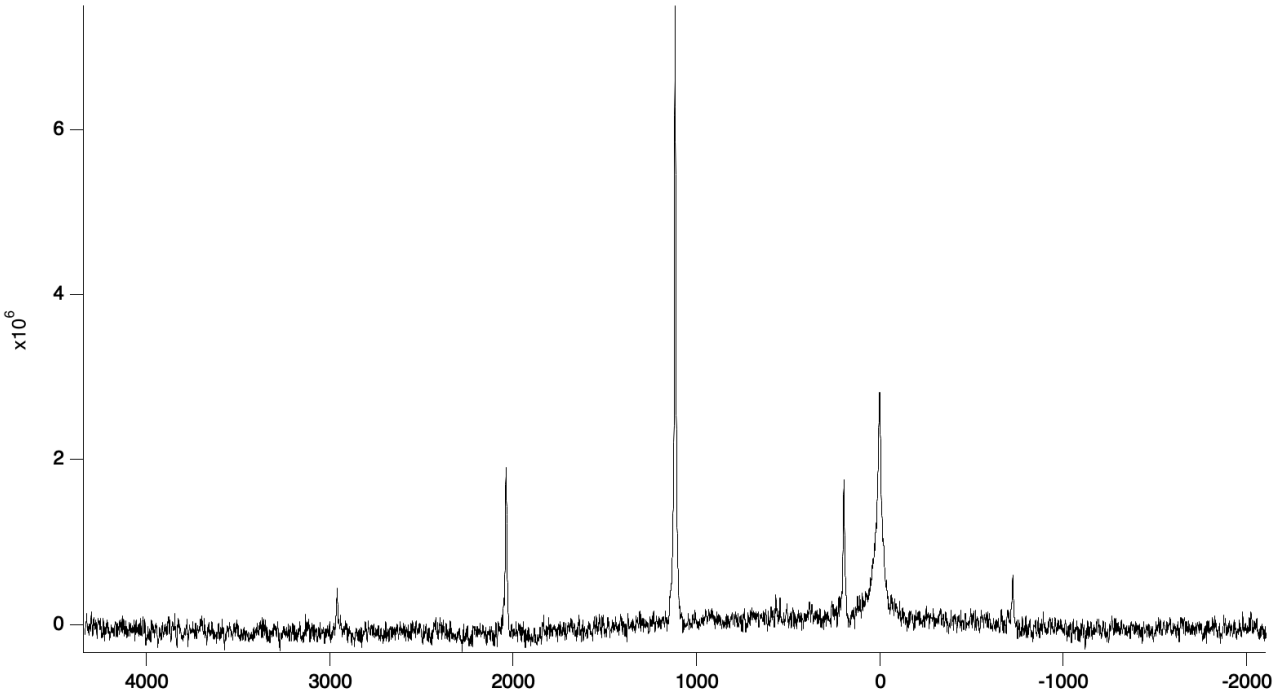

Figure 6-48 Spectra looks quite similar to the previous spectra on studtite at Figure 6-21 with the exception of a slight increase in area of oxygen peak for bound water molecules centred about 0 ppm.

Results

From the first method, there are no equatorial oxygen signal, which means that prior to formation of studtite, the hydrogen peroxide molecules do not exchange readily with ^{17}O enriched water as the equatorial peroxide bridges must be derived directly from the peroxide ions in hydrogen peroxide. Therefore, it is reasonable to conclude peroxide ions (O-O) are not susceptible to passive isotopic exchange.

From the second method, after formation of the peroxide bridges in studtite, equatorial oxygen was not observed to exchange readily with oxygen from the surrounding enriched water molecules, which implies strong bonds at the O-O levels. This led us to confidently deduce that the O_2^{2-} equatorial oxygen in studtite does not exchange readily with surrounding oxygen, unlike other ions such as uranyl ions (U = O).

Given the longer bond length (weaker bond) of the uranium-equatorial oxygen bond length of 2.351 Å to the shorter bond length (stronger bond) of the uranium- yl oxygen bond length of 1.769 Å, there seems to be no reason why the exchange of the equatorial oxygen were prohibited due to interaction of the uranium atom. The only plausible reason must be the strong interaction of the peroxide group itself, which formed a tightly bound equatorial bridge (O-O) for studtite which will not undergo passive isotopic enrichment as hydrogen peroxide or studtite.

The only way to enrich and detect ^{17}O NMR spectra of equatorial oxygen in studtite will be to enrich it at the synthesis of hydrogen peroxide. A possible method will be alpha radiolysis of ^{17}O enriched water. Although not executed in this thesis, this will be useful for future work where properties of equatorial oxygen bonds are of interest. This is important as studtite and metastudtite are the only known peroxide minerals in nature from the reaction of hydrogen peroxide and uranium dioxide. (Hydrogen peroxide is formed naturally from radiolysis of water due to ionisation of ground water with alpha particles with short penetration range.) It is probable that compounds formed in the vicinity of water dosed with alpha radiation will take on peroxide structure, albeit with unknown stability which may be shorter than extraction and detection time. Applications may include studies of leakage of alpha emitters in ground water with alpha radiolysis at the near surface (such as spent nuclear fuel in Figure 7-2), where peroxide compounds are possible.

6.7.2 Uranyl bond length and corresponding ^{17}O chemical shift

By consolidating the experimental data from the NMR spectra, an empirical calibration of chemical shifts with respect to the uranyl bond lengths was achieved. Nuclear magnetic resonance is a technique that analyses the chemical shifts of the NMR-active nuclide with respect to chemical shielding from their neighbours. All of the synthesized minerals possess uranyl oxygen nuclei (U = O) whose primary interaction is with the uranium atom, however there are some secondary interactions with the different atoms in its vicinity due to the different chemical composition of the mineral and crystal structure. This final consolidated graph shows similar gradient for all the minerals. This gradient ranges from +70 ppm to +150 ppm per 0.1 Å increase in bond distance. Nonetheless, it is still possible to differentiate convincingly with parts-per-million accuracy the different uranyl bond lengths and their associated chemical shifts for these minerals as seen in the below figure.

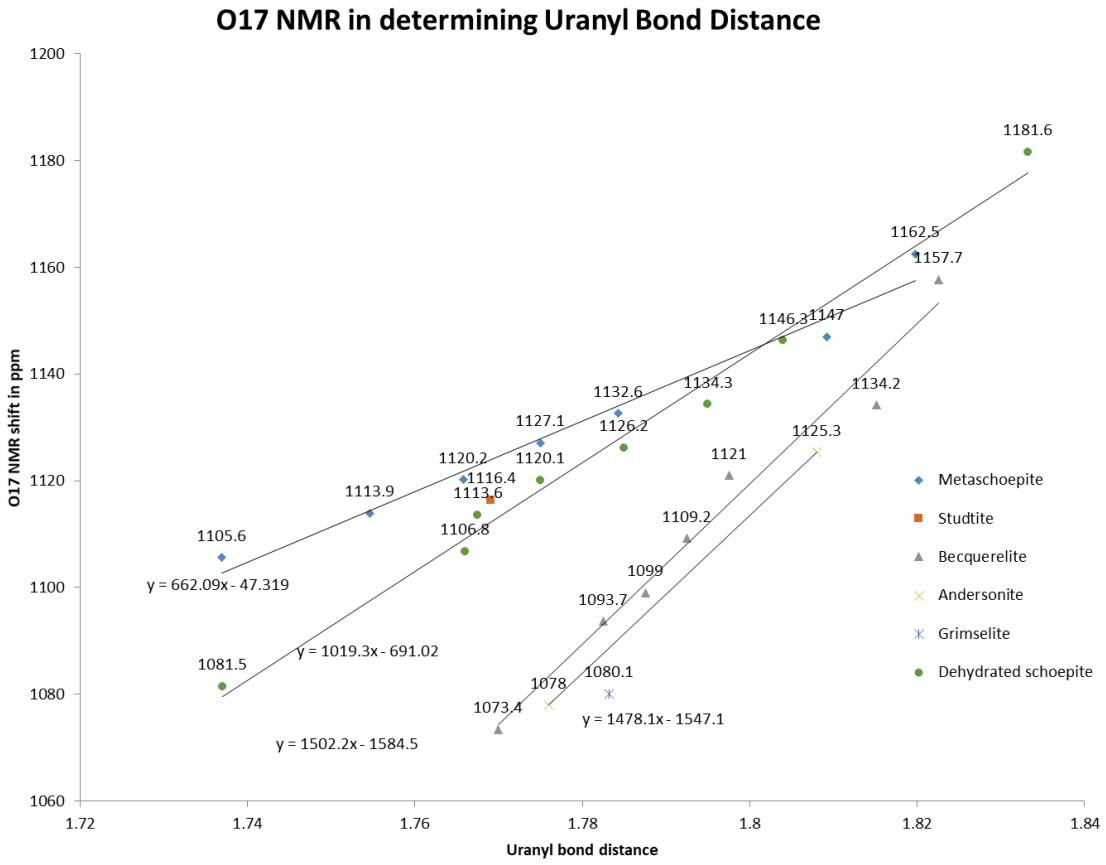

Figure 6-49 Consolidated plot of experimentally obtained chemical shifts with respect to uranyl bond lengths.

It might be interesting to note that the uranyl compounds with only oxygen and hydrogen atoms such as metaschoepite, dehydrated schoepite and studtite have higher chemical shifts, hence

they are located on the left side of the curve. Enriched compounds with sodium, potassium or calcium are located on the right side of the curve and have uranyl oxygens with lower chemical shifts and also a smaller spread of gradients, that are nearer to + 150 ppm chemical shift per 0.1 Å increase in bond distance. However, due to the limited minerals synthesized, this observation require more studies of minerals with same constitution and varying arrangements. Future work can also include expanding the amount of minerals synthesized and analysed to create a larger database of uranium minerals with their associated chemical shifts.

Due to the ubiquitous nature of oxygen, most uranyl-containing minerals can be analysed easily with just an easy intermediate step of passive oxygen transfer which have been proven to work with uranyl bonds as detailed in Chapter 6.7.1 Studtite ($UO_2(O_2).4H_2O$) Equatorial Oxygen Enrichment Attempt. With this information, future minerals can be identified easily if they fit the data (with confidence if they have varying uranyl bond differences greater than 0.001 Å.)

The trend that have been obtained is in broad agreement with DFT calculations on uranyl complexes in solution by Marchenko *et al* (Marchenko, Truflandier and Autschbach, 2017) , though his calculations constantly overestimate the chemical shift with respect to uranyl bond distances. In his work, to simulate general actinide complexes, Car- Parrinello Molecular Dynamics (CPMD) based upon Kohn−Sham (KS) density functional theory (DFT) was used for computation of the chemical environment quantum mechanically with molecular dynamics calculations being performed with DFT code Quantum Espresso and NMR chemical shift computations with the NMR module of the Amsterdam Density Functional Package (ADF) (version 2014, revision 51267)

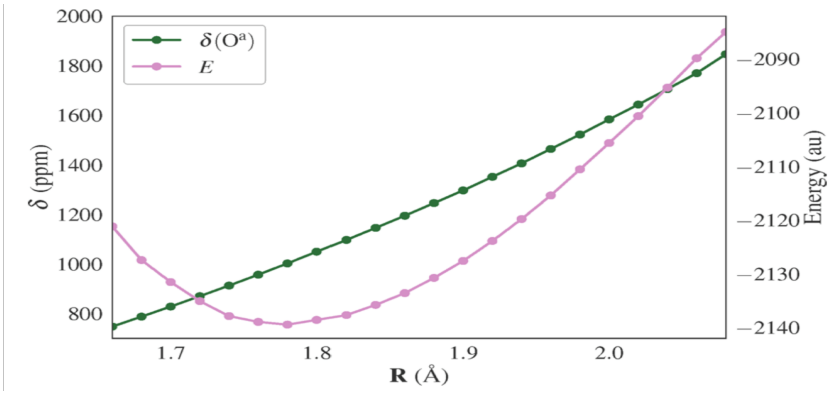

Figure 6-50 Dependence of chemical shift (green) with respect to the uranyl bond length at ADF PW91/SR plus COSMO level of theory of $UO_2(OH_2)_5$. For each data point, the uranyl bond length was constrained while the rest of the system was relaxed structurally.

Using the P91XC functional and Scalar Relativistic (SR) corrections (ADF PW91/SR) on free uranyl ion in solution with energetically-favoured penta-coordination, $UO_2(OH)_5$ shown in Figure 6-50 Dependence of chemical shift (green) with respect to the uranyl bond length at ADF PW91/SR plus COSMO level of theory of $UO_2(OH_2)_5$. For each data point, the uranyl bond length was constrained while the rest of the system was relaxed structurally. A clear linear trend (green) of chemical shift against uranyl bond lengths was shown in his paper where the rate of change calculated was higher at +260 ppm per 0.1 Å increase, which was an overestimate compared to the +70 to +150 ppm per 0.1 Å obtained here.

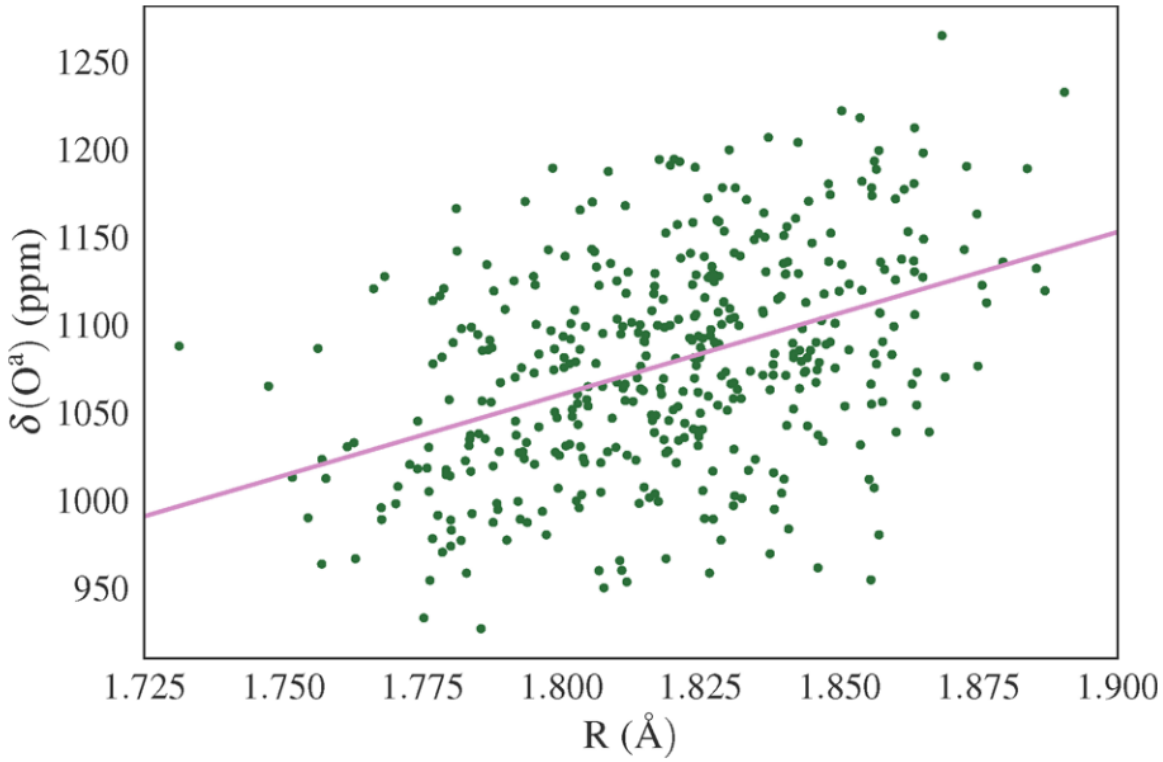

Figure 6-51 Correlation between uranyl bond length and chemical shift for the uranyl complex dynamics with ADF PW91/SR. The least-squares linear regression analysis is a guide for the eye only. The estimate for the rate of change of the chemical shift is 130 ppm per 0.1 Å.

Simulations of the effects of the uranyl bond length on the uranyl oxygen chemical shift estimates a rate of change of about 260 ppm per 0.1 Å for $UO_2(OH)_5$ and 130 ppm per 0.1 Å for the $UO_2(CO_3)_3^{4-}$ shown above. From these calculations, it seems that simulation of the more complex uranium carbonate is more in line with my empirical data, which shows a much clearer linear trend with differences in uranyl oxygen shifts arising from the different crystal structures and chemical composition. Furthermore, the experimentally- obtained empirical data with better linear regression validates these DFT calculations as reasonable estimates and can be used to improve on the simulations' accuracy and correlation.

6.7.3 Advantages of CASTEP Simulation

Simulations enable me to geometrically relax the structures and determine the number of peaks that should be achieved in an ideal crystalline structure. The starting parameters of crystalline structure for fabricated samples are however hard to obtain in real life, especially with radioactive substances. Another difficulty stems from the long computational time that is required for characterizing complicated samples as months was spent on running geometric optimization and subsequent magnetic resonance on them, many of the experiments did not run to completion due to insufficient memory at the end.

Nonetheless, there are many advantages of performing nuclear magnetic resonance simulations with CASTEP. For certain isotopes, such as ^{17}O, enrichment via isotopic exchange is ineffective as seen in equatorial oxygen of peroxide bonds in Chapter 6.7.1 Studtite ($UO_2(O_2).4H_2O$) Equatorial Oxygen Enrichment Attempt. Even in the event of successful enrichment, it is an expensive process as each ml of 40% ^{17}O enriched water costs over £500.

In the case of successful simulation runs of more complicated structure as in the case of becquerelite, the programme can be seen to assign the correct number of peaks for each unique chemical environment after relaxation of the crystal, which will result in high resolution structural information on the minerals, should the pseudopotentials of uranium be sufficiently accurate. That is in itself a challenge with the electrons of the uranium atoms precessing at near relativistic speeds close to the uranium nucleus.

Chapter 7 Thermal evolution from Studtite $(UO_2)O_2(H_2O)_4$ to Metastudtite $(UO_2)O_2(H_2O)_2$

Studtite and metastudtite are the two only naturally-occurring peroxide minerals and are highly likely to be formed as a result of reactor accidents or upon groundwater intrusion into nuclear repositories. (Sattonnay *et al.*, 2001; Amme, 2002; Hanson *et al.*, 2005; Guo *et al.*, 2014).

In a nuclear waste repository, high alpha dosage persists close to the surface after extended storage periods, as seen in Figure 7-1. In combination with ingressing groundwater, the alpha radiation will lead to the formation of H_2O_2 (Sattonnay *et al.*, 2001; Amme, 2002), which then leads to the production of peroxide minerals such as studtite and metastudtite even in the presence of prevailing reducing conditions. It was observed by Hanson *et al*. (Hanson *et al.*, 2005) that the two uranyl peroxide polymorphs, studtite and metastudtite were the only secondary phases left in a 2 year corrosion experiment on spent nuclear fuel. The reason for the pervasive uranyl peroxide polymorphs can be explained by the 2012 study conducted by Pacific National Nuclear Laboratory where alpha radiation was observed to be dominant near the surface of the spent fuel (~150 nm) in a 30-year simulation, which is of relatively short time scale. The energy differential between alpha and beta/gamma radiation increases further to 3 orders of magnitude for a 300-year simulation. The short range of alpha radiation results in energy dispersal and formation of radiolytic species being close to the reaction surface whereas gamma radiation travels further and distributes its energy over a greater volume with radiolytic species being a further average distance from the fuel's surface. For spent nuclear fuel that are disposed in repositories for thousands of years before possible ingress of groundwater, the effects of alpha radiation on spent nuclear fuel dissolution is worth investigating.

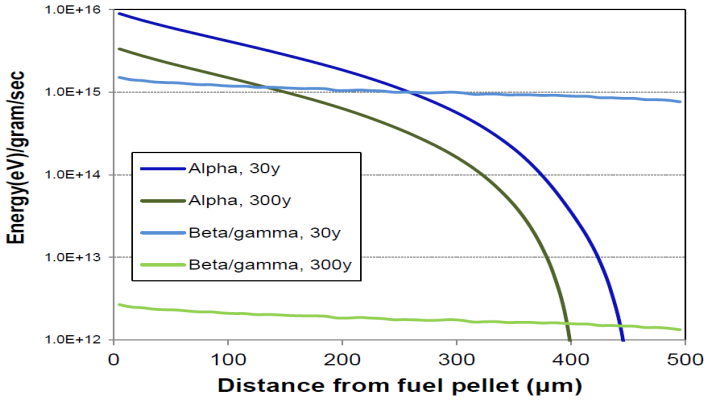

Figure 7-1: The dose to the surface of spent nuclear fuel exposed to a mixed water- air environment (10% water) is dominated by long-lived alpha radiation even at relatively short times out of reactor (Buck *et al.*, 2012)

Simulation with reaction kinetics (Christensen and Sunder, 2000) applied to the heterogenous system of UO_2 dissolution at a solid-aqueous boundary indicates a build-up of H_2O_2 and H_2 concentrations to µM concentration within 15 minutes which persists 1 mm from the surface of the fuel contrasting with the short diffusion lengths of the radicals.

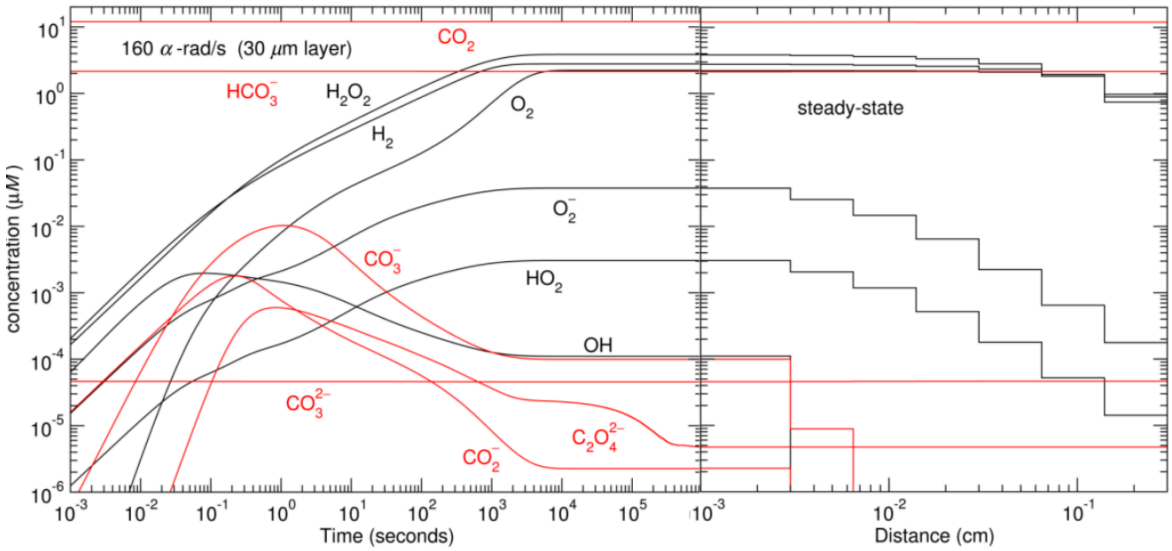

Figure 7-2 Calculated surface environment within 30 mm of a 160 rad/s alpha field in an anoxic environment illustrating the time dependence of dominant species.

In the reaction of spent nuclear fuel and peroxide formed from the alpha radiolysis of water, peroxide polymorphs of studtite and metastudtite are important products whose properties should be examined carefully. It was interesting to note that despite the structure of studtite being elucidated in 2003 (Burns and Hughes, 2003), the orthorhombic metastudtite with Pnma space group was reported for the first time in 2012 from a first principles simulation. (Weck *et al.*, 2012). This may be due to the amorphous formation of $(UO_2)O_2(H_2O)_2$ from dehydration of underlying studtite layers, $(UO_2)O_2(H_2O)_4$, that makes Rietveld refinement difficult.

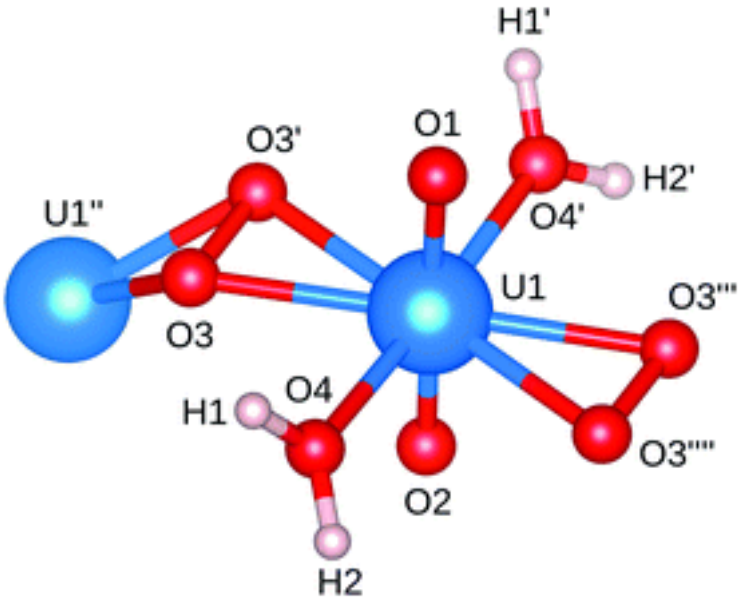

Figure 7-3 Chemical structure of studtite from XRD of a single crystal. (Burns and Hughes, 2003)

Upon inspection of Weck's simulation of metastudtite, there were two unique uranyl bonds of bond lengths (1.8035 Å and 1.8506 Å).

Using the relationship uncovered in Chapter 6, where an increase in uranyl bond length of 0.1 Å leads to a chemical shift of the isotropic uranyl NMR peak by +70 ppm to +150 ppm for the different uranyl containing minerals and a difference of 0.047 Å will yield a significant difference of > 30 ppm which was not observed in the following set of experiments where studtite was heated to transform it to metastudtite.

7.1 In-situ Variable Temperature NMR calibration

^{17}O Variable Temperature MAS NMR spectra were collected on a Varian Infinity 400 MHz spectrometer operating at 54.221 MHz with a 3.2 mm probe with a vacuum pump set up with the exhaust gas tube as mentioned (<u>6.1 Adaptations for NMR spectroscopy of uranyl-minerals</u>).

An important step before this can be done is to calibrate the temperature properly with the help of NMR of three different isotopes: Br – 79 for magic angle calibration, H – 1 for temperature fixing (stearic acid at 69.3 ^{0}C) and Pb – 207 for temperature calibration.

1) To conduct this 2-week long experiment, it was important to ensure that the magic angle was properly set up with the use of Br- 79 (KBr) as samples cannot be switched out during the heating process without introducing confounding variables.

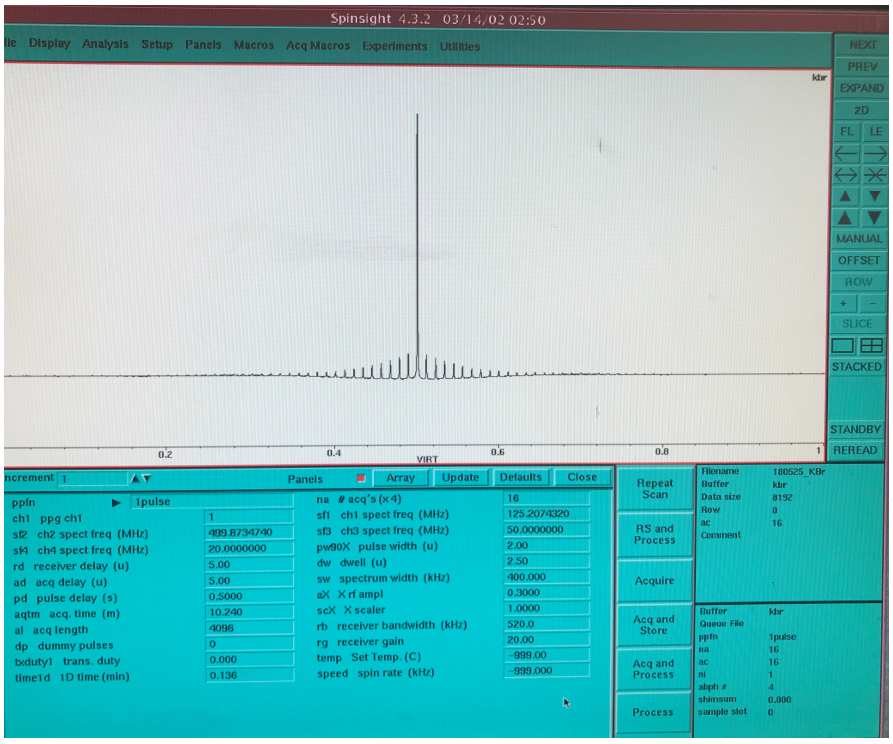

Figure 7-1 The large number of sidebands indicate that the magic angle is properly tuned.

2) Secondly, stearic acid was used to calibrate for temperature (Grant and Dunell, 1960). It has a well- defined melting point at 69.3^{0}C and produces a narrow proton magnetic resonance line width in its molten form that is distinct from the broad linewidth in solid state. By adjusting the heating gas, the temperature of the heating gas can be correlated with the sample temperature with stearic acid in the rotor at a rotational speed of 15kHz.

3) Thirdly, lead nitrate as a well- known reference (Bielecki and Burum, 1995; Takahashi *et al.*, 1999) was used as its chemical shift varies with respect to temperature with empirical equation stated in Equation 7—1, though the coefficient of $\boldsymbol{\delta^2}$ term was likely insignificant. The different sample temperatures in the rotor at different reading of the exhaust gases can be deduced by considering the fixed point of the melting point of stearic acid and the chemical shift of 30.5 ppm for the isotropic peak of lead.

$$-5.2 \times 10^{-4}\delta^2 + 1.3\delta + 30.1 = 69.3$$

Equation 7—1

With the fixed point and this formula, the calibration of the heating temperatures with the heating gas temperature proceeded.

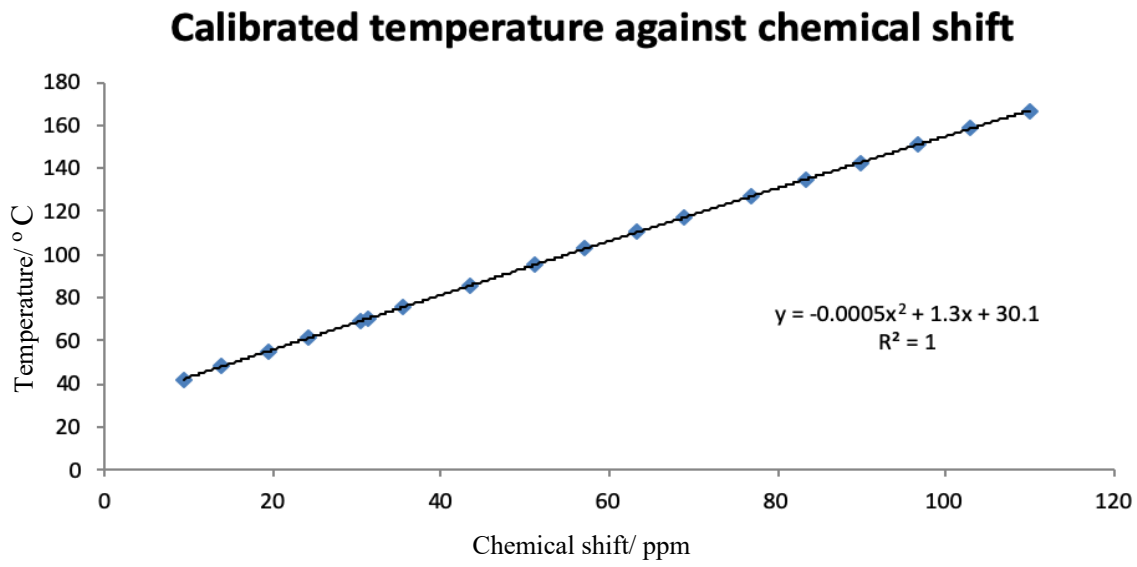

Figure 7-5 Calibration graph of temperature in °C against chemical shift in ppm.

Table 7-1 Calibration of heating gas temperature against actual sample temperature

Gas Temp/ ^{0}C	Peak/ ppm	Corrected ppm	Sample Temp/ °C
22	5.77	9.37	42.2
30	10.14	13.74	47.9
40	15.75	19.35	55.1
50	20.63	24.23	61.3

58	**26.93**	**30.53**	**69.3**
60	27.58	31.18	70.1
70	31.77	35.37	75.4
80	39.75	43.35	85.5
90	47.53	51.13	95.2
100	53.39	56.99	102.5
110	59.59	63.19	110.2
120	65.43	69.03	117.4
130	73.34	76.94	127.0
140	79.66	83.26	134.7
150	86.20	89.80	142.6
160	93.00	96.60	150.8
170	99.42	103.02	158.5
180	106.43	110.03	166.8

7.2 Variable temperature experimental data

Upon calibration of the temperature, analysis of the oxygen environments of studtite and metastudtite can be achieved. Previous work with thermogravimetry have determined the range of temperatures when studtite transforms to metastudtite (as the loss of water molecules from $(UO_2)O_2(H_2O)_4$ to $(UO_2)O_2(H_2O)_2$ and further dehydration to potentially amorphous U_2O_7) (Rey *et al.*, 2009; Odoh *et al.*, 2016). Reported transition temperatures ranges from 60 °C to 100 °C for the first transition from studtite to metastudtite and 145 to 220 °C for the subsequent conversion to UO_{2+x}.)

The large range for the first transition indicates that studtite to metastudtite transition is likely to be to an amorphous phase at the beginning, proceeding slowly with time. The even larger range for the second transition indicates likely multiple products of UO_{2+x} being formed during this transition.

Through single pulse excitation with ^{17}O at a spectrometer frequency of 54.23 MHz with a 34 mg of studtite in a 3.2mm rotor spinning at 18 kHz, the sidebands are separated from the centre band by 335 ppm. Only one uranyl resonance with sidebands was observed. The baseline showed a small broad distortion around 0 ppm.

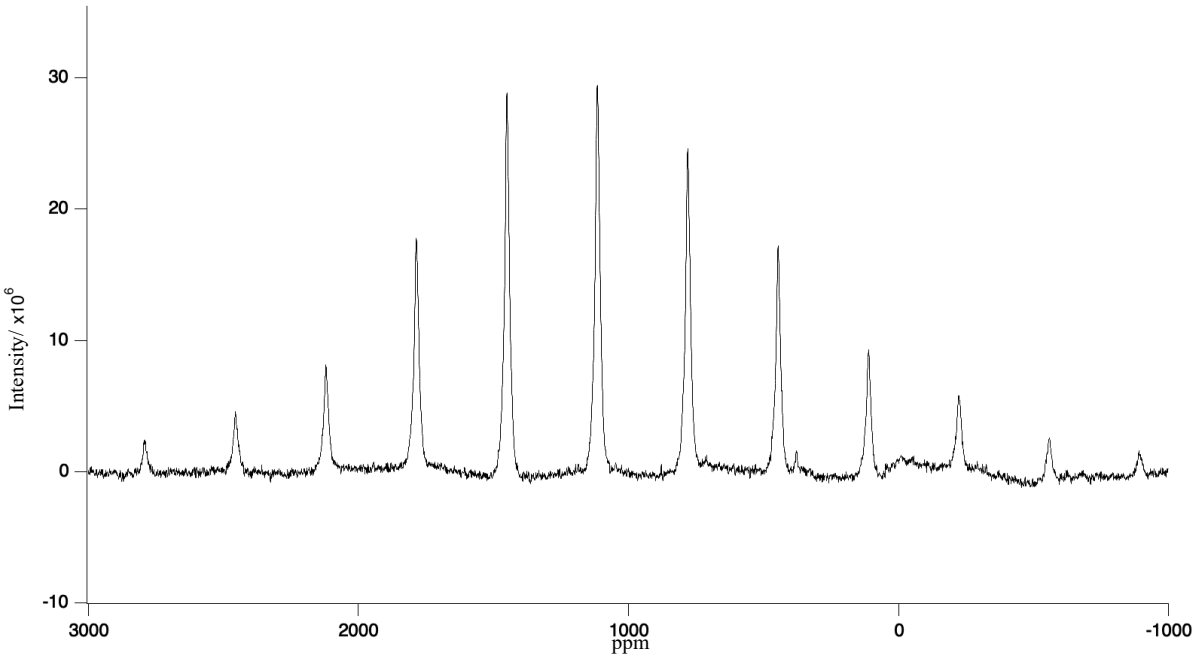

Figure 7-6 Studtite at 40 ^{0}C.

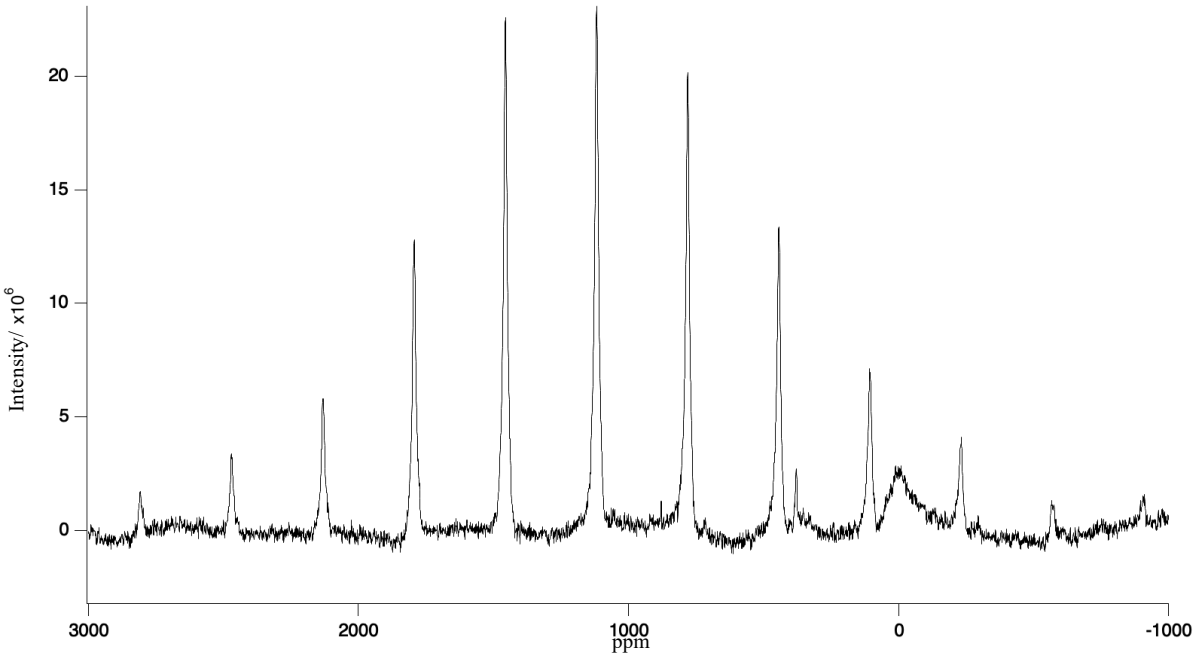

Figure 7-7 Studtite/ metastudtite at 100 ^{0}C

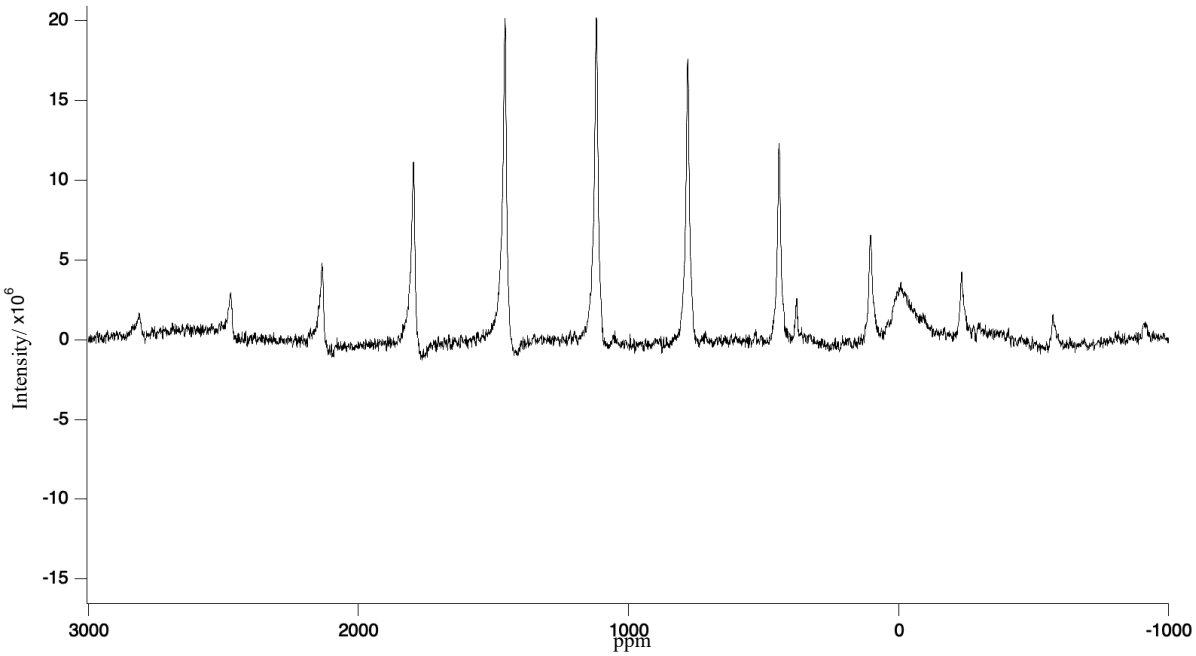

Figure 7-8 Metastudtite at 110 ° C

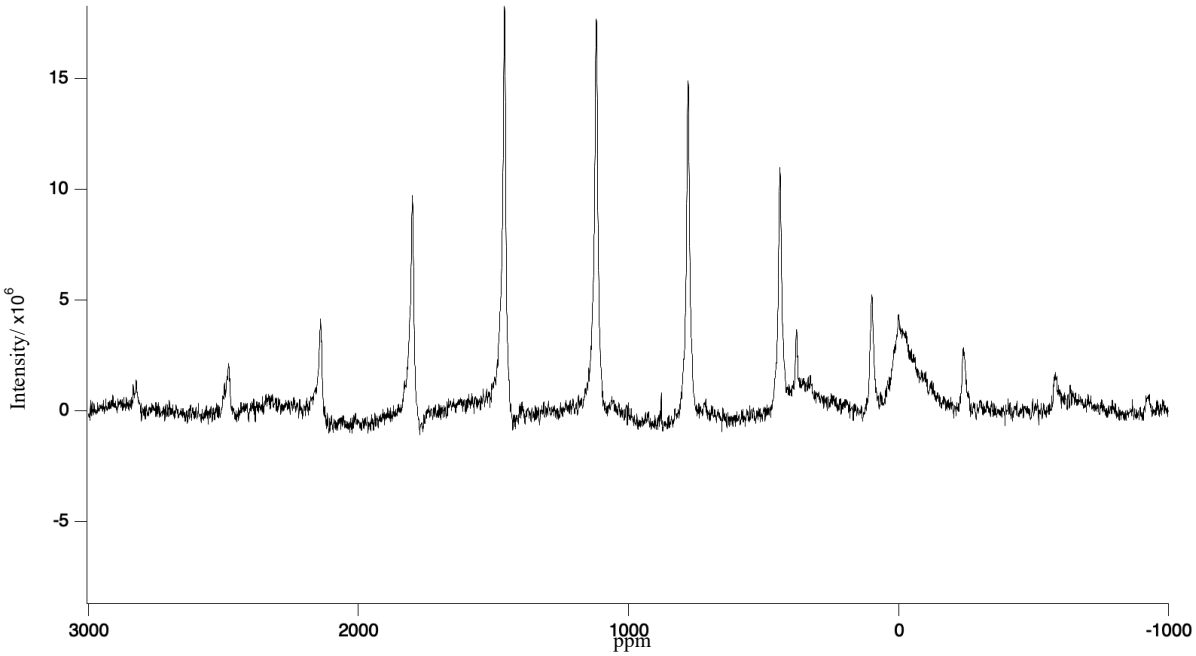

Figure 7-9 Metastudtite at 120 ° C

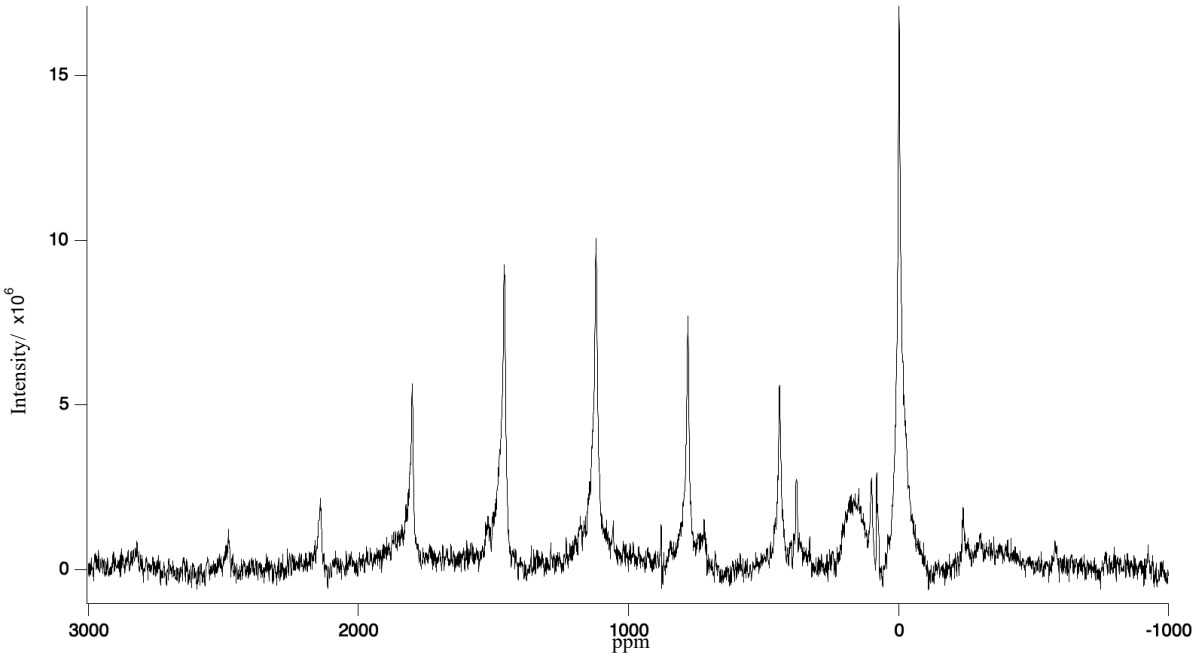

Figure 7-10 Metastudtite at 130 ° C

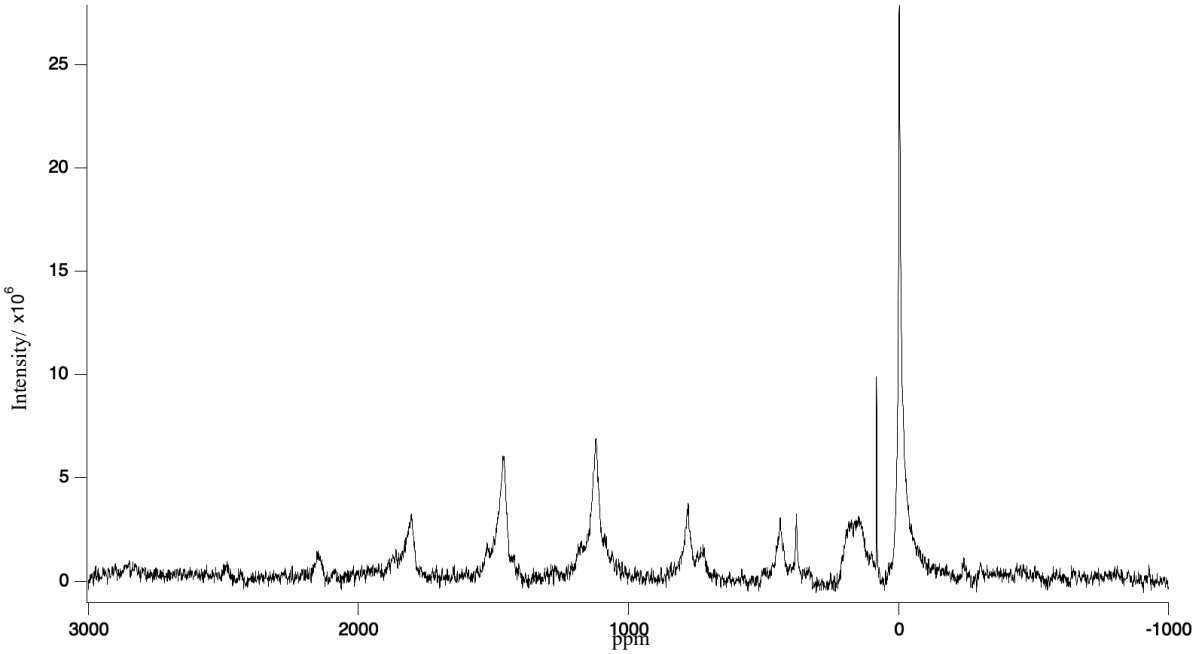

Figure 7-11 UO_{2+x} at 140 ° C

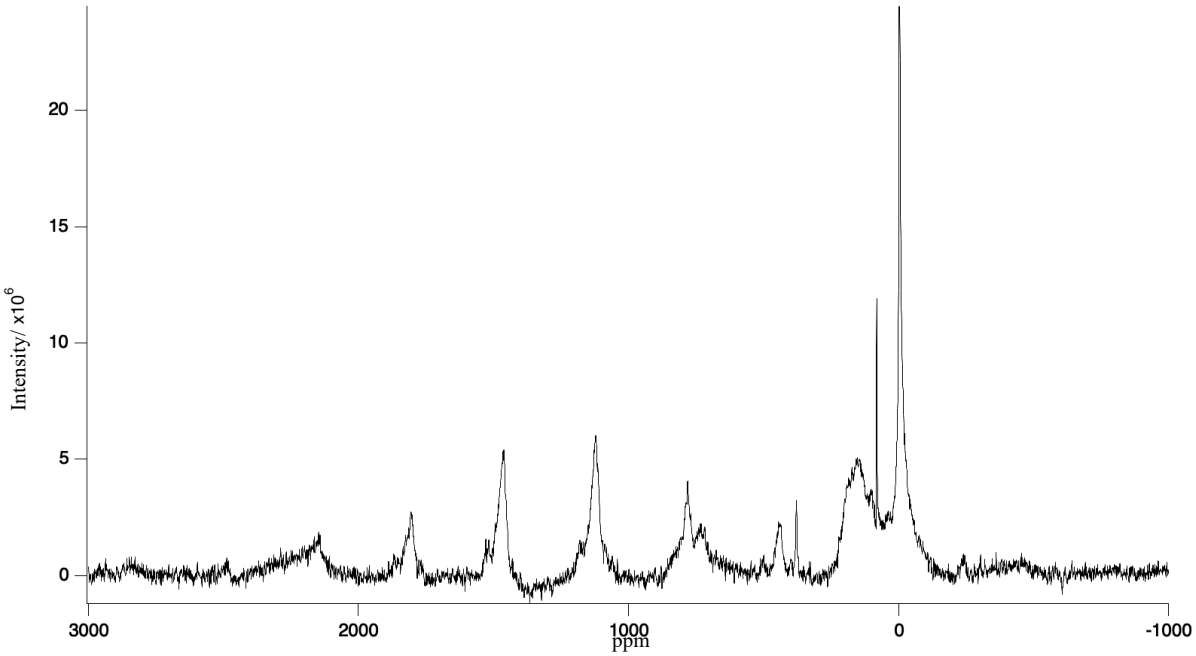

Figure 7-12 UO_{2+x} at 150 °C

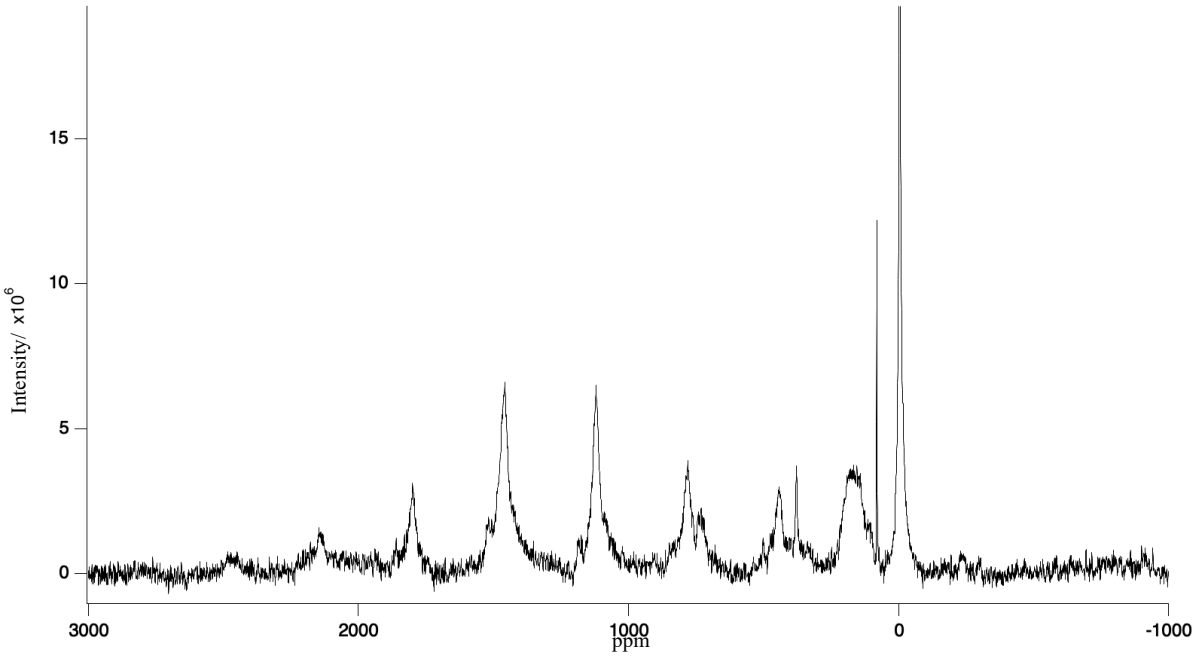

Figure 7-13 UO_{2+x} at 160 °C

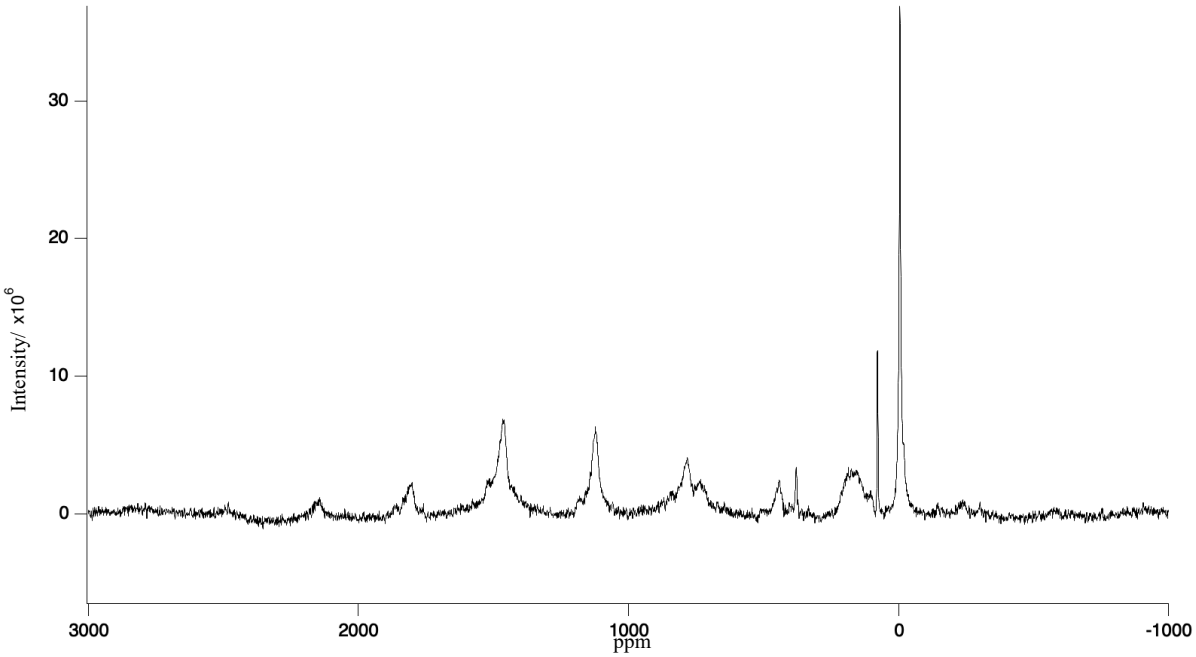

Figure 7-14 UO_{2+x} at 180 °C

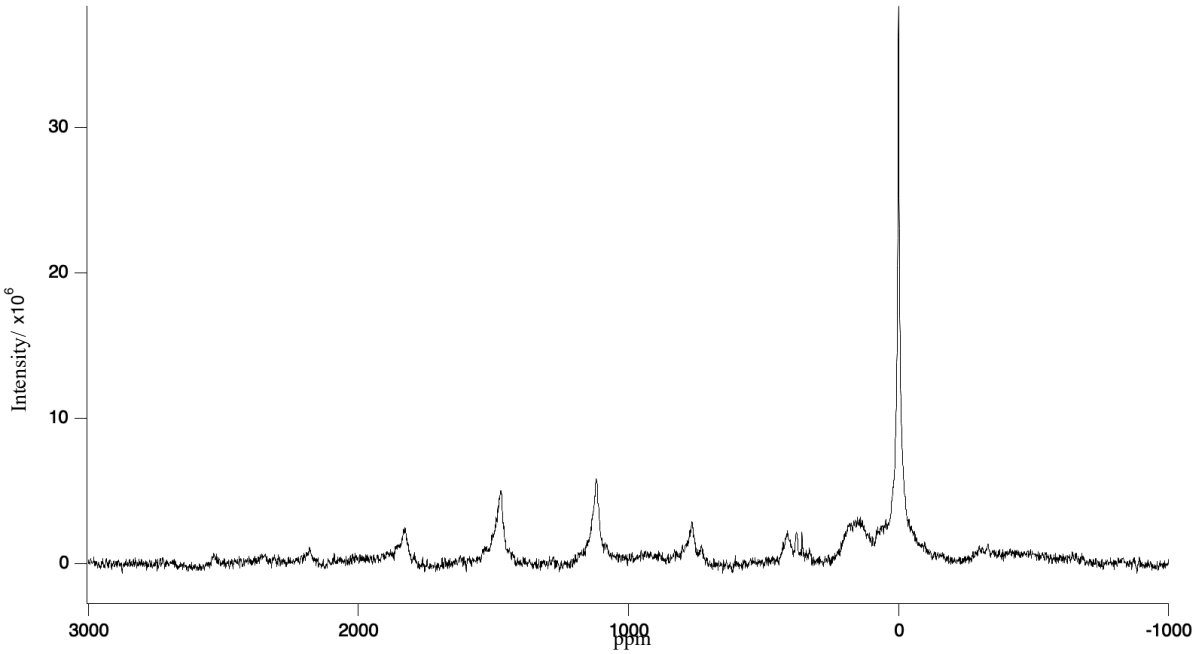

Figure 7-15 After heating and cooling back to room temperature for 48 hours.

7.3 Analysis of NMR data.

7.3.1 Uranyl bond length differences for studtite to metastudtite transition.

Table 7-2 Uranyl peak analysis

Temperature/ ° C	Position of Uranyl bond/ ppm	FWHM/ ppm
40(studtite)	1114.6	19.7
100 (metastudtite)	1118	16.3
110 (metastudtite)	1119.4	15.2
120 (metastudtite)	1119.5	14.0
130 (metastudtite)	1120.8	16.1
140 (UO_3/ U_2O_7)	1121.7	31.9
150 (UO_3/ U_2O_7)	1123.4	34.5
160 (UO_3/ U_2O_7)	1119.9	29.2
180 (UO_3/ U_2O_7)	1123.4	31.7
After Cooling	1120.2	27.5

An increase in bond length of about 0.01 A corresponding to 6 ppm was detected. This implies a very small increase in bond length of ~0.01 A. This is in line with Baker *et al.*'s paper on studtite of an increase of 0.01A. (Vitova *et al.*, 2018) In Baker *et al.*'s paper, studtite was observed with EXAFS, (which have a high resolution up to 10^{-4}Å (Purans *et al.*, 2009)) to have a U=O bond of 1.78 Å and metastudtite to be at 1.79 Å. This was in direct violation of calculations of the structural changes accompanying the dehydration of studtite to metastudtite with computational methods (using functionals PBE+U and PBE_{sol} +U), which had predicted a decrease of these bond lengths (Vitova *et al.*, 2018) by 0.02 and 0.03 Å respectively as well as work by Weck *et al.*(Weck *et al.*, 2012) that predicted uranyl bond lengths changing differently with an increase of 0.02 Å and decrease of 0.03 Å. In addition, it was noted that the U-O bond lengths calculated in all cases (Weck *et al.*, 2012; Vitova *et al.*, 2018) tend to exceed the experimental values determined by XRD, which is possibly due to an incomplete account

of the relativistic effects of the uranium in the functionals used. Experimental measurements on studtite and metastudtite earlier (7.2 Variable temperature experimental data) show an increase of 5 ppm corresponding to an increase of 0.01 Å in the uranyl bond lengths, which is in agreement with EXAFS. (Table 7-3: Bond lengths of studtite and metastudtite from the above cited paper (Vitova *et al.*, 2018).

Table 7-3: Bond lengths of studtite and metastudtite from the above cited paper (Vitova *et al.*, 2018).

	Studtite/ Å					Metastudtite/ Å				
bond	PW91	PBE+U	PBE_{sol}+U	EXAFS	**NMR**	PW91	PBE+U	PBE_{sol}+U	EXAFS	**NMR**
U=O	1.83/ 1.83	1.81	1.81	1.78	**1.78**	1.80/ 1.85	1.79	1.78	1.79	**1.79**

Considering identical fabrication process of studtite by Prof Robert Baker and his team at Trinity College (2.3.1 Studtite), the studtite to metastudtite transition should result in an extension of uranyl bond lengths of about 0.01 Å from 1.7690 (1.78 Å) to 1.79 Å. In these NMR readings, our chemical shift increases from 1114.6 ppm to about 1119.5 ppm, this corresponds to an increase of ~ + 5 ppm per 0.01 Å. This is in line with the previous measurements and serve to extend the range for our prediction to +50 ppm to +150 ppm for each 0.1 Å increase in uranyl containing minerals, with the range being dependent on atoms in the vicinity of the uranyl bond.

7.3.1 Uranyl bond length differences for metastudtite to UO_{2+x} transition.

Looking back at Table 7-2 Uranyl peak analysis, there was a big increase observed in the full width half maximum at 140 ^{0}C from 16 to 31ppm, the uranyl peak obtained from these regions from 1180 to 1080 ppm was deconvolved with an expectation of multiple uranyl peaks, which bear traces of the preliminary formation of UO_{2+x} , allowing this in situ observation even if it was in its amorphous forms

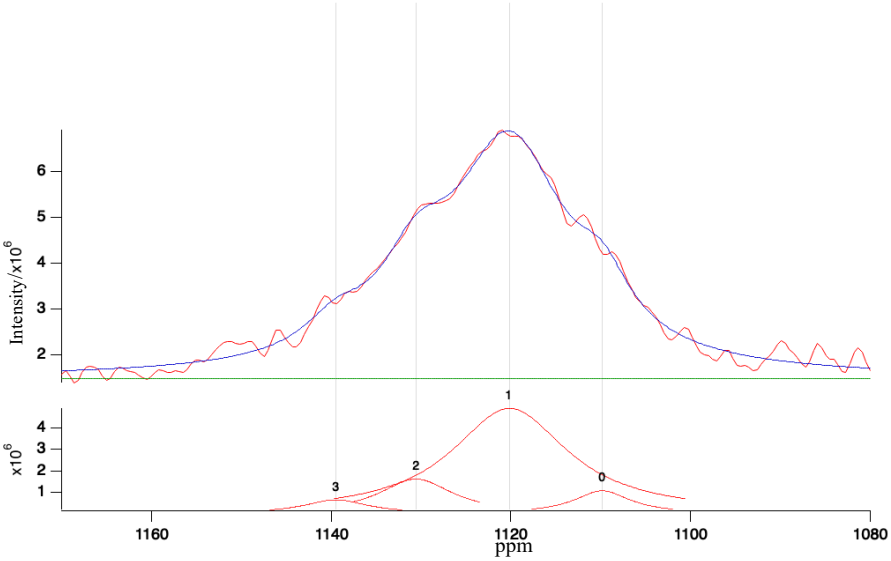

Figure 7-16 140 Degrees Celsius Deconvolution

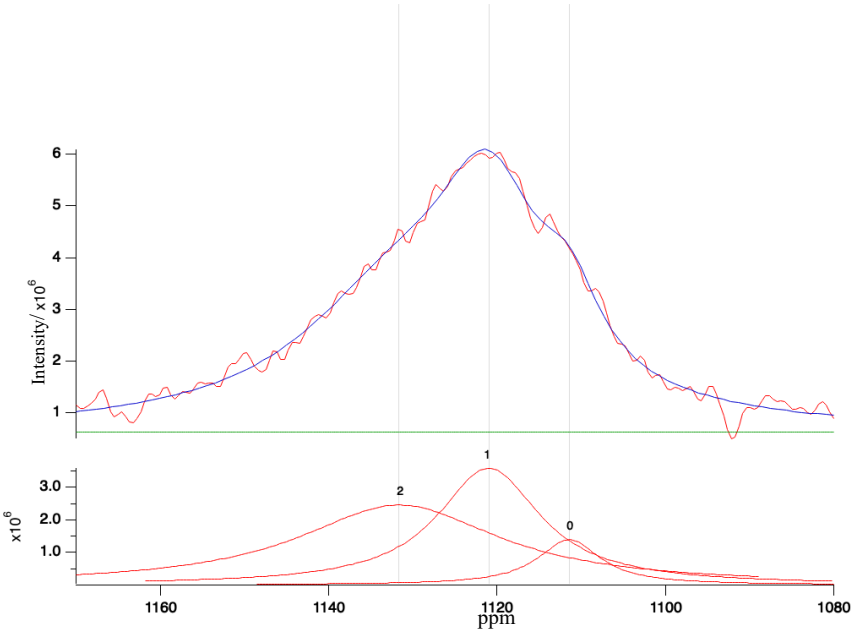

Figure 7-17 150 Degrees Celsius Deconvolution

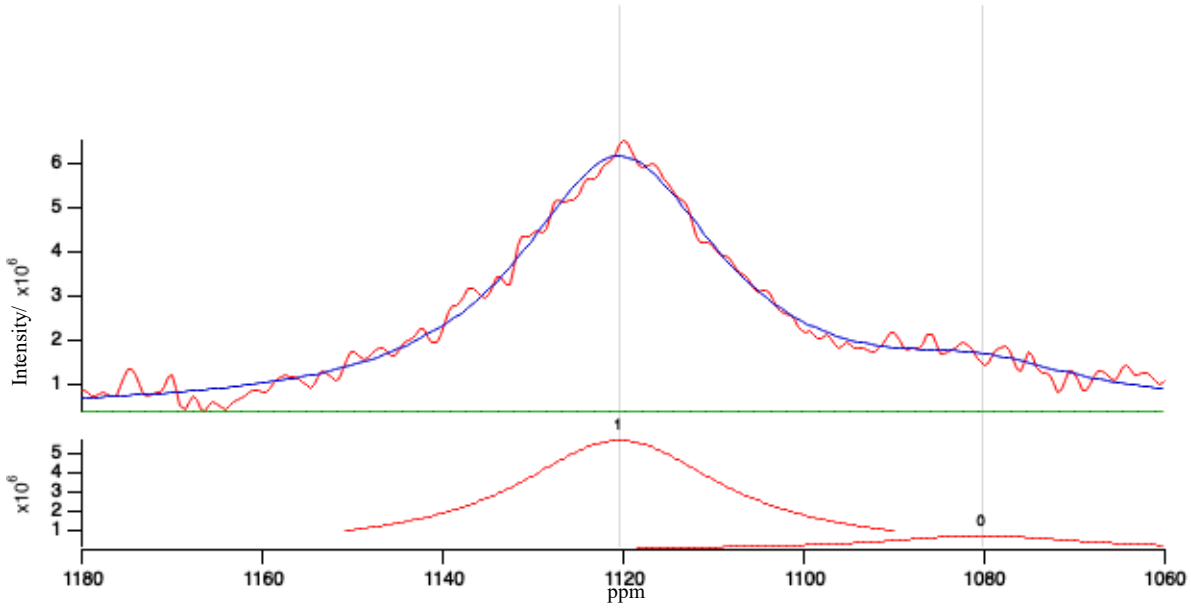

Figure 7-18 160 Degrees Celsius Deconvolution

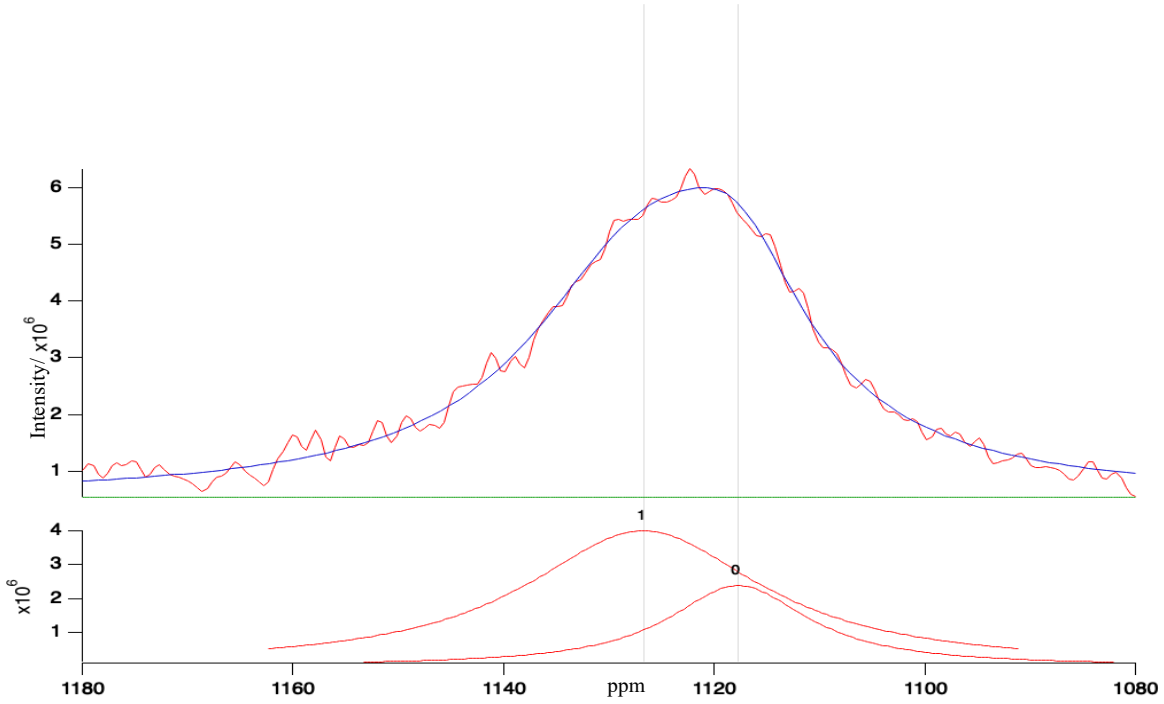

Figure 7-19 180 Degrees Celsius Deconvolution

Higher temperature may bring about a small change in the magic angle of spinning, which will result in broader peaks.

With the relationship obtained earlier, the following table was calculated to estimate the uranyl bond lengths present after further heating of metastudtite causes it to undergo transformation into amorphous UO_{2+x} (which could not be examined with XRD.)

Table 7-4 Deconvolution of broader uranyl peaks belonging to UO_{2+x}

Temp/^{0}C	Position	FWHM	Predicted Bond length	Position	FWHM	Predicted Bond Length	Position	FWHM	Predicted Bond Length
140	1109.8	8.2	1.768	1119.6	14.7	1.770	1130.1	19.7	1.772
150	1111.4	9	1.768	1121	15	1.770	1131.6	29.1	1.772
180	-	-	-	1117.7	16.2	1.770	1126.7	27.3	1.771
AC	1081.9	11.9	1.762	1117.9	19.3	1.770	1131	37.3	1.772

AC- After heating and cooling for 48 hours.

Transition of metastudtite to UO_{2+x} yields at least three different uranyl bond lengths (though there could be more distinct uranyl bond lengths at larger lengths given the increased FWHM, but the resolution of the data renders further deconvolution difficult). The wide variance of x could be reason for the increase in FWHM.

There is confident observation of a shorter uranyl bond length (1.768 Å) and at least one longer one (1.770 Å) which may have result in the distortion from metastudtite to UO_{2+x}. Given that there is a bending of the angle going from studtite to metastudtite in EXAFS studies (Vitova *et al.*, 2018) , it is likely that further heating will result in greater bending and distortion, resulting in variance of bond lengths.

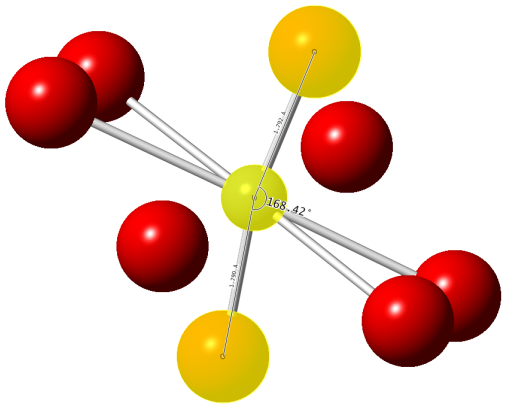

Figure 7-20 Change in bond angle from studtite to metastudtite.

Chapter 8 Discussions and Conclusions

8.1 Dissolution calculations

Phreeqc 3.4.0-13927 (Parkhurst and Appelo, 2013) calculates the equilibrium concentration of ions for a given combination of reactants in solution after inputting initial conditions, such as solubility, pH, Eh, concentration of dissolved oxygen and so forth. Using a referenced thermodynamic database, such as Hatches (Cross and Ewart, 1991), the equilibrium concentration of dissolved uranium ions was estimated by integrating the different speciation of uranium (IV, V, VI) at different concentrations of dissolved oxygen using existing solubility and reaction parameters for UO_2 from the Nuclear Energy Agency (NEA) database.

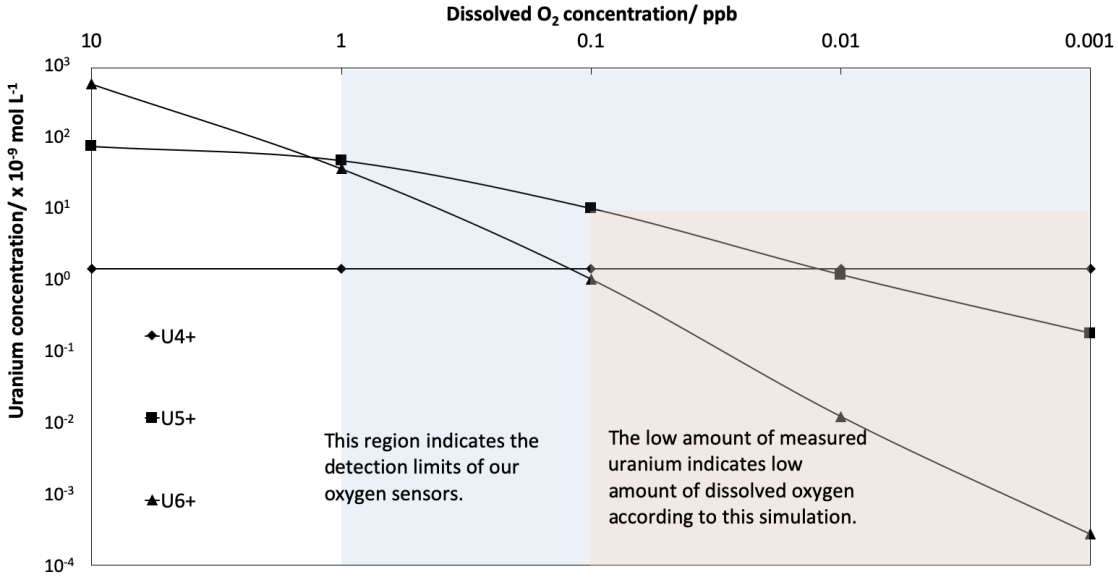

Figure 8-1 Phreeqc simulation of dissolved uranium concentration at equilibrium as a function of oxygen content for UO_2 (NEA) dissolution in deionized water at room temperature, where log K_0 of UO_2 = 54.5 ± 1.0.

Given a starting condition of stoichiometric tetravalent uranium dioxide, oxidation of uranium dioxide, U(IV)O_2 to U^{5+} and U^{6+} are dominant in solution at concentrations of dissolved oxygen above 0.1 ppb. Based on the highest dissolved uranium concentration readings in all the experiments (Figure 5-1) of about 6×10^{-9} mol L^{-1}, from the sum of uranium in all oxidation states, the upper limit of dissolved oxygen in the system is about 0.1 ppb.

Simulations (Figure 8-1) show constant equilibrium concentration of tetravalent uranium at these low levels of dissolved oxygen indicating that anoxic dissolution of uranium dioxide in its tetravalent form proceeds invariably at a limiting rate due to low associated solubility and such tetravalent dissolution becomes dominant at low levels of dissolved oxygen for

stoichiometric uranium dioxide where oxidation of uranium dioxide to higher oxidation levels is seen to drop off sharply according to these thermodynamic calculations.

8.2. Dissolution discussions

There is some variability in reported uranium concentrations for the anoxic dissolution of uranium dioxide, ranging from 10^{-7} mol L^{-1} to 10^{-10} mol L^{-1} (Neck and Kim, 2001) and these have been noted in the NEA database (Grenthe *et al.*, 1992) to result from a range of solids with different thermodynamic stabilities. The common theme from the results of this series of experiments, with different physical forms of UO_2, is that the dissolved uranium concentration is ~10^{-9} mol L^{-1} and in all cases less than 10^{-8} mol L^{-1}, for all physical forms when care is taken to control the oxygen content of the water and therefore oxidation potential of the water. Thermodynamic calculations indicate that concentrations in this range represent the solubility limit of uranium in its tetravalent oxidation state.

The dissolved uranium concentration for the sintered uranium dioxide pellet at 6×10^{-9} mol L^{-1} is slightly higher, about twice the concentration of dissolved uranium concentration of the uranium thin film at 3×10^{-9} mol L^{-1}. This small difference is larger than the error bar and is likely to be real. This may be due to greater dissolution at grain boundaries formed during and despite the sintering process. Preferential dissolution at grain boundaries have been reported for CeO_2 and ThO_2(Corkhill *et al.*, 2016) and it seems to be the case for UO_2 as well.

For the first time, well-defined growth of precipitates at low uranium concentration was observed (Tan *et al.*, 2019). This contradicts the notion of an oxidative dissolution mechanism for U with it transforming to hexavalent form prior to dissolution, as U^{6+} has solubility limits (~10^{-6} mol / L) (Shoesmith, 2000) that are 3 orders of magnitude higher than the U concentration values observed (~10^{-9} mol / L). This difference in solubilities is also observed with anoxic dissolution as ICP-MS results from pre-washes are noted to contain a higher concentration of uranium, which was attributed to preferential dissolution of U^{5+} and U^{6+} in slightly oxidized uranium dioxide.

The low concentration of dissolved uranium ions and the high solubility of hexavalent uranium implies that no secondary phase formation should take place at this concentration if dissolution was going through the hexavalent pathway. Hence, the observation of these uranium

precipitates leads us to conclude that anoxic dissolution of uranium must proceed through the tetravalent phase. Anoxic dissolution of stoichiometric uranium over time is made up of two simultaneous and competing processes.

1) A widely-accepted mechanism of uranium dissolution (Shoesmith, 2000) is a dissolved oxygen-dependent transformation of $U(IV)_{(solid)}$ to $U(V,VI)_{(solid)}$ then $U(VI)_{(aqueous)}$,

This will lead to $U(VI)_{(precipitates)}$ at a high concentration of dissolved uranium ions at its solubility limit, as in the case of oxic dissolution. A small amount of transformation of uranium to higher oxidation states was observed indirectly through the increase in oxygen levels with EDX at the surface of the solid pellet electrode dissolution experiments and from Raman evidence of higher numbers of interstitial oxygens in leached samples, but no significant increase in the dissolved uranium concentration was observed.

2) A proposed non-oxygen dependent $U(IV)_{(solid)}$ to $U(IV)_{(aqueous)}$ then $U(IV)_{(precipitates)}$

Process 2 has been demonstrated to prevail in these sets of anoxic experiments (Tan *et al.*, 2019) and thus has significance in real-life nuclear repositories which are expected be anoxic (Cui *et al.*, 2008).

From the solid pellet experiment, it can be concluded that in anoxic dissolution with low levels of oxygen at 2.0 ppm O_2, it is still possible to observe surface oxidation indirectly from Raman spectroscopy inferences, open circuit potential and EDX measurements. Despite this, the dissolved uranium concentration remains low at 6×10^{-9} mol / L. According to thermodynamic calculations with Phreeqc® in the preceding section, the low concentration of uranium ions implies low amount of dissolved oxygen. More importantly, it also implies that mainly tetravalent uranium ions are present in solution with their characteristic low solubility. Should hexavalent uranium ions be present, the dissolved uranium concentration will be much higher with their high solubility.

Though, with pellet studies, the higher surface roughness inhibits clear observations of any secondary phases that may be formed. Nevertheless, an observation from ICP-MS results of the acid post-washes of the leaching vessel was the detection of an average of 3×10^{-9} mol / L of dissolved uranium in 250 cm^3 of 3.0 M nitric acid. This highlights the presence of uranium sorption/precipitation on the wall of the PTFE vessels as observed before (Carbol *et al*., 2009; Popel *et al*., 2018). Again, the precipitation phenomenon at low uranium concentrations hints

at low solubility being the underlying driver, which highlights tetravalent uranium ions being dissolved and precipitating on the surface of the container.

Considering an accidental container corrosion scenario of 500-1000 years when the container fails and groundwater ingresses, the temperature of spent nuclear fuel interacting with groundwater will be higher than the prevailing underground repository temperatures depending on the fuel burn-up and the waste canisters. Thus, temperatures in the vicinity of the spent nuclear fuel will vary from ~45 ºC to ~130 ºC (Yang and Yeh, 2009).

High-surface area powder dissolution conducted at elevated temperatures for 390 days showed uranium concentrations falling within a range between 0.1×10^{-9} to 2×10^{-9} mol / L. A slight decrease in the mean dissolved uranium concentrations was observed at higher temperatures, albeit within the error bars. Although, it should be noted that the aliquot extraction was performed at an ambient glove box temperature of ~25 °C.

Slightly higher concentration of dissolved uranium concentrations in the solid pellet experiment (6.0×10^{-9} mol / L) might be attributed to a thin layer of higher oxidized uranium on its surface as these samples were not annealed in a reducing environment like the others with values of about 3.0×10^{-9} mol / L. Since the uranium concentration values in the contact solutions were essentially of the same order of magnitude ($\sim 10^{-9}$ mol / L) for the pellet, thin film and powder samples, and formation of a uranium containing secondary phase took place, it can be suggested that the equilibrium uranium concentration in the solution is limited by the solubility of the nucleating secondary phase and is independent of the UO_2 form (bulk pellet, thin film or powder). Just as schoepite's solubility (Cera *et al.*, 2001) forms the upper limit of uranium dissolution in oxic conditions, the limitation of uranium dioxide dissolution in anoxic conditions will be limited by solubility of these uranium (IV) secondary nucleates. Hence, parameters such as specific surface area, density of reactive surface sites, particle sizes and sample crystallinity (amorphous vs. crystalline) should not affect the uranium concentration established in the solution in the long-term and may only affect the kinetic aspects of the process (Batuk, 2007).

8.3 Dissolution Conclusions

For extended durations up to 390 days, the conclusion is that the baseline scenario of uranium dioxide dissolution in deionized water will result in dissolved uranium dioxide concentration

of the order of 10^{-9} mol / L, which is indicative of U^{4+} dissolution. Relatively slight variation in uranium concentrations of less than one order of magnitude are observed between different sets of UO_2 samples (pellets, thin film and powder) which is likely due to increased uranium dioxide dissolution of energetically reactive surface features at grain boundaries of the sintered pellet. Variable temperature dissolution was conducted over a duration of 390 days and the concentration of dissolved uranium did not increase with elevated temperatures.

The dissolved uranium concentration of these long-term anoxic uranium dissolution experiments went through a maximum before decreasing. This is indicative of a dissolution and precipitation mechanism, which is verified by the observed uranium containing secondary phases. At such low dissolved uranium concentration, dissolution and precipitation of uranium is hypothesized to proceed through the tetravalent form. This hypothesis is reinforced by clear observations of clusters (~500 nm) of homogenous uranium-containing precipitates of 20–100 nm grains in the thin film dissolution experiment.

From these experiments, it was concluded that anoxic uranium dissolution with deionized water proceeds in 2 forms simultaneously at the surface.

- a dissolved oxygen-dependent step of $U(IV)_{(solid)}$ to $U(V, VI)_{(solid)}$ then $U(VI)_{(aqueous)}$
- a non oxygen-dependent $U(IV)_{(solid)}$ to $U(IV)_{(aqueous)}$ process to $U(IV)_{(precipitates)}$

$$UO_{2(s,defective)} + 2H_2O_{(l)} \rightarrow U(OH)_{4(aqueous)} \rightleftharpoons UO_{2(s,less\ defective)} + 2H_2O_{(l)},\ \Delta H < 0$$

Equation 8—1

8.4 Development of NMR as a superior analytical technique for uranyl bond lengths.

The research was successful in high-resolution ^{17}O NMR analysis of uranyl-containing compounds, which could resolve uranyl bond-length differences down to a conservative 0.001Å. This is important as NMR is non-destructive and other high- resolution techniques, such as XRD, have been shown to dehydrate and amorphize water-containing crystalline compounds such as studtite, shown in Figure 6-1 where the XRD pattern of studtite which underwent amorphization with extended X-ray radiation in a capillary pXRD measurement in this work. The absence of long-range order meant no Bragg reflections could be observed after 12 hours. Recent attempts to compare bond lengths with non-destructive analysis, such as Raman spectroscopy, have been made by others. In an attempt to characterise uranyl bond length for uranium (VI) phosphates, Clavier et. al related the vibrational bands associated to the uranyl ion, UO_2^{2+} to the U = O bond length for ankoleite ($K(UO_2)PO_4.nH_2O$) and chernikovite ($H_3O(UO_2)PO_4.nH_2O$) with the empirical relationship (Bartlett and Cooney, 1989).

$$\mathbf{R_{U=O} = 10650 \times \left[\nu_1\left(UO_2^{2+}\right)\right]^{-\frac{2}{3}} + 57.5}\text{, where } R_{U=O} \textit{ is in picometers.}$$

Equation 8—2

Table 8-1 Table of recorded Raman signal and corresponding bond length.

Mineral	Measured wavenumber (cm^{-1})	Calculated uranyl bond length,	Reference data from XRD
$K(UO_2)PO_4.nH_2O$ (ankoleite)	826 831	1.79 ± 0.04 1.78 ± 0.04	1.797 ± 0.005 1.777 ± 0.005
$H_3O(UO_2)PO_4.nH_2O$ (chernikovite)	842	1.77 ± 0.04	1.78 ± 0.01 1.75 ± 0.01

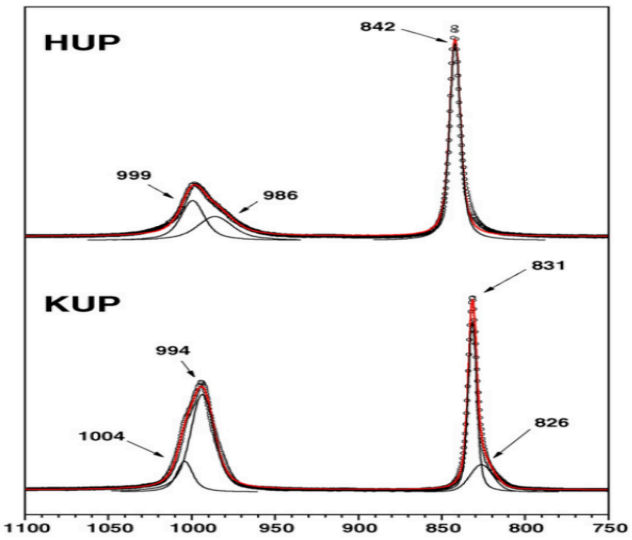

Figure 8-2 Deconvolution of Raman signals

From XRD literature, both these minerals contained 2 unique uranyl bond lengths. Two challenges arose from matching uranyl bond lengths with corresponding Raman signals which can be mitigated with NMR. Firstly, Raman experiments conducted and presented earlier, see Figure 5-4, which demonstrated that even for a homogeneous phase, sample variability and surface roughness require average of multiple readings and subsequent peak fitting to produce representative Raman measurement which can be affected by fluorescence from impurities. This is not the case with NMR where the measurement is a sum of all the signals from the specific NMR-active nuclei in the rotor and for rare isotope, such as ^{17}O, contamination is not an issue.

Secondly, the FWHM of these Raman peaks ranges from 10 cm^{-1} to 20 cm^{-1}. According to Equation 9—1 for typical ranges of uranyl bond lengths shown in Table 9-1 Table of recorded Raman signal and corresponding bond length., the resolutions of the peaks are limited to bond lengths of 0.01Å at best, resulting in difficulty in resolving close peaks as seen in the difficulty to resolve chernikovite. This can be mitigated by NMR with a one order of magnitude increase in resolution as a non-destructive method in analysing uranyl- based compounds.

Considering FWHM, studtite has a FWHM of 9.4 ppm (Table 6-3). Considering the conclusion of Chapter 6, where the relationship between chemical shift and bond length is 60 to 150 ppm per 0.1 Å, this implies that the spread of bond lengths for studtite to be within a range of 0.006 to 0.015 Å, hence uranyl bond lengths for lab synthesis of studtite with hydrogen peroxide produces studtite with nearly uniform uranyl bond lengths of 1.769 ± 0.015 Å.

8.5 Future Work

Due to multiple research pathways that I have undertaken, these pathways diverges to even more pathways for future works.

8.5.1 Nuclear Magnetic Resonance Experiments.

With the calculated bond lengths as an additional identifier, a paper may be produced on how these bond lengths are first identified through NMR and the superior resolution as compared to other non-destructive techniques such as Raman or FTIR spectroscopy in analysing amorphous samples or uranium-containing compounds that are prone to amorphize under X rays (such as studtite).

Unidentified uranium minerals or deposits from short term storage or spent-fuel pools may be analysed with this technique to identify and determine quantitatively the amount of uranium that has dissolved from the storage and reprecipitated as uranium secondary phases. This can be done after some isotropic exchange with ^{17}O water.

It is interesting to observe that uranium compounds containing only oxygen and hydrogen have higher ^{17}O chemical shifts compared to the same compounds with additional calcium, potassium and sodium. With synthesis of suitable uranyl minerals, it will be possible to confirm this observation and arrive hopefully at the ^{17}O chemical shift of uranyl oxygen vis-à-vis the different cations in uranium minerals. For a start, we can focus on other minerals containing cations that are ubiquitous in ground waters such as calcium, potassium and sodium. Subsequently, we can then test our hypothesis that minerals with similar cations and hence similar electronic charge distributions should have similar gradients in terms of chemical shift to bond length.

8.5.2 Nuclear Magnetic Calculations.

Nuclear magnetic resonance simulations build credibility in discerning the origins of NMR spectrum obtained empirically, especially the case for complicated structures where the NMR-active nuclei are found in many sites of different chemical environment or where a simple crystal is prone to distortion which varies bond lengths and angles, such as the UO_3 polymorphs. Apart from being able to discern the origins of NMR peaks in physical and electronic structure, simulations will also allow the analysis of samples that may be difficult to obtain or enrich.

Oxygen peaks from the bound water were calculated to be broad and spread over a range of 60 ppm from *+160 ppm* to *+100 ppm*. Experimentally, it was observed to span a range of 130 ppm between *+50 ppm* to *-80 ppm* however the discrepancy may be in part due to the low signal to noise ratio. This discrepancy is not large and future work will involve better execution of CASTEP NMR calculations of known minerals to refine the pseudopotentials for uranium-based minerals with empirical data justifications, which will increase the reliability of CASTEP in calculation of these compounds.

8.5.3 Variable temperature experiments

Variable temperature NMR has been part of the textbook literature, but these has been typically low temperature NMR with convenient access to liquid nitrogen for cooling of the magnet. Even for high temperature NMR, upper limit of 150 ^{o}C applies for equipment protection. With this new configuration, higher temperature and a larger temperature range is achievable and in-situ evolution of minerals can be observed. The sensitivity of chemical shifts to slight bond length differences will likely extend to other NMR-active nuclei as well, allowing wider applications of this technique.

8.5.4 Dissolution studies

For the unidentified agglomerates and precipitates that has been visually detected in the thin film experiment reported on 5.5 Thin film- SEM results, they can be sent for identification with other powerful techniques, such as transmission electron microscopy (TEM) which can allow the analysis of samples that are less than 100 nm thick and are able to identify these unknown phases. This will require permission in labs with sufficient safety clearances and work with nuclear materials and significant funding.

Dissolution studies has been conducted as a baseline studies. Before departing UK, a solid pellet experiment with calcium as a dopant was executed and a write-up is pending. Determining how different dopants have on the solubility of uranium will enable us to project the amount of uranium leaching out of a nuclear repository in the case of groundwater ingress and such knowledge will influence repository design and fuel fabrication. This will be a nice extension that can be easily executed as most of equipment has been procured. Also, the kinetics of UO_2 dissolution is a topic worth investigating which may also build on the same current experimental set up.

Lastly, it is important to recap that the emphasis of studying uranium dioxide dissolution lies in the determination of the release of radioactivity from spent nuclear fuel but this is only a part of the problem. Apart from that, instant release fractions (Serrano-Purroy *et al.*, 2012; Lemmens *et al.*, 2017) of several percent of total inventory for some radionuclides is also an important and difficult area of research. Together, these will form a holistic study of how radioactivity is released into the environment in the short term and long run as a by-product of nuclear energy, which is projected to play an increasingly important role in mankind's attempts to reduce carbon emissions and arrest global warming.

References

Ahmad, A. and Ramana, M. V. (2014) 'Too costly to matter: Economics of nuclear power for Saudi Arabia', *Energy*. Elsevier Ltd, 69, pp. 682–694. doi: 10.1016/j.energy.2014.03.064.

Allen, G. C., Butler, I. S. and Nguyen, A. T. (1987) 'Characterisation of uranium oxides by micro-Raman spectroscopy', *Journal of Nuclear Materials*, 144(1–2), pp. 17–19. doi: 10.1016/0022-3115(87)90274-1.

Altmaier, M. *et al.* (2017) 'Solubility of U(VI) in chloride solutions. I. The stable oxides/hydroxides in NaCl systems, solubility products, hydrolysis constants and SIT coefficients', *Journal of Chemical Thermodynamics*, 114, pp. 2–13. doi: 10.1016/j.jct.2017.05.039.

Amme, M. (2002) 'Contrary effects of the water radiolysis product H2O2 upon the dissolution of nuclear fuel in natural ground water and deionized water.', *Radiochimica Acta*, 90(7), pp. 399–406.

Amme, M. *et al.* (2005) 'Uranium secondary phase formation during anoxic hydrothermal leaching processes of UO_2 nuclear fuel', *Journal of Nuclear Materials*, 341(2–3), pp. 209–223. doi: 10.1016/j.jnucmat.2005.02.004.

Anderson, B. J. S., Roberts, L. E. J. and Harper, E. A. (1949) Part VII. The Oxidation of Uranium Dioxide in 'The Oxides of Uranium'.

Apperley, D., Harris, R. and Hodgkinson, P. (2012) *Solid-State NMR: Basic Principles & Practice*. Momentum Press. doi: 10.5643/9781606503522.

Ashbrook, S. E. *et al.* (2007) 'First-principles calculations of solid-state ^{17}O and ^{29}Si NMR spectra of Mg_2SiO_4 polymorphs', *Phys. Chem. Chem. Phys.*, 9(13), pp. 1587–1598. doi: 10.1039/B618211A.

Toby, B. (2006) 'R factors in Rietveld analysis: How good is good enough?' in *Powder Diffraction*, pp. 67–70.

Bachmann, F., Hielscher, R. and Schaeben, H. (2010) 'Texture Analysis with MTEX – Free and Open Source Software Toolbox', *Solid State Phenomena*, 160, pp. 63–68. doi: 10.4028/www.scientific.net/SSP.160.63.

Bartlett, J. R. and Cooney, R. P. (1989) 'On the determination of uranium oxygen bond lengths

in dioxouranium(VI) compounds by Raman spectroscopy', *Journal of Molecular Structure*, 193(C), pp. 295–300. doi: 10.1016/0022-2860(89)80140-1.

Batuk, O. N. (2007) 'Behaviour of Uranium Dioxide under Oxidative Hydrothermal Conditions', *PhD Thesis, Lomonosov Moscow Sate University*.

Bernstein, S., Hielscher, R. and Schaeben, H. (2009) *Mathematical Methods in the Applied Sciences*.

Bielecki, A. and Burum, D. P. (1995) 'Temperature Dependence of 207Pb MAS Spectra of Solid Lead Nitrate. An Accurate, Sensitive Thermometer for Variable-Temperature MAS', *Journal of Magnetic Resonance, Series A*, 116(2), pp. 215–220. doi: 10.1006/jmra.1995.0010.

Bonhomme, C. *et al.* (2012) 'First-principles calculation of NMR parameters using the gauge including projector augmented wave method: A chemists point of view', *Chemical Reviews*, 112(11), pp. 5733–5779. doi: 10.1021/cr300108a.

Brugger, J. *et al.* (2011) 'Paulscherrerite from the Number 2 Workings, Mount Painter Inlier, Northern Flinders Ranges, South Australia: "Dehydrated schoepite" is a mineral after all', *American Mineralogist*, 96(2–3), pp. 229–240. doi: 10.2138/am.2011.3601.

Bruker Nano GmbH, Berlin, G. (2010) 'QUANTAX CrystAlign.'

Bruno, J. and Ewing, R. C. (2006) 'Spent nuclear fuel', *Elements*, 2(6), pp. 343–349. doi: 10.2113/gselements.2.6.343.

Buck, E. C. *et al.* (2012) 'Radiolysis Process Modeling Results for Scenarios', *U.S. Doe*. doi: FCRD-UFD-2012-000199.

Burns, P. C., Ewing, R. C. and Miller, M. L. (1997) 'Incorporation mechanisms of actinide elements into the structures of U^{6+} phases formed during the oxidation of spent nuclear fuel', *Journal of Nuclear Materials*, 245(1), pp. 1–9. doi: 10.1016/S0022-3115(97)00006-8.

Burns, P. C. and Hughes, K. A. (2003) 'Studtite,$[(UO_2)(O_2)(H_2O)_2](H_2O)_2$: The first structure of a peroxide mineral', *American Mineralogist*, 88, pp. 1165–1168.

Caldeira, K. *et al.* (2013) *Top climate change scientists issue open letter to policy influencers - CNN*, *CNN*. Available at: https://edition.cnn.com/2013/11/03/world/nuclear-energy-climate-change-scientists-letter/index.html (Accessed: 14 November 2019).

Carbol, P. *et al.* (2009) 'Corrosion of irradiated MOX fuel in presence of dissolved H_2', *Journal*

of Nuclear Materials. Elsevier B.V., 392(1), pp. 45–54. doi: 10.1016/j.jnucmat.2009.03.044.

Celebre, G. (2007) 'An explicit relationship between the dielectric anisotropy and the average electric field gradient in nematic solvents', *Journal of Physical Chemistry B*, 111(10), pp. 2565–2572. doi: 10.1021/jp067309a.

Cera, E. *et al.* (2001) *Modelling of the UO_2 dissolution mechanisms in synthetic groundwater solutions Dissolution experiments carried out under oxic conditions*.

Christensen, H. and Sunder, S. (2000) 'Current state of knowledge of water radiolysis effect on spent nuclear fuel corrosion', *Nuclear Technology*, 131(July).

Clark, D. L. *et al.* (1995) ^{13}O and ^{17}O NMR Binding Constant Studies of Uranyl Carbonate Complexes in Near-Neutral Aqueous Solution in *Yucca Mountain Project Milestone Report 3351*. doi: 10.1007/s00270-017-1725-y.

Clark, S. J. *et al.* (2005) 'First principles methods using CASTEP', *Zeitschrift für Kristallographie - Crystalline Materials*, 220(5/6). doi: 10.1524/zkri.220.5.567.65075.

Clearfield, A. (2008) *Principles and Application of Powder Diffraction*. 1st editio. Wiley-Blackwell.

Coda, B.Y.A. *et al.* (1981) 'The Structure of Synthetic Andersonite, $Na_2Ca[UO_2(CO_3)_3].xH_20$ (x ~ 5.6)', *Acta. Cryst.* pp. 1496–1500.

Cologna, M. *et al.* (2016) 'Sub-micrometre grained UO_2 pellets consolidated from sol gel beads using spark plasma sintering (SPS)', *Ceramics International*. Elsevier, 42(6), pp. 6619–6623. doi: 10.1016/J.CERAMINT.2015.12.172.

Conradson, S. D. *et al.* (2004) 'Local structure and charge distribution in the UO_2 – U_4O_9 system.', *Inorg. Chem.*, (43), pp. 6922–6935.

Corkhill, C. L. *et al.* (2014) 'Contribution of energetically reactive surface features to the dissolution of CeO_2 and ThO_2 analogues for spent nuclear fuel microstructures', *ACS Applied Materials and Interfaces*, 6(15), pp. 12279–12289. doi: 10.1021/am5018978.

Corkhill, C. L. *et al.* (2016) 'Role of Microstructure and Surface Defects on the Dissolution Kinetics of CeO_2, a UO_2 Fuel Analogue', *ACS Applied Materials and Interfaces*, 8(16), pp. 10562–10571. doi: 10.1021/acsami.5b11323.

Costin, D. T. *et al.* (2011) 'How to explain the difficulties in the coffinite synthesis from the

study of uranothorite?', *Inorganic Chemistry*, 50(21), pp. 11117–11126. doi: 10.1021/ic2016758.

Cross, J. E. and Ewart, F. T. (1991) 'Hatches — A Thermodynamic Database And Management System', *Radiochimica Acta*, 52–53(2), pp. 421–422. doi: 10.1524/ract.1991.5253.2.421.

Cui, D. *et al.* (2008) 'The Interaction of Dissolved Hydrogen with Spent Fuel or UO_2 Doped with Alpha', in *Mater. Res. Soc. Symp. Proc.*

Desgranges, L. *et al.* (2010) 'Influence of the U_3O_7 domain structure on cracking during the oxidation of UO_2', *Journal of Nuclear Materials*, 402(2–3), pp. 167–172. doi: 10.1016/j.jnucmat.2010.05.014.

Desgranges, L. *et al.* (2012) 'Raman spectrum of U_4O_9: A new interpretation of damage lines in UO_2', *Journal of Raman Spectroscopy*, 43(3), pp. 455–458. doi: 10.1002/jrs.3054.

Dreissig, I. *et al.* (2011) 'Formation of uranium(IV)-silica colloids at near-neutral pH', *Geochimica et Cosmochimica Acta*, 75(2), pp. 352–367. doi: 10.1016/j.gca.2010.10.011.

Duer, M. J. (2008) *Solid-State NMR Spectroscopy*.

Elorrieta, J. M. *et al.* (2016) 'A detailed Raman and X-ray study of UO_{2+x} oxides and related structure transitions', *Phys. Chem. Chem. Phys.*, 18(40), pp. 28209–28216. doi: 10.1039/C6CP03800J.

Elorrieta, J. M. *et al.* (2018) 'Laser-induced oxidation of UO_2 : A Raman study', *Journal of Raman Spectroscopy*, (December 2017), pp. 878–884. doi: 10.1002/jrs.5347.

Farnan, I. and Berthon, C. (2016) 'Applications of NMR in nuclear chemistry', in Ramesh, V (ed.) *Nuclear Magnetic Resonance, Vol 45*., pp. 96–141. doi: 10.1039/9781782624103-00096.

Feiveson, H. *et al.* (2011) 'Spent Fuel from Nuclear Power Reactors: An Overview of a New Study by the International Panel on Fissile Materials', *International Panel on Fissile Materials*, pp. 1–21.

Fernández, A. *et al.* (2002) 'Transmutation of actinides', *Journal of the American Ceramic Society*, 85(3), pp. 694–696.

Finch, R. J. *et al.* (1996) 'The crystal structure of schoepite, $[(UO_2)_8O_2(OH)_{12}](H_2O)_{12}$', *Canadian Mineralogist*, 34(5), pp. 1071–1088.

Finch, R. J. and Hawthorne, F. C. (1998) 'Structural relations among schoepite , metaschoepite ,

and dehydrated schoepite.', (June).

Forbes, T. Z. *et al.* (2011) 'Alteration of dehydrated schoepite and soddyite to studtite, $[(UO_2)(O_2)(H_2O)_2](H_2O)_2$', *American Mineralogist*, 96(1), pp. 202–206. doi: 10.2138/am.2011.3517.

Fujiwara, K. *et al.* (2005) 'Solubility product of hexavalent uranium hydrous oxide', *Journal of Nuclear Science and Technology*, 42(3), pp. 289–294. doi: 10.1080/18811248.2005.9726392.

Gao, Y. *et al.* (2014) 'Structural and electronic properties of uranium-encapsulated Au 14 cage', *Scientific Reports*, 4. doi: 10.1038/srep05862.

Grant, R. F. and Dunell, B. A. (1960) 'Proton Magnetic Resonance Absorption in the C-Form of Stearic Acid', *Canadian Journal of Chemistry*, 38(3), pp. 359–364. doi: 10.1139/v60-051.

Grenthe, I. *et al.* (1992) 'Chemical Thermodynamics of Uranium', *1992*, p. 715. doi: 10.1063/1.473182.

Guimbretière, G. *et al.* (2013) 'In situ Raman monitoring of He^{2+} irradiation induced damage in a UO_2 ceramic', *Applied Physics Letters*, 103(4). doi: 10.1063/1.4816285.

Guo, X. *et al.* (2014) 'Energetics of metastudtite and implications for nuclear waste alteration', *Proceedings of the National Academy of Sciences*, 111(50), pp. 17737–17742. doi: 10.1073/pnas.1421144111.

Guo, X. *et al.* (2016) 'Thermodynamic studies of studtite thermal decomposition pathways via amorphous intermediates UO_3, U_2O_7, and UO_4', *Journal of Nuclear Materials*, 478, pp. 158–163. doi: 10.1016/j.jnucmat.2016.06.014.

Haeberlen, U. (1976) *High resolution NMR in solids : selective averaging*. Academic Press.

Hanson, B. *et al.* (2005) 'Corrosion of commercial spent nuclear fuel. 1. Formation of studtite and metastudtite', *Radiochimica Acta*, 93(3), pp. 159–168. doi: 10.1524/ract.93.3.159.61613.

He, H. *et al.* (2012) *Corrosion of nuclear fuel (UO_2) inside a failed nuclear waste container | NWMO TR-2012-09*.

He, H., Qin, Z. and Shoesmith, D. W. (2010) 'Characterizing the relationship between hyperstoichiometry, defect structure and local corrosion kinetics of uranium dioxide', *Electrochimica Acta*. Elsevier Ltd, 56(1), pp. 53–60. doi: 10.1016/j.electacta.2010.09.064.

He, H. and Shoesmith, D. (2010) ‘Raman spectroscopic studies of defect structures and phase transition in hyper-stoichiometric UO_{2+x}’, *Physical Chemistry Chemical Physics*, 12(28), p. 8108. doi: 10.1039/b925495a.

Hiemenz, P. C. and Rajagopalan, R. (1997) *Surface Tension and Contact Angle: Application to Pure Substances*, *Principles of Colloid and Surface Chemistry*. doi: 10.1201/9781315274287.

Hiezl, Z. *et al.* (2015) ‘Processing and microstructural characterisation of a UO_2-based ceramic for disposal studies on spent AGR fuel’, *Journal of Nuclear Materials*. Elsevier B.V., 456, pp. 74–84. doi: 10.1016/j.jnucmat.2014.09.002.

Hunger, M. and Brunner, E. (2004) ‘NMR Spectroscopy’, in Karge, H. G. and Weitkamp, J. (eds) *Characterization I: -/-*. Berlin, Heidelberg: Springer Berlin Heidelberg, pp. 201–293. doi: 10.1007/b94236.

Kaminski, M. D. *et al.* (2005) ‘Colloids from the aqueous corrosion of uranium nuclear fuel’, *Journal of Nuclear Materials*, 347(1–2), pp. 77–87. doi: 10.1016/j.jnucmat.2005.07.009.

Klingensmith, A. L. *et al.* (2007) ‘Neptunium incorporation in sodium-substituted metaschoepite’, *American Mineralogist*, 92(4), pp. 662–669. doi: 10.2138/am.2007.2350.

Kohanoff, J. (2006) *Electronic structure calculations for solids and molecules: Theory and computational methods*, *Electronic Structure Calculations for Solids and Molecules: Theory and Computational Methods*. Cambridge University Press. doi: 10.1017/CBO9780511755613.

Kohn, W. and Sham, L. J. (1965) ‘Self-consistent equations including exchange and correlation effects’, *Physical Review*, 140(4A). doi: 10.1103/PhysRev.140.A1133.

Kong, X. *et al.* (2015) ‘Solid-state ^{17}O NMR spectroscopy of paramagnetic coordination compounds’, *Angewandte Chemie - International Edition*, 54(16), pp. 4753–4757. doi: 10.1002/anie.201409888.

Kónya, J. and Nagy, N. M. (2012) ‘Nuclear Energy Production’, *Nuclear and Radiochemistry*. Elsevier, pp. 153–176. doi: 10.1016/B978-0-12-391430-9.00007-X.

Leinders, G. *et al.* (2015) ‘Accurate lattice parameter measurements of stoichiometric uranium dioxide’, *Journal of Nuclear Materials*. Elsevier B.V., 459, pp. 135–142. doi: 10.1016/j.jnucmat.2015.01.029.

Leinders, G. (2018) 'Low-Temperature Oxidation of Fine UO_2 Powders: Thermochemistry and Kinetics', *Inorganic Chemistry*, 9, pp. 2–10. doi: 10.1021/acs.inorgchem.8b00517.

Lemmens, K. *et al.* (2017) 'Instant release of fission products in leaching experiments with high burn-up nuclear fuels in the framework of the Euratom project FIRST- Nuclides', *Journal of Nuclear Materials*. Elsevier Ltd, 484, pp. 307–323. doi: 10.1016/j.jnucmat.2016.10.048.

Levitt, M. H. (2000) 'Spin Dynamics Basics of Nuclear Magnetic Resonance', p. 653.

Li, Y. and Burns, P. C. (2001) 'The Crystal Structure of Synthetic Grimselite, $K_3Na[(UO_2)(CO_3)_3](H_2O)$', *The Canadian Mineralogist*, 39, pp. 1147–1151.

MacKenzie, K. J. D. and Smith, M. E. (2002) *Multinuclear solid-state NMR of inorganic materials*. Pergamon.

Minas da Piedade, Manuel E. and Berberan-Santos, Mario N. (1998) Atomic Emission Spectra Using a UV-Vis Spectrophotometer and an Optical Fiber Guided Light Source, *Journal of Chemical Education*, 75(8), pp 1013-1017

Marchenko, A., Truflandier, L. A. and Autschbach, J. (2017) 'Uranyl Carbonate Complexes in Aqueous Solution and Their Ligand NMR Chemical Shifts and ^{17}O Quadrupolar Relaxation Studied by ab Initio Molecular Dynamics', *Inorganic Chemistry*, 56(13), pp. 7384–7396. doi: 10.1021/acs.inorgchem.7b00396.

Maslakov, K. I. *et al.* (2018) 'XPS study of the surface chemistry of UO_2 (111) single crystal film', *Applied Surface Science*. Elsevier B.V., 433, pp. 582–588. doi: 10.1016/j.apsusc.2017.10.019.

Maslova, O. A. *et al.* (2017) 'Raman imaging and principal component analysis-based data processing on uranium oxide ceramics', *Materials Characterization*. Elsevier, 129(May), pp. 260–269. doi: 10.1016/j.matchar.2017.05.015.

McMahon, C. *et al.* (2013) 'Boundary identification in EBSD data with a generalization of fast multiscale clustering', *Ultramicroscopy*. Elsevier, 133, pp. 16–25. doi: 10.1016/j.ultramic.2013.04.009.

MIT (2011) *The Future of the Nuclear Fuel Cycle*, *Massachusetts Institute of Technology*. Available at http://medcontent.metapress.com/index/A65RM03P4874243N.pdf%0Ahttps://mitei.mit.edu/system/files/The_Nuclear_Fuel_Cycle-all.pdf.

Moran, R. F., Dawson, D. M. and Ashbrook, S. E. (2017) 'Exploiting NMR spectroscopy for the study of disorder in solids', *International Reviews in Physical Chemistry*. Taylor & Francis, 36(1), pp. 39–115. doi: 10.1080/0144235X.2017.1256604.

NDA (2010) *Geological disposal steps*, *NDA Report*.

Neck, V. and Kim, J. I. (2001) 'Solubility and hydrolysis of tetravalent actinides', *Radiochimica Acta*, 89(1), pp. 1–16. doi: 10.1524/ract.2001.89.1.001.

Nerikar, P. *et al.* (2009) 'Energetics of intrinsic point defects in uranium dioxide from electronic-structure calculations.', *J.Nucl.Mater*, (384), pp. 61–69.

Nikolayev, D. I. and Schaeben, H. (1999) *Inverse Problems*.

Nonbol, E. (1996) *Description of the Advanced Gas Cooled Type of Reactor (AGR)*. Denmark.

Odoh, S. O. *et al.* (2016) 'Structure and Reactivity of X-ray Amorphous Uranyl Peroxide, U2O7', *Inorganic Chemistry*, 55(7), pp. 3541–3546. doi: 10.1021/acs.inorgchem.6b00017.

Okada, Y. and Tokumaru, Y. (1984) 'Precise determination of lattice parameter and thermal expansion coefficient of silicon between 300 and 1500 K', *Journal of Applied Physics*, 56(2), pp. 314–320. doi: 10.1063/1.333965.

Ollila, K., Olin, M. and Lipponen, M. (1996) 'Solubility and Oxidation State of Uranium under Anoxic Conditions (N 2 Atmosphere)', *Radiochimica Acta*, 74, pp. 9–13. Available at: https://www.degruyter.com/downloadpdf/j/ract.1996.74.issue-s1/ract.1996.74.special-issue.9/ract.1996.74.special-issue.9.pdf.

Opel, K. *et al.* (2007) 'Study of the solubility of amorphous and crystalline uranium dioxide by combined spectroscopic methods', *Radiochimica Acta*, 95(3), pp. 143–149. doi: 10.1524/ract.2007.95.3.143.

Parkhurst, D. L. and Appelo, C. A. . (2013) *Description of input and examples for PHREEQC version 3-- A computer program for speciation, batch- reaction, one- dimensional transport, and inverse geochemical calculations*.

Pickard, C. J. and Mauri, F. (2001) 'All-electron magnetic response with pseudopotentials: NMR chemical shifts', *Physical Review B*, 63, pp. 1–13. doi: 10.1103/PhysRevB.63.245101.

Pijolat, M. *et al.* (1997) 'Reduction of uranium oxide U_3O_8 to UO_2 by hydrogen', *Solid State Ionics*. Elsevier, 101–103, pp. 931–935. doi: 10.1016/S0167-2738(97)00385-8.

Plášil, J. *et al.* (2012) 'The crystal chemistry of the uranyl carbonate mineral grimselite, (K, $Na)_3Na[(UO_2)(CO_3)_3](H2O)$, from Jáchymov, Czech Republic', *Mineralogical Magazine*. Cambridge University Press, 76(03), pp. 443–453. doi: 10.1180/minmag.2012.076.3.01.

Plášil, J. and Čejka, J. (2015) 'A note on the molecular water content in uranyl carbonate mineral andersonite', *Journal of Geosciences (Czech Republic)*, 60(3), pp. 181–187. doi: 10.3190/jgeosci.193.

Popel, A. J. *et al.* (2017) 'The effect of fission-energy Xe ion irradiation on dissolution of UO_2 thin films', *Journal of Alloys and Compounds*, 721, pp. 586–592. doi: 10.1016/j.jallcom.2017.05.084.

Popel, A. J. *et al.* (2018) 'The effect of ion irradiation on the dissolution of UO_2 and UO_2-based simulant fuel', *Journal of Alloys and Compounds*. Elsevier B.V, 735, pp. 1350–1356. doi: 10.1016/j.jallcom.2017.11.216.

Poturaj-Gutniak, S. and Taube, M. (1968) 'Some remarks about 5f → 6d and charge transfer transitions in uranium(IV) and plutonium(IV) complexes', *Journal of Inorganic and Nuclear Chemistry*, 30(4), pp. 1005–1012. doi: 10.1016/0022-1902(68)80319-7.

Princeton Instruments (2012) 'Raman Spectroscopy Basics - Application Note', *Internet: http://content. piacton. com/Uploads/Princeton/*, pp. 1–5. Available at: http://content.piacton.com/Uploads/Princeton/Documents/Library/UpdatedLibrary/Raman_Spectroscopy_Basics.pdf.

Profeta, M., Mauri, F. and Pickard, C. J. (2003) 'Accurate first principles prediction of ^{17}O NMR parameters in SiO_2: Assignment of the zeolite ferrierite spectrum', *Journal of the American Chemical Society*, 125(2), pp. 541–548. doi: 10.1021/ja027124r.

Purans, J. *et al.* (2009) 'Femtometer accuracy EXAFS measurements: Isotopic effect in the first, second and third coordination shells of germanium', *Journal of Physics: Conference Series*, 190(November). doi: 10.1088/1742-6596/190/1/012063.

Rai, D., Felmy, A. R. and Ryan, J. L. (1990) 'Uranium(IV) Hydrolysis Constants and Solubility Product of $UO_2 \cdot xH_2O$(am)', *Inorganic Chemistry*, 29(2), pp. 260–264. doi: 10.1021/ic00327a022.

Razdan, M. and Shoesmith, D. W. (2013) 'Influence of Trivalent-Dopants on the Structural and Electrochemical Properties of Uranium Dioxide (UO_2)', *Journal of the Electrochemical*

Society, 161(3), pp. H105–H113. doi: 10.1149/2.047403jes.

Rey, A. *et al.* (2009) 'Effect of temperature on studtite stability: Thermogravimetry and differential scanning calorimetry investigations', *Journal of Nuclear Materials*. Elsevier B.V., 385(2), pp. 467–473. doi: 10.1016/j.jnucmat.2008.12.045.

Sattonnay, G. *et al.* (2001) 'Alpha-radiolysis effects on UO_2 alteration in water', *Journal of Nuclear Materials*, 288(1), pp. 11–19. doi: 10.1016/S0022-3115(00)00714-5.

Schwertmann, U. (1991) 'Solubility and dissolution of iron oxides', *Plant and Soil*, 130(1–2), pp. 1–25. doi: 10.1007/BF00011851.

Segall, M. and Probert, M. (2002) 'First-Principles Simulation : Ideas , Illustrations and the CASTEP Code', (July 2015). doi: 10.1088/0953-8984/14/11/301.

Serrano-Purroy, D. *et al.* (2012) 'Instant release fraction and matrix release of high burn-up UO_2 spent nuclear fuel: Effect of high burn-up structure and leaching solution composition', *Journal of Nuclear Materials*. Elsevier B.V., 427(1–3), pp. 249–258. doi: 10.1016/j.jnucmat.2012.04.036.

Shoesmith, D. W. (2000) 'Fuel corrosion processes under waste disposal conditions', *Journal of Nuclear Materials*, 282(1), pp. 1–31. doi: 10.1016/S0022-3115(00)00392-5.

Shoesmith, D. W. and Sunder, S. (1992) 'The prediction of nuclear fuel (UO_2) dissolution rates under waste disposal conditions', *Journal of Nuclear Materials*, 190(C), pp. 20–35. doi: 10.1016/0022-3115(92)90072-S.

Solid-State NMR Spectroscopy Principles and Applications (2001). doi: 10.1002/9780470999394.

Stumm, W. (1997) 'Reactivity at the mineral-water interface: Dissolution and inhibition', *Colloids and Surfaces A: Physicochemical and Engineering Aspects*, 120(1–3), pp. 143–166. doi: 10.1016/S0927-7757(96)03866-6.

Sturniolo, S. *et al.* (2016) 'Visualization and processing of computed solid-state NMR parameters: MagresView and MagresPython', *Solid State Nuclear Magnetic Resonance*. Elsevier, 78, pp. 64–70. doi: 10.1016/j.ssnmr.2016.05.004.

Szenknect, S. *et al.* (2016) 'First experimental determination of the solubility constant of coffinite', *Geochimica et Cosmochimica Acta*, 181, pp. 36–53. doi: 10.1016/j.gca.2016.02.010.

Takahashi, T. *et al.* (1999) '207Pb chemical shift thermometer at high temperature for magic angle spinning experiments', *Solid State Nuclear Magnetic Resonance*, 15(2), pp. 119–123. doi: 10.1016/S0926-2040(99)00039-9.

Tan, B. T. *et al.* (2019) 'Surface and electrochemical controls on UO_2 dissolution under anoxic conditions', *Journal of Nuclear Materials*. Elsevier B.V, 520, pp. 41–55. doi: 10.1016/j.jnucmat.2019.03.047.

Taylor, J. C. *et al.* (1972) 'A Study of the Beta to Alpha Phase Transition in $UO_2(OH)_2$ by Dilatometric , Microcalorimetric and X-Ray Diffraction Techniques', 7269(2), pp. 291–299.

Taylor, J. C. and Hurst, H. J. (1971) 'The hydrogen-atom locations in the alpha and beta forms of uranyl hydroxide', *Acta Crystallography*. International Union of Crystallography, (B27), pp. 2018–2022. doi: 10.1107/S0567740871005259.

The MathWorks, N. (2016) 'MATLAB 2016a',.

Ulrich, K. U. *et al.* (2009) 'Comparative dissolution kinetics of biogenic and chemogenic uraninite under oxidizing conditions in the presence of carbonate', *Geochimica et Cosmochimica Acta*. Elsevier Ltd, 73(20), pp. 6065–6083. doi: 10.1016/j.gca.2009.07.012.

Vitova, T. *et al.* (2018) 'Dehydration of the Uranyl Peroxide Studtite, $[UO_2(n^2\text{-}O_2)(H_2O)_2]\cdot 2H_2O$, Affords a Drastic Change in the Electronic Structure: A Combined X-ray Spectroscopic and Theoretical Analysis', *Inorganic Chemistry*, 57(4), pp. 1735–1743. doi: 10.1021/acs.inorgchem.7b02326.

Van De Walle, C. G. and Blöchl, P. E. (1993) 'First-principles calculations of hyperfine parameters', *Physical Review B*, 47(8), pp. 4244–4255. doi: 10.1103/PhysRevB.47.4244.

Weck, P. F. *et al.* (2012) 'Structures of uranyl peroxide hydrates: a first-principles study of studtite and metastudtite', *Dalton Transactions*, 41(32), p. 9748. doi: 10.1039/c2dt31242e.

Weck, P. F. and Kim, E. (2014) 'Layered uranium(vi) hydroxides: Structural and thermodynamic properties of dehydrated schoepite α-$UO_2(OH)_2$', *Dalton Transactions*. Royal Society of Chemistry, 43(45), pp. 17191–17199. doi: 10.1039/c4dt02455a.

Whittaker, E. J. (1982) 'Cleavage energies of minerals', *Mineralogical Magazine*, 46(September), pp. 398–9.

Widdifield, C. M. and Schurko, R. W. (2008) 'Understanding chemical shielding tensors using

group theory, MO analysis, and modern density-function', in *Concepts in Magnetic Resonance*. Wiley Interscience, pp. 91–123.

Wilbraham, R. J. *et al.* (2015) 'The effect of hydrogen peroxide on uranium oxide films on 316L stainless steel', *Journal of Nuclear Materials*. Elsevier B.V., 464, pp. 86–96. doi: 10.1016/j.jnucmat.2015.04.007.

World Nuclear Association (2018a) *Nuclear Power in China*. World Nuclear Association. Available at: http://www.world-nuclear.org/information-library/country-profiles/countries-a-f/china-nuclear-power.aspx (Accessed: 30 September 2018).

World Nuclear Association (2018b) *Nuclear Power in Saudi Arabia*, *May*. Available at: http://www.world-nuclear.org/information-library/country-profiles/countries-o-s/saudi-arabia.aspx (Accessed: 30 September 2018).

World Nuclear Association (2018c) 'World Nuclear Performance Report', *World Nuclear Association*, 1, p. 32. doi: 10.1109/PVSC.2009.5411432.

Yager, K. (2014) *Atomic scattering factors - GISAXS*. Available at: http://gisaxs.com/index.php/Atomic_scattering_factors (Accessed: 16 September 2019).

Yang, S. Y. and Yeh, H. D. (2009) 'Modeling transient heat transfer in nuclear waste repositories', *Journal of Hazardous Materials*, 169(1–3), pp. 108–112. doi: 10.1016/j.jhazmat.2009.03.068.

Zänker, H. and Hennig, C. (2014) 'Colloid-borne forms of tetravalent actinides: A brief review', *Journal of Contaminant Hydrology*. Elsevier B.V., 157, pp. 87–105. doi: 10.1016/j.jconhyd.2013.11.004.

Zhang, T. Y. and Zhao, M. H. (2002) 'Equilibrium depth and spacing of cracks in a tensile residual stressed thin film deposited on a brittle substrate', *Engineering Fracture Mechanics*, 69(5), pp. 589–596. doi: 10.1016/S0013-7944(01)00098-4.

Appendix

Appendix 1: Power reactors under construction

Start	Location	Reactor	Model	Gross MWe
2019	Finland, TVO	Olkilouto 3	EPR	1720
2019	Russia, Rosenergoatom	Pevek FNPP	KLT40S x 2	70
2019	China, CGN	Fangchenggang 3	Hualong One	1150
2019	China, CGN	Hongyanhe 5	ACPR-1000	1080
2019	China, CGN	Yangjiang 6	ACPR-1000	1087
2019	China, CNNC	Fuqing 5	Hualong One	1161
2019	China, CNNC	Tianwan 4	VVER-1000	1060
2019	China, CGN	Taishan 2	EPR	1750
2019	France, EDF	Flamanville 3	EPR	1750
2019	Korea, KHNP	Shin-Kori 4	APR1400	1400
2019	Korea, KHNP	Shin-Hanul 2	APR1400	1400
2019	Slovakia, SE	Mochovce 3	VVER-440	471
2019	Belarus, BNPP	Ostrovets 1	VVER-1200	1194
2020	Russia, Rosenergoatom	Novovoronezh II-2	VVER-1200	1200
2020	China, CGN	Hongyanhe 6	ACPR-1000	1080
2020	China, CGN	Fangchenggang 4	Hualong One	1150
2020	China, CNNC	Tianwan 5	ACPR-1000	1080
2020	China, CNNC	Fuqing 6	Hualong One	1161
2020	China, CGN	Bohai shipyard	ACPR50S	60
2020	UAE, ENEC	Barakah 1	APR1400	1400
2020	UAE, ENEC	Barakah 2	APR1400	1400
2020	Belarus, BNPP	Ostrovets 2	VVER-1200	1194
2020	Slovakia, SE	Mochovce 4	VVER-440	471
2020	Japan, Chugoku	Shimane 3	ABWR	1373

Appendix 2: China Nuclear Exports

Country	Plant	Type	Est. cost (billion USD)	Company
Pakistan	Chasma 3&4	CNP-300	2.37	CNNC
	Karachi Coastal 1&2	Hualong One	9.6	CNNC
Romania	Cernavoda 3&4	Candu 6	8.9	CGN
Argentina	Atucha 3	Candu 6	5.8	CNNC
	5th Argentine reactor	Hualong One	7	CNNC
UK	Bradwell	Hualong One		CGN
Iran	Makran coast	2 x 100 MWe		CNNC
Turkey	Igneada	AP1000 and CAP1400		SNPTC
South Africa	Thyspunt	CAP1400		SNPTC
Kenya		Hualong 1		CGN
Egypt		Hualong 1		CNNC
Sudan		ACP600		CNNC
Armenia	Metsamor	1 reactor		CNNC
Kazakhstan		Fuel plant JV		CGN

Appendix 3: Studtite Geometric Optimisation Parameters.

comment : CASTEP calculation on hpcf	
continuation = default	*Continuation contains a string which specifies the model file used to continue the job. Default (case-insensitve) means that the file seedname.check will be used.*
task : geometry optimisation	*The task GeometryOptimization searches for a minimum energy structure.*
ELEC_METHOD=EDFT	*Ensemble Density Functional Theory (EDFT) is a stable but slow method of solving the Kohn-Sham equations. In EDFT, the density is always computed directly from the estimated ground-state wavefunction, and these wavefunctions are only ever updated in a way which brings them closer to the ground state.*
max_scf_cycles = 200	*This keyword determines the maximum number of SCF cycles performed in an electronic minimization. It will end after this many cycles, regardless of whether the convergence criteria have been met.*
geom_max_iter = 400	*This keyword determines the maximum number of steps in a geometry optimization.*
geom_method=BFGS	*This keyword determines the method used for geometry optimization. Broyden–Fletcher–Goldfarb–Shanno (BFGS) algorithm is an iterative method for cell optimization, including optimization at fixed external stress. It uses a starting Hessian which is recursively updated during optimization.*
xc_functional : PBE	*Gradient-corrected exchange-correlation functionals, GGA functionals provide a better overall description of the electronic subsystem than the LDA but it tends to underbind atoms resulting in slightly longer bond lengths. PBE is the default exchange-correlation functional and reliable for bulk calculations. .*
fix_occupancy = true	*Fixed occupancy option is suitable for insulators.*
opt_strategy : speed	*Optimization strategy of speed maximizes performance at the cost of additional memory usage.*
basis_precision : extreme	*This keyword specifies the precision of the basis set by choosing the level of convergence of atomic energies with respect to the plane wave cutoff energy for the pseudopotentials used in the calculation. At extreme setting, the convergence is about 0.01 eV/ atom.*
write_cell_structure: T write_cif_structure: T	*The output crystal structure is produced as a cif file and a cell file. The cell file will be needed as an input for subsequent CASTEP calculation whereas CIF files are crystallographic information files which is the standard text file format and can be used with many visualization software such as Crystalmaker®.*

Appendix 4: Studtite Magres Parameters.

comment : CASTEP calculation on hpcf

continuation = default	*Continuation contains a string which specifies the model file used to continue the job. Default (case-insensitve) means that the file seedname.check will be used.*
task : magres magres_task : NMR	*The task magres performs an NMR calculation with the input cell file.*
ELEC_METHOD=EDFT	*Ensemble Density Functional Theory (EDFT) is a stable but slow method of solving the Kohn-Sham equations. In EDFT, the density is always computed directly from the estimated ground-state wavefunction, and these wavefunctions are only ever updated in a way which brings them closer to the ground state.*
max_scf_cycles = 400	*This keyword determines the maximum number of SCF cycles performed in an electronic minimization. It will end after this many cycles, regardless of whether the convergence criteria have been met.*
xc_functional : PBE	*Gradient-corrected exchange-correlation functionals, GGA functionals provide a better overall description of the electronic subsystem than the LDA but it tends to underbind atoms resulting in slightly longer bond lengths. PBE is the default exchange-correlation functional and reliable for bulk calculations. .*
fix_occupancy = true	*Fixed occupancy option is suitable for insulators.*
opt_strategy : speed	*Optimization strategy of speed maximizes performance at the cost of additional memory usage.*
BASIS_PRECISION : extreme	*This keyword specifies the precision of the basis set by choosing the level of convergence of atomic energies with respect to the plane wave cutoff energy for the pseudopotentials used in the calculation. At extreme setting, the convergence is about 0.01 eV/ atom.*
Relativistic _treatment = ZORA	*This keyword selects the method used to treat relativistic effects. ZORA is a scalar relativistic treatment, which is equivalent to the zeroth-order expansion of the Koelling-Harmon equation.*

Filename: finale 4k.docx
Directory: /Users/bryan/Library/Containers/com.microsoft.Word/Data/Documents
Template: /Users/bryan/Library/Group Containers/UBF8T346G9.Office/User Content.localized/Templates.localized/Normal.dotm
Title: Alteration mechanisms of spent nuclear fuel and investigative studies into potential uranium secondary phases.
Subject:
Author: Beng Thye Tan
Keywords:
Comments:
Creation Date: 17/02/2020 12:35:00
Change Number: 5
Last Saved On: 22/02/2020 09:30:00
Last Saved By: B.T. Tan
Total Editing Time: 10 Minutes
Last Printed On: 22/02/2020 09:31:00
As of Last Complete Printing
Number of Pages: 205
Number of Words: 48,881 (approx.)
Number of Characters: 278,622 (approx.)